GROWTH AND CHARACTERIZATION OF TWO DIMENSIONAL CARBON NANOSTRUCTURES

WANG HAOMIN

NATIONAL UNIVERSITY OF SINGAPORE

2009

GROWTH AND CHARACTERIZATION OF TWO DIMENSIONAL CARBON NANOSTRUCTURES

WANG HAOMIN

(B. Eng., M. Eng., Huazhong University of Science and Technology, P. R. China)

A THESIS SUBMITTED

FOR THE DEGREE OF DOCTOR OF PHILOSOPHY

DEPARTMENT OF ELECTRICAL AND COMPUTER ENGINEERING

NATIONAL UNIVERSITY OF SINGAPORE

2009

ACKNOWLEDGEMENTS

The work in this thesis could not have been accomplished without the contribution of guidance, support and friendship of many people.

First of all, great gratitude should be extended to my supervisor, Professor Wu Yihong, for his valuable guidance and helpful technical support throughout my PhD study. Had it not been for his advice, direction, patience and encouragement, this thesis would certainly not be possible. Not only his serious attitude towards research but also his courage to face difficulties makes a great impact on me.

I am grateful to my co-supervisor, A/P Teo Kie Leong for his kind help and encouragement over the entire course of my Ph. D project.

I am glad that I have so many considerate and supportive labmates. I bother them whenever I want: Dr. Yang Binjun helped me with the MPECVD system and SEM observations in the beginning of my research study; Mr. Liu Tie imparted me his experimental skills in photo/e-beam lithography, the cryostat system and electrical characterization; Ms. Ji Rong let me know how to use Raman spectrometer in DSI; Mr. Tsan Jing Ming assisted me in the CNWs growth experiments; Ms. Delaram Abedi helped me in the Raman characterization on CNWs; Mr. Chen Junhao helped me in the low temperature measurement on CNW devices; Mr. Teo Guoquan conducted the simulation on visibility study of graphene in multilayered structure; Mr. Xiong Feng set up the lock-in measurement system and helped conduct electrical characterization on graphene devices at low temperature; Dr. Ni Zhenhua and Ms. Wang Yingying helped me in the Raman and contrast characterization on grapheme flakes; Prof. Shen Zhexiang and Dr. Yu Ting allowed us to use their Raman spectrometer in NTU; Dr. Zhao

Zheliang and Dr. Wang Junzhong maintained the cryostat system in good condition; Ms. Naganivetha Thiyagarajah was willing to show me her techniques in using E-beam lithography system; Dr. Sunny Lua and Dr. Li Hongliang shared their experience in e-beam evaporator; Dr. Han Gang showed me how to operate the mini-sputtering system; Special thanks go to Ms. Catherine Choong who has helped conduct the laborious low-temperature measurement on most of my CNW devices.

Sincere thanks should also go to all the staff in both Information Storage and Materials Laboratory (ISML) of the National University of Singapore (NUS) and Data Storage Institute (DSI). They are true professionals. They have been important for smooth experiments for the users. They have helped me in one way or another in my studies and daily life. I also want to acknowledge the excellent experimental and study environment provided by both NUS and DSI.

I am indebted to other fellow group members. Working with Mr. Liu Wei, Dr. Maureen Tay, Dr. K. S. Sunil, and Mr. Saidur Rahman Bakaul, has been a lot of fun. Their friendship and happy time spent with them throughout four years of studies. I am also grateful to everyone else of my friends for their deep concern and enthusiastic support. Sharing with them the joy and frustration has made my life fruitful and complete.

The scholarship provided by the National University of Singapore for my PhD is gratefully acknowledged. Lastly but most importantly, I deeply am thankful for the continuous care and support of my family throughout my whole course of study.

TABLE OF CONTENTS

ABSTRACT

This dissertation focuses on the electronic transport properties of carbon nanowalls and graphene flakes. The former has been carried out by using both normal metal (Ti) and superconductor (Nb) electrodes. Bottom electrodes are employed in the experiments. Comparing to top-electrode configuration, this configuration could help to narrow the electrode spacing of devices down below 1 μm.

In the Ti/CNW/Ti junctions, the experimental results show the presence of a narrow band gap and conductance fluctuations within a certain temperature range. Excess conductance fluctuations observed between 4 and 300 K are attributed to the quantum interference effect under the influence of thermally induced carrier excitation across a narrow bandgap. The sharp suppression of conductance fluctuation below 2.1 K is accounted for by the formation of a layer of He 4 superfluid on the nanowalls. The results obtained here have important implications for potential application of CNWs in electronic devices. A giant gap-like behavior of dI/dV is also observed in some samples. The gap indicates that some phase transition may happen in those CNWs at low temperature.

For Nb/CNW/Nb junctions, superconducting proximity effect was observed in two samples with short electrode spacing. Their temperature dependence of critical current is in good agreement with both Josephson coupling in long diffusive model and Ginzburg-Landau relationship. The above-gap feature and Andrev reflection were observed in the two samples. Their magnetic field dependence was also discussed. However, in other Nb/CNWs/Nb devices, results of proximity effect with respect to the electrode spacing are not consistent. This may be due to many reasons, such as the orientation of CNWs, quality of CNW sheet, the transparency of Nb/CNWs interface.

In the second part of this thesis, we discuss the electric transport properties of graphene on SiO_2 substrate with different number of layer under ambient condition. By examining carrier mobility, minimal conductivity and conductance hysteresis in graphene devices, it is found that the substrate interface and surface impurity may greatly affect the transport properties of graphene on SiO_2 substrate. Our experimental results indicate that magneto transport and conductance fluctuation in graphene devices are greatly affected by the charged impurities at the substrate/graphene interface.

LIST OF TABLES

LIST OF FIGURES

NOMENCLATURE

A	area
B	magentic induction
C	contrast spectrum
C_g	capacitance per unit area
d	thickness
D	diffusion coefficient
e	electron charge
E_c	Thouless energy
E_C	bottom of conduction band
E_F	Fermi energy
E_V	top of valance band
E_J	Josephson coupling energy
G	conductance
H	magnetic field strength
H_c	coercivity
I	current
I_c	critical supercurrent.

k	wavevector
k_B	Boltzmann constant
L	length
L_{mfp}	mean free path
L_T	thermal length
n_S	reflective index
N	carrier density of electrons
N_{it}	interface traps
N_{ot}	oxide traps
$N(E_F)$	density of state of the electron at the Fermi level
p	the carrier density of holes
R	resistance
R_a	surface roughness
R_c	contact resistance
R_N	the normal state resistance
R_{xx}	longitudinal resistance
R_{xy}	transversel resistance
t	time
T	temperature
Tc	Critical temperature

V	voltage
V_{np}	the voltage at the neutriality point of graphene
V_g	the gate voltage
W	width
Z	barrier strength.
ΔE_g	energy gap
a	lattice constant
$\vec{a}_1$	lattice vector
γ_0	in-plane nearest neighbor tight-binding parameter
Δ	superconducting gap
ε	dielectric constant
δn	charge nonuniformity
ε_0	the permittivity of free space
$\hbar$	reduced plank constant
λ	wavelength
λ_F	Fermi wavelengh
v_F	Fermi velocity
μ	carrier mobility
μ_{FE}	field effect mobility
ρ	resistivity

σ_{2D}	two dimensional conductivity
ξ	superconducting coherence length,
τ_{Φ}	phase relaxation time
ϕ	phase difference
Φ	work function

ACRONYMS

AC	alternating current
AFM	atomic force microscopy
AR	Andreev reflection
ARPES	angle resolved photoemission spectroscopy
WAL	weak anti-localization
BCS	Bardeen-Cooper-Schriefer theory
BLG	bilayer graphene
CDW	charge density wave
CMOS	complementary metal–oxide–semiconductor
CNT	carbon nanotube
CNW	carbon nanowall
CVD	chemical vapor deposition
DC	direct current
DI	deionised
DOS	density of state
EBL	e-beam lithography
FET	field effect transistor
FLG	few layer graphene
GIC	graphite intercalated compound
GND	graphene nanodot

GNF	graphene nanoflake
GNR	graphene nanoribbon
HRTEM	high resolution transmisssion electron micrscope
HOPG	highly ordered pyrolytic graphite
IPA	isopropanol
LDOS	local density of states
MAR	multiple Andreev reflection
MBE	molecular beam epitaxy
MCNT	multiwalled carbon nanotube
MIBK	methyl isobutyl ketone
MPECVD	microwave plasma enhanced chemical vapor deposition
MR	magnetoresistance
NA	numerical aperture
NP	charge neutrality point
PE	proximity effect
PMMA	poly methyl methacrylate
QHE	quantum Hall Effect
SEM	scanning electron micrscope
SLG	single layer graphene
SPW	spin density wave
SQUID	superconducting quantum interference device

STB	simple two band model
STM	scanning tunneling microscopy
STS	scanning tunneling spectroscopy
SWCNT	single walled carbon nanotube
TEM	transmisssion electron micrscope
UCF	universal conductance fluctuations
UHV	ultrahigh vacuum
WL	weak localization
XRD	X-ray diffraction
ZBR	zero bias resistance
0D	zero-dimensional
1D	one-dimensional
2D	two-dimensional
3D	three-dimensional

CHAPTER 1

INTRODUCTION

Over the last several decades, scaling of device dimensions as described by Moore's law [1] has generated amazing improvement cycles in technologies of silicon based electronics. As a result, complementary metal–oxide–semiconductor (CMOS) technology stands out as a fundamental technology and helps build the global information society. Looking ahead, silicon based technologies are expected to continue dominating electronic applications for some time, but innovations no longer stem from simple geometrical scaling according to Moore's law. Instead, an era of material-based scaling has emerged. Novel materials must be introduced into the standard CMOS processes to further reduce the manufacturing cost, improve performance and/or save power. Being a member of the same group of the element periodic table as silicon, carbon is believed to be the most promising candidate for next generation nano-electronics. Like silicon, carbon has four valence electrons. However, the four valence electrons have very similar energies, as such their wave functions mix easily facilitating hybridization. In carbon, these valence electrons give rise to 2s, $2p_x$, $2p_y$, $2p_z$ orbitals while the other 2 inner shell electrons belong to a spherically symmetric 1s orbital that is tightly bound and have lower energy than outer shell electrons. For these reasons, only electrons of 2s, 2p orbitals can contribute to the solid state properties of carbon. Possessing the unique ability of hybridization, carbon atoms give rise to many different chemical bonding configurations, which result in the different allotropes of carbon. Some examples of allotropes of carbon include diamond, graphite, carbon nanotubes (CNTs) [2] and fullerenes [3].

1.1 Carbon-based Nanostructures of Different Dimensionality

The allotropes of carbon with different relative sizes in different spatial directions can be classified into categories of different dimensionality, such as three-dimensional (3D), two-dimensional (2D), one-dimensional (1D) and zero-dimensional (0D) (Figure 1.1).

Diamond, a very hard, isotropic and electronically insulating material, is composed of a fully 3D tetrahedral sp^3-hybridised C–C bonding configuration. Graphite, another example of 3D carbon, is a semi-metal with an insignificant overlap of bands (about 40 meV). The 2D planar structure in graphite, called graphene, is represented with a trigonal sp^2 network which forms hexagonal rings of single and double C bonds and each planar layer interacts with weak van der Waals π bond. The best representation of a 2D carbon system is characterized by graphene. Graphene is an ideal 2D system. 1D carbon is characterized by cylindrical forms of carbon, such as single- and multiwalled nanotubes. Carbon nanotubes can be either semiconductors or metals, depending on their geometric structure. In addition, fullerene, which has the shape of a soccer ball, is considered as a 0D carbon.

Over the past two decades, most research on carbon nanostructures has been focused on the 0D system and 1D system.[4-7] Harold Kroto at the University of Sussex discovered carbon clusters containing C60 or C70 atoms in 1985.[3] This sparked the interests of researchers in determining the properties of fullerenes and the accuracy of their predicted properties based on their shape and chemical bonds between each carbon atoms. [8] Multiwalled carbon nanotubes (MWNTs) were discovered by Sumio Iijima of NEC laboratory in Tsukuba in 1991. [2] In the latter

research, it was found that CNTs can be metal or semiconductors, which offer a wide range of electronic properties.

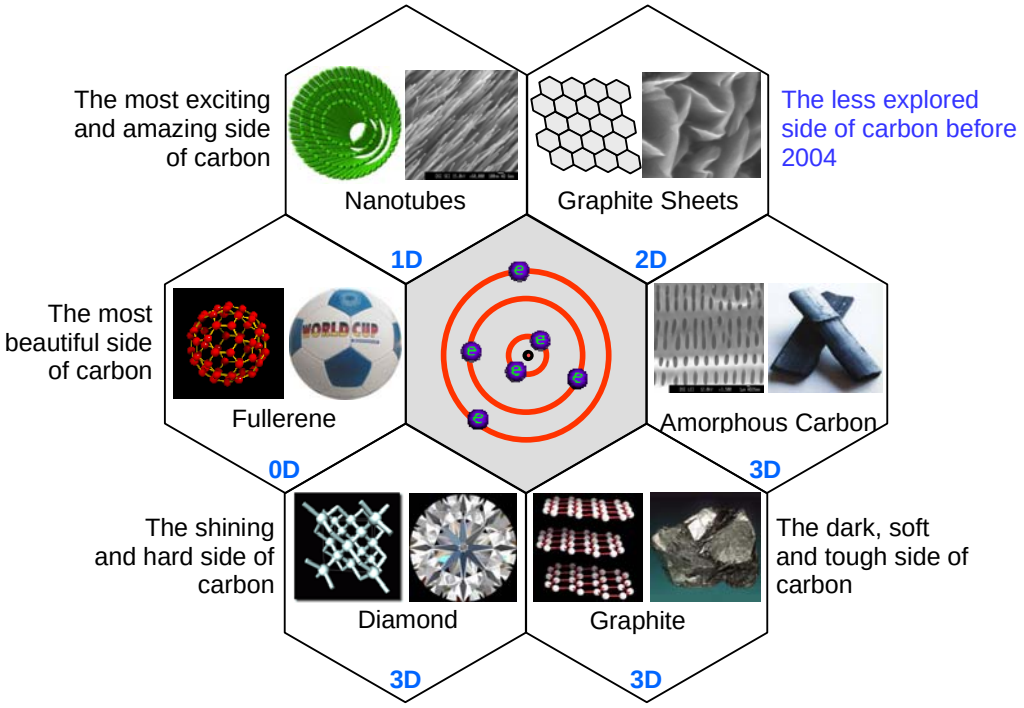

FIG. 1.1 The carbon family (adapted from EE5209 lecture notes by Prof. Wu Yihong).

As far as structure is concerned, 0D fullerene and 1D carbon nanotube are regarded as being wrapped up from 2D graphene. In addition, 3D graphite can be stacked by 2D graphene. As such, 2D graphene is always regarded as a foundation for 0D, 1D and 3D graphitic carbon. However, graphene was presumed not to exist in free states. About 70 years ago, Peierls and Landau argued that strictly 2D crystals were thermodynamically unstable and could not exist. [9,10] They pointed out that a divergent contribution of thermal fluctuations in 2D crystal lattices should lead to such displacements of atoms that they become comparable to inter-atomic distances at any finite temperature. [11] For these reasons, graphene was only described as a theoretical toy and was believed to be unstable with respect to the formation of curved structures

such as fullerenes and nanotubes. [12] Recently, the "academic" material came into reality, when free-standing graphene was successfully found in many ways. Generally speaking, the methods that are developed in getting 2D carbon fall into two categories: the bottom-up approach and the top-down approach.

Following the bottom-up approach, one starts with carbon atoms and tries to assemble graphene sheets from atoms by chemical pathways. In 2001, vertically aligned 2D carbon nanosheets (or nanowalls) were successfully grown by Wu et al. [13, 14]. They demonstrated that thin graphite flakes can be deposited by using microwave plasma enhanced chemical vapor deposition (MPECVD), regardless of the type of substrate. They have also pointed out specifically that high quality 2D carbon can be obtained by "peeling off" the carbon sheet layer-by-layer from graphite.[15] In 2004, W. A. de Heer group in Georgia Institute of Technology exemplified that thin graphite films can be grown via thermal decomposition on the (0001) surface of 6H-SiC. [16] These methods pave the way to large scale integration of nanoelectronics based on graphene, but so far the growth and identification of the monolayer graphene remains an obstacle.

On the other hand, the top down approach starts with bulk graphite, which is essentially graphene sheets stacked together, and tries to extract graphene sheets from the bulk mechanically. In 2004, Novoselov et al. demonstrated that two dimensional graphene sheets are thermodynamically stable, [17] and especially when the follow-up experiments confirmed that its charge carriers were indeed massless Dirac fermions. [18,19]

As a new and unique carbon nanostructure, 2D carbon provides an excellent research opportunity to study their transport properties and possible applications. In what follows, we will briefly provide a review on the electronic structure of graphene.

1.2 Energy Band Structure of Two Dimensional Carbon

Graphene is one atomic layer of carbon atoms that are arranged into a hexagonal lattice. It can be regarded as a large two dimensional molecule. The crystal structure of graphene is shown in Figure 1.2(a). The lattice vectors can be written as:

$$\vec{a}_1 = (\frac{3}{2}a, -\frac{\sqrt{3}}{2}a, 0), \quad \vec{a}_2 = (\frac{3}{2}a, \frac{\sqrt{3}}{2}a, 0) \tag{1-1}$$

In the (x, y) coordinates, $a = 1.42\text{Å}$ is the bond length between the nearest carbon neighbors. The vectors of its reciprocal lattice are given by:

$$\vec{g}_1 = \frac{4\pi}{3\sqrt{3}a}(\frac{\sqrt{3}}{2}, -\frac{3}{2}, 0), \quad \vec{g}_2 = \frac{4\pi}{3\sqrt{3}a}(\frac{\sqrt{3}}{2}, \frac{3}{2}, 0), \quad \vec{g}_3 = \frac{2\pi}{c}(0, 0, -1) \tag{1-2}$$

The wave vectors in reciprocal space are shown in Figure 1.2 (b).

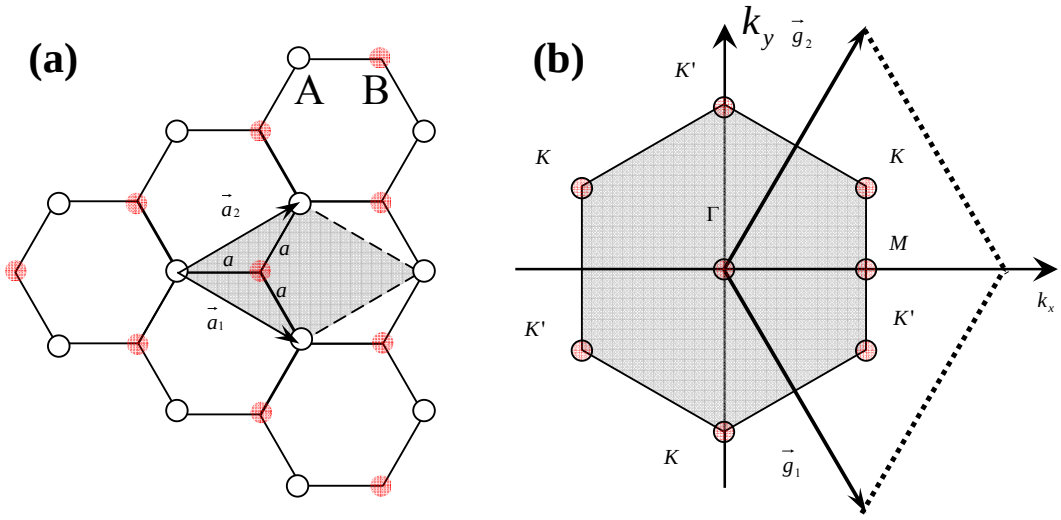

FIG. 1.2 Graphene and its reciprocal lattice. a) Lattice structure of graphene, $\vec{a}_1$ and $\vec{a}_2$ are the lattice vectors. There are two carbon atom (A and B) in one unit cell (shaded area). b) The reciprocal lattice of graphene defined by $\vec{g}_1$ and $\vec{g}_2$. The corresponding first Brillouin zone is depicted as the shaded hexagonal. The Dirac cones located at K and K' points.

As shown in Figure 1.2, there are two carbon atoms in one unit cell in real space. Every carbon atom has four valence electrons, of which three are used for the chemical bonds in the graphene plane. We refer them as σ bonds. The fourth electron is in a $2p_z$ orbit which is oriented perpendicular to the plane. Since the σ bonds are extremely localized and do not contribute to the electronic conduction, we are only concerned with the energy band structure of the fourth electron, called π band. Note that there are two such electrons in one unit cell, therefore, there should be two π bands, π and π*, with π corresponding to valence band and π* corresponding to the conduction band.

The band structure of graphene was firstly calculated using tight-banding method in 1947. [20] The energy dispersion relation is given by:

$$\begin{aligned} E(k) &= \pm\gamma_0 \left| f(k) \right| \\ &= \pm\gamma_0 \sqrt{1 + 4\cos(\frac{3}{2}k_x a)\cos(\frac{\sqrt{3}}{2}k_y a) + 4\cos^2(\frac{\sqrt{3}}{2}k_y a)} \end{aligned} \tag{1-3}$$

where k_x and k_y are the components of wavevector k in the x and y directions respectively as shown in Figure 1.3. The positive sign applies to the upper (π) and the negative sign the lower (π*) band. In Figure 1.3, we show the full band structure of graphene. In the same figure, we also show a zoom-in of the band structure close to one of the Dirac points, indicating clearly that the dispersion is linear.

As far as overall electronic structure is concerned, we are interested in the low energy region just around K and K' points. In this regime, the Hamiltonian can be approximated by its first order expansion. We first look at K point, around which we write a very simple dispersion relation:

$$E(k) = \pm\hbar v_F \left| k \right| \tag{1-4}$$

where v_F is the Fermi velocity given by the constant:

$$v_F = \frac{3\gamma_0 a}{2\hbar} \tag{1-5}$$

Taking the known values for $\hbar$ (1.054×10^{-34} Js), γ_0 (2.9eV) and the lattice constant a (1.42 Å), v_F is estimated to be $10^6\ m/s$. Therefore, even though the carriers move at a speed 300 times slower than the speed of light, it is remarkable to see that they behave as if they are relativistic particles with zero mass.

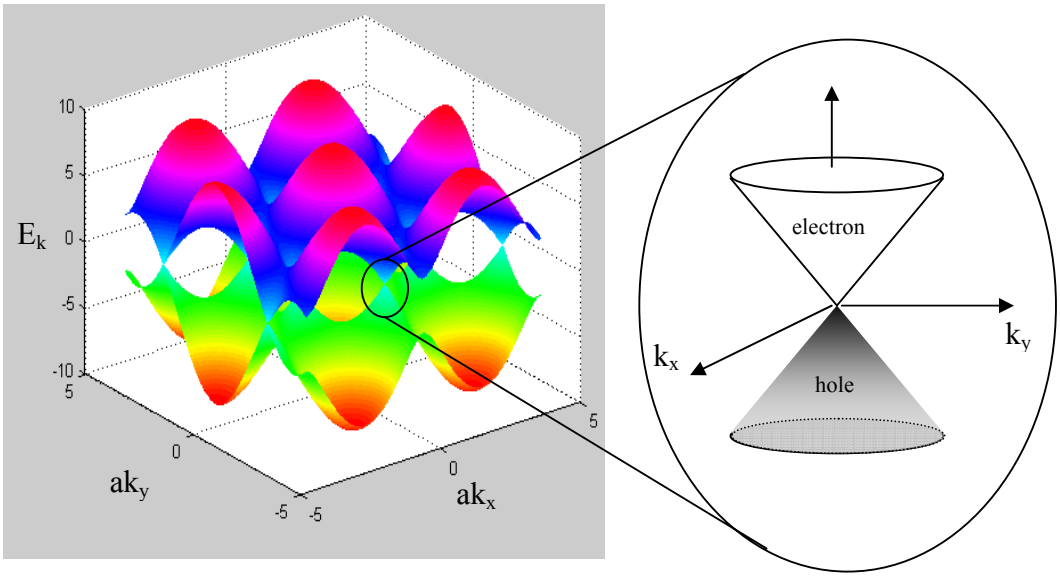

FIG. 1.3 Electronic energy band structure of graphene. The valence band (lower band) and the conduction band (upper band). Right: magnification of the energy bands close to one of the Dirac point, showing the energy dispersion relation is linear.

It is worth noting that, even though a simple one-orbital tight binding model with only the nearest neighbors is taken into account, the result ($E(k) = \pm\hbar v_F |k|$) is robust against any approximations regarding wavefunctions and is a result of the symmetry of graphene with spin orbital coupling being neglected. [21]

After discussing the electronic dispersion of graphene in this section, a brief summary on the research work conducted on carbon nanowalls and graphene thus far will be described.

1.3 Carbon Nanowalls – Disordered 2D Carbon

1.3.1 Fabrication of Carbon Nanowalls

Since the discovery of 1D carbon nanotubes [2], researchers started attempting to fabricate 2D carbon nanostructures. Parallel to the developments of carbon nanotubes, a new type of two dimensional carbon material, carbon nanowalls (CNWs), was reported by Wu et al. [13, 14, 22- 24] in 2002. The CNWs are fabricated by microwave plasma-enhanced chemical vapor deposition. The CNW flakes are composed of the stacks of graphene layers standing almost vertically on the substrate, forming wall-like structures. The thickness of CNWs ranges from few nanometers to few tens of nanometers. Unlike the case of carbon nanotube, catalysts are not required during the deposition of CNWs, and CNWs can be described as the 2D graphitic nanostructures with boundaries. Besides CNWs [25-36], similar carbon nanostructures fabricated by CVD are also called, carbon nanoflakes [37-40], carbon nanosheets [41-47], carbon nanoflower [48], and graphene nanoflakes [49-51].

For practical applications, many investigations were carried out to enable control over the structure and electronic properties of CNWs as well as to establish the CNW fabrication system with high productivity. Table 1.1 summary the various preparation methods for carbon nanowall nanostructure. As shown in Table 1.1, CNWs have been grown by various PECVD methods using microwave plasma [13-15, 22-24, 27, 28, 50, 51], DC discharge CVD [40,56] radio frequency (rf) inductively coupled plasma [26,

30, 34, 41-47, 52-54, 57], rf capacitively coupled plasma assisted by H radical injection [25, 33], helicon-wave plasma [31] and hot filament [38]. Typically, CNWs can be grown directly on a variety of metallic, semiconducting and insulating substrates at temperatures ranging from 500 to 900°C, by various CVD techniques. Furthermore, the operating pressure ranges from a few mTorr to 100 Torr. Most reactants use methane as the carbon source. In addition, the hydrogen (H) element plays a very important role in the formation of CNWs.

Table 1.1 Literature review about the research work on fabrication of CNWs by CVD method.

Fabrication Technique	Working Gas	Substrate	Growth temperature	Characterization methods
Microwave plasma enhanced CVD [13-15, 22-24]	H_2:CH_4=5:1	Any substrate	650-700 ºC	SEM, TEM, Raman, field emission, and transport measurement
Microwave plasma enhanced CVD [27, 51]	H_2:CH_4=4:1 or 16:1	No catalyst, Stainless steel, Mo, Ta, Ti, Ni, Ge, Pt, Si, SiO_2	650-700 ºC	SEM, TEM, STM, XRD, and XPS
Microwave plasma enhanced CVD [28]	NH_3:C_2H_2=16:1	No catalyst, Copper stage	600 ºC	SEM, Raman
Microwave plasma enhanced CVD [50]	CH_4 and N_2	Si	>1000 ºC	SEM, TEM.
DC arc-discharge evaporation [37]	Graphite and H_2	Graphite	25 ºC	SEM, TEM
DC discharge CVD [40,56]	H_2:CH_4=9:1	Si, Ni.	~1000 ºC	SEM, field emission, Raman spectra, X-ray and ultraviolate, secondary electron spectra, and transport measurement
RF capacitively coupled plasma-enhanced CVD [25, 26, 30, 34, 57]	H_2:CH_4, or H_2:CF_4, or H_2:C_2F_6	Si, fused silica, sapphire	500 ºC	SEM, Raman, transport properties
RF plasma enhanced CVD [41-47,52-54]	H_2(5-90%) and CH_4	Si, SiO_2, Al_2O_3, Mo, Zr, Ti, Hf, Nb, W, Ta, Cu, Stainless steel	680-900 ºC	SEM, TEM, Raman, field emission, and XPS
RF PECVD [32]	Ar:C_2H_2:H_2 =500:8:1	SiO_2 capped with 5 nm Ni	> 600 ºC	SEM, Raman and XRD

Dual RF plasma CVD [39]	CH_4	Ni, Ni/Ti/Glass, Si, Ni/Ti/Si	680 ºC	SEM
Catalytic CVD [29]	CH_4	Stainless steel, Ni on quartz substrate	400-500 ºC	SEM, Raman, Field emission
Hot filament CVD [36]	H_2 and C_2H_2(3-15%)	Si	400-700 ºC	SEM, XPS, Raman, Field emission

Growth mechanisms for carbon nanowalls were discussed in many reports. Wu and Yang [24] attributed nanowall growth to the existence of a strong lateral field: the tubular structures do not close and connect laterally to form continuous wall structure. Zhu *et al.* [52] argued that vertical orientation of carbon nanosheets results from the local electric field near the substrate surface. In the initial growth stage, ionic species and local electric field near the substrate surface may contribute to the nucleation of CNWs. Hiramatsu *et al.* [25] suggested that, in the nucleation stage, carbon species condense to form nanoislands which develop into nanoflakes in disordered orientation and eventually grow into continuous wall-like structure due to self-screening effect of the high-grown structures. Shang *et al.* [38] reported that a similar nanostructure (carbon nanoflakes) started as nanorods on the substrate and grows anisotropically into nanowalls. Chuang *et al.*[28] demonstrated that carbon nanowalls were allowed to grow spherically and form 3D grape-like structures. Their observation indicated that dominating growth mechanism was not due to limited supply of reactive species. A. Malesevic [32] demonstrated the combination growth of CNT/CNWs double layer without making any change to the growth parameters. The result indicates that the growth mechanism of the carbon nanowall material is still unclear. The only thing clear is that, in these CVD synthesis processes, the formation of carbon nanowalls is energy intensive, and most CNWs grow at regions with plasma discharge.

1.3.2 Structure and Morphology

Carbon nanowalls are thin sheets of graphite layer vertically aligned on the surface of substrate. [15] These sheets have small curvatures and are typically several nanometers thick. As shown in Figure 1.4 (a) and (b), these individual sheets are interconnected to form a self supported network structure.

The quality of the carbon nanowalls is of great importance to transport properties. The growth temperature could greatly affect the quality of carbon nanowalls. In our case, the carbon nanowalls are deposited at 600-700 ^{o}C due to the limitation of the microwave power in our CVD machine. Such a low growth temperature results in the presence of disorder in carbon nanowalls. Such disorder can be observed from the high resolution transmission electron microscopy (HRTEM) image. The HRTEM image of carbon nanowalls shows that the CNWs are characterized by a high degree of graphitization in spite of a few disordered regions and some amorphous phases (Figure 1.4(c) and (d)).

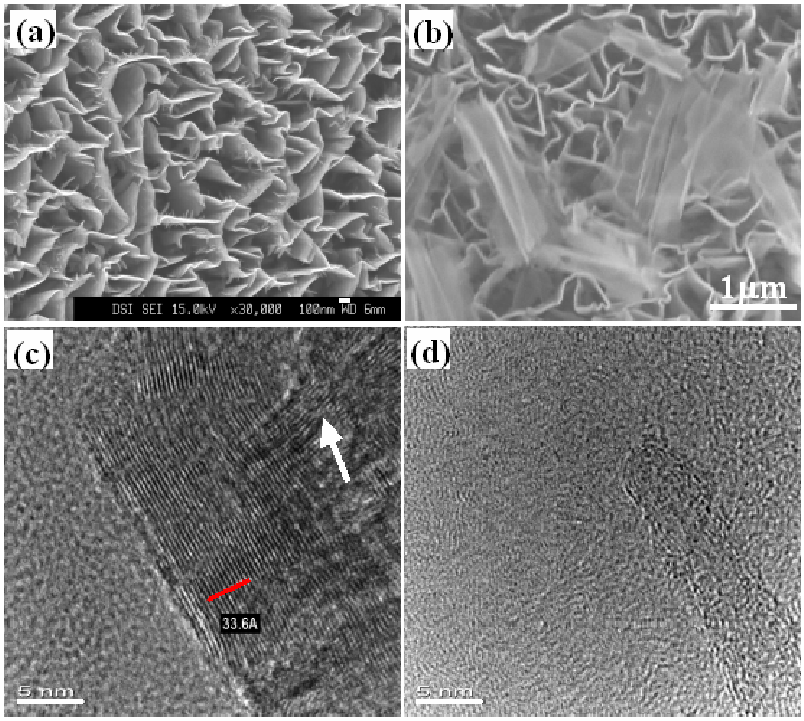

FIG. 1.4 SEM ((a) and (b)) and HRTEM ((c) and (d)) images of carbon nanowalls. Scale bars: (a) 100 nm, (b) 1 μm, (c) and (d) 5 nm. (a) was taken at a tilt angle of 25°. (Refer to Ref. 15)

Recently, French *et al.* [53] [54] investigated the structure and morphology of carbon nanowalls by X-ray diffraction (XRD) and scanning electron microscopy (SEM). XRD results indicate that CNWs contain both turbostratic and non-turbostratic graphite sheets. In the turbostratic graphite sheets, the graphene layers stack with slight rotation. Also it is found that the graphene layer spacing decreases with the increase of the thickness of the CNW sheet. Later, Kobayashi et al. [55] investigated the nanostructure of carbon nanowalls by transmission electron microscopy. Their results revealed that numerous graphite regions with an average size of about 20 nm, named "nanographite domains", were formed in their CNWs. The formation of "nanographite domains" could originate from the introduction of lattice defects such as dislocations and the slight rotation of the graphite sheets.

Above features indicate that CNWs are a unique 2D graphitic material. The unique structure features are expected to give CNWs unique physical properties that might not be present in other graphite based carbon materials.

1.3.3 Transport Properties of Carbon Nanowalls

The unique morphology of the carbon nanowalls is believed to give rise to fascinating transport properties. So far, there have been a few works done in the transport of CNWs. Most of them focus on a large amount of carbon nanowalls. In 2004, Wu, et al. [15] carried out systematic transport studies of the carbon nanowalls in a superconducting quantum interference device (SQUID). The details will be introduced later. In 2006, A.I. Romanenko et al. [56] investigated the temperature dependence of electrical conductivity within a temperature range of 4.2–300 K in CNWs and the magnetoconductivity in the magnetic field range of 0–12 kGauss at 4.2 K. The results indicated that charge carriers preferred motion in a quasi-two-dimensional plane of the graphene layers in CNWs system. In 2008, W. Takeuchi et al. [57] reported that the conduction type of the CNWs changes from p type to n type by introducing nitrogen during the CNW growth process. Among the investigations, the transport studies of the carbon nanowalls conducted by Wu et al. are the most interesting. They examined the temperature dependence of the resistance of CNWs nanostructures. In addition, the magnetoresistance was measured. The results will be described briefly as follows.

As shown in the inset of Figure 1.5, the resistance decreases when decreasing the temperature from 300 to about 106 K, and then shows an upturn at lower temperatures. After fitting by using a simple model, three mechanisms may contribute to the temperature dependence of resistance indicated. They are metallic characters, a

quasi 1D characteric of a network structure and hopping/tunneling resistance of junctions. The rate of change of resistance with temperature (dR/dT) is also shown in the inset of Figure 1.5.

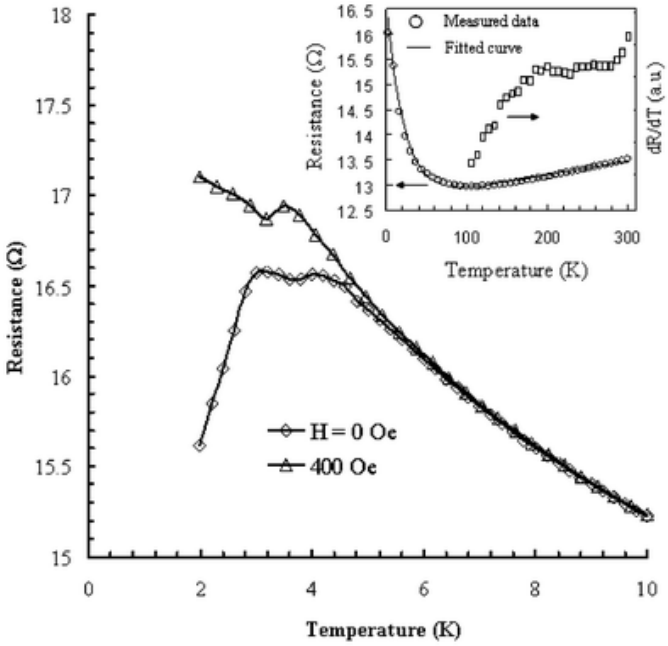

FIG. 1.5 Temperature dependence of the resistance of the carbon nanowalls at low temperature at zero-field and a field of 400 Oe. Inset is the temperature dependence of the resistance over a wider temperature range. Also shown is the first derivative of the resistance with respect to the temperature. (Refer to Ref. [15])

The temperature dependence of resistance at different applied magnetic field between 0 to 400 Oe was also measured in the temperature range from 2 to 10 K.(in the main graph of Figure 1.5) In the absence of magnetic field, the resistance continues to increase with decreasing temperature, reaching the first local maximum at about 4.2 K; after a local minimum is reached at about 3.6 K, it increases again until the temperature decreases to 3 K below which the resistance decreases monotonically until reaching 2K. When a magnetic field is applied in the direction perpendicular to the substrate surface, the resistance, in general, also increases with the magnetic field. It is

interesting to note that the resistance is unaffected by the applied field at temperatures higher than 7 K. The mechanism behind such phenomenon has yet to be conclusive.

The magnetoresistance curve at different temperature is presented in Figure 1.6(a) after removing the background signal. Oscillations are found to set in at about 7 K and increase by more than 3 orders of magnitude as the sample is cooled below 6 K. Quasi-periodicity of the oscillations can be seen from Figure 1.6(a). To illustrate this trend, a portion of the magnetoresistance curve at 4.31 K is shown in Figure 1.6(b), with the inset showing a Fourier transform spectrum in which three peaks correspond to the different periodicities. The phenomena are interesting and of immense importance. It is worth further studies to reveal the physics behind the phenomena.

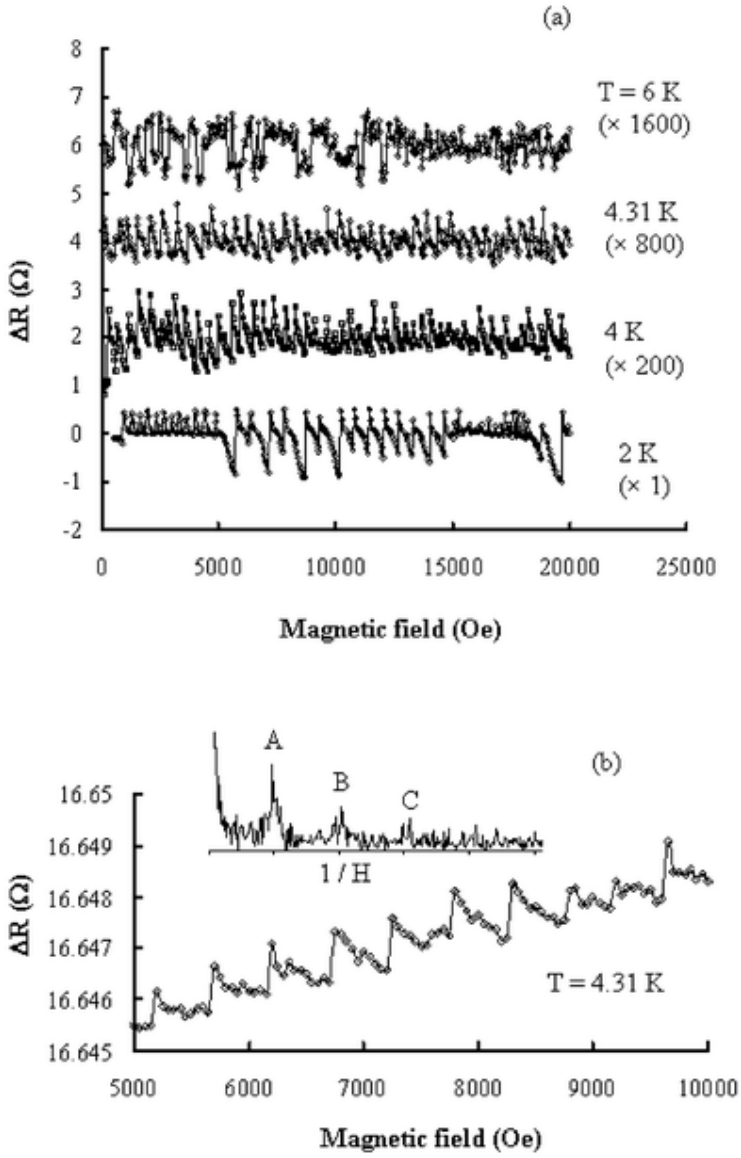

FIG. 1.6 Magnetoresistance curves of the carbon nanowalls measured at different temperatures (a), and enlarged portion of the curve at 4.31 K (b). The inset of (b) is the Fourier transform spectrum of the entire curve at 4.31 K shown in (a). (Refer to Ref. [15])

Besides the electronic transport properties, electrical field emission study was carried out in almost all the CNWs research groups. Due to the atomic-scale edge structure and good electrical conductivity, carbon nanowalls have been considered as a promising cold cathode material for application in vacuum microelectronic devices. To date, the carbon nanowalls have shown good field emission characteristics including

low threshold field, high emission total current, excellent emission stability and reproducibility. Ultrathin edges that give rise to a very high field enhancement factor, and outboard positive charge centres that lower the work function. The high density of vertical sheets also provides a significant emission area. Uniform and enhanced field emission has been achieved by surface milling [58] or coating [59, 60]. In addition, the large surface area and sharp edges of CNWs may provide us with opportunities for other applications. In particular vertically standing CNWs with high surface-to-volume ratio can serve as an ideal material for catalyst support [15, 22, 23] and gas storage [61].

Those previous results on transport properties of carbon nanowalls are appealing and interesting, however, most of them have yet been understood. Further detailed studies are required to determine the exact physics and properties of the unique two dimensional carbon nanowalls. More experimental work has to be conducted in order to fully explore the properties of carbon nanowalls and transform them into useful applications.

1.4 Graphene - 2D Carbon of High Perfection

Graphene is two dimensional sp^2 hybridized forms of single layer carbon. Graphene sheets can be stacked up to form a layered bulk material, known as graphite.[20] The distance between graphene planes is about 0.335 nm in graphite. Those graphene sheets are held together by van der Waals forces. The weak interaction between the sheets allows them to slide easily across each other. This gives pencils their writing ability and graphite its lubricating properties. Bulk graphite has been studied for decades, [20] but until recently there were no experiments on graphene. This was due to the difficulty in separating and isolating single layers of graphene for study.

1.4.1 Fabrication of Graphene

The fabrication methods for graphene sheets can be classified into two categories: top-down and bottom-up approach. The most common method of top-down fabrication is mechanical exfoliation from bulk graphite. It is just as simple as writing with a graphite pencil. By writing with a pencil, one could create many graphene sheets spread over the paper. Unfortunately this method is uncontrollable and typically leaves many sheets of varying thicknesses at random places. As such, it is very difficult to locate and identify those monolayer graphene sheets. Andre Geim's group in Manchester solved the difficulties in 2004. [17] By gently rubbing or pressing a freshly cleaved graphite crystal on silicon wafer capping a correct thickness of oxide, single atomic layers are visible under an optical microscope due to thin film interference effects.[62] An optical image of a few-layer graphene sheets and schematic view of a graphene device are shown in Figure 1.7 (a). This technique simplifies the process of locating single graphene sheets and makes it possible to fabricate devices for research purposes. However, it may be time-consuming to find suitable single layers. There are recent attempts to improve the quality and yield of exfoliation techniques. These include stamping methods which use graphite pillars to transfer graphene flakes [63, 64] or electrostatic voltage assisted exfoliation which uses electrostatic forces to controllably separate graphene from bulk crystals.[65] Figure 1.7 (b) shows a nanopencil used to extract few layer graphene flakes from highly ordered pyrolytic graphite (HOPG).

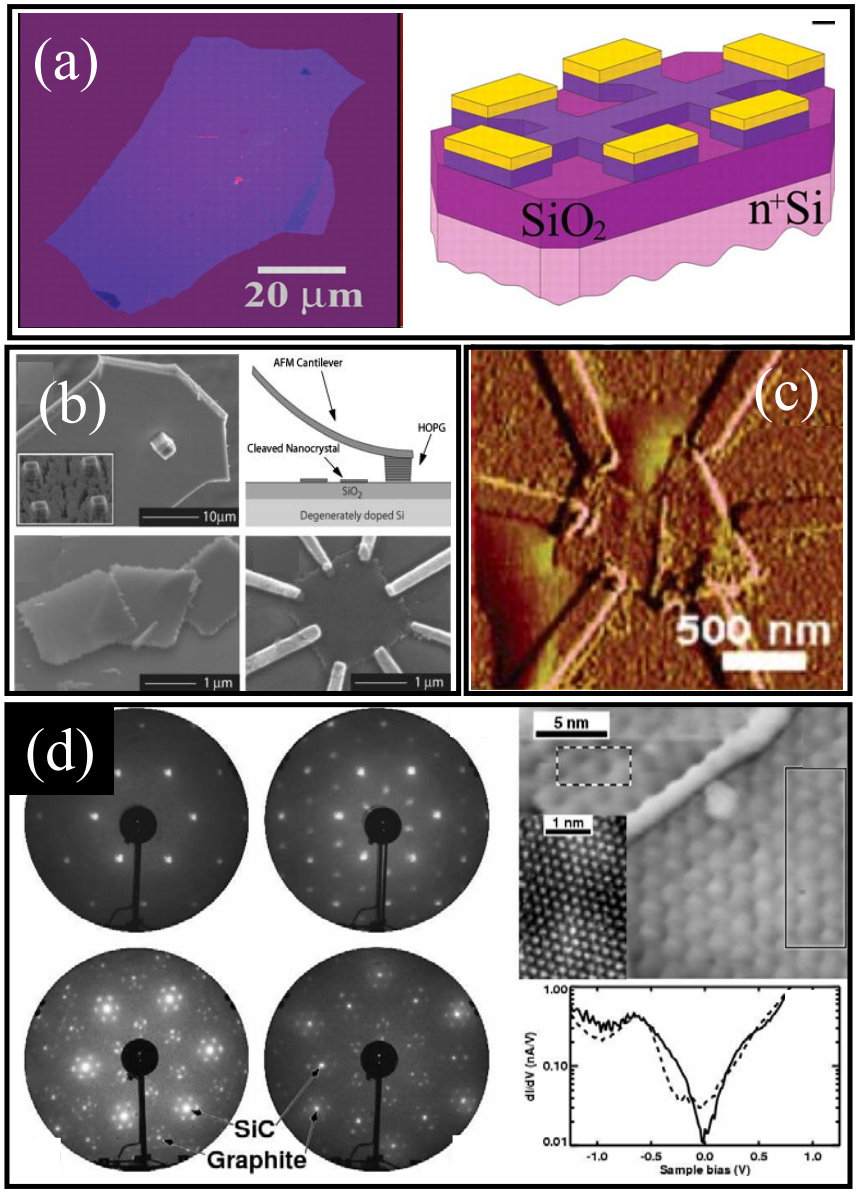

FIG. 1.7 a) Optical image of a few-layer graphene sheet and schematic view of a graphene device. Figures from Ref.[17]. b) Nanopencil used to extract few layer graphene flakes from HOPG. (Figures from Ref. [63]). c) AFM image of a few layer graphene quantum dot fabricated by dispersion from solution. (Figures adapted from Figures from Ref.[66]). d) Growing graphene layers on SiC. (Figures from Ref.[16]).

Another common top down approach of graphene fabrication is to disperse graphene from solution. [66-69] Graphite flakes are sonicated in a solution. Long sonication time is needed to break the van der Waals force in graphite. This, however, also results in small flakes. Following this step, the graphene flakes are then dispersed

onto a wafer. Atomic force microscopy (AFM) is used to locate individual sheets. (Figure 1.7 (c)) Recently a similar technique was used to fabricate graphene ribbons with nm-scale widths [70] and graphene oxide. [71] Although the graphene samples with chemical exfoliation preserved the sp^2 network, they are still far from pristine. In addition, an increase in the yield for large single-layer sheets is needed. In above parts, we have been talking about the top-down approaches for large size graphene. In fact, bottom-up approaches are also important because they could be potential ways to mass-produce graphene, particularly for electronics.

Generally speaking, bottom-up approaches start with carbon atoms and try to assemble graphene sheets. Chemical vapor deposition (CVD) and molecular beam epitaxy (MBE) are two typical bottom-up approaches. Carbon nanowalls have been successfully grown using CVD as discussed in previous sections. We noticed that very recently, large size graphene sheets were fabricated in different groups by CVD and annealing growth. [72-77] Typically epitaxial graphene forms on SiC surface by heating a SiC wafer, as shown in Figure 1.7 (d). [16] The number of layers and the sheet sizes can be controlled easily.[78] However, the mobilities of epitaxial graphene are comparatively lower than those of exfoliated graphene.[79] Furthermore, isolating single sheets is difficult and additional lithography is required to pattern electrostatic gates on top of epitaxial graphene. Transition-metal-catalysed graphene growth was demonstrated to yield macroscopic single-crystalline graphene domains with very low defect density and outstanding thickness control.[80] It is still a challenge to find a way to transfer the graphene layers to an insulating surface. Those recent successful demonstrations of fabrication of large graphene by CVD/Epitaxial growth pave ways to mass-produce graphene. However, the progresses are still far from over. A true leap

forward should be atomically precise synthesis of graphene nanostructures by 'bottom-up' approaches.

In summary, exfoliation remains the preferred method for most of the experimental research groups around the world. Recent successful fabrication of large graphene by CVD/Epitaxial growth opened ways to mass-produce graphene. These various methods have led to high-quality single-crystalline graphene systems, which can be used for further fundamental research, as well as large-scale graphene wafers, which can be employed in device fabrication and integration.

1.4.2 Electrical Properties of Graphene

So far there have been a lot of experimental works on graphene which are focused on the electronic transport properties. At the beginning of these researches, a pronounced ambipolar electric field effect was found in graphene. The charge carriers could be continuously tuned from holes to electrons in the concentration of about 10^{13} cm^{-2}, as shown in Figure 1.8(a). This ambipolar effect is more obvious in the thinner samples due to screening of the electric field from the neighboring graphene layers. Also of interest, the charge carriers in graphene mimic relativistic particles, which have no rest mass and are described by the two-dimensional Dirac equation with an effective speed of 10^6 m/s. As a consequence of the unique quantum electrodynamics in graphene, a new chiral quantum Hall effect was observed. [18,19] At low temperatures and high magnetic fields, the new quantum Hall Effect (QHE) for both electrons and holes was observed, and is shown in Figure 1.8(b). The new QHE in graphene is different from the conventional QHE. Its QHE plateaus occur at half integers of $\frac{4e^2}{h}$, instead of the typical value of $\frac{4e^2}{h}$. From the view of practical application, the absence of energy gap is a major problem and limits the application of

graphene. Therefore, to open a semiconductor gap on graphene is critically important. External electrical field could open a gap of up to 0.3 eV in bilayer graphene. In monolayer graphene, energy gaps could be induced by spatial confinement. The opening of a band gap in graphene ribbons has recently been observed in wide ribbon devices lithographically patterned from large graphene flakes [81] and in narrow chemically synthesized graphene ribbons [82].

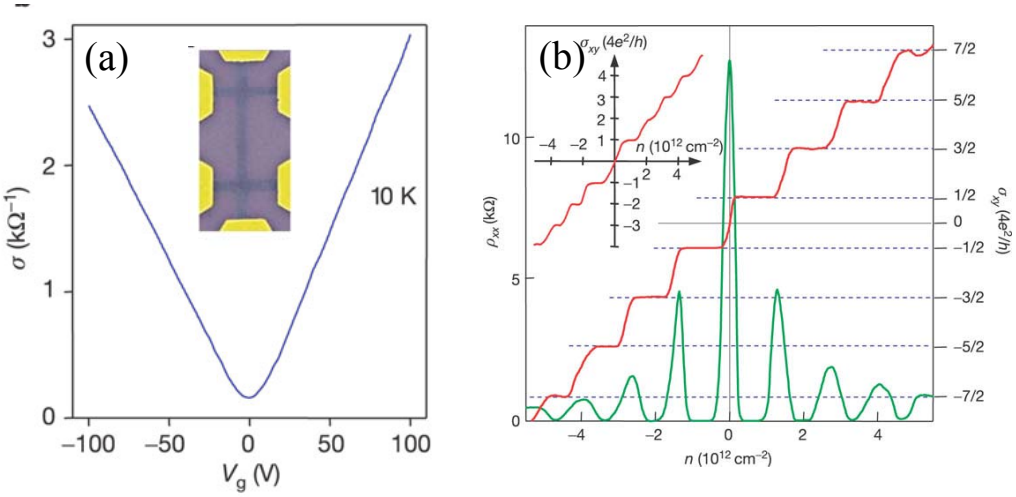

FIG. 1.8 a) The conductivity of monolayer of graphene vs. gate voltage. b) The Quantum Hall Effect in single layer graphene. (Figures taken from Ref.[18])

In this section, we have reviewed some work in graphene fabrication and basic transport properties. As research on 2D carbon is still at its beginning stage, it is worth to further investigate their transport properties in order to make use of them in the next generation of nanoelectronic devices.

1.5 Motivation

Many of graphene's properties, especially in modified graphene, have not been studied experimentally and are currently theoretical subjects under intense debate. The detailed literature review on this will be given in Chapter 2. The understanding of the nature of disorder and how it affects the transport properties (a problem of fundamental

importance for applications), the nature of electron-electron interactions and how they modify its physical properties, the question of how stacking affects in-plane properties in graphene multilayers, are still issues that have not been explored in experiments. Most of the researches on disordered graphene are theoretical predictions. Recent theory [83-87] predicts that edge states and topological disorder enhance the density of states in graphene and may lead to excitonic instabilities, such as magnetism, superconductivity and charge density wave. Furthermore, similar excitonic phenomena in multilayer graphene have also been theoretically expected. So far, very few experiments have been carried out to investigate the transport properties of 2D carbon with disorder.

On the other hand, as introduced in Section 1.3, CNW sheet is one example of 2D carbon characterized with open boundaries, some defects and disorders. Also, nanosize fishscale-like graphite domains are found at the surface of CNW sheets. As mixtures of CH_4 and H_2 are used as reaction gases for CNWs, a lot of hydrogen terminated edges and C−H functionality form in CNW sheets during the deposition. These features may introduce edge states and localized states into the electronic structure of CNW sheet, which may greatly enhance DOS near Fermi level. On top of that, CNW sheets have thickness of several nm and height of about 1-2μm. The width of CNW sheet is in the range of 0.1-2 μm. Electronic confinement under this scale could open a small conduction gap in the CNWs. The interlayer distance between neighboring graphene planes of CNWs is comparatively larger than that of bulk multilayer graphene. In addition, CNW sheets are also oriented perpendicularly to substrate surface and form self-supported network. The unique morphology allows us to fabricate direct electrical contacts at the edges of CNWs for transport measurement.

In summary, although many theoretical studies on edge state or localized states on 2D carbon have been carried out, few experiments were carried out to characterize the transport properties of 2D carbon with disorder and edges. CNW sheets can serve as the subject for the transport investigation. So far, carbon nanowall sheets have not been thoroughly investigated, especially by transport measurement. In early transport study of carbon nanowalls, at least thousands of CNWs sheets were involved. The investigations on few CNWs sheets, even individual ones, have considerable interests. Thus, further study on their transport properties may provide additional information about their structure, edges, and defects. The results of transport investigations can allow one to understand the influence of the nanosize 2D crystallites on their electronic kinetic properties.

1.6 Objectives

In this study, we focused on the fabrication and characterization of 2D carbon: CNWs and graphene. In early work, the difficulties for the transport measurement on carbon nanowall sheet are mainly in the placement of electrodes. In order to overcome the difficulties, we introduce bottom electrodes to form contact directly and only at the edges of CNWs. The bottom electrodes also enable the excellent control of the electrode spacing in the range of less than 1 μm. Following the fabrication of carbon nanowall device, we will investigate the transport properties of carbon nanowalls using two types of electrode materials: normal metal (Ti) and superconductor (Nb). The transport measurements will be carried out in a low temperature cryostat.

When we were investigating the transport properties of carbon nanowalls, graphene flakes were discovered. Because graphene is a well defined monolayer crystal of 2D carbon, the transport should be different from carbon nanowalls. In

addition, graphene flakes are always isolated on supporting substrates, compare to the vertical aligned carbon nanowalls. Investigation on the transport of graphene flakes in SiO_2 is helpful in understanding the effect of substrate and absorbant. More importantly, we could also draw some guidelines to achieve high quality graphene devices. High quality graphene devices are extremely important in further investigation in tailoring the electronic properties of graphene in a controlled way. It is possible to assess how specific edge or defect perturbs the graphene's electronic band structure and how this impacts their physical properties such as magneto and transport behavior. This work will make it possible to extract and clarify the exact causes for the interesting phenomena observed in our CNW samples.

The main objectives of this work are to conduct a systematic transport study of CNWs prepared between normal or superconducting electrodes in different range of spacing. Special attentions should be paid to address several questions: 1) Can one observe an energy gap in micron-size CNW sheets? 2) Do the edges and defects affect the transport properties of CNW sheets? 3) Do excitonic states theoretically predicted exist in CNW sheets? 4) Can superconducting proximity effect be observed in CNW sheets? 5) Could those phenomena appear in graphene flakes? 6) How should we verify the theoretical prediction about the disorder induced states in graphene flakes by top-down approach? The study will enhance our understanding on the transport properties of 2D carbon. Further study on the influence of different edges, defects and layer stacking may provide additional information about practical application of 2D carbon on nanoelectric devices.

1.7 Organization of the Thesis

Having provided a brief background of this research, we will continue this thesis in Chapter 2 which gives an overview of the work done so far on modified graphene. In Chapter 3, we will introduce our sample preparation procedures and measurement techniques. We first discuss the deposition and characterization of carbon nanowalls. Following that, the fabrication of CNW devices is introduced. In the section of graphene, we discuss the fabrication of graphene, and the thickness determination using Raman and optical contrast spectroscopy. Later, we summarize the e-beam lithography fabrication method for graphene based devices. In addition, we introduce a model to study the visibility of graphene on different substrates, and we also present some ideas how to produce a free standing graphene device with the help of the model. Finally measurement setup and techniques that have been used to characterize transport properties of samples in this study are also discussed.

In Chapter 4, we first introduce the transport mechanism of two dimensional carbons. Next, investigation of transport properties of CNWs nanostructure is introduced. Following that, the mesoscopic transport properties of the Ti/CNWs/Ti junction under low temperature are discussed. The experimental results show the presence of a narrow band gap and conductance fluctuations within a certain temperature range.

In Chapter 5, we introduce some transport phenomena in superconductor junctions. The experimental data based on superconductor-CNW-superconductor junctions indicate the existence of proximity effect of superconductivity.

In Chapter 6, we first discuss the electric characterization of graphene device on SiO_2 substrate with different number of layer under ambient condition. By examining carrier mobility, minimal conductivity and conductance hysteresis in

graphene devices, it is found that substrate interface and the surface impurity may greatly affect the transport properties of graphene on SiO_2 substrate. Following that, transport properties of those devices at low temperature will be discussed. Our experimental results indicate that magneto transport and conductance fluctuation in graphene devices are greatly affected by the charged impurities existing at the substrate/graphene surface. The work is of great importance to achieve high quality graphene devices for further investigation. By deliberately isolating and magnifying each of all possible modification factors on the transport properties of graphene devices, we may study the disorder 2D carbon in graphene by top-down approaches.

In Chapter 7, we recapitulate the major conclusions of the thesis and give some recommendations for future study.

References:

[1] G. E. Moore, "Cramming more components onto integrated circuits", *Electronics*, vol.38, pp.114-117, 1965.

[2] S. Iijima, "Helical microtubules of graphitic carbon", *Nature,* vol.354, pp.56-58, 1991.

[3] H.W. Kroto, J.R. Heath, S.C.O'Brien, R.F.Curl, and R.E.Smally, "C60: Buckminsterfullerene", *Nature*, vol.318, pp.162-163, 1985.

[4] Thomas Ebbesen, *Carbon Molecules and Materials*, vol.6, pp.179, 2002.

[5] C.M. Lieber, "Nanoscale Science and Technology: Building a Big Future from Small Things," *MRS Bull.,* vol.28, pp.486-491, 2003.

[6] J. D. Aiken and R. G. Finke, "A review of modern transition-metal nanoclusters: their synthesis, characterization, and applications in catalysis", *J. Mol. Catal. A: Chem.,* vol.145, pp.1-44, 1991.

[7] E. Borovitskaya and M. S. Shur, *Quantum Dots, World Scientific, New Jersey*, 2002.

[8] G. Vaughan, *Carbon Molecules and Materials*, vol.6, pp.201, 2002.

[9] R. E. Peierls, "Quelques proprietes typiques des corpses solides", *Ann. I. H. Poincare,* vol.5, pp.177-222, 1935.

[10] L. D. Landau, *Zur Theorie der phasenumwandlungen II. Phys. Z. Sowjetunion,* vol.11, pp.26-35, 1937.

[11] L. D. Landau, and E. M. Lifshitz, *Statistical Physics*, Part I , Pergamon, Oxford, 1980.

[12] E. Fradkin, "Critical behavior of disordered degenerate semiconductors", *Phys. Rev. B,* vol.33, pp.3263, 1986.

[13] Y. H. Wu and T. C. Chong, *MRS 2001 Spring Meeting*, abstract No. W8.3, San Francisco, USA, April 16-20. 2001.

[14] Y. Wu, P. Qiao, T. Chong, Z. Shen, "Carbon nanowalls grown by microwave plasma enhanced chemical vapor deposition", *Adv. Mater.,* vol.14, pp.64-67, 2002.

[15] Y. Wu, B. Yang, B. Zong, H. Sun, Z. Shen and Y. Feng, "Carbon nanowalls and related materials", *J. Mater. Chem*., vol.14, pp.469-477, 2004.

[16] C. Berger, Z. Song, T. Li, X. Li, A. Y. Ogbazghi, R. Feng, Z. Dai, A. N. Marchenkov, E. H. Conrad, P. N. First, and W. A. de Heer, "Ultrathin epitaxial

graphite: 2D electron gas properties and a route toward graphene-based nanoelectronics", *J. Phys. Chem. B*, vol.108, pp.19912-19916, 2004.

[17] K. S. Novoselov, A.K. Geim, S.V. Morozov, D. Jiang, Y. Zhang, S.V. Dubonos, I.V. Grigorieva, and A.A. Firsov, "Electric Field Effect in Atomically Thin Carbon Films", *Science,* vol. 306, pp. 666-669, 2004.

[18] K.S. Novoselov, A.K. Geim, S.V. Morozov, D. Jiang, M.I. Katsnelson, I.V. Grigorieva, S.V. Dubonos, and A.A. Firsov, "Two-Dimensional Gas of Massless Dirac Fermions in Graphene", *Nature,* vol.438, pp.197-200, 2005.

[19] Y. Zhang, Y.-W. Tan, H. Stormer, and P. Kim, "Experimental observation of the quantum Hall effect and Berry's phase in graphene", *Nature,* vol.438, pp.201-204, 2005.

[20] P. R. Wallace, "The Band Theory of Graphite", *Phys. Rev.,* vol.71, pp.622–634, 1947.

[21] J. C. Slonczewski and P.R. Weiss. Band Structure of graphite. *Phys. Rev.,* vol.109, pp.272-279, 1958.

[22] B. Yang, Y. Wu, B. Zong, Z. Shen, "Electrochemical synthesis and characterization of magnetic nanoparticles on carbon nanowall templates", *Nano Lett.*, vol.2, pp.751-754, 2002.

[23] Y. Wu, B. Yang, G. Han, B. Zong, H. Ni, P. Luo, "Fabrication of a class of nanostructured materials using carbon nanowalls as templates", *Adv. Funct. Mater*., vol.12, pp.489-494, 2002.

[24] Y. H. Wu, B.J. Yang, "Effects of Localized Electric Field on the Growth of Carbon Nanowalls", *Nano Lett.,* vol.2, pp.355, 2002.

[25] M. Hiramatsu, K. Shiji, H. Amano, and M. Hori, "Fabrication of vertically aligned carbon nanowalls using capacitively coupled plasma-enhanced chemical vapor deposition assisted by hydrogen radical injection", *Appl. Phys. Lett.,* vol.84, pp.4708, 2004.

[26] K. Shiji, M. Hiramatsu, A. Enomoto, M. Nakamura, H. Amano and M. Horic, "Vertical growth of carbon nanowalls using rf plasma-enhanced chemical vapor deposition", *Diamond and Related Materials*, vol.14, pp.831-834, 2005.

[27] K. Tanaka, M. Yoshimura, A. Okamoto, K. Ueda, "Growth of carbon nanowalls on a SiO2 substrate by microwave plasma-enhanced chemical vapor deposition", *Jpn. J. Appl. Phys*., vol.44, pp.2074-2076, 2005.

[28] A.T.H. Chuang, B.O. Boskovic and J. Robertson, "Freestanding carbon nanowalls by microwave plasma-enhanced chemical vapour deposition", *Diamond and Related Materials*, vol.15, pp.1103-1106, 2006.

[29] T. Itoha, S. Shimabukuro, S. Kawamura and S. Nonomura, "Preparation and electron field emission of carbon nanowall by Cat-CVD", *Thin Solid Films*, vol.501, pp.314-317, 2006.

[30] M. Hiramatsu and M. Hori, "Fabrication of Carbon Nanowalls Using Novel Plasma Processing*", Jpn. J. Appl. Phys*., vol.45, pp.5522-5527, 2006.

[31] G. Sato, T. Morio, T. Kato and R. Hatakeyama, "Fast Growth of Carbon Nanowalls from Pure Methane using Helicon Plasma-Enhanced Chemical Vapor Deposition", *Jpn. J. Appl. Phys.,* vol.45, pp.5210-5212, 2006.

[32] A. Malesevica, S. Vizireanuc, R. Kempsa, A. Vanhulsela, C. Van Haesendonckb and G. Dinescuc, "Combined growth of carbon nanotubes and carbon nanowalls by plasma-enhanced chemical vapor deposition", *Carbon*, vol.45, pp.2932-2937, 2007.

[33] S. Kondo, M. Hori, K. Yamakawa, S. Den, and H. Kano, "Highly reliable growth process of carbon nanowalls using radical injection plasma-enhanced chemical vapor deposition*", J. Vac. Sci. Technol*. B, vol.26, pp.1294-1300, 2008.

[34] T. Moria, M. Hiramatsu, K. Yamakawab, K. Takedac and M. Horic, "Fabrication of carbon nanowalls using electron beam excited plasma-enhanced chemical vapor deposition", *Diamond and Related Materials*, vol.17, pp.513-1517, 2008.

[35] H. Wang, X. Quan, H. Yua and S. Chena , "Fabrication of a TiO_2/carbon nanowall heterojunction and its photocatalytic ability", *Carbon,* vol.46, pp.1126-1132, 2008.

[36] N. G. Shang, P. Papakonstantinou, M. McMullan, M. Chu, A. Stamboulis, A. Potenza, S. S. Dhesi , H. Marchetto, "Catalyst-Free Efficient Growth, Orientation and Biosensing Properties of Multilayer Graphene Nanoflake Films with Sharp Edge Planes", *Advanced Functional Materials*, vol.18, pp.3506-3514, 2008.

[37] Y. Ando, X. Zhao, M. Ohkohchi, "Production of Petal-like Graphite sheets by Hydrogen Arc Discharge", *Carbon,* vol.35, pp.153-158, 1997.

[38] N. G. Shang, F. C. K. Au, X. M. Meng, C. S. Lee, I. Bello and S. T. Lee,"Uniform carbon nanoflake films and their field emissions", *Chemical Physics Letters*, vol.358, pp.187-191, 2002.

[39] T. Hirao, K. Ito, H. Furuta, Y. K. Yap, T. Ikuno, S. Honda, Y. Mori, T. Sasaki and K. Oura, "Formation of Vertically Aligned Carbon Nanotubes by Dual-RF-Plasma Chemical Vapor Deposition", *Jpn. J. Appl. Phys*., vol.40, pp.L631-L634, 2001.

[40] A. N. Obraztsov, A. P. Volkov, K. S. Nagovitsyn, K. Nishimura, K. Morisawa, Y. Nakano and A. Hiraki, "CVD growth and field emission properties of nanostructured carbon films", *J. Phys. D: Appl. Phys.* vol.35, pp.357-362, 2002.

[41] J. Wang, M. Zhu, R. A. Outlaw, X. Zhao, D. M. Manos, and B. C. Holloway, "Free-standing subnanometer graphite sheets", *Appl. Phys. Lett*., vol.85, pp.1265-1267, 2004.

[42] X. Zhao, R. A. Outlaw, J. J. Wang, M. Y. Zhu, G. D. Smith, and B. C. Holloway, "Thermal desorption of hydrogen from carbon nanosheets", *J. Chem. Phys*., vol.124, pp.194704, 2006.

[43] J.J. Wang, M.Y. Zhu, R.A. Outlaw, X. Zhao, D.M. Manos, B.C. Holloway, "Synthesis of carbon nanosheets by inductively coupled radio-frequency plasma enhanced chemical vapor deposition", *Carbon*, vol.42, pp.2867-2872, 2004.

[44] S. Wang, J. Wang, P. Miraldo, M. Zhu, R. Outlaw, K. Hou, X. Zhao, B. C. Holloway, D. Manos, T. Tyler, O. Shenderova, M. Ray, J. Dalton, and G. McGuire, "High field emission reproducibility and stability of carbon nanosheets and nanosheet-based backgated triode emission devices", *Appl. Phys. Lett*., vol.89, pp.183103, 2006.

[45] K. Hou, R. A. Outlaw, S. Wang, M. Zhu, R. A. Quinlan, D. M. Manos, M. E. Kordesch, U. Arp, and B. C. Holloway, "Uniform and enhanced field emission from chromium oxide coated carbon nanosheets ", *Appl. Phys. Lett.,* vol.92, pp.133112, 2008.

[46] J. Wang, M. Zhu, X. Zhao, R. A. Outlaw, D. M. Manos, B. C. Holloway, C. Park, Tim Anderson, and Victor P. Mammana "Synthesis and field-emission testing of carbon nanoflake edge emitters", *J. Vac. Sci. Technol. B,* vol.22, pp.1269, 2004.

[47] M. Bagge-Hansen, R. A. Outlaw, P. Miraldo, M. Y. Zhu, K. Hou, N. D. Theodore, X. Zhao, and D. M. Manos, "Field emission from Mo_2C coated carbon nanosheets", *J. Appl. Phys*., vol.103, pp.014311, 2008.

[48] J.M. Du, Z.M. Liu, Z.H. Li, B.X. Han, Z.Y. Sun, Y. Huang, "Carbon nanoflowers synthesized by a reduction–pyrolysis–catalysis route", *Materials Letters,* vol.59, pp.456-458, 2004.

[49] A. Dato, V. Radmilovic, Z. Lee, J. Phillips and M. Frenklach, "Substrate-Free Gas-Phase Synthesis of Graphene Sheets", *Nano Lett.*, vol.8 , pp.2012–2016, 2008.

[50] N. G. Shang, P. Papakonstantinou, M. McMullan, M. Chu, A. Stamboulis, A. Potenza, S. S. Dhesi, and H. Marchetto, "Catalyst-Free Efficient Growth, Orientation and Biosensing Properties of Multilayer Graphene Nanoflake Films with Sharp Edge Planes", *Adv. Funct. Mater*., vol.18, pp.3506–3514, 2008.

[51] A. Malesevic, et al, "Synthesis of few-layer graphene via microwave plasma-enhanced chemical vapour deposition", *Nanotechnology,* vol.19 pp.305604, 2008.

[52] M. Zhu, J. Wang, B.C. Holloway, R.A. Outlaw, X. Zhao, K. Hou, V. Shutthanandan and D. M. Manos, "A mechanism for carbon nanosheet formation", *Carbon*, vol.45, pp.2229-2234, 2007.

[53] B.L. French, J.J. Wang, M.Y. Zhu and B.C. Holloway, "Evolution of structure and morphology during plasma-enhanced chemical vapor deposition of carbon nanosheets", *Thin Solid Films*, vol.494, pp.105-109, 2006.

[54] B.L. French, J.J. Wang, M.Y. Zhu, and B.C. Holloway, "Structural characterization of carbon nanosheets via x-ray scattering", *J. Appl. Phys.,* vol.97, pp.114317, 2005.

[55] K. Kobayashi, M. Tanimura, H. Nakai, A. Yoshimura, H. Yoshimura, K. Kojima, and M. Tachibana, *J. Appl. Phys*., vol.101, pp.094306, 2007.

[56] A.I. Romanenko, O.B. Anikeeva, V.L. Kuznetsov, A.N. Obrastsov, A.P. Volkov and A.V. Garshev, "Quasi-two-dimensional conductivity and magnetoconductivity of graphite-like nanosize crystallites", *Sol. Stat. Comm*., vol.137, pp.625-629, 2006.

[57] W. Takeuchi, M. Ura, M. Hiramatsu, Y. Tokuda, H. Kano, and M. Hori, "Electrical conduction control of carbon nanowalls", *Appl. Phys. Lett*., vol.92, pp.213103, 2008.

[58] A.N. Obraztsov, O. Gröning, A.A. Zolotukhin, A.A. Zakhidov and A.P. Volkov, "Correlation of field emission properties with morphology and surface composition of CVD nanocarbon films", *Diamond and Related Materials,* vol.15, pp.838-841, 2006.

[59] M Bagge-Hansen, R A Outlaw, P Miraldo, M Y Zhu, K Hou, N D Theodore, X Zhao, and D M Manos, "Field emission from Mo2C coated carbon nanosheets", *J. Appl. Phys.*, vol.103, pp.14311, 2008.

[60] K. Hou, R. A. Outlaw, S. Wang, M. Zhu, Ronald A. Quinlan, D. M. Manos, M. E. Kordesch, U. Arp, and B. C. Holloway, "Uniform and enhanced field emission from chromium oxide coated carbon nanosheets", *Appl. Phys. Lett*., vol.92, pp.133112, 2008.

[61] X. Zhao, R. A. Outlaw, J. J. Wang, M. Y. Zhu, G. D. Smith, and B. C. Holloway, "Thermal desorption of hydrogen from carbon nanosheets", *J. Chem. Phys*., vol.124, pp.194704, 2006.

[62] P. Blake, K. S. Novoselov, A. H. Castro Neto, D. Jiang, R. Yang, T. J. Booth, A. K. Geim, and E. W. Hill, "Making graphene visible", *Appl. Phys. Lett*., vol.91, pp.063124, 2007.

[63] Y. Zhang, J. P. Small, W. V. Pontius, and P. Kim, "Fabrication and Electric Field Dependent Transport Measurements of Mesoscopic Graphite Devices", *Appl. Phys. Lett.,* vol.86, pp.073104, 2005.

[64] X. Liang, Z. Fu, and S. Y. Chou, "Graphene Transistors Fabricated via Transfer-Printing In Device Active-Areas on Large Wafer", *Nano Lett.,* vol.7, pp.3840-3844, 2007.

[65] X. Liang, A. S. P. Chang, Y. Zhang, B. D. Harteneck, H. Choo, D. L. Olynick and S. Cabrini ,"Electrostatic Force Assisted Exfoliation of Prepatterned Few-Layer Graphenes into Device Sites", *Nano Lett*., vol.9, pp.467-472, 2009.

[66] J.S. Bunch, Y. Yaish, M. Brink, K. Bolotin, and P. L. McEuen, "Coulomb oscillations and Hall effect in quasi-2D graphite quantum dots," *Nano Lett*., vol.5, pp.287-290, 2005.

[67] P. Blake, et al. "Graphene-based liquid crystal device", *Nano Lett*., vol.8, pp.1704-1708, 2008.

[68] X. Li, G. Zhang, X. Bai, X. Sun, X. Wang, E. Wang and H. Dai, "Highly conducting graphene sheets and Langmuir–Blodgett films", *Nature Nano*., vol.3, pp.538- 542, 2008.

[69] Y. Hernandez, et al. "High-yield production of graphene by liquid-phase exfoliation of graphite", *Nature Nano*., vol.3, pp.563-568, 2008.

[70] X. Li, X. Wang, L. Zhang, S. Lee, and H. Dai, "Chemically Derived, Ultrasmooth Graphene Nanoribbon Semiconductors" *Science*, vol.319, pp.1229-1232, 2008.

[71] D. A. Dikin, S. Stankovich, E. J. Zimney, R. D. Piner, G. H. B. Dommett, G. Evmenenko, S. T. Nguyen, R. S. Ruoff, "Preparation and characterization of graphene oxide paper", *Nature*, vol.448, pp.457-460, 2007.

[72] P. W. Sutter, J.-I. Flege, and E. A. Sutter, "Epitaxial graphene on ruthenium. *Nature Mater*., vol.7, pp.406-411, 2008.

[73] Q. Yu, J. Lian, S. Siriponglert, H. Li, Y.P. Chen, and S. Pei, "Graphene segregated on Ni surfaces and transferred to insulators", *Appl. Phys. Lett.,* vol.93, pp.113103, 2008.

[74] Y. Pan, H. Zhang, D. Shi, J. Sun, S. Du, F. Liu, H. Gao, "Highly Ordered, Millimeter-Scale, Continuous, Single-Crystalline Graphene Monolayer Formed on Ru (0001)", *Adv. Mater*., vol.20, pp.1-4, 2008.

[75] G.D. Yuana, W.J. Zhang, Y. Yang, Y.B. Tang, Y.Q. Li, J.X. Wang, X.M. Meng, Z.B. He, C.M.L. Wu, I. Bello, C.S. Lee, and S.T. Lee, "Graphene sheets via microwave chemical vapor deposition", *Chem. Phys. Lett*., vol.467, pp.361-364, 2009.

[76] A. Reina, X. Jia, J. Ho, D. Nezich, H. Son, V. Bulovic, M. S. Dresselhaus and J. Kong, "Large Area, Few-Layer Graphene Films on Arbitrary Substrates by Chemical Vapor Deposition", *Nano Lett*.,vol.9, pp.30–35, 2009.

[77] K.S. Kim, Y. Zhao, H. Jang, S. Y. Lee, J.M. Kim, K.S. Kim, J.-H. Ahn, P. Kim, J.-Y. Choi & B.H. Hong, "Large-scale pattern growth of graphene films for stretchable transparent electrodes", *Nature,* vol.457, pp.706-710, 2009.

[78] K.V. Emtsev, et al., "Towards wafer-size graphene layers by atmospheric pressure graphitization of silicon carbide", *Nat. Mater.,* vol. 8, pp.203-207, 2009.

[79] Walt A. de Heer, C. Berger, X. Wu, P.N. First, E.H. Conrad, X. Li, T. Li, M. Sprinkle, J. Hass, M.L. Sadowski, M. Potemski, G. Martinez , "Epitaxial graphene", *Solid State Commun*., vol.143, pp.92-100, 2007.

[80] P.W. Sutter, J.-I. Flege, and E.A. Sutter, "Epitaxial graphene on ruthenium", *Nature Mater*., vol.7, pp.406–411, 2008.

[81] M.Y. Han, B. Oezyilmaz, Y. Zhang, and P. Kim, "Energy Band Gap Engineering of Graphene Nanoribbons", *Phys. Rev. Lett.*, vol.98, pp.206805, 2007.

[82] X. Li, X. Wang, L. Zhang, S. Lee, and H. Dai. "Chemically Derived, Ultrasmooth Graphene Nanoribbon Semiconductors", *Science*, vol.319, pp.1229-1232, 2008.

[83] K. Nakada, M. Fujita, G. Dresselhaus, M. S. Dresselhaus, "Edge state in graphene ribbons: nanometer size effect and edge shape dependence", *Phys. Rev. B,* vol.54, pp.17954-17961, 1996.

[84] K. Wakabayashi, M. Fujita, H. Ajiki, M. Sigrist, "Electronic and magnetic properties of nanographite ribbons", *Phys. Rev. B*, vol.59, pp8271-8282, 1999.

[85] O.E. Andersson, B.L.V. Prasad, H. Sato, T. Enoki, Y. Hishiyama, Y. Kaburagi, M. Yoshikawa and S. Bandow, "Structure and electronic properties of graphite nanoparticles", *Phys. Rev. B*, vol.58, pp.16387-16395, 1998.

[86] B.L.V. Prasad, H. Sato, T. Enoki, Y. Hishiyama, Y. Kaburagi, A.M. Rao, "Heat-treatment effect on the nanosized graphite π electron system during diamond to graphite conversion", *Phys. Rev. B*, vol. 62, pp.11209-11218, 2000.

[87] A.M. Affoune, B.L.V. Prasad, H. Sato, T. Enoki, Y. Kaburagi, and Y. Hishiyama, "Experimental evidence of a single nano-graphene", *J. Chem. Lett.*, vol. 348, pp.17-20, 2001.

CHAPTER 2

GRAPHENE UNDER MODIFICATIONS

In Chapter 1, we gave a general introduction about 2D carbon (such as, CNWs and graphene). In this chapter, an overview of both the theoretical and experimental work reported so far on the electronic properties of 2D carbon under modification, such as, graphene bilayer/multilayer, graphene nanoribbon, nanoflakes (nonodots), functionalized graphene and extrinsic graphene will first be presented. The detailed background will convince us that the transport properties of 2D carbon nanostructure are worth investigating. Therefore, we choose 2D carbon nanostructures as our research objects.

2.1 Introduction

As discussed in Chapter 1, graphene is a unique system in many ways. [1-5] Graphene is truly two dimensional, and its electronic excitation is described in terms of Dirac fermions. The features (such as gapless and zero density of states near Dirac point) make the properties of graphene rather different from those of normal semiconductors or metals. In addition, the carriers in graphene have very long mean free paths because they are almost insensitive to disorder and electron-electron interactions. Interestingly, these properties can be modified with addition of layers, shrinking down to mesoscopic or atomic scales, chemical/physical functionalization, interaction with environment. These various modifications make graphene one of the most versatile systems for both fundamental research and electronic applications. In

the rest of this chapter, an overview of both the theoretical and experimental work reported so far on graphene under various modifications will be presented.

2.2 Bilayer and Multilayer Graphene

Recently the attention has turned to graphene multilayers because of their special properties. [4-6] Many of the special properties of graphene multilayer have their origin in the lattice structures. As shown in Figure 2.1 and 2.2, various lattice structures lead to the peculiar band structure. Among them, bilayer graphene is of particular interest. Graphene bilayer shows anomalies in the integer quantum Hall effect [7] and has received a lot of theoretical attention [8, 9].

In normal bilayer graphene, two carbon layers are placed on top of each other according to the usual Bernal AB stacking. (See Figure 2.3(a)) The low energy properties are described by massive Dirac Fermion, with a quadratic dispersion close to the neutrality point.[10] However, as shown in Figure 2.3(b), recent calculation indicates that an external electric field applied perpendicular to the graphene surface could tune the electronic structure of the bilayer system.[11 - 14] Subsequent experiments[15-17] proved that a finite bias voltage between graphene planes gives rise to a finite gap, whose size could be controlled by the external electrical field. However, the external electrical field could not open an electronic gap in a graphene bilayer with a stacking rotation.[18] Such a misoriented bilayer system[19] could exhibit similar Shubnikov–de Haas oscillations as monolayer. The observation is in accord with results in epitaxial multilayer graphene.[20] In addition, a linear low energy dispersion of the electronic structure near zero energy was observed in misoriented bilayer graphene, while the Fermi velocity became comparatively smaller than the value of monolayer.[21, 22]

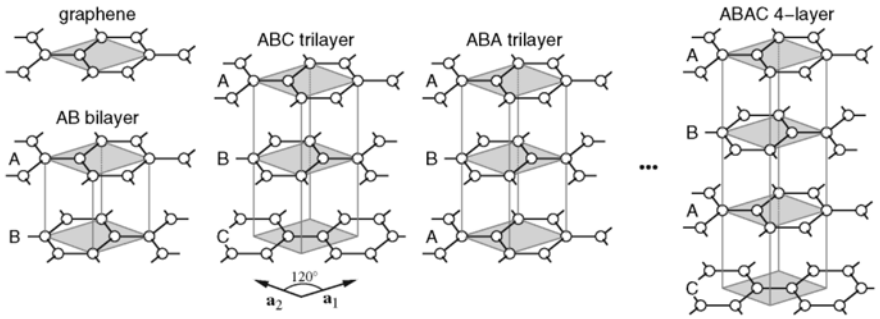

FIG. 2.1 The 2D primitive cells of few layer graphene with different stacking orders. (Refer to Ref. [30])

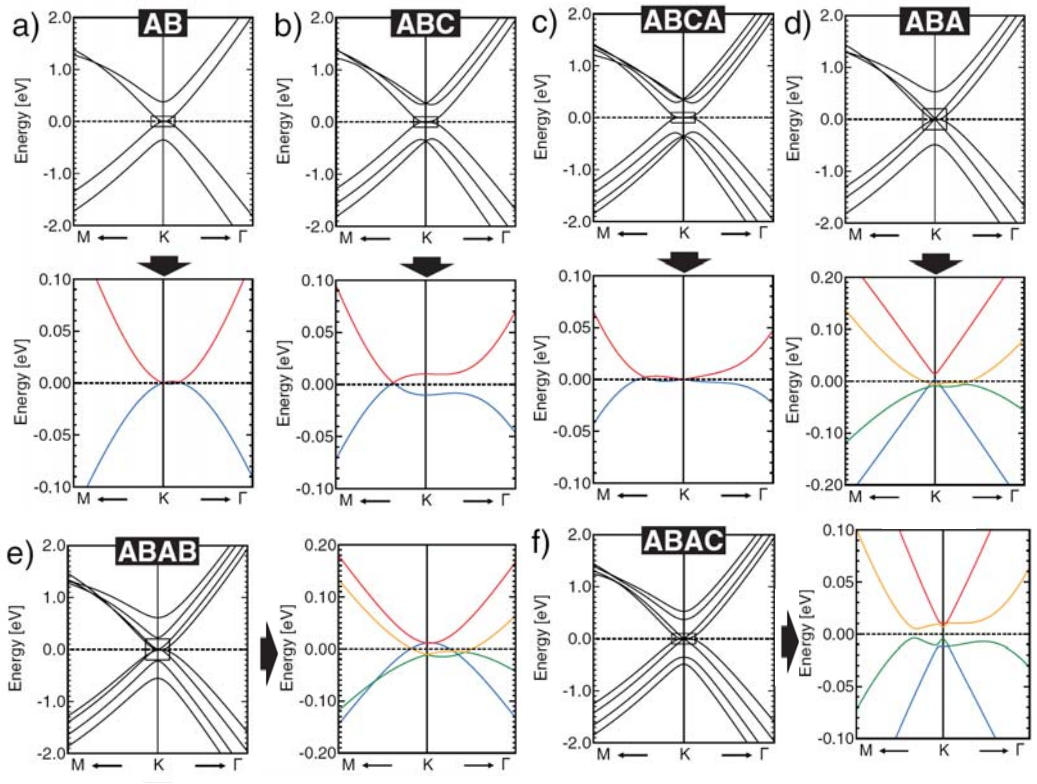

FIG. 2.2 Details of few layer graphene band structures in the vicinity of K point and near the Fermi level (always set as zero), noting that the bands of the ABAC 4-layers are not crossing and a gap is open. (Refer to Ref. [30])

Moreover, graphene bilayer is also prone to show strong electron-electron correlation effects, such as magnetism [23] and charge density wave [24] phases,

because of its finite density of states at the Dirac point. When applying a high voltage across a bilayer graphene with certain layer spacing, electron-hole pair condensation could form in the pair of bilayer with opposite polarity. (See in Figure 2.3(c) and (d)) High-temperature superfluidity [25-28] in the "excitonic condensation" are expected in the electron-hole bilayer. It is noted that the attractive Coulomb interaction between electrons and holes could lead to instability toward formation of electron-hole pairs. [29]

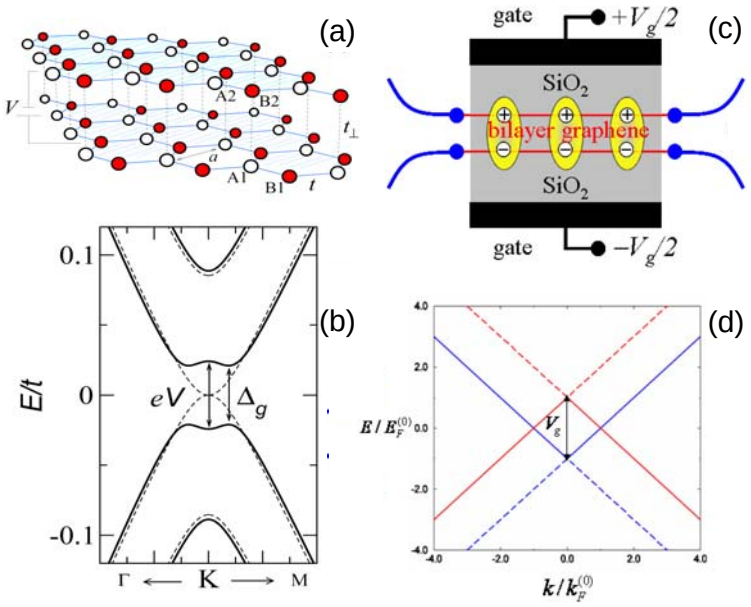

Fig. 2.3 (a) Lattice structure of a bilayer graphene with Bernal stacking. The A and B sublattices are indicated by white and red spheres, respectively. (b) Band structure of bilayer graphene near the Dirac points for V=150meV (solid line) and V=0 (dashed line).(Refer to Ref. [17]) (c) Schematic illustration of a graphene bilayer excitonic condensate channel in which two monolayer graphene sheets are separated by a dielectric barrier. The electron and hole carriers induced by an external electrical field will form a high temperature excitonic condensate. (d) The two band model indicated by solid lines, the two remote bands indicated by dashed lines. (Refer to Ref. [25])

According the previous discussion, graphene bilayer has very unconventional behavior in its spectral transport properties, which are rather different from those of

monolayer. In fact, multilayer graphene systems also have similar anomalous properties. Multilayer systems would be variety of stacking structures, which determine their band structures. [30-32] The high complexity of layer stacking in multilayer graphene system allows great flexibility in tailoring its electronic properties.[33] The properties may be of interest for physics and device applications. It is well known that graphite exhibits large diamagnetism, and this has been explained theoretically. [34] Recent experimental evidence indicates that intrinsic ferromagnetism and high temperature superconductivity exist in large scale multilayer graphene flakes. [35] In addition, experimental phenomena such as, magnetically driven metal-insultor transition, [36, 37] quantum Hall effect, [38] and the existence of 2D Dirac fermions in graphite, [39-41] clearly indicate that much of the physics in multilayer graphene has not been fully understood. We anticipate that multilayer graphene samples will be as interesting as monolayer graphene in both physics and applications.

2.3 Carbon Nanoribbon: Electronic Confinement and Edge State

2.3.1 Confinement

Graphene nanoribbon (GNR) is known as unrolled single-walled carbon nanotube or a narrow strip of graphene. Electronic structure of GNRs greatly depends on the edge shapes. In 1996, M. Fujita et al. originally introduced graphene ribbon as a theoretical model to study edges and quantum confinement effect.[42-44] Basically, there are two types of edges in GNRs, i.e., armchair edge, zigzag edge (see Figure 2.4 (a) and (b)).Tight binding calculations predict that zigzag GNRs are always metallic

while armchair GNRs can be either metallic or semiconducting, depending on their width. [42-44] (see Figure 2.4(c)) However, recent Density functional theory (DFT) calculations show that all armchair nanoribbons are semiconducting with an energy gap scaling with the inverse of GNR width.[45-47] Later, first-principles approach indicated that, in GNRs with either armchair or zigzag shaped edges on both sides with hydrogen passivation, both varieties of ribbons are shown to have band gaps as a function of the GNRs' widths.[48] The origin of energy gaps for armchair GNRs arises from both quantum confinement and the edges shapes. For zigzag GNRs, gaps appear because of a staggered sublattice potential on the hexagonal lattice. Zone-folding approximations [49], π-orbital tight-binding models [50, 51], and first principle calculations [52, 53] predict a scaling rule for the band gaps: $\Delta E_g = \alpha / W$ with the nanoribbon width W, where α ranges between $0.2 \sim 1.5 eV \cdot nm$, depending on the model and the crystallographic direction [54].

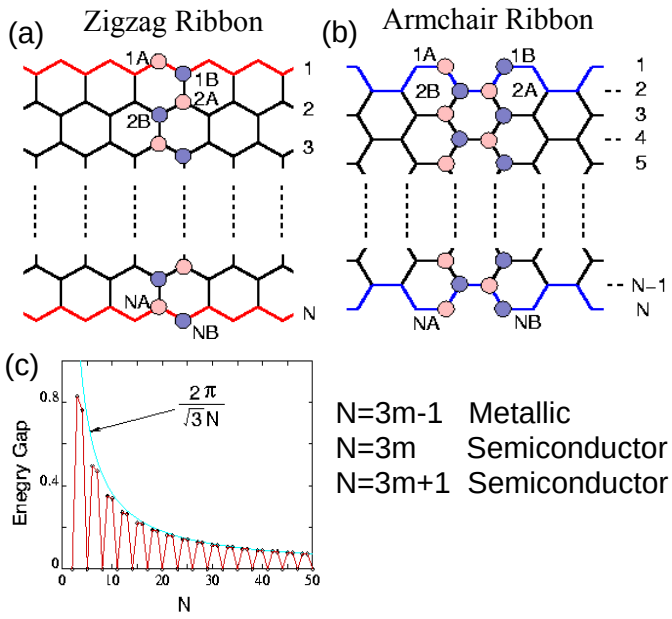

FIG. 2.4 Two types of edge shape for graphene ribbons: (a) zigzag edge and (b) armchair edge. The edges are indicated by the hold lines. The red and blue circles show the A and B site carbon atoms, respectively; (c) the relationship of energy gap and the width N in armchair ribbon, whose 2/3 show the semiconducting gap. (Figures adapted from K. Wakabayashi, 2003)

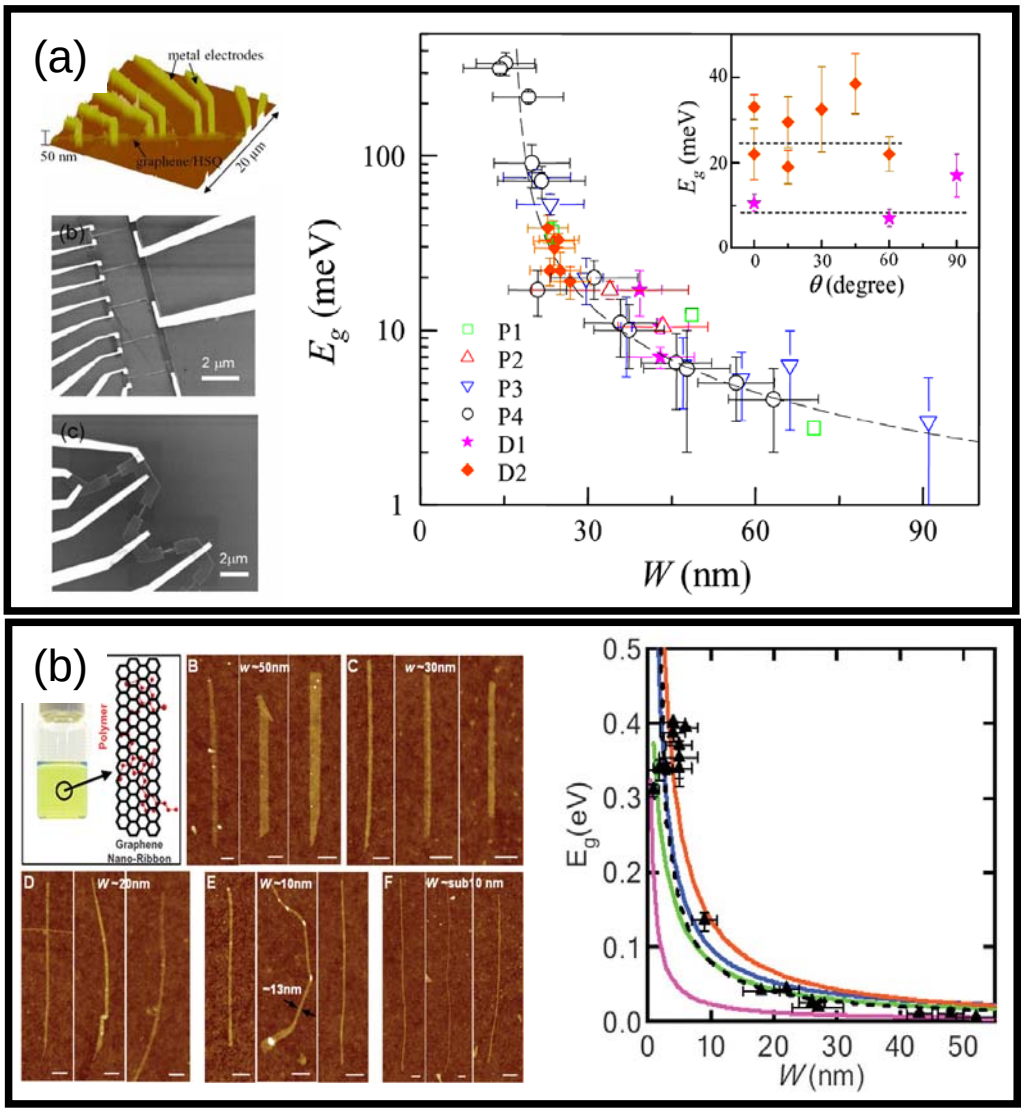

FIG. 2.5 (a) Atomic force microscope (AFM) and scanning electron microscope (SEM) images of GNRs fabricated by plasma etching, and the relationship between conduction gap and the width of GNR (refer to Ref.[57]). (b) Atomic force microscope (AFM) image of chemically derived GNRs down to sub-10 nm width, and the relationship between conduction gap and the width of GNRs. (Refer to Ref. [58])

Recently, experimental studies on GNRs fabricated by plasma etching show a thermally activated conductivity [55]. The phenomena suggest the presence of a size dependent energy gap. The energy gaps are inversely proportional to GNR width. [56-59]. Berger et al. [56] showed that energy gap ΔE_g in epitaxial GNRs follows the

relationship: $\Delta E_g = \Delta E(W) \approx \frac{2eV \cdot nm}{W\ nm}$ with the nanoribbon width (W). Later, M. Han et al, [57] demonstrated that the size of the gap follows the approximate law: $\Delta E_g = \frac{0.2\,\mathrm{eV} \cdot \mathrm{nm}}{(W-16)nm}$ in lithographically patterned GNRs. (See Figure 2.5(a)). Most recently, Li. et al.[58] showed that the band gaps were fit into an empirical form of $\Delta E_g = \frac{0.8\,\mathrm{eV} \cdot \mathrm{nm}}{W\ nm}$ in chemically exfoliated GNRs. (See Figure 2.5(b)) Unfortunately, to date, no experimental results have measured the energy gap of a GNR which is identified at the exact edge structure. Investigations on GNRs of different orientations with respect to graphene lattice [57] indicated the absence of well-defined crystallographic edges in the lithographically patterned GNRs.

Interestingly, it is found that all the observed conduction gaps are larger than those expected from a single-particle confinement picture in the absence of lattice effects at the edges.[60] There are several alternative explanations which were purposed to explain the comparatively large energy scale of conduction gap. Han et al. [57] believes that atomic-scale disorders lead to a nonconductive "dead zone" at the ribbon edges and therefore cause the effective conducting ribbon width to be narrower than the physical width. M. Evaldsson et al. [61] argues that localized states rising from the atomically disordered edges extend into the ribbon body. On the other hand, S. Adam et al. [62] proposed that both random charged impurities and the confinement gap have caused a metal-insulator transition. Some other researchers suggested that the roughness of lithographic edge may create a series of quantum dots defined by nanometer-scale variations in ribbon width.[63, 64] Very recently, researchers [60, 65, 66] experimentally find two independent energy scales characterizing conduction gaps. One is charging energy among quantum dots along the ribbon. The other one is

dominated by the strength of disorder potential along the ribbon, and depends on the gap induced by confinement due to the ribbon boundaries. These results are greatly important in understanding the transport in graphene nanostructures and development of future graphene-based devices.

2.3.2 Edge State

Beside electronic confinement, the electronic states near edges are of great interest in GNRs. Electronic states of GNR greatly depend on the edge structures (armchair or zigzag). The tight binding band calculations predicted the existence of peculiar electronic states localized only at zigzag edges, as shown in Figure 2.6. [42-44] This localized state is known as "edge state". No such localized state appears in armchair edges. The special characteristics of edge states play an important role in determining the density of states near the Fermi level for GNRs. They are expected to have additional modification in electronic properties from confinement quantization. The edge states create a peak in the local density of states (LDOS) at the Fermi energy (E_F). If GNR is wide enough, the influence of edge states on total density of states may be negligible. Actually, edge states near zigzag edges would be observable with the scanning tunneling spectroscopy (STS) technique. A similar edge state is also obtained for multilayer ribbons of stacking from the first-principles calculations. [67] This indicates that the edge state would exist in all graphitic systems, such as step edges at bulk graphite surfaces.[68]

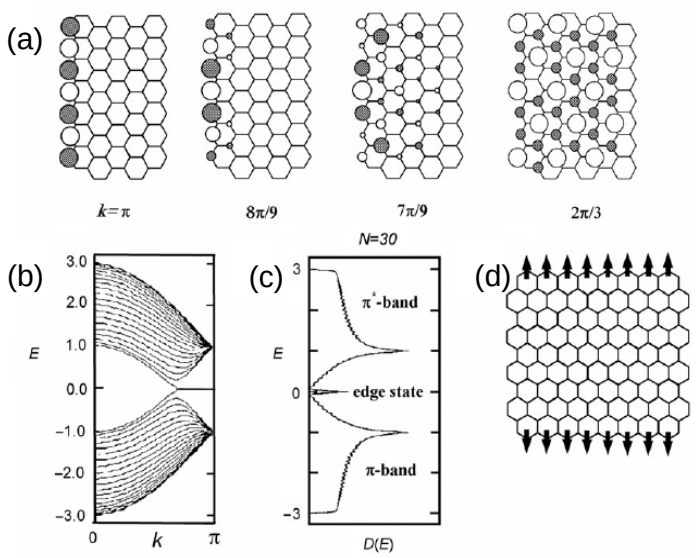

FIG. 2.6 (a) The wavenumber dependence of the populations of the edge state; (b) the energy dispersions of nanographene ribbon having zigzag edges with a width of 30 unit cells; (c) the density of states, and (d) Ferromagnetic spin arrangement at the zigzag edges. All the edge carbon atoms are terminated with hydrogen atoms. (Refer to Ref.[42])

In order to clarify the features of edge states in atomic resolution and understand the relationship between electronic properties and atomic edge structures, experimental efforts have been made using scanning tunneling microscopy (STM)/scanning tunneling spectroscopy (STS) in ultra-high vacuum (UHV) conditions [69-71]. The graphene edges are well defined by hydrogen-termination. The edge dependence of LDOS distribution is clearly shown in Figure 2.7. The peak of dI/dV curve near zero bias clearly verifies the presence of edge states at zigzag edge. However, the dI/dV curve at armchair edge has not such a peak, as shown in Figure 2.7(c). In addition, STS measurements were performed near circular edges of graphite nanopits etched by either hydrogen [72] or oxygen [73], a broad maximum was observed in dI/dV curve, and it was attributed to the edge state near Fermi level. Unfortunately, the authors did not give any clear edge structures.

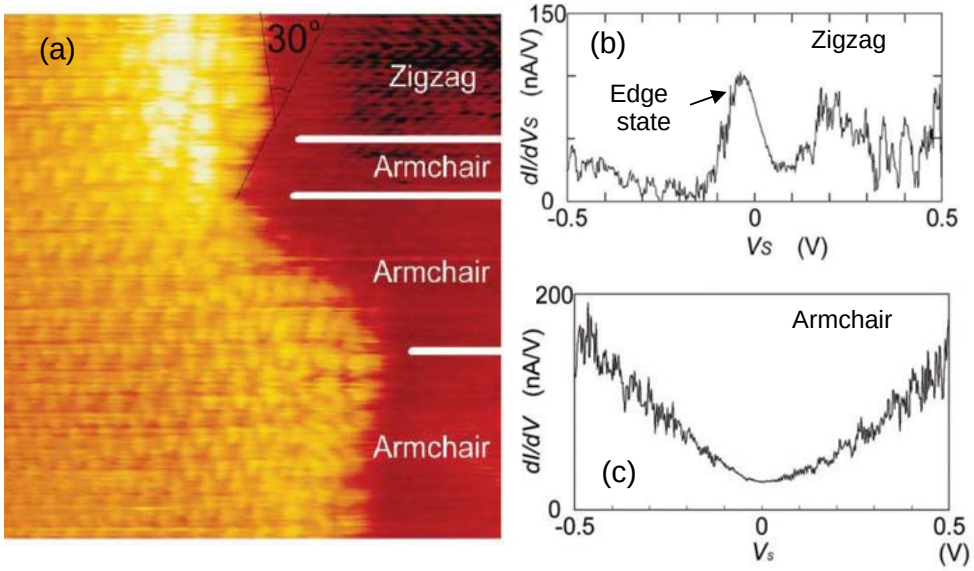

FIG. 2.7 (a) An atomically resolved UHV STM image of zigzag and armchair edges ($9\times9nm^2$) observed in constant height mode with bias voltage V_s= 0.02 V and current I = 0.7 nA. (b) The dI/dV curve from STS data at a zigzag edge. (c) A dI/dV curve from STS measurements taken at an armchair edge. (Refer to Ref.[69])

Edge states in electronic structures are very important in determining the transport properties in graphitic materials. Intrinsic superconductivity of CNTs has been observed in bundles of large-diameter SWCNTs [74 , 75], zeolite-inserted SWCNTs of small (4 Å) diameter [76], and MWCNTs encapsulated in large pores of zeolite [77]. The intrinsic superconductivity may originate from zigzag edge states which are specific to graphene. [78] In addition, the magnetism at zigzag [79-81] or armchair edges [82] has been used to explain observed magnetic properties in nanographite materials. Very recently, first principle calculations predicted half metallicity in graphene nanoribbons with zigzag edges.[83] The half metallicity is caused by opposite responses of edge states to the external electric field for the up and down spins.

It is worth mentioning that edge states originate from the symmetry breaking phenomenon of Dirac electrons under the boundary condition at zigzag edges [84, 85].

Since the edge state appears as a half-filled state at the Fermi level, zigzag edges are not well energetically stabilized in comparison with armchair-edges.[86] In other words, armchair edges are generally long and defect-free whereas zigzag edges tend to be short and defective.

2.4 Graphene Nanoflake or Nanodot

We refer arbitrarily shaped finite graphene fragments as graphene nanoflakes (GNFs) or nanodots (GNDs). As GNRs has 1D straight edges, it can be considered as a special case of GNFs. Because the basic components of future electronics devices will be at nanometer scale according to Moore's law, it is important to understand the properties of GNFs. In fact, all GNFs also have similar anomalous properties with GNRs. As shown in Figure 2.8, the higher complexity of edge shape in GNFs allows for greater flexibility in tailoring their electronic properties. So far, there are few theoretical or experimental studies on GNFs as GNRs due to the high complexity of the edge shape.

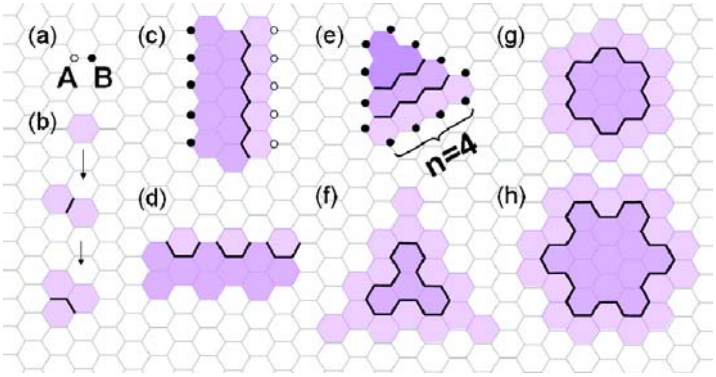

FIG. 2.8 Various types of graphene nanoflakes stitched up from smaller subflakes (darker shade). Black lines are stitches, and the hydrogen termination along the edges is not shown. (Refer to Ref.[87])

Actually, quantum confinement, as well as variation of edges, raises rich electronic and magnetic properties in hydrogen-passivated GNFs. As shown in Figure 2.9 (a), Wang et al. suggested that confinement creates an energy gap of 0.3-0.5eV at the Fermi level in hydrogen-terminated GNFs in first-principle.[87] Beside the presence of the big energy gap, the magnetic moments at the edges of the triangular graphene flake may exist even at room temperature.[87-90] (See in Figure 2.9 (b),) This principle further suggests many ways of carving patterns out of a graphene plane (such as dots, stripes, and circuits) with desired spin distribution. Figure 2.9 (c) gives an example of a GNF attached to a GNR, forming a possible spintronic component. These results suggest the potential applications of GNFs on nano spintronics.

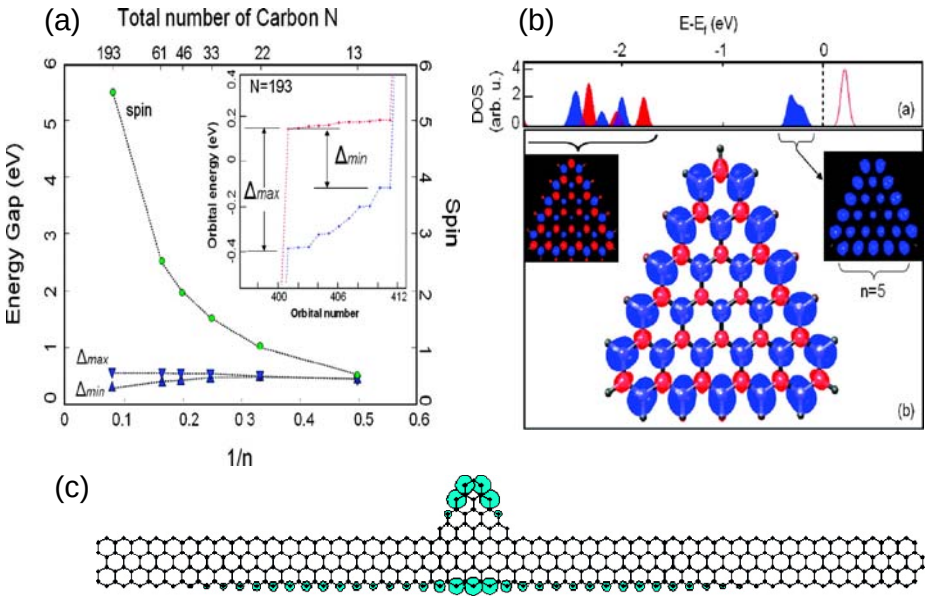

FIG. 2.9 (a) Scaling of spin and energy gap with the inverse linear size (1/n) of zigzag-edged triangular graphene flakes. (b) Zigzag-edged triangular graphene flakes with ferrimagnetic order and linearly scaling net spin. (c) An example of a GNF attached to a GNR, forming a possible spintronic component. (Refer to Ref.[87])

Recent experiments have achieved graphene flakes at the scale of tens of nanometers.[91 - 93] Coulomb blockade phenomena are observed in several

experiments on transport of quantum dots made from patterned graphene [91-93] and chemical exfoliated graphite [94]. More recently, edge features [95] are studied experimentally on few nanometer GNFs at room temperature.[96, 97] As shown in Figure 2.10, the magnitude of the measured energy gaps is inversely proportional to the width of predominantly armchair-edge GNFs. GNFs with a higher fraction of zigzag edges exhibit a smaller energy gap than a predominantly armchair-edge one.

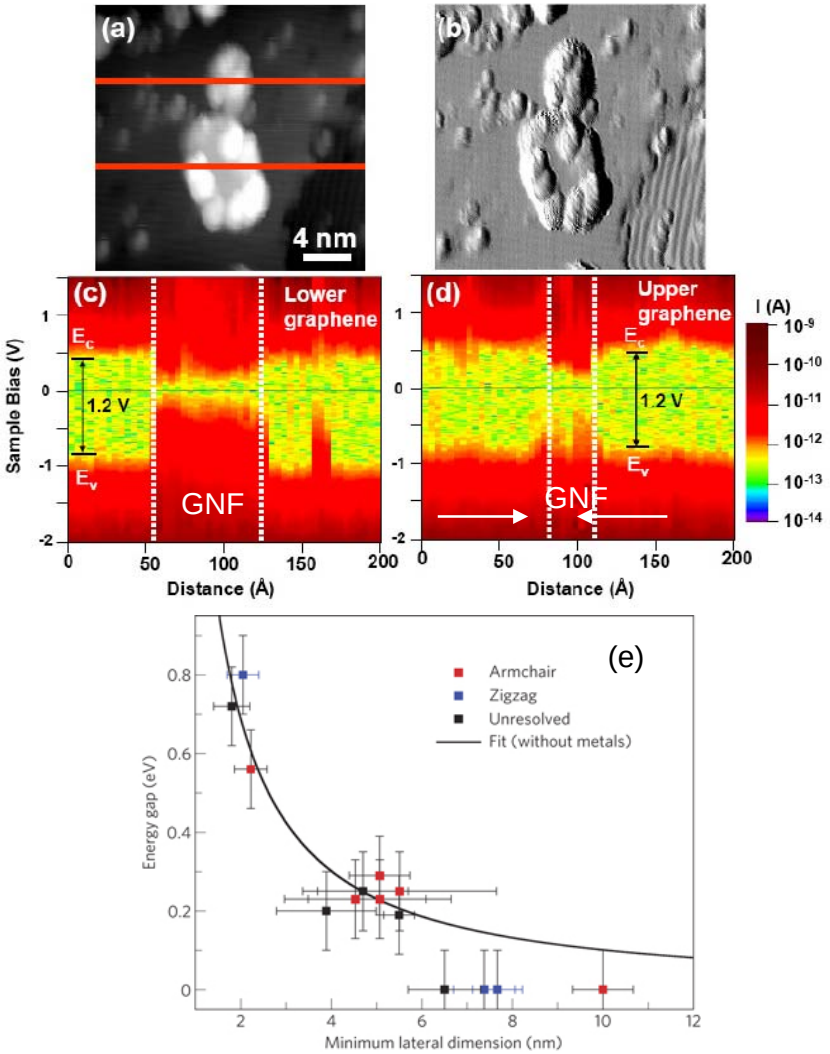

FIG. 2.10 (a) STM topograph and (b) topographic spatial derivative of a 5nm (lower feature) and 2nm wide (upper) feature single layer graphene pieces. Log(I)-V spectra plotted as a function of position for the (c) 5nm and (d) 2nm wide graphene monolayers, (e) Energy gap (E_g) vs width of GNF (L) in 10 semiconducting graphene

nanoflakes, which follows the relationship: E_g (eV)=1.57± 0.21 eV nm/$L^{1.19\pm 0.15}$. (Refer to Ref. [96] and [97])

2.5 Graphene Functionalization

Functionalization can be exploited to control electronic and charge transport properties of graphene devices. There are two types of chemical functionalization, namely, physisorption and chemisorption.

2.5.1 Physisorption

In case of physisorption, noncovalent adsorption enables graphene functionalization while it still preserves its electronic structure, since the original sp^2 hybridized bonding remains unaltered. It only gives a weak control of graphene conductance.

As demonstrated by S. Das Sarma and co-workers [98], the scattering efficiency rising from physisorbed molecules is small in graphene, owing to the weak interaction between both of the systems. The electronic properties of graphene can be tuned by donor and/or acceptor doping from physisorption. In this regard, a recent measurement of Hall effect by Schedin et al.[99] show, that NO_2, H_2O, and iodine act as electron acceptors whereas NH_3, CO, and ethanol present electron donor behavior on graphene. The absorption did not reduce the mobility of graphene devices. These results were recently confirmed through theoretical calculations.[100] After that, T.O. Wehling et al, [101] proved that NO_2 molecules adsorbed on graphene create and control the occupancy of flat impurity bands near the Dirac point as well as they can lead to exchange scattering. Flat bands near the Fermi level may be an origin of ferromagnetism, [102 , 103] superconductivity,[104] charge density wave or other

related electronic instabilities. These results may lead to a possible pathway to high temperature magnetic order in graphene.

The energy gap in graphene layers can also be achieved through noncovalent functionalization with chemical species [105,106] since the doping can induce a gap opening because of the A-B sublattice symmetry breaking. Therefore, the gap opens in epitaxial graphene by interaction with SiC substrate.[107] Recent calculations show that it is possible to open a gap in the electronic band structure and induce spin polarization in graphene when CrO_2 [108] or SiO_2 [109] were brought contact with graphene.

2.5.2 Chemisorption

In the case of chemisorption, covalent functionalization on graphene changes the hybridization of carbon atoms from sp^2 into sp^3, which suggests a stronger alteration of clean graphene electronic properties. The recent calculation shows us that attaching atomic hydrogen to each site of the graphene lattice creates graphane, and opens an energy gap.[110] (See Figure 2.11) Calculation also shows that hydrogen chemisorption defect creates magnetism in graphene by creating a flat band in LDOS, (See Figure 2.11 (d)) when two hydrogen atoms are located on the same sublattice of graphene.[111 - 115] However, graphene absorbed by two hydrogen atoms that correspond to the different sublattices was predicted to be antiferromagnetic [112,115] or nonmagnetic[111] from first-principles calculations.

Recently, S. Ryu [116] show us that, by forming sp^3 C−H functionality on the basal plane of graphene, hydrogenation leads to hole doping of the graphene. Later, D.C. Elias [117] demonstrated that hydrogenation reactions lead to the change in hybridization from sp^2 to sp^3 , the chemisorption results in longer C-C bonds that

would suppress conduction ability in graphene and introduce localized states into the band structure. (See Figure 2.11) Beside hydrogenated graphene, graphene oxide also proves to be an insulator with high disorder. It is often regarded as a graphene sheet bonded to oxygen in the form of carboxyl, hydroxyl or epoxy groups [118-122]. The structure of graphene oxide is mostly amorphous due to distortion from the high fraction of sp^3 C-O bonds. Interestingly, magnetic moments could be induced by chemical C-O, C-F and C-N bonding in graphene, while no magnetic moment is detected on graphene absorbed with these atoms.[123] Recently, room-temperature ferromagnetism of chemically functionalized graphene sheets was experimentally observed.[124] Although the ferromagnetism remains to be explored in-depth, it is believed due to the existence of various chemically functionalized graphene structures as the spin units and the possible long-range ordered coupling among them.

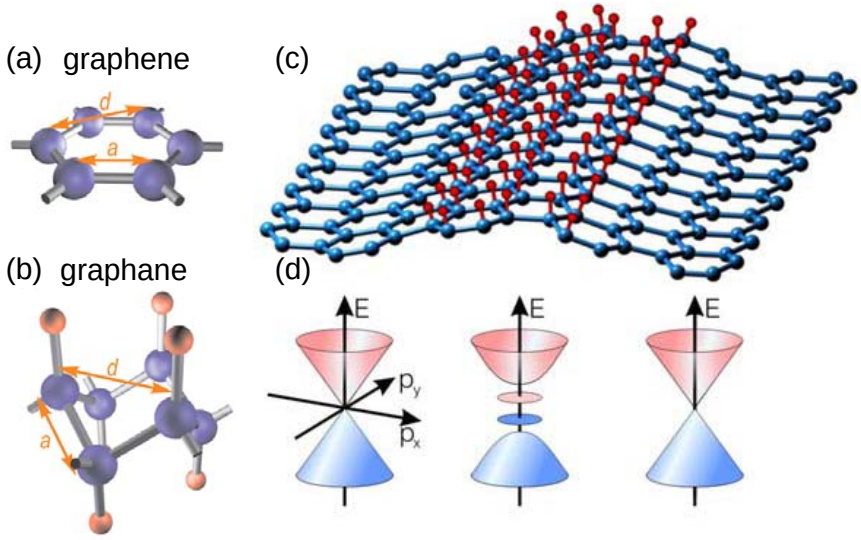

FIG. 2.11 Schematics of crystal structure of (a) graphene and (b) graphane, where blue (red) spheres represent the carbon (hydrogen) atoms. (c) A derivative model: one side hydrogenated region is adjoined by two non-hydrogenated ones. (d) Schematic band diagrams for the three regions shown in (c). The diagrams are positioned under the corresponding graphene regions. Hydrogenated regions are represented by a gapped spectrum whereas the non-hydrogenated regions are assumed to be gapless. The ellipsoids inside the gap represent localized states. (Refer to Ref.[117])

Adsorption of metallic atoms also can chemically tailor electronic properties of graphene. The electronic properties depend strongly on the ionic and/or covalent characters of the bonds formed between carbon and metals. The strong ionic bonding in graphene could be produced in the presence of alkaline metals.[125] Simultaneously, in some graphite intercalated compounds (GICs), the metallic bands are also affected by the presence of the metal in graphene lattices.[126] As a result, superconductivity may be generated in alkaline coated graphene. [127] Transition metals are prone to form strong covalent bonds in contact with graphene. The covalent bonds could induce magnetic instabilities in graphene because of the strong electron-electron interactions. Transition metals coated graphene may open another route to spintronics through new spin-valve devices. Similar effects have been studied in carbon nanotubes. [128]

2.6 Extrinsic Graphene

2.6.1 Defect in Graphene

Similar to conventional nanostructures, graphene is sensitive to disorder; as such its electronic properties are expected to be strongly influenced by the presence of defects. Here, we are talking about the effects of local defects (vacancies and random impurities) in the electronic structure of bulk graphene. Extended defects (edges or grain boundaries) were discussed in previous sections. In the case of vacancies, the DOS features a strong deviation close to Fermi level, through forming quasilocalized states decaying as (1/r) around the vacancies. [129-132]. “r” is the distance away from the defect. As shown in Figure 2.12, the particular case of lattices with uncompensated vacancies is quite interesting. In this case, the energy gap appears and its size becomes proportional to the concentration of vacancies. In addition to the gap, the localized

states are generated in the middle of this gap. Such states might be at the origin of local magnetic moments, which would explain the magnetism seen experimentally in proton bombarded graphite. [133, 134] What is more, the localized states from defect may be relevant superconducting states.[129] In addition, five-, six-, and seven-membered rings in 2D sp^2 lattices may trigger superconductivity in graphene layer. [135,136]

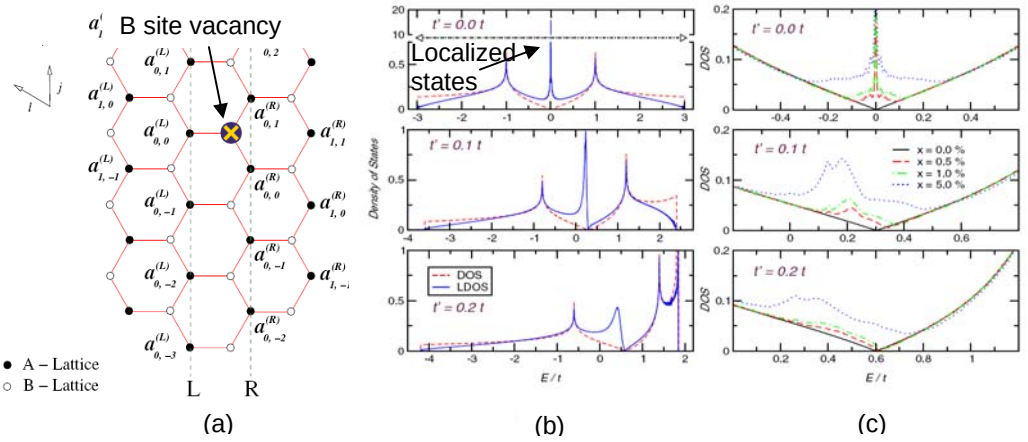

FIG. 2.12 (a) Sketch of the geometry considered for the study of a single *B*-site vacancy. (b) Comparison between the local DOS in the vicinity of a vacancy (blue/solid) with the bulk DOS (red/ dashed) in clean systems. (c) Total DOS in the vicinity of the Dirac points for clusters with $4x10^6$ sites, at selected vacancy concentrations. (Refer to Ref. [129])

STM has been proven a useful tool in examining the effects of defects on graphitic materials. [137,138] Recently, the LDOS near defect sites are experimentally tested in graphene samples through STM techniques. G.M. Rutter et al. [139] investigated native defects of bilayer epitaxial graphene grown on SiC. Energy resolved maps of the local density of states reveal the quantum interference of quasi particle near defects. Later, L. Tapasztó et al. [140] investigated the mechanically exfoliated graphene layers irradiated with Ar+ ions by scanning tunneling microscopy and spectroscopy. The effect of atomic scale defects on the low-energy electronic structure of graphene was studied. The investigation reveal that defect sites act as

scattering centers for electrons through local modification of the on-site potential. The localized state near the defect sites was observed in the spectroscopy. As shown in Figure 2.13, a broad maximum in dI/dV curve was observed, and the peak was attributed to the localized state near Fermi level.

In addition, the effects of defects on the global DOS of graphene should reflect themselves in the electric transport. For example, the material defects in graphene can reduce the mobility and possibly the minimum conductivity.

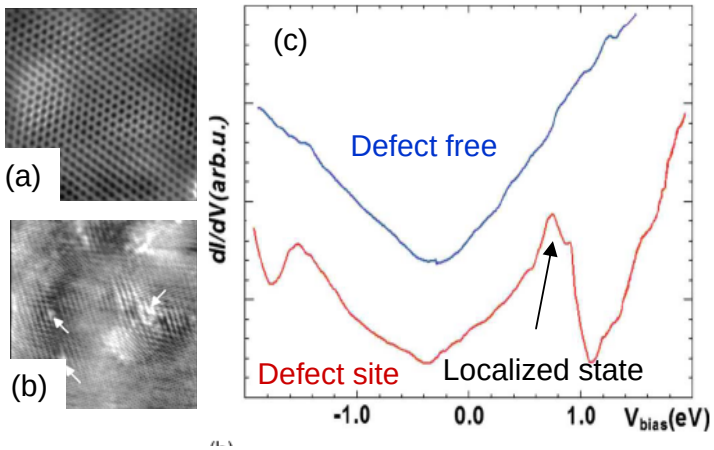

FIG. 2.13 (a) Atomic resolution STM image 6×6 nm^2, a single graphene on SiO_2. (b) Atomic resolution STM image 20×20 nm^2, irradiated graphene on SiO_2, defect sites are indicated by arrows. (c) Scanning tunneling spectra of graphene taken on the defect free region and a defect site of the irradiated graphene. (Refer to Ref. [140])

2.6.2 Environment Factors

Beside defects, the interaction with the substrate and environment is another unavoidable source of disorder in graphene. The additional disorder in graphene is also one of our concerns. So far, in most experiments, graphene samples are deposited over SiO_2. Experiments reveal that the substrate plays a very important role in the structural properties of graphene. STM measurements suggest that monolayer graphene follows the corrugation of SiO_2 substrate. [141, 142] and electromechanical experiment indicates that the substrate induces large stresses in graphene samples. [143] Moreover,

the substrate contact under graphene can influence the transport properties at finite temperature through controlling out of plane mechanical vibrations.[144,145]

Both substrate and surroundings have a direct influence in the electronic properties of graphene.[146] Recent experiments suggest that charged impurities in the SiO_2 substrate cause the short range scattering, which limits the carrier mobility in graphene at low temperature [147-149] while thermal excited ripples [144] and ripple induced charge inhomogeneity [150] suppressed the high temperature mobility of the carriers by long range scattering. Actually, SiO_2 substrates give clear corrections to the carrier mobility in carbon based electronic devices. [151-153] In recent experiment, extremely high mobility were observed in suspended graphene. [154,155] Beside substrates, the presence of water molecules [156-158] and lithographic polymer residues [159] also may induce doping and Coulomb scattering in graphene. Of course, the effect of the adsorbents can in principle be eliminated by an appropriate baking. In addition, the invasiveness of metallic contacts always leads to doping of the graphene. [160-162] The charge transfer at the metal/graphene interface causes the band alteration of graphene under the metal and nearby. It induces a strong electron-hole asymmetry in electrical transport measurement.

In summary, extrinsic factors include the materials quality, lithography process, gas contamination, metallic leads and substrate. The factors affect the quality of graphene devices and modify the transport properties graphene. The extrinsic factors do not modify the electronic structure of graphene.

2.7 Summary

Graphene is a unique two dimensional system, whose electronic band structure is described in terms of Dirac fermions. Because of the finite density of states at the

Dirac point, graphene can be easily modified with the application of electric and magnetic field, addition of layers, scaling down, chemical/physical functionalization, and interaction with environment. The influences of various modifications on electronic properties of graphene are summarized in Figure 2.14.

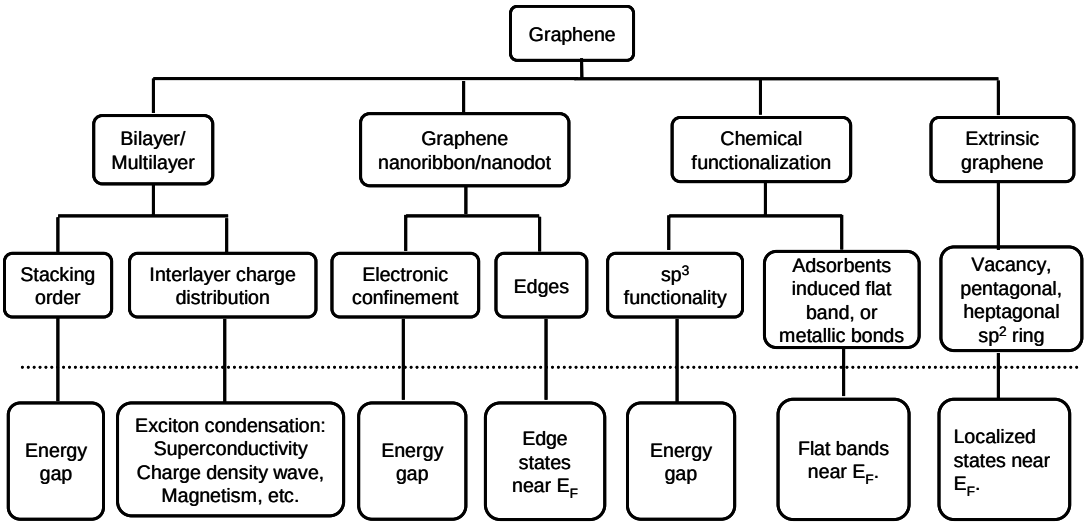

FIG. 2.14 Schematic illustration of electronic properties in graphene under various modifications. The possible electronic properties are summarized below the dashed line.

In bilayer graphene with Bernal stacking, perpendicular electric field gives rise to a finite gap in the electronic structure. Moreover, graphene bilayer is also prone to show strong electron-electron correlation effects, such as magnetism, charge density wave phases and superfluidity under the external electric field. In fact, multilayer graphene systems also have similar properties with bilayer graphene. Higher complexity of multilayer graphene may be of interest for fundamental physics and practical applications since it allows higher flexibility in tailoring the electronic properties.

Under confinement, calculations based on tight binding predict that GNRs and GNFs with zigzag edges are always metallic, while armchairs can be either metallic or

semiconducting, depending on their width. Theoretical work also suggests that the armchair edge is energetically more stable than the zigzag edge that has an edge state close to the Fermi level. Experiments show that a conduction gap in GNRs or GNFs with armchair edges exhibits a relationship with the inverse of the sample width. GNRs with a higher fraction of zigzag edges exhibit a smaller energy gap.

Edge states exist in zigzag edges of graphitic system, while no such localized state appears at armchair edges. The edge states are very important to determine the possible magnetic properties and superconductivity in graphitic materials. STM/STS experiments are used to characterize graphene edges with hydrogen-termination. A peak of dI/dV curve indicates the flat band nature of edge state near Fermi level at zigzag edges.

There are two types of chemical functionalization on graphene, namely, physisorption and chemisorption. Normal physisorption just introduces the doping into graphene devices. Some certain kind of molecules adsorbed on graphene may create the occupancy of flat impurity bands near the Dirac point. Flat bands near the Fermi level may be an origin of ferromagnetism, superconductivity, charge density wave and other related electronic instabilities. In case of chemisorption, covalent bonds could be created. The covalent functionalization of graphene changes the hybridization of carbon atoms from sp^2 into sp^3, which suggests a stronger alteration of clean graphene electronic properties. Large scale covalent functionalization can open a gap in graphene. However, the non-uniform covalent functionalization could suppress conduction ability in graphene.

In extrinsic graphene, defects could create the localized states and introduce flat band/energy gap into the electronic structure of graphene. Such states might be the origin of local magnetic moments or superconducting states. The localized state near

the defect sites were experimentally observed in the STM/STS spectroscopy. In addition, a few defects in graphene can reduce the mobility and possibly the minimum conductivity. Some other extrinsic factors, (such as the materials quality, lithography process, gas contamination, metallic leads and substrates) usually affect the quality of graphene devices and modify the electronic transport properties graphene. At this point in time, it is not clear whether the extrinsic factors modify the electronic structure of graphene, especially in multilayer graphene. Because of the finite density of states near the Dirac point, extrinsic multilayer graphene may show strong electron-electron correlation effects. It is noted that the investigation on the effect of electron-electron interactions in graphene and multilayer graphene is still at the beginning stage.

In the chapter, we reviewed recent theoretical and experimental work in graphene under modification. The modified graphene may exhibit many new fundamental properties and give great potential for electronic applications. Actually, most of properties are currently subjects under intense research and debate. And the related researches are still at their beginning stage. Therefore, it is worth further investigation in their transport properties.

The following chapters will describe details of our experiments and discuss the results of the experiments.

References:

[1] A.H. Castro Neto, et al., "The electronic properties of graphene", *Rev. Mod. Phys*., vol.81, pp.109, 2009.

[2] A.K. Geim and K.S. Novoselov, "The rise of graphene", *Nat. Mater*., vol.6, pp.183-191, 2007.

[3] P. Avouris, Z. Chen, and V. Perebeinos, "Carbon Based Electronics", *Nat. Nanotechnol.,* vol.2, pp.605-615, 2007.

[4] J. Nilsson, A.H. Castro Neto, F. Guinea, and N.M.R. Peres, "Electronic properties of bilayer and multilayer graphene", *Phys. Rev. B,* vol.78, pp.045405, 2008.

[5] H. Min, A.H. MacDonald, "Electronic structure of multilayer graphene", *Phys. Rev. B,* vol.77, pp.155416, 2008.

[6] C. Berger, Z. Song, T. Li, X. Li, A.Y. Ogbazghi, R. Feng, Z. Dai, A.N. Marchenkov, E.H. Conrad, P.N. First, and W.A. de Heer, "Ultrathin Epitaxial Graphite: 2D Electron Gas Properties and a Route toward Graphene-based Nanoelectronics", *J. Phys. Chem.,* vol.108, pp.19912-19916, 2004.

[7] K.S. Novoselov, E. McCann, S.V. Morozov, V.I. Fal'ko, M.I. Katsnelson, U. Zeitler, D. Jiang, F. Schedin and A.K. Geim, "Unconventional quantum Hall effect and Berry's phase of 2π in bilayer graphene", *Nat. Phys*., vol.2, pp.177-180, 2006.

[8] E. McCann and V.I. Fal'ko, "Landau-Level Degeneracy and Quantum Hall Effect in a Graphite Bilayer", *Phys. Rev. Lett.,* vol.96, pp.086805, 2006.

[9] J. Nilsson, A.H. Castro Neto, N.M.R. Peres, and F. Guinea, "Electron-electron interactions and the phase diagram of a graphene bilayer", *Phys. Rev. B,* vol.73, pp.214418, 2006.

[10] E. McCann and V.I. Fal'ko, "Landau level degeneracy and quantum Hall effect in a graphite bilayer", *Phys. Rev. Lett.,* vol.96, pp.086805, 2006.

[11] F. Guinea, A.H. Castro Neto, and N.M.R. Peres, "Electronic states and Landau levels in graphene stacks", *Phys. Rev. B,* vol.73, pp.245426, 2006.

[12] E. McCann, "Asymmetry gap in the electronic band structure of bilayer graphene", *Phys. Rev. B,* vol.74, pp.161403(R), 2006.

[13] H. Min, B. Sahu, S.K. Banerjee, and A. H. MacDonald, "Ab initio theory of gate induced gaps in graphene bilayers", *Phys. Rev. B*, vol.75, pp.155115, 2007.

[14] M. Aoki and H. Amawashi, "Dependence of band structures on stacking and field in layered graphene", *Solid State Commun.,* vol.142, pp.123-127, 2007.

[15] T. Ohta, A. Bostwick, T. Seyller, K. Horn, E. Rotenberg, "Controlling the Electronic Structure of Bilayer Graphene", *Science,* vol.313, pp.951-954, 2006

[16] J.B. Oostinga, H.B. Heersche, X.L. Liu, A.F. Morpurgo and L.M.K. Vandersypen, "Gate-induced insulating state in bilayer graphene devices", *Nat. Mat.*, vol.7, pp.151-157, 2008.

[17] E.V. Castro, K.S. Novoselov, S.V. Morozov, N.M.R. Peres, J.M.B. Lopes dos Santos, J. Nilsson, F. Guinea, A.K. Geim, and A.H. Castro Neto, "Biased Bilayer Graphene: Semiconductor with a Gap Tunable by the Electric Field Effect", *Phys. Rev. Lett.,* vol.99, pp.216802, 2007.

[18] J.M.B. Lopes dos Santos, N.M.R. Peres, and A.H. Castro Neto, "Graphene Bilayer with a Twist: Electronic Structure", *Phys. Rev. Lett.,* vol.99, pp.256802, 2007.

[19] H. Schmidt, T. Lüdtke, P. Barthold, E. McCann, V.I. Fal'ko, and R.J. Haug, "Tunable graphene system with two decoupled monolayers", *Appl. Phys. Lett.,* vol.93, pp.172108, 2008.

[20] J. Hass, F. Varchon, J.E. Milla´n-Otoya, M. Sprinkle, N. Sharma, W.A. de Heer, C. Berger, P.N. First, L. Magaud, and E.H. Conrad, "Why Multilayer Graphene on 4H-SiC (0001) Behaves Like a Single Sheet of Graphene", *Phys. Rev. Lett.*, vol.100, pp.125504, 2008.

[21] P. Poncharal, A. Ayari, T. Michel, and J.-L. Sauvajol, "Raman spectra of misoriented bilayer graphene", *Phys. Rev. B*, vol.78, pp.113407, 2008.

[22] Z. Ni, Y. Wang, T. Yu, Y. You, and Z. Shen, "Reduction of Fermi velocity in folded graphene observed by resonance Raman spectroscopy", *Phys. Rev. B*, vol.77, pp.235403, 2008.

[23] J. Nilsson, A.H. Castro Neto, N.M.R. Peres, and F. Guinea, "Electron-electron interactions and the phase diagram of a graphene bilayer", *Phys. Rev. B,* vol.73, pp.214418, 2006.

[24] H. P. Dahal, T.O. Wehling, K.S. Bedell, J.-X. Zhu, and A.V. Balatsky, "Wigner crystallization in a single and bilayer graphene", arXiv:0706.1689.

[25] H. Min, R. Bistritzer, J.-J. Su, and A.H. MacDonald, "Room-temperature superfluidity in graphene bilayers", *Phys. Rev. B,* vol.78, pp.121401, 2008.

[26] C.-H. Zhang and Y.N. Joglekar, "Excitonic condensation of massless fermions in graphene bilayers", *Phys. Rev. B*, vol.77, pp.233405, 2008.

[27] B. Seradjeh, H. Weber, and M. Franz, "Vortices, Zero Modes, and Fractionalization in the Bilayer-Graphene Exciton Condensate", *Phys. Rev. Lett.* vol.101, pp.246404, 2008.

[28] R. Bistritzer and A.H. MacDonald,"Influence of Disorder on Electron-Hole Pair Condensation in Graphene Bilayers", *Phys. Rev. Lett.,* vol.101, pp.256406, 2008.

[29] M. Yu. Kharitonov and K. B. Efetov, "Electron screening and excitonic condensation in double-layer graphene systems", arXiv:0808.2164v1.

[30] S. Latil and L. Henrard, "Charge Carriers in Few-Layer Graphene Films", *Phys. Rev. Lett.,* vol.97, pp.036803, 2006.

[31] F. Guinea, A.H. Castro Neto, and N.M.R. Peres, "Electronic states and Landau levels in graphene stacks", *Phys. Rev. B,* vol. 73, pp.245426, 2006.

[32] J.L. Mañes, F. Guinea, and María A.H. Vozmediano, "Existence and topological stability of Fermi points in multilayered graphene", *Phys. Rev. B,* vol.75, pp.155424, 2007.

[33] J. Nilsson, A. H. Castro Neto, F. Guinea, and N. M. R. Peres, "Electronic Properties of Graphene Multilayers", *Phys. Rev. Lett.,* vol. 97, pp.266801, 2006.

[34] J. W. McClure, "Diamagnetism of Graphite", *Phys. Rev.,* vol.104, pp.666-671, 1956.

[35] Y. Kopelevich and P. Esquinazi, "Ferromagnetism and Superconductivity in Carbon based Systems", *Journal of Low Temperature Physics*, vol.146, pp.629-639, 2007.

[36] X. Du, S.-W. Tsai, D.L. Maslov, and A.F. Hebard, "Metal-Insulator-Like Behavior in Semimetallic Bismuth and Graphite", *Phys. Rev. Lett.,* vol.94, pp.166601, 2005.

[37] H. Kempa, Y. Kopelevich, F. Mrowka, A. Setzer, J. H. S. Torres, R. Höhne, and P. Esquinazi, "Magnetic-field-driven superconductor-insulator-type transition in graphite", *Solid State Commun.,* vol.115, pp.539-542, 2000.

[38] Y. Kopelevich, J. H. S. Torres, R. R. da Silva, F. Mrowka, H. Kempa, and P. Esquinazi, *Phys. Rev. Lett.,* vol. 90, pp.156402, 2003.

[39] I. A. Luk'yanchuk and Y. Kopelevich, "Phase Analysis of Quantum Oscillations in Graphite", *Phys. Rev. Lett.,* vol.93, pp.166402, 2004.

[40] S.Y. Zhou, G.-H. Gweon, J. Graf, A.V. Fedorov, C.D. Spataru, R.D. Diehl, Y. Kopelevich, D.-H. Lee, S.G. Louie, and A. Lanzara, "First direct observation of Dirac fermions in graphite", *Nat. Phys.,* vol.2, pp.595-599, 2006.

[41] G. Li, and E.Y. Andrei, "Observation of Landau levels of Dirac fermions in graphite", *Nat. Phys.,* vol.3, pp.623-627, 2007.

[42] M. Fujita, K. Wakabayashi, K. Nakada and K. Kusakabe, "Peculiar Localized State at Zigzag Graphite Edge", *J. Phys. Soc. Jpn*., vol.65, pp.1920, 1996.

[43] K. Nakada, M. Fujita, G. Dresselhaus and M.S. Dresselhaus, "Edge state in graphene ribbons: Nanometer size effect and edge shape dependence", *Phys. Rev. B,* vol.54, pp.17954, 1996.

[44] K. Wakabayashi, M. Fujita, H. Ajiki and M. Sigrist, "Electronic and magnetic properties of nanographite ribbons", *Phys. Rev. B,* vol.59, pp.8271, 1999.

[45] V. Barone, O. Hod and G.E. Scuseria, "Electronic Structure and Stability of Semiconducting Graphene Nanoribbons", *Nano Lett.,* vol.6, pp.2748, 2006.

[46] M. Ezawa, "Peculiar width dependence of the electronic properties of carbon nanoribbons", Phys. Rev. B, vol.73, pp.045432, 2006.

[47] S.D. Dalosto and Z.H. Levine, "Controlling the Band Gap in Zigzag Graphene Nanoribbons with an Electric Field Induced by a Polar Molecule", *J. Phys. Chem. C,* vol.112, pp. 8196–8199, 2008.

[48] Y.-W Son, M.L. Cohen, and S.G. Louie, "Energy Gaps in Graphene Nanoribbons", *Phys. Rev. Lett.,* vol.97, pp.216803, 2006.

[49] C.T. White, J. Li, D. Gunlycke, and J.W. Mintmire, "Hidden One-Electron Interactions in Carbon Nanotubes Revealed in Graphene Nanostrips", *Nano Lett.,* vol.7, pp.825, 2007.

[50] N.M.R. Peres, A.H. Castro Neto, and F. Guinea, "Conductance quantization in mesoscopic graphene", *Phys. Rev. B,* vol.73, pp.195411, 2006.

[51] D. Dunlycke, D.A. Areshkin, and C.T. White, "Semiconducting graphene nanostrips with edge disorder", *Appl. Phys. Lett.,* vol.90, pp.142104, 2007.

[52] J. Fernandez-Rossier, J.J. Palacios, and L. Brey, "Electronic structure of gated graphene and graphene ribbons", *Phys. Rev. B,* vol.75, pp.205441, 2007.

[53] L. Yang, C.-H. Park, Y.-W. Son, M.L. Cohen, and S.G. Louie, "Quasiparticle Energies and Band Gaps in Graphene Nanoribbons", *Phys. Rev. Lett.,* vol.99, pp.186801, 2007.

[54] Y.-M. Lin, V. Perebeinos, Z. Chen, and P. Avouris, "Electrical observation of subband formation in graphene nanoribbons", *Phys. Rev. B,* vol.78, pp.161409R, 2008.

[55] Z. Chen, Y.-M. Lin, M.J. Rooks, P. Avouris, "Graphene Nano-Ribbon Electronics", *Physica E: Low-dimensional Systems and Nanostructures*, vol. 40, pp 228-232, 2007.

[56] C. Berger, Z.M. Song, X.B. Li, X.S. Wu, N. Brown, C. Naud, D. Mayou, T.B. Li, J. Hass, A.N. Marchenkov, E.H. Conrad, P.N. First and W.A. de Heer, "Electronic confinement and coherence in patterned epitaxial graphene", *Science,* vol.312, pp.1191-1194, 2006.

[57] M.Y. Han, B. Özyilmaz, Y. Zhang, and P. Kim, "Energy Band-Gap Engineering of Graphene Nanoribbons", *Phys. Rev. Lett.,* vol. 98, pp.206805, 2007.

[58] X. Li, X. Wang, L. Zhang, S. Lee, and H. Dai, "Chemically Derived, Ultrasmooth Graphene Nanoribbon Semiconductors", *Science,* vol.319, pp.1229-1232, 2008.

[59] X. Wang, Y. Ouyang, X. Li, H. Wang, J. Guo, and H. Dai, "Room-Temperature All-Semiconducting Sub-10-nm Graphene Nanoribbon Field-Effect Transistors", *Phys. Rev. Lett*., vol.100, pp.206803, 2008.

[60] C. Stampfer, J. Güttinger, S. Hellmüller, F. Molitor, K. Ensslin, and T. Ihn, "Energy Gaps in Etched Graphene Nanoribbons", *Phys. Rev. Lett.,* vol.102, pp.056403, 2009.

[61] M. Evaldsson, I.V. Zozoulenko, H. Xu, and T. Heinzel, "Edge disorder induced Anderson localization and conduction gap in graphene nanoribbons", *Phys. Rev. B*, vol.78, pp.161407(R), 2008.

[62] S. Adam, S. Cho, M. S. Fuhrer, and S. Das Sarma, "Density Inhomogeneity Driven Percolation Metal-Insulator Transition and Dimensional Crossover in Graphene Nanoribbons", *Phys. Rev. Lett.* vol.101, pp.046404, 2008.

[63] F. Sols, F. Guinea, and A.H. Castro Neto, "Coulomb Blockade in Graphene Nanoribbons", Phys. Rev. Lett., vol.99, pp.166803, 2007.

[64] E.R. Mucciolo, A.H. Castro Neto, and C.H. Lewenkopf, "Conductance quantization and transport gap in disordered graphene nanoribbons", *Phys. Rev. B,* vol.79, pp.075407, 2009.

[65] K. Todd, H.-T. Chou, S. Amasha and D. Goldhaber-Gordon, "Quantum Dot Behavior in Graphene Nanoconstrictions", *Nano Lett.,* vol.9, pp.416-421, 2009.

[66] X. Liu, J.B. Oostinga, A.F. Morpurgo, and L.M.K. Vandersypen, "Coulomb blockade in top-gated graphene nano-ribbons", arXiv:0812.4038.

[67] Y. Miyamoto, K. Nakada, and M. Fujita, "First-principles study of edge states of H-terminated graphitic ribbons", *Phys. Rev. B,* vol.59, pp.9858-9861, 1999.

[68] K. Sasaki, K. Sato, R. Saito, J. Jiang, S. Onari and Y. Tanaka, "Local density of states at zigzag edges of carbon nanotubes and graphene", *Phys. Rev. B,* vol.75, pp.235430, 2007.

[69] Y. Kobayashi, K. Fukui, T. Enoki, K. Kusakabe, and Y. Kaburagi, "Observation of zigzag and armchair edges of graphite using scanning tunneling microscopy and spectroscopy", *Phys. Rev. B,* vol. 71, pp.193406, 2005.

[70] Y. Kobayashi, K. Fukui, T. Enoki, and K. Kusakabe, "Edge state on hydrogen-terminated graphite edges investigated by scanning tunneling microscopy", *Phys. Rev. B,* vol. 73, pp.125415, 2006.

[71] Y. Niimi, T. Matsui, H. Kambara, K. Tagami, M. Tsukada, and H. Fukuyama, "Scanning tunneling microscopy and spectroscopy of the electronic local density of states of graphite surfaces near monoatomic step edges", *Phys. Rev. B*, vol.73, pp.085421, 2006.

[72] Z. Klusek, "Scanning tunneling spectroscopy study of the edge surface states on oxygen-etched graphite surface with the presence of liquid crystal steps", *Vacuum,* vol. 63, pp.139-144, 2001.

[73] Z. Klusek, Z. Waqar, E. A. Denisov, T.N. Kompaniets, I.V. Makarenko, A.N. Titkov, and A.S. Bhatti, "Observations of local electron states on the edges of the circular pits on hydrogen-etched graphite surface by scanning tunneling spectroscopy", *Appl. Surf. Sci.,* vol.161, pp.508-514, 2000.

[74] M. Kociak, , A.Y. Kasumov, S. Guéron, B. Reulet, I.I. Khodos, Yu.B. Gorbatov, V.T. Volkov, L. Vaccarini, and H. Bouchiat, "Superconductivity in Ropes of Single-Walled Carbon Nanotubes", *Phys. Rev. Lett.,* vol. 86, pp.2416, 2001.

[75] A. Kasumov, M. Kociak, M. Ferrier, R. Deblock, S. Guéron, B. Reulet, I. Khodos, O. Stéphan, and H. Bouchiat, "Quantum transport through carbon nanotubes: Proximity-induced and intrinsic superconductivity", *Phys. Rev. B,* vol.68, pp.214521, 2003.

[76] Z.K. Tang, L. Zhang, N. Wang, X.X. Zhang, G.H. Wen, G.D. Li, J.N. Wang, C.T. Chan, and P. Sheng, "Superconductivity in 4 Angstrom Single-Walled Carbon Nanotubes", *Science,* vol.292, pp.2462-2465, 2001.

[77] I. Takesue, J. Haruyama, N. Kobayashi, S. Chiashi, S. Maruyama, T. Sugai, and H. Shinohara, "Superconductivity in Entirely End-Bonded Multiwalled Carbon Nanotubes", *Phys. Rev. Lett.* vol.96, pp.057001, 2006.

[78] K. Sasaki, J. Jiang, R. Saito, S. Onari, and Y. Tanaka, "Theory of Superconductivity of Carbon Nanotubes and Graphene", *J. Phys. Soc. Jpn.,* vol.76, pp.033702, 2007.

[79] Y. Shibayama, H. Sato, T. Enoki, and M. Endo, "Disordered magnetism at the metal-insulator threshold in nano-graphite based carbon materials", *Phys. Rev. Lett.,* vol.84, pp.1744, 2000.

[80] T. Enoki and Y. Kobayashi, "Magnetic nanographite: an approach to molecular magnetism", *J. Mater. Chem.,* vol.15, pp.3999-4002, 2005.

[81] Y. H. Lee, Y.-W. Son, N. Park, S. Han, and J. Yu, "Magnetic ordering at the edges of graphitic fragments: Magnetic tail interactions between the edge-localized states", *Phys. Rev. B,* vol.72, pp.174431, 2006.

[82] Y.-C. Lee and H.-H Lin, "Flat-band ferromagnetism in armchair graphene nanoribbons", arXiv:0901.4387.

[83] Y.-W. Son, M.L. Cohen, and S.G. Louie, "Half-metallic graphene nanoribbons", *Nature,* vol.444, pp.347-349, 2006.

[84] K. Wakabayashi, M. Fujita, H. Ajiki, and M. Sigrist, "Electronic and magnetic properties of nanographite ribbons", *Phys. Rev. B,* vol.59, pp.8271-8282, 1999.

[85] T. Enoki, Y. Kobayashi, K. Fukui, "Electronic structures of graphene edges and nanographene", *International Reviews in Physical Chemistry*, vol.26, pp.609-645, 2007.

[86] S.E. Stein and R.L. Brown, "Pi-electron properties of large condensed polyaromatic hydrocarbons", *J. Am. Chem. Soc.,* vol.109, pp.3721-3729, 1987.

[87] W.L. Wang, S. Meng, and E. Kaxiras, "Graphene NanoFlakes with Large Spin", *Nano Lett*., vol.8, pp.241-245, 2008.

[88] J. Fernández-Rossier and J. J. Palacios, "Magnetism in Graphene Nanoislands", *Phys. Rev. Lett.,* vol.99, pp.177204, 2007.

[89] O. Hod, V. Barone, G. E. Scuseria, "Half-metallic graphene nanodots", *Phys. Rev. B,* vol.77, pp.035411, 2008.

[90] M. Ezawa, "Metallic Graphene Nanodisks", *Phys. Rev. B*, 76, pp.245415, 2007.

[91] L.A. Ponomarenko et al., "Chaotic Dirac Billiard in Graphene Quantum Dots", *Science,* vol.320, pp.356, 2008.

[92] C. Stampfer, J. Güttinger, F. Molitor, D. Graf, T. Ihn, and K. Ensslin, "Tunable Coulomb blockade in nanostructured graphene", *Appl. Phys. Lett*., vol.92, pp.012102, 2008.

[93] S. Schnez et al., "Observation of excited states in a graphene quantum dot", *Appl. Phys. Lett.,* vol.94, pp.012107, 2009.

[94] J.S. Bunch, Y. Yaish, M. Brink, K. Bolotin, and P.L. McEuen, "Coulomb Oscillations and Hall Effect in Quasi-2D Graphite Quantum Dots", *Nano Lett.,* vol.5, pp.287, 2005.

[95] Igor Romanovsky et al., "Edge states in graphene quantum dots: Fractional quantum Hall effect analogies and differences at zero magnetic field", *Phys. Rev. B,* vol.79, pp.075311, 2009.

[96] K.A. Ritter and J.W. Lyding, "Characterization of nanometer-sized, mechanically exfoliated graphene on the H-passivated Si(100) surface using scanning tunneling microscopy", *Nanotechnology,* vol.19, pp.015704, 2008.

[97] K.A. Ritter, and J.W. Lyding, "The influence of edge structure on the electronic properties of graphene quantum dots and nanoribbons", *Nature Materials,* vol.8, pp.235-242, 2009.

[98] E.H. Hwang, S. Adam, and S. Das Sarma, "Transport in chemically doped graphene in the presence of adsorbed molecules", *Phys. Rev. B,* vol.76, pp.195421, 2007.

[99] F. Schedin, A.K. Geim, S.V. Morozov, E.W. Hill, P. Blake, M.I. Katsnelson, and K.S. Novoselov, "Detection of individual gas molecules adsorbed on graphene", *Nat. Mater*., vol.6, pp.652, 2007.

[100] O. Leenaerts, B. Partoens, and F. M. Peeters, "Adsorption of H_2O, NH_3, CO, NO_2, and NO on graphene: A first-principles study", *Phys. Rev. B,* vol.77, pp.125416, 2008.

[101] T.O. Wehling, K.S. Novoselov, S.V. Morozov, E.E. Vdovin, M.I. Katsnelson, A.K. Geim, and A.I. Lichtenstein, "Molecular doping of graphene", *Nano Lett.,* vol.8, pp.173, 2008.

[102] T.O. Wehling, A.V. Balatsky, M.I. Katsnelson, A.I. Lichtenstein, K. Scharnberg, and R. Wiesendanger, "Local electronic signatures of impurity states in graphene", *Phys. Rev. B,* vol.75, pp.125425, 2007.

[103] D. M.Edwards, M.I. Katsnelson, "High-temperature ferromagnetism of sp electrons in narrow impurity bands: application to CaB6", *J. Phys.: Condens. Matter,* vol.18, pp.7209−7225, 2006

[104] B. Uchoa and A.H. Castro Neto, "Superconducting states of pure and doped graphene", *Phys. Rev. Lett.,* vol.98, pp.146801, 2007.

[105] T. Ohta, A. Bostwick, T. Seyller, K. Horn, and E. Rotenberg, "Controlling the Electronic Structure of Bilayer Graphene", *Science,* vol.313, pp.951-954, 2006.

[106] E.V. Castro et al., "Biased Bilayer Graphene: Semiconductor with a Gap Tunable by the Electric Field Effect", *Phys. Rev. Lett.,* vol.99, pp.216802, 2007.

[107] S.Y. Zhou, G.-H. Gweon, A.V. Fedorov, P.N. First, W.A. de Heer, D.-H. Lee, F. Guinea, A.H. Castro Neto, and A. Lanzara, "Substrate-induced bandgap opening in epitaxial graphene", *Nat. Mater.,* vol.6, pp.770-774, 2007.

[108] I. Zanella, S. Guerini, S.B. Fagan, J. Mendes Filho, A.G. Souza Filho, "Chemical doping-induced gap opening and spin polarization in graphene", *Phys. Rev. B,* vol.77, pp.073404, 2008.

[109] P. Shemella and S.K. Nayak "Electronic structure and band-gap modulation of graphene via substrate surface chemistry", *Appl. Phys. Lett.,* vol.94, pp.032101, 2009.

[110] J.O. Sofo, A.S. Chaudhari, and G.D. Barber, "Graphane: A two-dimensional hydrocarbon", *Phys. Rev. B,* vol.75, pp.153401, 2007.

[111] D.W. Boukhvalov, M.I. Katsnelson, and A.I. Lichtenstein, "Hydrogen on graphene: Electronic structure, total energy, structural distortions and magnetism from first-principles calculations", *Phys. Rev. B,* vol.77, pp.035427, 2008.

[112] O.V. Yazyev and L. Helm, "Defect-induced magnetism in graphene", *Phys. Rev. B*, vol.75, pp.125408, 2007.

[113] Y. Ferro, D. Teillet-Billy, N. Rougeau, V. Sidis, S. Morisset, and A. Allouche, "Stability and magnetism of hydrogen dimers on graphene", *Phys. Rev. B,* vol.78, pp.085417, 2008.

[114] S. Saremi, "RKKY in half-filled bipartite lattices: Graphene as an example", *Phys. Rev. B,* vol.76, pp.184430, 2007.

[115] L. Brey, H.A. Fertig, and S.Das Sarma, "Diluted Graphene Antiferromagnet", *Phys. Rev. Lett*., vol.99, pp.116802, 2007.

[116] S. Ryu, M. Y. Han, J. Maultzsch, T.F. Heinz, P. Kim, M.L. Steigerwald and L.E. Brus, "Reversible Basal Plane Hydrogenation of Graphene", *Nano Lett.,* vol. 8, pp. 4597-4602, 2008.

[117] D.C. Elias, R.R. Nair, T.M.G. Mohiuddin, S.V. Morozov, P. Blake, M.P. Halsall, A.C. Ferrari, D.W. Boukhvalov, M.I. Katsnelson, A.K. Geim, and K.S. Novoselov, "Control of Graphene's Properties by Reversible Hydrogenation: Evidence for Graphane", *Science*, vol.323, pp.610-613, 2009.

[118] S. Stankovich, R.D. Piner, X. Chen, N. Wu, S.T. Nguyen and R.S. Ruoff, "Stable aqueous dispersions of graphitic nanoplatelets via the reduction of exfoliated graphite oxide in the presence of poly(sodium 4-styrenesulfonate)", *J. Mater. Chem.,* vol.16, pp.155, 2006.

[119] S. Stankovich et al., "Graphene-based composite materials", *Nature,* vol.442, pp.282, 2006.

[120] X. Wang, L. Zhi, and K. Mullen, "Transparent, Conductive Graphene Electrodes for Dye-Sensitized Solar Cells", *Nano Lett.,* vol. 8, pp.323, 2008.

[121] S. Gilje, S. Han, M. Wang, K.L. Wang, and R.B. Kaner, "A Chemical Route to Graphene for Device Applications", *Nano Lett*., vol.7, pp.3394, 2007.

[122] C. Gomez-Navarro, et al., "Electronic Transport Properties of Individual Chemically Reduced Graphene Oxide Sheets", *Nano Lett*., vol.7, pp.3499, 2007.

[123] M. Wu, En-Zuo Liu, and J. Z. Jiang, "Magnetic behavior of graphene absorbed with N, O, and F atoms: A first-principles study", *Appl. Phys. Lett*., vol.93, pp.082504, 2008.

[124] Y. Wang, Y. Huang, Y. Song, X. Zhang, Y. Ma, J. Liang and Y. Chen, " Room-Temperature Ferromagnetism of Graphene", *Nano Lett.,* vol.9, pp 220-224, 2009.

[125] T. Ohta, A. Bostwick, T. Seyller, K. Horn, and E. Rotenberg, "Controlling the Electronic Structure of Bilayer Graphene", *Science,* vol.313, pp.951-954, 2006.

[126] G. Csanyi, P. B. Littlewood, A. H. Nevidomskyy, C. J. Pickard, and B. D. Simons, "Electronic structure of superconducting graphite intercalate compounds: The role of the interlayer state", *Nat. Phys*., vol.1, pp.42-45, 2006.

[127] B. Uchoa and A. H. Castro Neto, "Superconducting States of Pure and Doped Graphene", *Phys. Rev. Lett.*, vol.98, pp.146801, 2007.

[128] S.B. Fagan, R. Mota, A.J.R. da Silva, and A. Fazzio, *Phys. Rev. B,* vol.67, pp.205414, 2003, and references therein.

[129] V.M. Pereira, F. Guinea, J.M.B. Lopes dos Santos, N.M.R. Peres, and A.H. Castro Neto, "Disorder Induced Localized States in Graphene", *Phys. Rev. Lett.*, vol.96, pp.036801, 2006.

[130] V.M. Pereira, J. M. B. Lopes dos Santos, and A. H. Castro Neto, "Modeling disorder in graphene", *Phys. Rev. B,* vol.77, pp.115109, 2008.

[131] N.M.R. Peres, F. Guinea, and A. H. Castro Neto, "Electronic properties of disordered two-dimensional carbon", *Phys. Rev. B,* vol.73, pp.125411, 2006.

[132] A. F. Morpurgo and F. Guinea, "Intervalley Scattering, Long-Range Disorder, and Effective Time-Reversal Symmetry Breaking in Graphene", *Phys. Rev. Lett.*, vol.97, pp.196804, 2006.

[133] P. Esquinazi, D. Spemann, R. Höhne, A. Setzer, K.-H. Han, and T. Butz, "Induced Magnetic Ordering by Proton Irradiation in Graphite", *Phys. Rev. Lett.*, vol. 91, pp.227201, 2003.

[134] J. Barzola-Quiquia, P. Esquinazi, M. Rothermel, D. Spemann, T. Butz, and N. Garcia, "Experimental evidence for two-dimensional magnetic order in proton bombarded graphite", *Phys. Rev. B,* vol.76, pp.161403(R), 2007.

[135] H. Terrones, M. Terrones, E. Hernández, N. Grobert, J-C. Charlier, and P. M. Ajayan, "New Metallic Allotropes of Planar and Tubular Carbon", *Phys. Rev. Lett.*, vol.84, pp.1716, 2000.

[136] A. M. Black-Schaffer and S. Doniach, "Resonating valence bonds and mean-field d-wave superconductivity in graphite", *Phys. Rev. B,* vol.75, pp.134512, 2007.

[137] M. Ouyang, J. L. Huang, and C. M. Lieber, "One-Dimensional Energy Dispersion of Single-Walled Carbon Nanotubes by Resonant Electron Scattering", *Phys. Rev. Lett.*, vol. 88, pp.066804, 2002.

[138] L. Tapasztó, P. Nemes-Incze, Z. Osváth, A. Darabont, P. Lambin, and L. P. Biró, "Electron scattering in a multiwall carbon nanotube bend junction studied by scanning tunneling microscopy", *Phys. Rev. B,* vol.74, pp.235422, 2006.

[139] G. M. Rutter, J. N. Crain, N. P. Guisinger, T. Li, P. N. First, and J. A. Stroscio, "Scattering and Interference in Epitaxial Graphene", *Science,* vol.317, pp.219-222, 2007.

[140] L. Tapasztó, G. Dobrik, P. Nemes-Incze, G. Vertesy, Ph. Lambin, and L. P. Biró, "Tuning the electronic structure of graphene by ion irradiation", *Phys. Rev. B,* vol.78, pp.233407, 2008.

[141] M. Ishigami, J. Chen, W. Cullen, M. Fuhrer, and E. Williams, "Atomic Structure of Graphene on SiO_2", *Nano Lett.,* vol.7, pp.1643-1648, 2007.

[142] E. Stolyarova, K.T. Rim, S. Ryu, J. Maultzsch, P. Kim, L.E. Brus, T.F. Heinz, M.S. Hybertsen, and G.W. Flynn, "High-resolution scanning tunneling microscopy imaging of mesoscopic graphene sheets on an insulating surface", *Proc. Natl. Acad. Sci. U.S.A.,* vol. 104, pp.9209-9212, 2007.

[143] J.S. Bunch, A.M. van der Zande, S.S. Verbridge, I.W. Frank, D.M. Tanenbaum, J.M. Parpia, H.G. Craighead, and P.L. McEuen, "Electromechanical Resonators from Graphene Sheets", *Science,* vol.315, pp.490-493, 2007.

[144] M.I. Katsnelson and A.K. Geim, "Electron scattering on microscopic corrugations in graphene", *Philos. Trans. R. Soc. London, Ser. A,* vol.366, pp.195-204, 2008.

[145] S. Morozov, et. al, "Giant Intrinsic Carrier Mobilities in Graphene and Its Bilayer", *Phys. Rev. Lett*., vol.100, pp.016602, 2008.

[146] J. Sabio, C. Seoánez, S. Fratini, F. Guinea, A. H. Castro Neto, and F. Sols, "Electrostatic interactions between graphene layers and their environment", *Phys. Rev. B,* vol.77, pp.195409, 2008.

[147] K. Nomura and A. H. MacDonald, "Quantum Transport of Massless Dirac Fermions", *Phys. Rev. Lett*., vol.98, pp.076602, 2007.

[148] S. Adam, E.H. Hwang, V.M. Galitski, and S. Das Sarma, "A self-consistent theory for graphene transport", *Proc. Natl. Acad. Sci. U.S.A.,* vol. 104, pp.18392, 2007.

[149] V. Geringer, M. Liebmann, T. Echtermeyer, S. Runte, M. Schmidt, R. Ru¨ckamp, M. C. Lemme, and M. Morgenstern, "Intrinsic and extrinsic corrugation of monolayer graphene deposited on SiO_2", *Phys. Rev. Lett.,* vol.102, pp.076102, 2009.

[150] L. Brey and J. J. Palacios, "Exchange induced charge inhomogeneities in rippled neutral graphene", *Phys. Rev. B*, vol.77, pp.041403, 2008.

[151] A.G. Petrov and S.V. Rotkin, "Energy relaxation of hot carriers in single-wall carbon nanotubes by surface optical phonons of the substrate", *JETP Lett.,* vol.84, pp.156, 2006.

[152] S. Fratini and F. Guinea, "Substrate limited electron dynamics in graphene", *Phys. Rev. B,* vol.77, pp.195415, 2008.

[153] J.H. Chen, C. Jang, S. Xiao, M. Ishigami, and M.S. Fuhrer, "Intrinsic and extrinsic performance limits of graphene devices on SiO_2", *Nat. Nanotechnol*., vol.3, pp.206-209, 2008.

[154] K.I. Bolotin, K.J. Sikes, Z. Jiang, G. Fudenberg, J. Hone, P. Kim, and H.L. Stormer, "Ultrahigh electron mobility in suspended graphene", *Solid State Comm*., vol.146, pp.351-355, 2008.

[155] X. Du, I. Skachko, A. Barker, and E. Y. Andrei, "Suspended Graphene: a bridge to the Dirac point", *Nat. Nanotechnol.,* vol.3, pp.491-495, 2008.

[156] F. Schedin, A.K. Geim, S.V. Morozov, D. Jiang, E.H. Hill, P. Blake, and K.S. Novoselov, "Detection of individual gas molecules adsorbed on graphene", *Nat. Mater.,* vol. 6, pp.652-655, 2007.

[157] J. Moser, A. Verdaguer, D. Jiménez, A. Barreiro, and A. Bachtold, "The environment of graphene probed by electrostatic force microscopy", Appl. Phys. Lett., vol. 92, pp.123507, 2008.

[158] C. Jang, S. Adam, J.-H. Chen, E. D. Williams, S. Das Sarma, M. S. Fuhrer, "Tuning the effective fine structure constant in graphene: opposing effects of dielectric screening on short- and long-range potential scattering", *Phys. Rev. Lett.,* vol.101, pp.146805, 2008.

[159] X. Du, I. Skachko, E.Y. Andrei, "Towards ballistic transport in graphene", *International Journal of Modern Physics B (IJMPB),* vol.22, pp.4579-4588, 2008.

[160] B. Huard, N. Stander, J.A. Sulpizio, and D. Goldhaber-Gordon, "Evidence of the role of contacts on the observed electron-hole asymmetry in graphene", *Phys. Rev. B* , vol.78, pp.121402(R), 2008.

[161] R. Nouchi, M. Shiraishi, and Y. Suzuki, "Transfer characteristics in graphene field-effect transistors with Co contacts", *Appl. Phys. Lett*., vol.93, pp.152104, 2008.

[162] G. Giovannetti, P.A. Khomyakov, G. Brocks, V.M. Karpan, J. van den Brink, and P. J. Kelly, "Doping Graphene with Metal Contacts", *Phys. Rev. Lett.,* vol.101, pp.026803, 2008.

CHAPTER 3

EXPERIMENTAL DETAILS

This chapter presents the fabrication and measurement techniques used for CNW and graphene samples. We first discuss the deposition and characterization of carbon nanowalls, followed by the fabrication of CNW devices. In the graphene part, we first discuss the fabrication of graphene and its thickness determination using Raman and optical contrast spectroscopy, followed by the e-beam lithography (EBL) fabrication processes for graphene based devices. A model to study the visibility of graphene on different substrates is also introduced. Finally, measurement setup and techniques that have been used to characterize transport properties of samples in this study are discussed.

3.1 Growth of Carbon Nanowalls

CNWs were originally discovered during the deposition of carbon nanotubes by Wu et al. in 2002. [1] The 2D carbons vertically align on the substrate and form a self-supported network structure which enhances their stability. CNWs can grow on either conducting or insulating substrates without catalysts. It is also found that electrical field plays an important role in the growth of CNWs. Here, we briefly describe the CNW deposition on silicon substrate with a silicon dioxide overlayer, which is related to the fabrication of CNW devices.

3.1.1 Substrate Preparation

In this work, silicon substrates with a silicon dioxide layer were used. To ensure the quality and uniformity of CNWs deposited, the substrates were thoroughly

cleaned to remove all contaminants such as absorbed molecules, particulates and organic impurities. These contaminants may give rise to poor adhesion, bad uniformity and degrade the device performance.

The wafer was first rinsed with deionised water (DI water) for approximately 15 mins and then dried by a critical point drier. Following that, the wafer was soaked in acetone for 10 minutes with ultrasonic bathing. This step removed the organic residues on the substrate. As acetone also leaves its own residues on the substrate, an isopropanol (IPA) immersion for another 10 minutes is required with ultrasonic bathing. Finally, the wafer was rinsed by DI water again for 5 mins. The wafer was then dried by blowing nitrogen gas.

3.1.2 MPECVD

MPECVD was used to deposit carbon nanowalls. The CVD deposition system (CN-CVD-100) is produced by ULVAC Ltd., Japan. Its schematic diagram is shown in Figure 3.1. According to the function, the MPECVD system consists of four main components: deposition system, the pumping system, gas feed system, and control system.

The deposition system consists of a quartz tube, a 500 W microwave generator and a transverse rectangular waveguide. The quartz tube is positioned in a longitudinal direction and houses two plate electrodes. The transverse rectangular waveguide couples with the microwave to generate the plasma in the quartz tube.

The working pressure in the chamber is maintained by a 100 Liters/min rotary pump and a controllable valve. The pressure in the chamber can be read by the gas pressure gauge. The reactant gases of hydrogen and methane are fed into the chamber via mass flow controllers, respectively. The flow rates of the gases are maintained

automatically by the mass flow controllers. Nitrogen gas is also available to vent the chamber and dilute the exhaust gases before discharge into the air. The venting flow rate of the nitrogen gas is manually controllable through a valve.

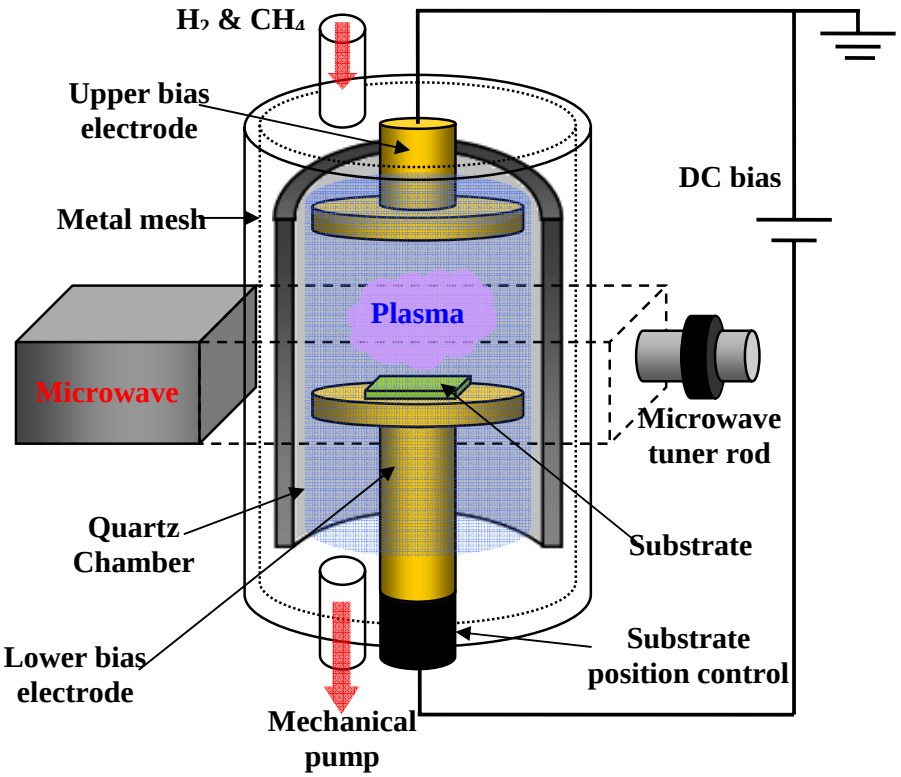

FIG. 3.1 Schematic diagram of MPECVD setup. The reactant gases flow through the flowing meters and through the quartz chamber. The microwave generates plasma in the chamber, where the carbon nanowalls grow.

In the deposition chamber, a controllable DC bias could be applied across the two parallel plate electrodes. The distance between the electrodes is adjustable. The substrate can be placed on the lower electrode while the top one is grounded. In addition, the MPECVD system is equipped with a control panel which controls the valves for work gases, initiates the microwave and determines the deposition time. The

timing function allows the system to stop the deposition automatically once the time set is out.

3.1.3 Growth Conditions

Before deposition, the clean substrate is placed on the lower electrode in MPECVD system. The reactant gases are a mixture of hydrogen and methane. The typical flow rates of hydrogen and methane are 40 and 5 sccm, respectively. Because our MPECVD system is not equipped with any source to heat the substrate, the substrate is preheated by hydrogen plasma preheating. Before CH_4 was introduced to the quartz tube to commence the growth of CNWs, the substrate was pre-heated to about 650-700 °C (limited by the power of the microwave) in hydrogen plasma for 10-15 minutes. The typical growth time was 2-5 minutes. During the preheating and growth, a bias of 50 V is applied on to the parallel plate electrodes. And the pressure of the chamber is maintained at 1 Torr throughout the entire process.

3.2 Characterization of Carbon Nanowalls (SEM, TEM, Raman Spectroscopy)

Typical SEM images of carbon nanowalls are shown in Figure 3.2(a). CNWs stand vertically as supported by a network structure. CNWs eventually cover the entire 1 cm x 1 cm substrate after 2-5 minutes growth. The density and height of carbon nanowalls depend on the position of the substrate on the lower plate electrode. A typical carbon nanowall sheet is approximately 1.5 μm tall and has a thickness of less than 10 nm. When the substrate is placed further from the microwave source, the nanowalls are sparser and appear smaller in size. Figure 3.2 (b) shows the transmission

electron microscopy (TEM) image of a carbon nanowall sheet. The image proves that a CNW sheet is a graphite flake with some disorder and defects.

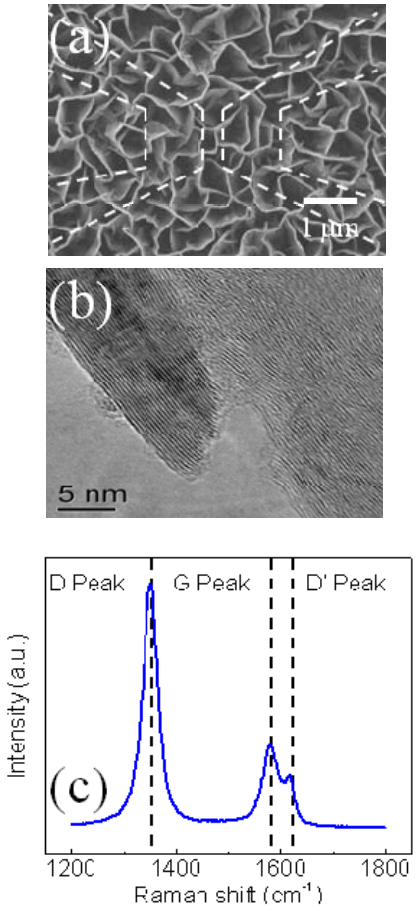

FIG. 3.2 (a) SEM image of CNWs. Dotted lines represent the electrodes configuration; (b) HRTEM image of CNWs; (c) Raman spectrum of CNWs.

The Raman spectrum of carbon nanowalls is shown in Figure 3.2(c). Raman spectra are obtained with T64000 Triple Grating System using a 514.5 nm Ar line as an excitation source. Two major peaks are registered near 1360 cm^{-1} and 1580 cm^{-1} and are known as the D band and G band peaks respectively. The G band represents crystalline graphite while the D band indicates defects and disorder in the lattice. A shoulder band is also observed at 1620 cm^{-1}, called D' band. This small peak is also believed to be associated with crystalline defects or edges. The high intensity of D

band indicates that some disorder exists in CNWs. Both TEM image and Raman spectra prove that CNW sheet is a thin graphite flake with some disorder and defects. The properties of such a single piece of carbon sheet are of great interest if electrodes can be placed precisely onto it.

3.3 Fabrication of Carbon Nanowalls Devices

Because of the curved surface morphology, it is difficult to apply electrodes with small spacing on top of CNW sheets. In order to overcome this difficulty, bottom electrodes are employed to form the electrical contacts to the nanowalls. The use of bottom electrodes has three advantages over the top ones: (i) it is possible to fabricate electrodes with a spacing down to sub-micron using EBL, (ii) the pre-cleaning in hydrogen plasma prior to the growth and simultaneous annealing during the growth make it possible to form a low resistance contact between CNWs and titanium (Ti) or niobium (Nb) (100 nm in thickness) and (iii) vertically aligned CNWs allows to form direct contact of all the layers with the electrodes.

Silicon oxide substrates with a size of 1 cm × 1 cm are first cleaned with agitation in acetone and IPA by using method discussed in Section 3.1.1. The bottom electrodes are first patterned on the substrate by using EBL (machine Elinox ELS-7700). The configuration of the electrodes is given in Figure 3.3. The electrodes are separated by a spacing that varies between 300 nm to 1μm. Current passes through the junction via the top electrodes and the voltage probes are placed on the bottom electrodes as indicated in Figure 3.3(b).

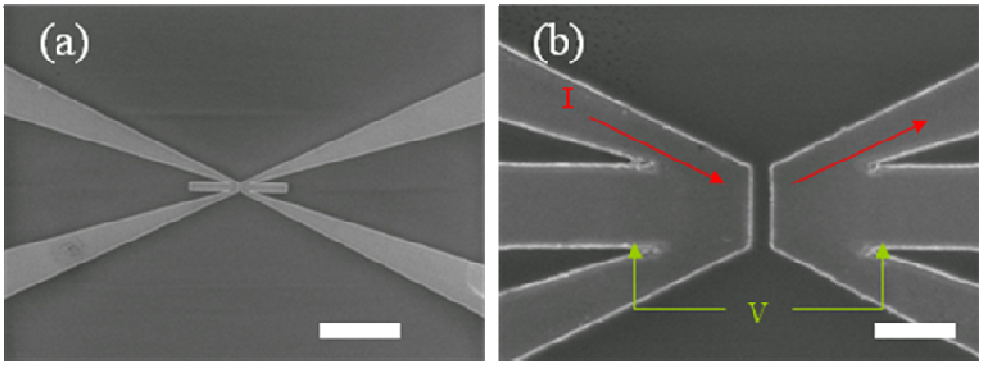

FIG. 3.3 SEM images of (a) bottom electrode configuration, scale bar corresponds to 10 μm. and (b) a close-up view of electrodes showing current flow and voltage probes, scale bar corresponds to 1 μm.

The detailed processes of electrodes formation is shown as follows. A layer of E-beam resist (Poly methyl methacrylate (PMMA) 950 and Anisole in ratio 4:5) is first coated onto the substrate at 3000 rpm for 45 seconds. After the wafer is baked at 180 ^{o}C for 90 seconds, a PMMA layer with 300 nm thickness is obtained. The typical beam current used is 100 pA with a resist dose of 400 μC/cm^2. The sample is then developed in a Methyl isobutyl ketone (MIBK) developer with MIBK:IPA=1:3. To achieve a high resolution, the developer is cooled to a temperature of 20.5 Celsius degree in a water bath. After 40 seconds of developing, the sample is rinsed in IPA to stop the development process and clean the sample.

After the pattern transfer by EBL, a thin layer (100 nm) of metal material such as Titanium (Ti) or Niobium (Nb) is deposited using r.f sputtering system. 3-5 nm of titanium (Ti) is deposited following Nb deposition to improve the transport transparency of the electrodes and to improve carbon nanowall adhesion to the electrodes. The carbon nanowalls are deposited onto the substrate using MPECVD introduced in Section 3-1. Carbon nanowalls grown on undesired region are gently removed by using cleanroom wipes. The top view of electrode structure is shown in

Figure 3.4 (a) and the schematic illustration of the device is shown in Figure 3.4 (b). The electrodes are separated by a gap of "d" which varies between 300 nm to 1μm.

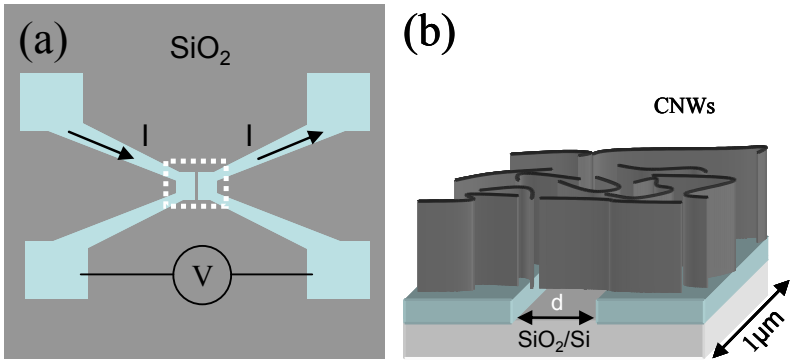

FIG. 3.4 (a) Schematic illustration of the electrodes before CNWs deposition. Current is passed and voltage is measured across the junction as indicated by the arrows. CNWs are deposited in the region encompassed by the dotted lines; (b) Schematic diagram of cross-sectional structure of the metal/CNWs/metal device after CNWs deposition. The electrodes are separated by a gap of "d" which varies between 300 nm and 1μm.

Electrodes of various gaps are fabricated and the devices are characterized using scanning electron microscopy. The image in Figure 3.2(a) shows the carbon nanowalls deposited on top of the electrodes. The superimposed dotted lines mark the electrodes configuration and allow us to estimate the number of carbon nanowalls that exist in the gap region. Usually, there are at most 3 carbon nanowalls between the electrodes for a junction gap of 450 nm.

3.4 Fabrication of Graphene

As mentioned earlier, the experimental research on fundamental properties of graphene is impeded by difficulties in obtaining single layer graphene. In the past few years, the technique to get graphene with high quality achieve breakthrough. Here, we introduce the method through which our graphene devices are obtained.

The method to fabricate graphene flakes was developed by Novoselov et al. [2,3] Here, we used highly ordered pyrolytic graphite (HOPG) from SPI [4] and natural graphite from China. A few graphite flakes are deposited on a piece of moderately sticky tape. Repeated folding and unfolding of the tape results in a homogenous distribution of graphite flakes on the tape, as shown in Figure 3.5(a) and (b). Subsequently, a freshly cleaned substrate with predefined marker pattern is pressed on the tape. In this way, graphite flakes of various thicknesses are deposited on the substrate. Figure 3.5(c) shows an example of graphene flakes on Si substrate with SiO_2. Our substrates are degenerately p-doped silicon wafers with a dry thermal oxide layer.

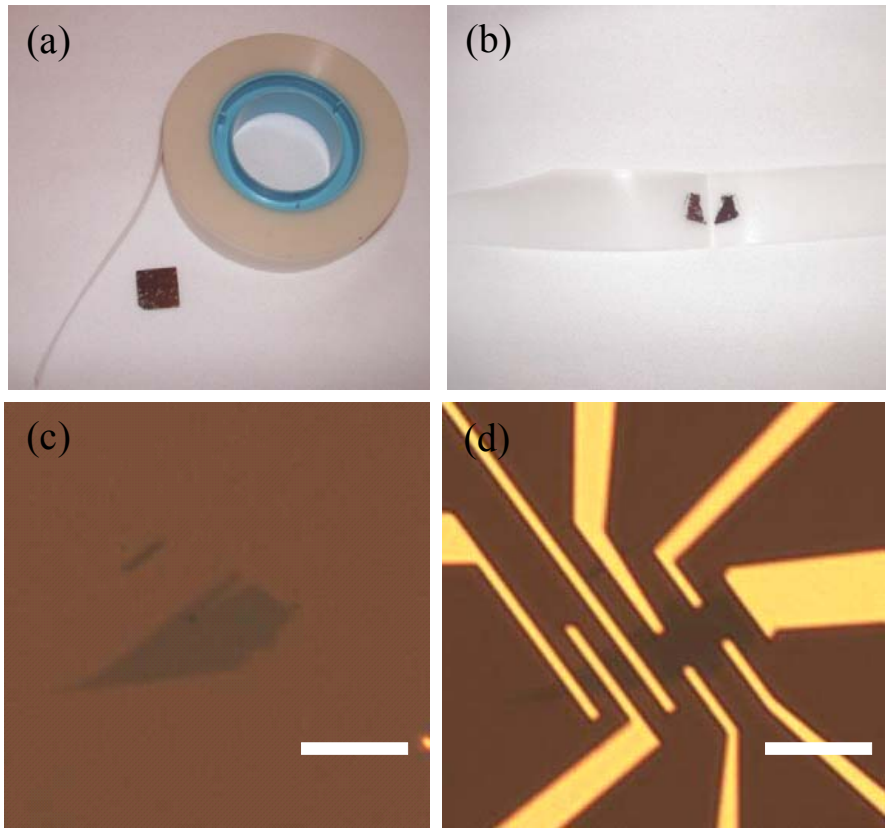

FIG. 3.5 (a) The graphite crystal and scotch tape; (b) The scotch tape used to exfoliate graphite. (c) Optical microscope image of thin graphite flake before and (d) after applying metallic electrodes. (Scale bar corresponds to 8 μm)

Optical microscopy is used to identify monolayer, bilayer and few layer graphene flakes. It is important that the SiO_2 thickness is close to 300 nm to maximize the color contrast between the bare substrate and the thin graphite flakes. The size of thin flakes is typically 10-20 square micrometres. By taking photograph, the position of the flake relative to a unique marker set is record for further processing.

The optical photographs of thin graphite flakes are imported in a CAD program in which the electrode design is made. After standard EBL, a bilayer of Ti (5 nm) and Au (30 nm) is evaporated, followed by a liftoff in warm acetone. The sample is now ready to be mounted in a chip carrier and wire bonded. An example of a graphene device with electrodes is shown in Figure 3.5(d).

AFM can be used to further investigate the thickness and homogeneity of the flake. However, it turned out AFM does not provide conclusive information about the number of graphene layers. Although the thickness of a graphene layer is 0.34 nm, the measured height (using tapping mode AFM) of a single layer of graphene is about 1.5 nm. The discrepancy can be explained by the difference in the strength of interaction between tip and SiO_2 or tip and graphene.

3.5 Selection of Graphene Flakes (Methods of Raman and Optical Contrast)

Identification of graphene under optical microscope by naked eye provided a good indication of the layer thickness of a graphite sheet, especially for thin layers. However, it is not a conclusive and reliable method. Raman spectroscopy is the potential candidate for non-destructive and quick inspection of thickness of graphene [5-7]. The Raman spectra and Raman image are achieved by WITEC CRM200 Raman

system. The excitation source is a 532 nm laser (2.33 eV, green) with power below 1 μW on the sample to avoid laser induced heating. A 100 x optical lens with a NA=0.95 is used both in the Raman and later reflection experiments.

The Raman spectrum of graphite and 1-4 layer graphene is shown in Figure 3.6. In the figure, the dominant peaks are the G line around 1580 cm^{-1} and the 2D band around 2700 cm^{-1}. The former results from an in-plane optical mode (E_{2g} mode phonon), close to Γ point, while the latter is due to double resonance.[8] We do not observe the D and D' bands which exist in CNWs. It indicates the high quality of crystalline in graphene flakes. The layer thickness can be inferred from the details of the Raman spectrum. The G peak intensity increases with the thickness of graphene flakes whereas the peak shifts to lower wave numbers at the same time. To compare the Raman spectra of graphene with different thicknesses, the intensity ratio I_{2D}/I_G in monolayer graphene is very high (usually >1.4). Moreover, the Raman 2D band is very sensitive to the number of layers of graphene [5, 6] and the second-order Raman 2D band of single layer graphene is much sharper and of higher symmetry than those of few layer graphene sheets, the 2D band becomes much broader mainly due to the change of electronic structure of graphene, which affects the process of double resonance effect.[7] Once the single-layer graphene is identified by the intensity ratio I_{2D}/I_G and the 2D band of Raman scattering, one can proceed further to determine the number of layers in thicker sheets from the intensity of G band as it increases almost linearly with the number of layers of graphene.[9]

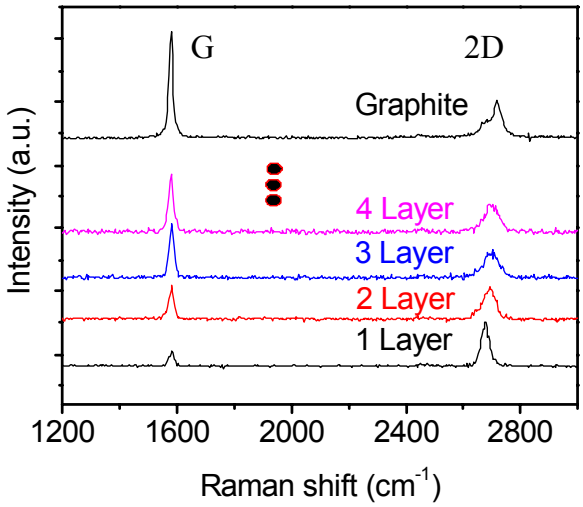

FIG. 3.6 Raman spectra of graphite and graphene with different number of layers.

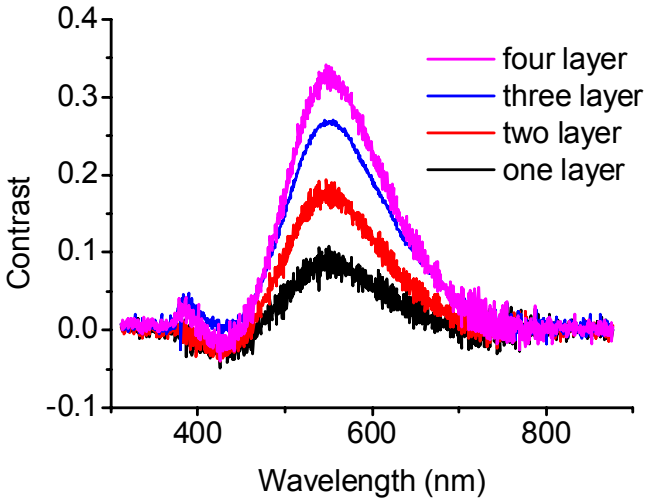

FIG. 3.7 The contrast spectra of graphene sheets with different number of layers.

Complementing with Raman scattering, contrast spectroscopy also plays an important role in determining the number of graphene layers. The contrast spectra of 1 to 4 layer graphene are shown in Figure 3.7. The contrast spectrum for monolayer graphene measured using a normal white light source exhibits a peak centered at 550

nm. The peak position remains almost unchanged (550 nm) when increasing the number of layers (N) up to 10, while the maximum contrast value varies with N as $C = 0.0046+0.0925N-0.00255N^2$.[10] Therefore, the combination of Raman and contrast spectra allows us to determine the number of layer with high accuracy.

Figure 3.8(a) shows the optical image of a graphene sample on Si substrate with 300 nm SiO_2 capping layer. The graphene sheet shows four different contrast regions, which can be understood as four different thicknesses. Following this, 3D mapping are then taken from the sample, as shown in Figure 3.8(b). In Figure 3.8(b), the 3D mapping image shows the clear steps which correspond to different number of layers. As shown, it is obvious that the whole graphene sheet contains one, two, three and four layers.

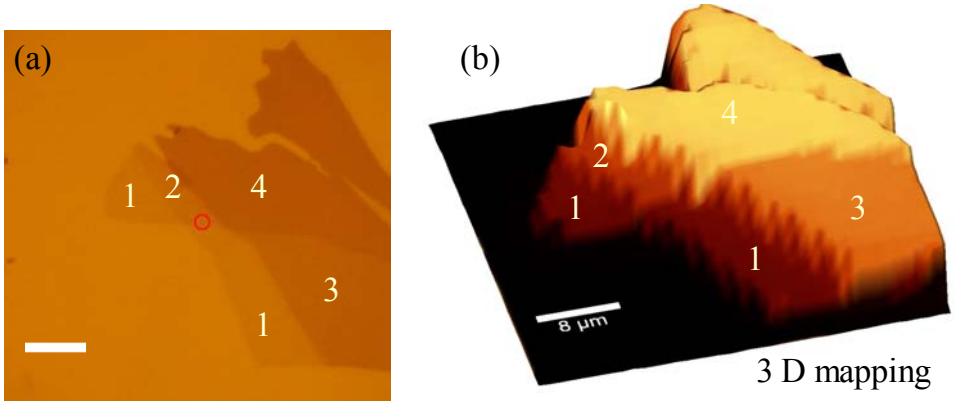

FIG 3.8 (a) The optical image of a graphene sample with 1 to 4 layers (Scale bar corresponds to 8 μm); (b) The 3D contrast image, which shows a better perspective view of the sample.

These preliminary measurements demonstrate that Raman and contrast spectroscopy are indeed useful methods to determine the layer thickness of graphene samples. They a serve a useful and efficient method to identify single layer, bilayer and few layer flakes that are suitable for device fabrication.

3.6 Fabrication of Graphene Based Devices

We have used EBL for defining the electrodes in a double layer of resist. This process is illustrated schematically in Figure 3.9 and consists of the following steps: 1) Deposition of graphene, 2) Spinning of resist, 3) E-beam exposure, 4) developing, 5) metal deposition, and 6) Lift-off.

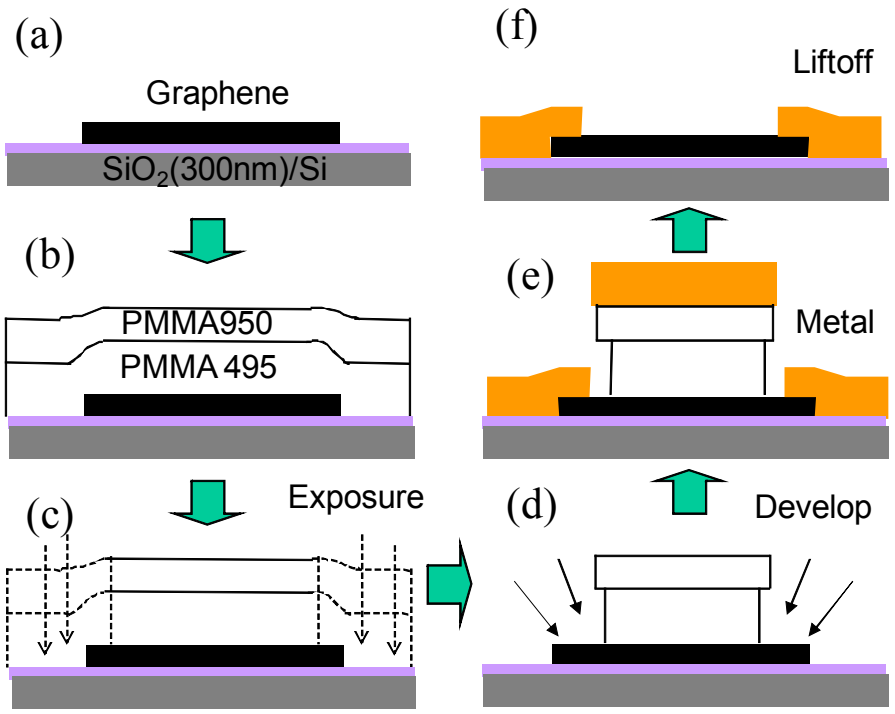

FIG. 3.9 Schematic of lithography for the electrode fabrication process. (a) put graphene on a clean wafer, (b) two layers of resist on top of the chip. (c) part of resist exposed. (d) exposed resist is removed by a developer. (e) a thin metal film is deposited. (f) the film on the resist is removed by lift off. The metal film where the resists was exposed is left. In the first step a double layer of ebeam resist (PMMA) is exposed using an ebeam pattern generator. Then the exposed areas are dissolved with a suitable developer and a metal film is deposited using evaporation. In the last step the remaining resist is removed using a solvent.

For this thesis we have used a double layer of PMMA. The double layer improves the lift-off process due to a better resist profile with an undercut. These results from higher sensitivity of the bottom layer compare to the top layer. The bottom layer (PMMA 495 A4) is spun for 45 seconds at 3000 rpm and subsequently baked at

180 °C for 90 seconds. The top layer (PMMA 950 A9) is spun at 3000 rpm for 45 seconds. We use a final bake at 180 °C for 180 seconds.

The designed patterns are written on the resist by an EBL system. Due to the exposure by an electron beam bonds in the polymer are broken and the resist becomes soluble in the developer. We have used MIBK:IPA=1:3 as a developer with a developing time of 45 seconds. Subsequently, the sample has been rinsed for 120 seconds in IPA, and then dried by blowing the nitrogen gas. Metal deposition is typically done by evaporation in a vacuum system with a background pressure of 10^{-6} mBar using a deposition rate of 0.2 Å/s. The final step in the fabrication process is lift-off. In this step the remaining resist is dissolved by immersing the sample in warm acetone. After that, the sample is dried by a critical point dryer.

3.7 Method to Fabricate Graphene Devices on Different Substrates

A single layer of graphene can become visible to our eyes under optical microscope just by choosing the right substrate and right light filters for the microscope. The optimum parameters can be found by modeling the optical response of visible light incident on a single layer of graphene on top of a substrate. The model calculation presented in the section is based on the experimental and theoretical results from Ref.[10,11]. The visibility of graphene on different types of substrates with or without under/ capping layer originates from both the relative phase shift and amplitude modification induced by the graphene layer. Although graphene is only one atomic layer thick, its refractive index was found to be very close to that of graphite. Therefore, the reflection spectrum of a multiple layer structure, not limited to a bi-layer or tri-layer structure containing graphene can also be readily obtained using the 2 by 2

matrix method. [12] Figure 3.10 shows a typical multilayer structure consisting of air, N layers of homogeneous media and supporting substrate.

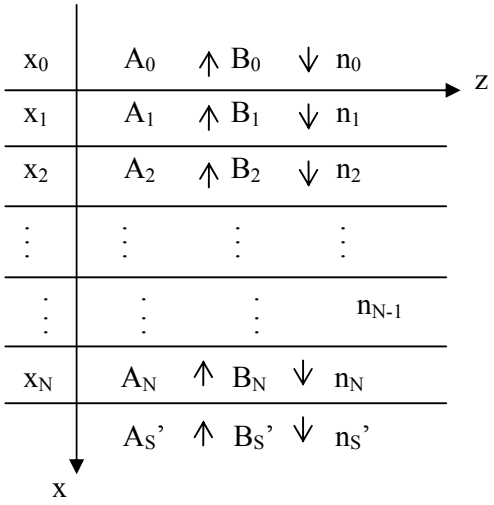

FIG. 3.10 A multilayer model used in the transfer matrix simulation.

The thickness and refractive index of each layer are d_0, d_i (i = 1 to N), d_S and n_0, n_i (i = 1 – N), n_S, respectively. Here, the reflective indices are in general complex numbers. We also assume that d_0 and d_s approaches infinity. Assuming that electromagnetic wave travels in zx plane and the media are homogeneous in z-direction, the electrical field that satisfies the Maxwell equation can be written as

$$E = \left[A(x) + B(x)\right]e^{i(\omega t - \beta z)}, \tag{3-1}$$

where β is the z component of the wave vector, ω is the angular frequency, *t* is time, and *A(x)* and *B(x)* are amplitude of the down-travelling and up-travelling waves, respectively. The electromagnetic wave can be either a p-wave or an s-wave. The amplitude of the electrical field inside the air and those after passing through the Nth layer and substrate interface are related by the following equation:

$$\begin{pmatrix} A_0 \\ B_0 \end{pmatrix} = D_0^{-1}\left[\prod_{m=1}^{N} D_m P_m D_m^{-1}\right] D_S \begin{pmatrix} A_S \\ B_S \end{pmatrix}, \tag{3-2}$$

where

$$D_m = \begin{pmatrix} 1 & 1 \\ n_m \cos\phi_m & -n_m \cos\phi_m \end{pmatrix} \quad \text{for s wave,} \tag{3-3}$$

$$D_m = \begin{pmatrix} \cos\phi_m & \cos\phi_m \\ n_m & -n_m \end{pmatrix} \quad \text{for p wave,} \tag{3-4}$$

$$P_m = \begin{pmatrix} e^{i\omega_m} & 0 \\ 0 & e^{-i\omega_m} \end{pmatrix}, \tag{3-5}$$

$$\omega_m = \frac{2\pi n_m d_m}{\lambda}. \tag{3-6}$$

Here, n_m is the refractive index of the *m*th layer, d_m is the thickness of *m*th layer, λ is wavelength, and ϕ_k is angle of incidence. If we let

$$D_0^{-1}\left[\prod_{m=1}^{N} D_m P_m D_m^{-1}\right] D_S = \begin{pmatrix} T_{11} & T_{12} \\ T_{21} & T_{22} \end{pmatrix}, \tag{3-7}$$

then the reflectance is given by

$$R = \left|\frac{T_{21}}{T_{11}}\right|^2. \tag{3-8}$$

For unpolarized light, one can take an average of the contributions from both the *s* wave and *p* wave .

$$R_{overall} = \frac{1}{2} R_{P-wave} + \frac{1}{2} R_{S-wave}. \tag{3-9}$$

In these studies, the contrast spectra C are obtained by taking the difference of the intensity of the reflection spectrum between absence of graphene and presence of graphene, which is calculated by

$$C = \frac{R(\text{no\_graphene}) - R(\text{with\_graphene})}{R(\text{no\_graphene})}, \tag{3-10}$$

where R is the reflection spectrum.

The simulation has been carried out using Matlab. The incident wave is assumed to be perpendicular to the plane of the multiple layers; hence the angle of incident ϕ_k was set at zero degree. This is a reasonable assumption because the total thickness of graphene and SiO_2 or PMMA/graphene is much smaller than the depth of focus of the objective lens used in most experiments (0.9 to1.8 μm for λ = 0.4 to 0.8 μm and NA = 0.95). Within the depth of focus, the wavefront of focused light is almost flat; therefore the light propagates in the optical axis direction. The complex refractive indices of all materials used are available from literature [13]. Single layer graphene is assumed to have a thickness 0.34 nm, and multilayer graphene which consists of n monolayers is assumed to have a thickness of n × 0.34 nm. The refractive index of graphene is assumed to be the same as that of bulk graphite and is independent of λ, i.e., $n_G(\lambda) = 2.6\text{-}1.3i$.

We start with a graphene layer on top of a Si/SiO_2 substrate where the Silicon is semi-finite in thickness and the SiO_2 has a thickness d. The model contains 4 media with different optical properties, the first is air, following a graphene layer, SiO_2 and the Si layer. Air has a refractive index close to one. For a 300 nm thick SiO_2 layer, we find that the best contrast for light in the green range, which is indicated by dashed line in Figure 3.11(a) and (b). Note that a maximum contrast of 9 % is expected for a single

layer. Our model predicts a contrast of about 18% for a bilayer, 23% for a trilayer, 31% for four-layer. Experiments verified that this is the case (Figure 3.7).

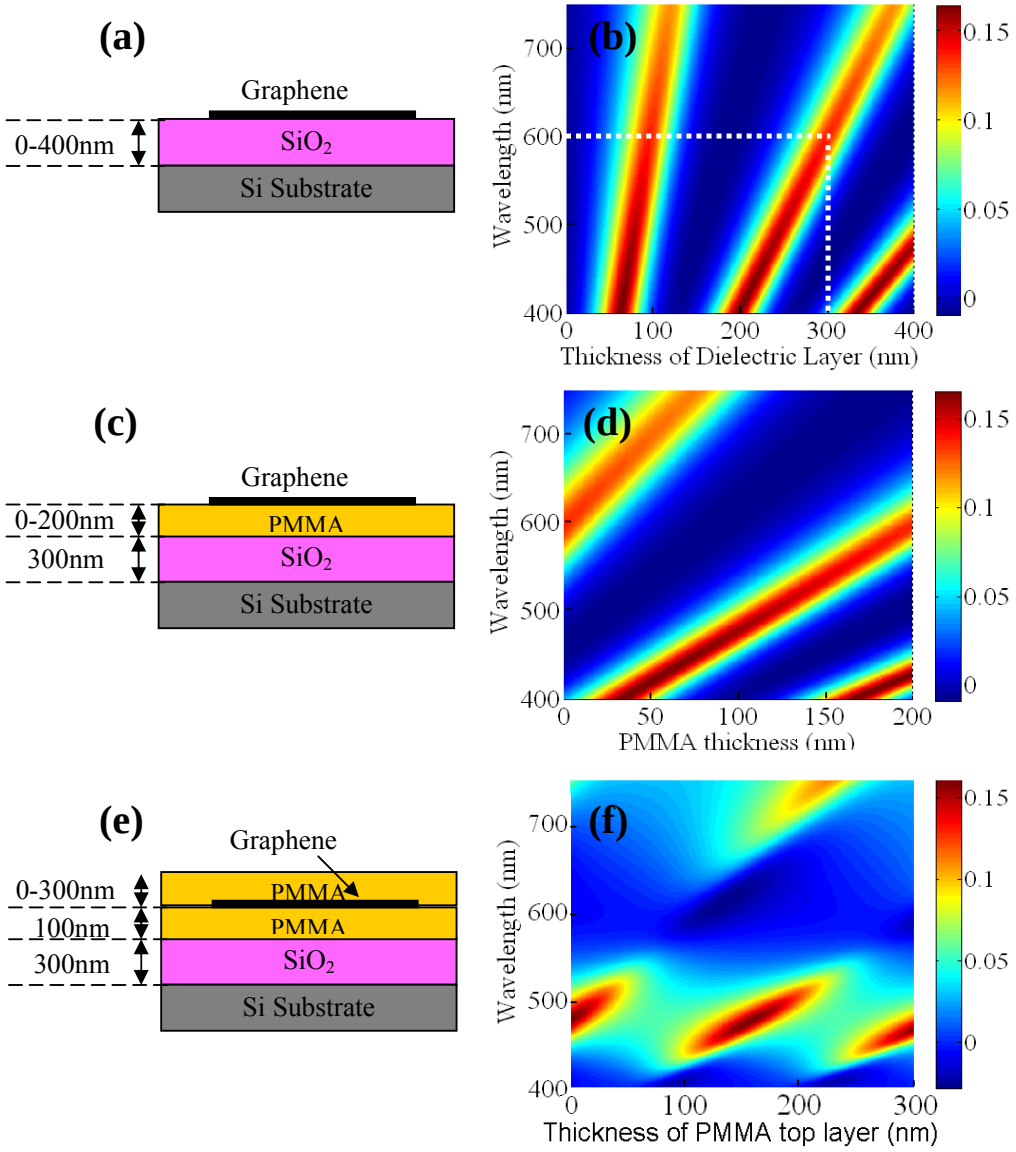

FIG. 3.11 (a) Schematic of structure for a graphene sheet on top of a Si substrate capped with SiO_2 thickness ranging from 0 to 400 nm. (b) Optical contrast spectra of monolayer graphene on SiO_2/Si substrate as a function of wavelength from 400 nm to 750 nm with variable SiO_2 thickness. (c) Schematic of structure for a graphene sheet on a layer of PMMA coated on top of a Si substrate with 300 nm SiO_2. (d) Optical contrast spectra of SLG on PMMA/SiO_2/Si substrate as a function of wavelength from 400 to 750 nm with PMMA thickness ranging from 0 to 200 nm on top of a SiO_2(300 nm) coated Si substrate.(e) Calculated contrast of graphene as a function of wavelength from 400 to 750 nm and PMMA thickness of top layer from 0 to 300 nm for the

structure of SLG sandwiched between two PMMA layers on top of a SiO_2(300nm) coated Si substrate. (f) Corresponding contrast spectra for the schematic described in (e).

Our model shows that we can increase the contrast of the graphene layer on top of the Si surface by a factor of 4 just by spinning a thin layer of PMMA on top of the sample. For this the PMMA thickness has to be about 103 nm thick. Monolayer graphene is invisible when it is placed directly on most of the semiconductor and metallic substrates. We found that coating of a resist layer with optimum thickness is an effective way to enhance the contrast of graphene on various types of substrates and makes single layer graphene visible on most semiconductor and metallic substrates.

A graphene layer on top of PMMA should also allow us to produce in a relatively easy way a free standing graphene flake on top of a Si/SiO_2 substrate. Crucial for the experiment is to be able observe a graphene layer by optical microscopy. The contrast of the graphene layer on PMMA can be found by using the above model. The media are in this case: air, graphene, PMMA, SiO_2, and Si. Using green light, the highest contrast (8 %) is found for 100nm thick PMMA layer on top of a 300nm thick SiO_2 layer. (Figure 3.11(c) and (d))

A proof of principle is depicted in Figure 3.12 where we show optical image, contrast and Raman spectra of monolayer graphene on top of PMMA(100 nm)/SiO_2(300 nm)/Si. The procedure is straightforward. We spin PMMA (950 A2) on 300 nm SiO_2 substrate at 2000 rpm. After annealing it for 3 mins at 180 ˚C, we obtain a 100 nm thick PMMA layer. We use the mechanical exfoliation technique to produce graphene flakes on PMMA. An optical microscope is used to select the graphene monolayer. The 2D peak has a full width half maximum of 32cm^{-1} which distinguishes a monolayer from few layer grahpene.

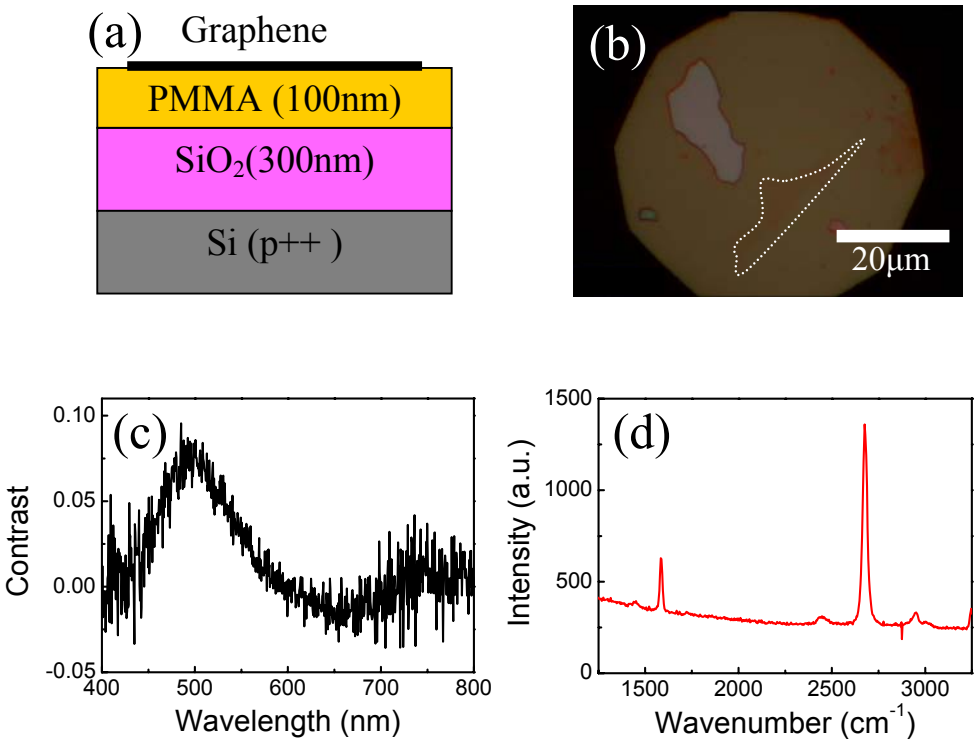

FIG. 3.12. a) Schematic of structure for a graphene sheet on a layer of 100nm PMMA placed on top of Si substrate with 300nm SiO_2. b) An optical image of monolayer graphene on PMMA(100nm)/SiO_2(300nm)/Si. The outline areas correspond to SLG, the scale bar is 20μm. c) Experimental results of contrast spectra of the graphene sample, d) Raman spectrum of the monolayer graphene flake. The position of G peak and the spectral features of the 2D band confirm the number of the layers.

After the graphene deposition, we coated another 300 nm PMMA 950 onto the substrate and baked it for 3 mins again. The graphene is still visible under microscope, according to our simulation results (Figure 3.11 (e) and (f)). The area at which we would like to produce a metallic contact to the graphene needs to be exposed with an electron beam. This contact will become free standing and therefore needs support pillars from both sides (free standing bridge) to the SiO_2. Good electrical contacts can be produced by thermal evaporation of 150 nm Ti. After liftoff, a free standing graphene is obtained. The fabrication processes are illustrated in Figure 3.13. The method may be an easy way to produce a working free standing graphene electronic device.

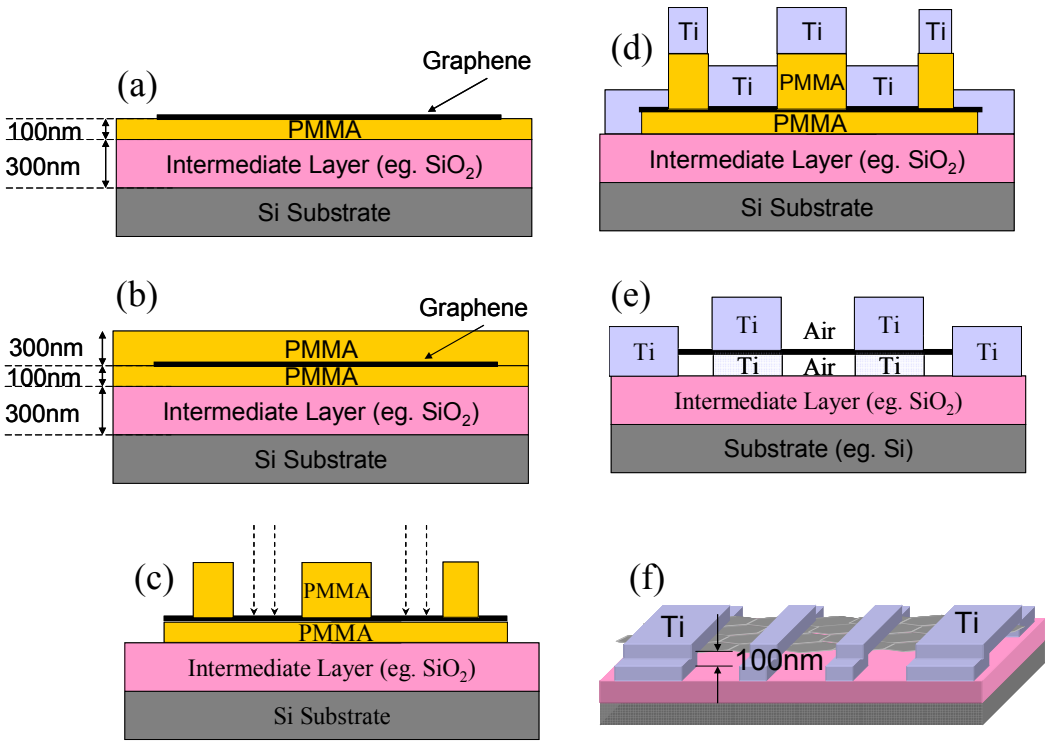

FIG. 3.13 Fabrication process for a free standing graphene device. (a) Graphene flakes are deposited onto the highly doped substrate coated with 300nm SiO_2 and 100nm PMMA. (b) Covering the sample with another thick layer of PMMA (about 300nm). (c) Exposure to e-beam and developing in MIBK solutions open windows for the electrodes. (d) Evaporation of Ti contacts. It is possible for Ti electrode to bridge when the total electrode thickness is comparable to bottom PMMA thickness. Metals are evaporated at 45 degree to the substrate surface. e) Resists are lifted off in PG remover. g) A free standing graphene device after lift off. Heating up the sample to 300˚C in a H_2/Ar environment for 1 hour should clean up all PMMA remains on graphene flakes.

In summary, due to the interference of the light waves that cause constructive and destructive interference, variation in the dielectric thickness results in series of reflection maxima and minima in the contrast spectrum. The coating of PMMA layers with optimum thickness is an effective way to enhance the contrast of SLG on all types of substrates investigated and it also makes SLG visible on most semiconductors and metals. As our method has the versatility to handle multilayer structure with many layers, it can help in fabrication of different graphene devices on various substrates.

3.8 Electrical Characteristic Setup

Before the measurement, samples with a typical size of 5×5 mm are wire-bonded on a chip carrier. Figure 3.14 shows a sample in chip carrier ready for measurement. The silver paint ensures a good electrical connection between the silicon substrate and the chip carrier which is important if we use the substrate as a global gate. Electrical connections from the chip to the chip carrier are made by ultrasonic bonding using gold wires. Because the electrical contacts on the chip are separated from the substrate by a thin silicon oxide of 300 nm, the bonding has to be operated carefully in order to avoid the breaking of the gate oxide.

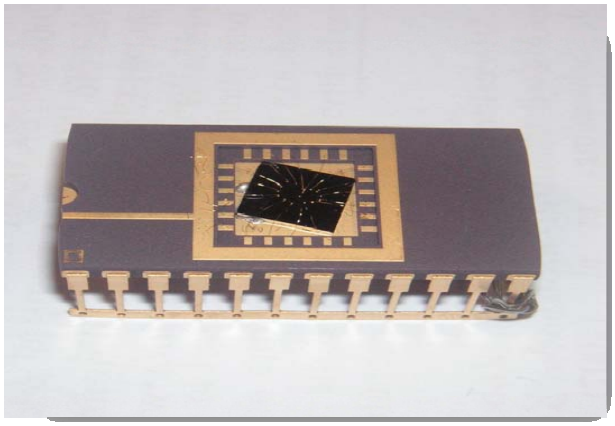

FIG. 3.14 A sample in chip carrier for measurement

The major part of my research here is related to electrical measurements on carbon nanowalls and graphene based devices. Measurements have been performed at low temperatures in order to study the quantum mechanical phenomena of interest, such as superconductivity and electronic quantum interference. The temperature ranges from 1.4 to 300 K. The magnetic field ranges from 0 to 6 T. We mount our sample on a dip stick which is immersed in a liquid helium dewar.

We use two methods to get differential conductance. Differential conductance measurements are conducted by either using the combination of Keithley 6221 current source and 2182A nanovoltmeter or using the combination of Keithley 6221 current source and Lock-in amplifier (SR830). The latter is much more time consuming than the former.

We also use both DC and AC measurements for gate electrical field measurements. DC measurement is done by Agilent semiconductor parameter analyzer, while AC measurement is done by using standard Lock-in measurement. Figure 3.15 shows a schematic of a basic measurement setup graphene FET. The current across samples is applied either as a DC current or as a low frequency AC current using the output from Keithley 6221. For DC current, the voltage accross the sample is measured using the Agilent semiconductor parameter analyzer, while for an AC bias, it is measured using the Stanford lock-in preamplifer SR830. The differences between the setups for DC and AC electronic measurements are shown in Figure 3.16.

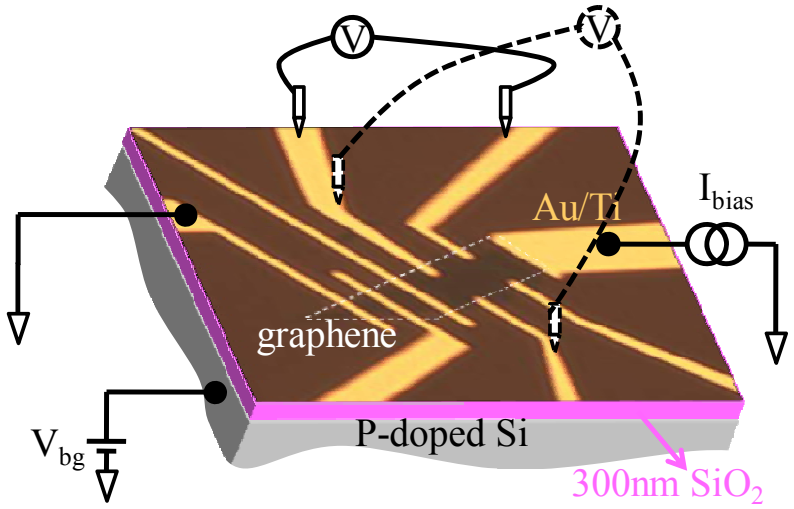

FIG. 3.15 An optical image of a graphene device with basic electrical setup in our investigations. The Fermi level in the graphene and the perpendicular electric field are controllable by means of the voltages applied to the back gate, V_{bg}. We study the resistivity of the graphene flake as a function of gate voltage by applying a current bias (I) and measuring the resulting voltage (V) across the device.

DC measurements:

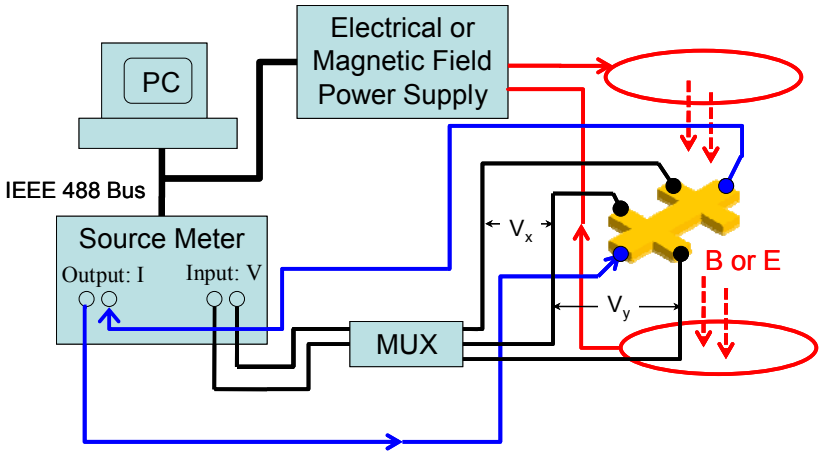

AC measurements:

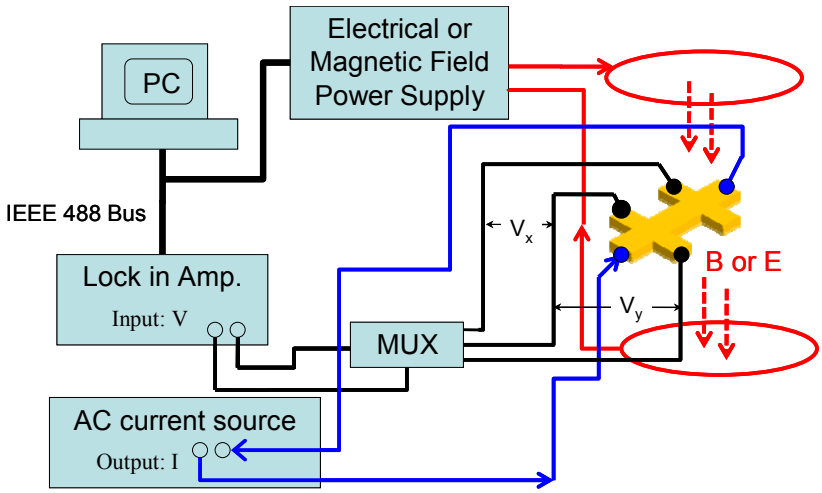

FIG. 3.16 Electrical measurement setup. A DC or AC current was applied to the sample while LabVIEW program was used to sweep the magnetic field (B) or electrical field (E) and to measure the voltage (V_x or V_y) passing across the sample.

All the instruments are computer controlled using the LabVIEW 6.1 program. The program sets and reads voltages on GPIB card, which is connected to all the instruments.

In the chapter, we briefly summarized the fabrication and measurement techniques used for carbon nanowalls and graphene sample preparation for characterization. From the next chapter, we start to discuss the transport properties in two dimensional carbons.

References:

[1] Y. H. Wu, P. W. Qiao, T. C. Chong, and Z. X. Shen, "Carbon nanowalls grown by microwave plasma enhanced chemical vapor deposition", *Adv. Mater.*, vol.14, pp.64-67, 2002.

[2] K. S. Novoselov, A. K. Geim, S. V. Morozov, D. Jiang, Y. Zhang, S. V. Dubonos, I. V. Grigorieva, and A. A. Firsov, "Electric Field Effect in Atomically Thin Carbon Films", *Science*, vol.306, pp.666-669, 2004.

[3] K. S. Novoselov, D. Jiang, F. Schedin F., T. J. Booth, V. V. Khotkevich V.V., S. V. Morozov, and A. K. Geim, "Two-dimensional atomic crystals", *PNAS*, vol.102, pp.10451-10453, 2005.

[4] www.2spi.com/catalog/new/hopgsub.shtml

[5] A. Gupta, G. Chen, P. Joshi, S. Tadigadapa and P. C. Eklund, " Raman Scattering from High-Frequency phonons in Supported n-Graphene Layer Films" *Nano Lett.,* vol.6, pp.2667-2673, 2006.

[6] A. C. Ferrari, J. C. Meyer, V. Scardaci, C. Casiraghi, M. Lazzeri, F. Mauri, S. Piscanec, D. Jiang, K. S. Novoselov, S. Roth, and A. K. Geim, "Raman spectrum of graphene and graphene layers ", *Phys. Rev. Lett.,* vol.97, pp.187401, 2006.

[7] D. Graf, F. Molitor, K. Ensslin, C. Stampfer, A. Jungen, C. Hierold and L. Wirtz, A. Jungen, C. Hierold and L. Wirtz, "Spatially Resolved Raman Spectroscopy of Single- and Few-Layer Graphene", *Nano Lett.,* vol.7, pp.238-242, 2007.

[8] C. Thomsen and S. Reich, "Double Resonant Raman Scattering in Graphite", *Phys. Rev. Lett.,* vol.85, pp.5214, 2000.

[9] Y. Y. Wang, Z. H. Ni, Z. X. Shen, H. M. Wang, and Y. H. Wu, "Interference enhancement of Raman signal of graphene", *Appl. Phys. Lett.*, vol.92, pp.043121, 2008.

[10] Z. H. Ni, H. M. Wang, J. Kasim, H. M. Fan, T. Yu, Y. H. Wu, Y. P. Feng and Z. X. Shen, "Graphene Thickness Determination Using Reflection and Contrast Spectroscopy", *Nano Lett.,* vol.7, pp.2758-2763, 2007.

[11] Guoquan Teo, Haomin Wang, Yihong Wu, Zaibing Guo, Jun Zhang, Zhenhua Ni and Zexiang Shen "Visibility study of graphene multilayer structures", *J. Appl. Phys.,* vol.103, pp.124302, 2008.

[12] P. Yeh, "Optical Waves in Layered Media", Wiley, New York, pp.102-111, 1988.

[13] E. D. Palik (ed.), "Handbook of Optical Constants of Solids", Academic Press, Orlando, 1985.

CHAPTER 4

ELECTRICONIC TRANSPORT PROPERTIES OF CARBON NANOWALLS USING NORMAL METAL ELECTRODES

4.1 Introduction

In this chapter, we first discuss the transport mechanism of two dimensional carbons. And then, transport properties of carbon nanowalls nanostructure are introduced. Following that, the mesoscopic transport properties of the Ti/CNWs/Ti junction under low temperature are discussed. We found that a small energy bandgap exists in the CNWs. Excess conductance fluctuations with peculiar temperature-dependence from 1.4 to 250 K were observed in CNWs with an electrode gap length of 300 and 450 nm, whereas the conductance fluctuation is greatly suppressed above 4.2 K when the electrode gap length increases to 800 and 1000 nm. The possible causes are discussed.

4.2 Mesoscopic Transport in Two Dimensional Carbon

CNWs are believed to have some similar properties to that of graphene. Theoretical studies conducted on nano-sized graphene ribbons uncover the opening of a small band gap at K and K' points. The small band gap is inversely proportional to the ribbon width. Similarly, a narrow band gap may also be present in CNWs samples.

Besides the confinement, the behavior of the electrons is strongly affected by disorders or impurities in the graphene lattice.[1] A large quantity of defects and disorder in carbon nanowalls may enrich the low temperature study in electronic transport. The interplay between disorder and quantum interference plays a crucial role

in determining the characteristics of electron transport in metals in the mesoscopic regime[2]. In a weakly disordered system, quantum interference between self-returned and multiply scattered paths of electrons on the scale of phase coherence length, L_ϕ, leads to quantum corrections to the electrical resistance, which manifests itself in the form of weak localization (WL) [3] and universal conductance fluctuations (UCF) [4]. The UCF is of universal nature because its magnitude, on the order of the conductance quanta e^2/h, depends on the shape of the conductor but not on its size or strength of disorder. In addition to UCF caused by internal scattering centers, the quantum interference among different transport channels or due to multiply reflected electron (hole) waves from the electrodes also causes fluctuations in the conductance. The latter should become more prominent in samples with reduced backscattering but a long coherent length. In this sense, nanostructured 2D carbons, including both single and multiple layer graphene sheets, are of particular interest for studying mesoscopic transport because of their unique electronic band structures [5] and the associated robust transport properties [6] even in highly disordered samples. The band structure of graphene is characterized by linearly dispersed conduction and valence bands which touch each other at the K and K' points in the Brillouin zone[7]. For nano-sized graphene or so-called graphene nano-ribbons, theoretical studies have shown that an energy gap opens at the K and K` points with a bandgap being inversely proportional to the ribbon width.[8] In addition to the bandgap, a narrow and flat band is also predicted to exist at the middle of the bandgap, depending on the atomic configuration of the edges or extended defects.[9] It has been reported in literature that a small bandgap is also present in nano-sized bilayer or few layers of graphene (FLG) sheets.[10] From the point of view of both fundamental physics studies and potential applications, it is of importance to understand how this small bandgap would affect the

transport properties of 2D nanocarbons in both the coherent and classic diffusive regimes. In the former case, of our particular interest are the structures in which (i) the bandgap is comparable to $E_\phi = \hbar D / L_\phi^2$ (or $E_B = \hbar v_F / L$ in the ballistic case) or $k_B T$ and (ii) $L \le \min(L_\phi, L_T)$, where D is the electron diffusion coefficient, L is the size of the sample, L_T is the thermal length, v_F is the Fermi velocity, $\hbar$ is the Planck constant and k_B is the Boltzmann constant. It is worth pointing out that most of the mesoscopic transport studies on semiconductors carried out so far have been focused on systems with a bandgap which is much larger than the aforementioned energy scales. The small bandgap and long coherence length of FLG ribbons make them distinguished from other systems and serve as an excellent platform for coherent transport studies.

4.3 Temperature Dependence of Carbon Nanowalls Network Structure

Titanium (Ti) will be used as electrode metal in order to form low resistance contact with CNWs.[11, 12] In general, the unfilled *d* orbitals of the transition metals enable the bonding between metals and carbon atoms. Considering its atomic structure ($3s^2p^6d^2\ 4s^2$), Ti is 3*d* metal with a substantial number of unfilled *d* states. They can form strong chemical bonds with carbon to produce highly stable carbide compounds. Moreover, the work function of Ti ($\Phi_{Ti} = 4.3\ eV$) is quite similar to that of graphite ($\Phi_{graphite} = 4.5\ eV$). [13, 14] The small mismatch of work functions minimizes the influence of metal doping at the interface between CNWs and metal. Therefore, titanium is adopted as electrode metal in our transport study.

In order to measure the resistance of CNW films, a CNW nanostructure in the shape of rectangle with different dimensions was prepared. All the electrodes are

deposited onto carbon nanowalls by using hard masks. The carbon nanowalls by four probes method were electrically characterized in the temperature T = 1.4 to 300 K. The temperature was controlled externally through the cryostat low temperature system. Two examples with different geometry are given in Figure 4.1. The inset shows the sample dimension between two voltage electrodes. In the first sample (Figure 4.1 (a)), the high temperature region (above 10 K) is well described by $R \sim T$ dependence, characteristic for metallic materials. Resistance at low temperatures can be described by the simple activation dependence $\exp(-\Delta / T)$, which indicates gap opening. In the second sample (Figure 4.1(b)), the high temperature region (above 10 K) is well described by $\exp(T_0 / T^{1/3})$ dependence, characteristic for variable range hopping in two dimensional system.[15] Resistance at low temperatures deviates from the variable range hopping dependence but can be described by the simple activation dependence $\exp(-\Delta / T)$. The activation dependence of resistance at low temperatures indicates that a narrow band gap may be present in our samples. In high temperature regime, the thermal energy could be higher than the narrow band gap, and then leads to the metallic behavior in CNWs. In addition, we attribute variable range hopping in some cases to weak tunneling like coupling between overlapping carbon nanowalls sheets.

The unique surface morphology of CNWs makes it difficult to form top electrodes with much smaller spacing. In order to overcome this difficulty, bottom electrodes are employed to form the electrical contacts to the nanowalls in the next work. The resistance by four probes method is measured as a function of temperature. Two examples with bottom electrodes are given in Figure 4.2. In both of the samples, the high temperature region (above 10 K) is well described by $R \sim T$ dependence, characteristic for metallic materials. Resistance at low temperatures deviates from the

variable range hopping dependence but can be described by the simple activation dependence $\exp(-\Delta/T)$.

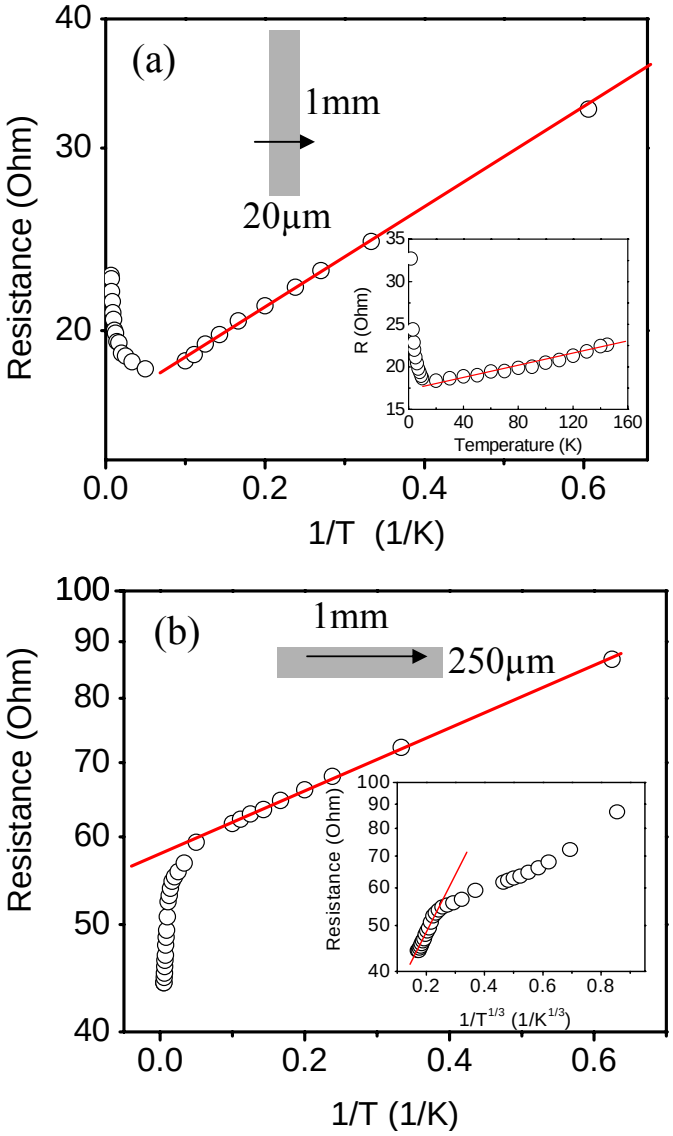

FIG. 4.1 (a) Temperature dependence of resistance ($R \sim \exp(\Delta/T)$) behavior in one CNWs sample is observed at $T < 15\ K$, where Δ is a constant . Inset: the same data but for the low temperature interval ($R \sim T$) behavior is observed at $T > 15\ K$); (b) Temperature dependence of resistance ($R \sim \exp(\Delta/T)$ behavior is observed in another CNWs sample with top electrodes at $T < 20\ K$, where Δ is a constant . Inset: the same data but for the low temperature interval ($R \sim \exp(T_0/T^{1/3})$) behavior is observed at $T > 20\ K$, where T_0 is a constant. The sample dimensions are given in μm and the current is shown as an arrow. The red lines are guides for the eye.

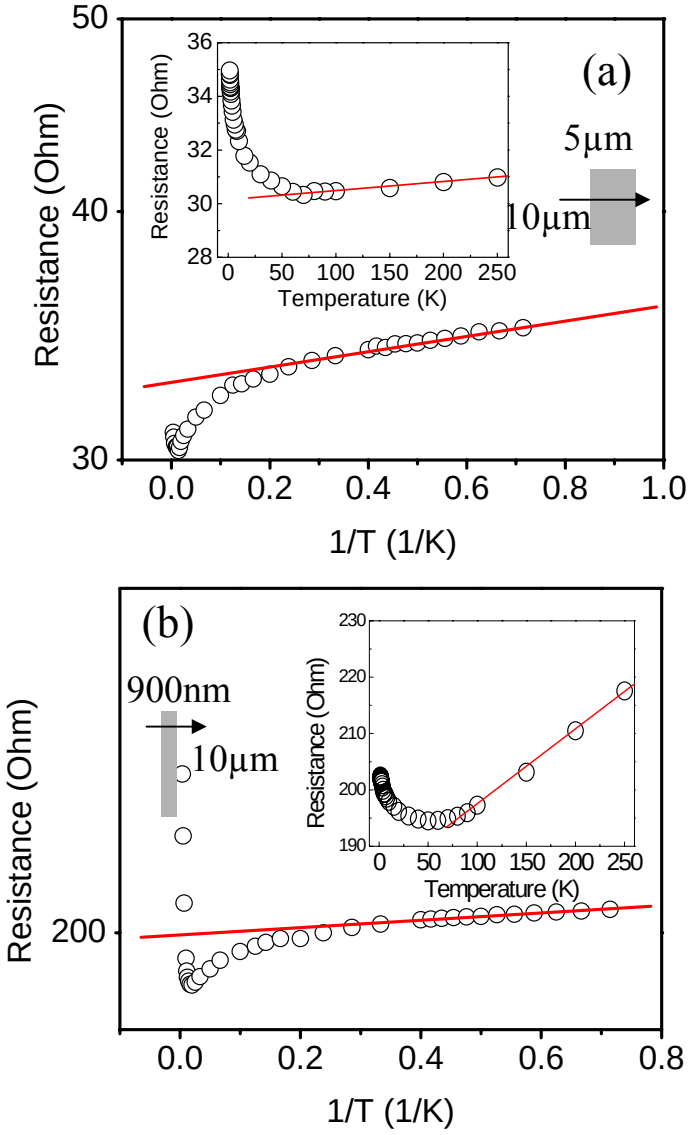

FIG. 4.2 (a) Temperature dependence of resistance ($R \sim \exp(\Delta/T)$) behavior is observed at $T < 5\ K$ in one CNWs sample with bottom electrodes, where Δ is a constant. Inset: the same data but for the high temperature interval ($R \sim T$) behavior is observed at $T > 50\ K$; (b) Temperature dependence of resistance ($R \sim \exp(\Delta/T)$) behavior is observed at $T < 5K$ in another CNWs sample with bottom electrodes, where Δ is a constant. Inset: the same data but for the high temperature interval ($R \sim T$) behavior is observed at $T > 70\ K$. The sample dimensions are given in μm and the current is shown as an arrow. The red lines are guides for the eye.

To our surprise, all the carbon nanowall samples measured exhibit a resistance which can be described by the simple activation dependence $\exp(-\Delta/T)$ at low

temperatures. The phenomenon indicates that a narrow band gap may be present in our samples. The existence of the small band gap may give rise to quantum interference with thermal activation in mesoscopic regime. However, electronic transport measurement has not been carried out in few pieces of carbon nanowall sheet due to the fact that the size of the sheets and the geometry of the devices are inadequate for the four probe measurement. In order to understand electronic properties in carbon nanowall sheets, we narrow down the electrode spacing and conduct the transport measurement in few sheets of carbon nanowalls by two probe measurement. And so we could study electronic transport properties of the small gap semiconductor in mesoscopic regime.

4.4 Semiconductor-like Behavior of Carbon Nanowalls Sheets

The electrodes were first prepared on cleaned SiO_2 substrate via EBL. The electrode configuration is detailed in Chapter 3 (Section 3.3.1.) Four samples were prepared and varied in the electrodes spacing (300, 500, 800 and 1000nm). The widths of the electrodes were fixed at 1 μm for all the four samples. Following the pattern transfer via EBL, titanium with the thickness of 100nm was deposited by sputtering. Finally the electrodes were formed after lifting off and ultrasonic bathing in acetone. The cleanliness of the samples was verified using SEM. This SEM image proves that the titanium in the gap was thoroughly lifted-up.

Carbon nanowalls were then deposited on the electrodes by MPECVD. The CNWs covered the whole substrate during the growth. The CNWs deposited on undesirable areas were gently removed using cleanroom wipes. To fabricate testing

devices, gold was evaporated on top of the Ti contact pads after shielding the carbon nanowalls with aluminum foil masks for bonding pads.

The electrical resistance of four Ti/CNWs/Ti samples with different junction spacing (300 nm, 450 nm, 800 nm and 1 μm) was measured at different temperature from 1.4 to 250 K. The resistances were deduced from the zero bias value of differential conductance (dI/dV) curves. As shown in Figure 4.3, the temperature dependence of zero bias resistance (ZBR) shows semiconductor-like characteristic for all the samples between 1.4 and 250 K. The existence of such semiconducting-like characteristic at low temperature is not new to the transport behavior of carbon nanostructures. The existence of crossover phenomenon from a negative dR/dT to a positive dR/dT in SWNT bundles has been found before, [16] which represents semiconductor-metal transition. A small energy band gap [17] was discovered after fitting the experimental results according to a simple two band (STB) model [18]. The opening of a small band gap gives rise to the change in electrical character of the sample from a semimetal to a semiconductor.

The existence of the narrow energy gap is not only shown in carbon nanotubes. Nanographite ribbons also display similar energy band structure with the presence of a narrow band gap [19-24]. Although there is a lack of theoretical studies on the electronic band structure of few layers of graphene and the presence of disorders and curvatures of our CNWs tend to complicate matters, we presumably propose that a small energy band gap may be present in our CNWs due to electronic quantum confinement.

In order to analyze the temperature dependent resistance data, we adopt the STB model, which is often used to illustrate the electron transport in bulk graphite [18]. The model is useful to describe different energy bands systems such as a possible

overlap between valence band and conduction band ($E_G < 0$) or a separation of energy ($E_G > 0$). In the STB model, the carrier densities of electrons (n) and holes (p) are given by:

$$n = C_n k_B T \ln(1 + \exp(-\frac{E_C - E_F}{k_B T})); \quad (4\text{-}1)$$

$$p = C_p k_B T \ln(1 + \exp(-\frac{E_F - E_V}{k_B T})) \quad (4\text{-}2)$$

respectively, where E_F, E_C and E_V are the energies at Fermi level, the bottom of conduction band and the top of valance band respectively, k_B is Boltzmann constant, C_n and C_p are constants. The mobility of the electrons and holes can be expressed as $\mu_e = A_1 T^{-1}$ and $\mu_h = A_2 T^{-1}$ respectively, A_1 and A_2 are constants related to electron-phonon scattering in graphite. Given that sample resistivity is defined as $\rho = (n\mu_n e + p\mu_p e)^{-1}$, where n and p are the carrier density of electrons and holes respectively, the temperature dependence of resistance can therefore be expressed as:

$$R = \frac{P_1}{\ln(1 + \exp(-\frac{E_C - E_F}{k_B T})) + P_2 \ln(1 + \exp(-\frac{E_F - E_V}{k_B T}))} + R_{contact} \quad (4\text{-}3)$$

Assuming that E_F lies within the energy gap and using $E_C - E_F$, $E_F - E_V$, P_1, P_2 and $R_{contact}$ as fitting parameters, this model fits well with our experimental observations for our four samples (Figure 4.3). From the fitting, we obtain E_g : are 1.64±0.39 meV, 3.73±0.53 meV, 2.04±0.29 meV and 2.29±0.25 meV for the samples with a gap of 300 nm, 450 nm, 800 nm and 1μm, respectively, while $R_{contact}$ varies from 10 Ohm to 25 Ohms. The origin of contact resistance is not clear. However, both small work function mismatch ($\Phi_{Ti} = 4.3\ eV$ *and* $\Phi_{graphene} = 4.5\ eV$) and highly stable carbide compounds formed during the fabrication of the devices may explain the

low contact resistance. These energy gap values achieved are in reasonable agreement with those in literature [25], which presents an empirical relationship between the energy gap E_g and width W in graphene ribbons: $E_g \approx 2eV \cdot nm/W$. If we use this formula to calculate the ribbon width based on the energy gaps obtained above, the width of the ribbon turned out to be in the range of 0.5 – 1 μm. The height of carbon nanowalls is about 1-1.5 μm. As we are unable to control the orientation of the nanowalls with respect to the electrode edges, the actual length of CNWs inside the gap is not necessarily the same as that of the spacing between the electrodes. As far as quantum confinement is concerned, the energy gap is determined by both the height and width of the CNWs (of course, thickness may also play a role here). These factors may explain why a smaller energy gap was not obtained for the sample with smaller electrode spacing among these samples.

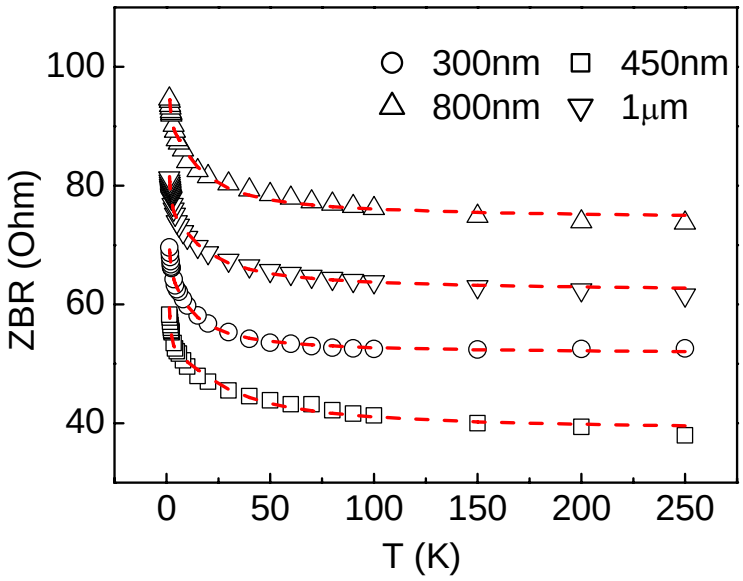

FIG. 4.3 Plot of zero bias resistance versus temperature for four Ti / CNWs / Ti samples with an electrode spacing of 300 nm (circle), 450 nm (square), 800 nm (upward triangle) and 1 μm (downward triangle), respectively. Dashed-lines are fits with the STB model.

Therefore, the measurements provide evidence that narrow energy gap of approximately of 1.6-3.7 meV existed in our CNWs after fitting with STB model. Such property is likely to influence the conductivity and other transport properties of the CNWs.

4.5 Differential Conductance Fluctuation

The conductance fluctuations in all the mesoscopic CNWs are also investigated. The underlying physics of UCF or quantum interference of multiple reflected electron waves is the difference in phase shifts experienced by electron waves that traverse a conductor along different trajectories within the phase coherence length. The phase of electron wave is sensitive to changes in configuration of scattering centers, magnetic field and electrostatic potential. The latter can arise from the modulation of chemical potential using a gate or application of a bias voltage in the electron traveling direction [26]. As the CNWs grow almost vertically on the substrate, the natural way to study both UCF and electron quantum interference due to scattering from the electrodes is to investigate how the conductance fluctuates with the DC bias rather than gate voltage or magnetic field. Hence, we have carried out detailed measurements of dI/dV curves at different temperatures for samples with different electrode gaps.

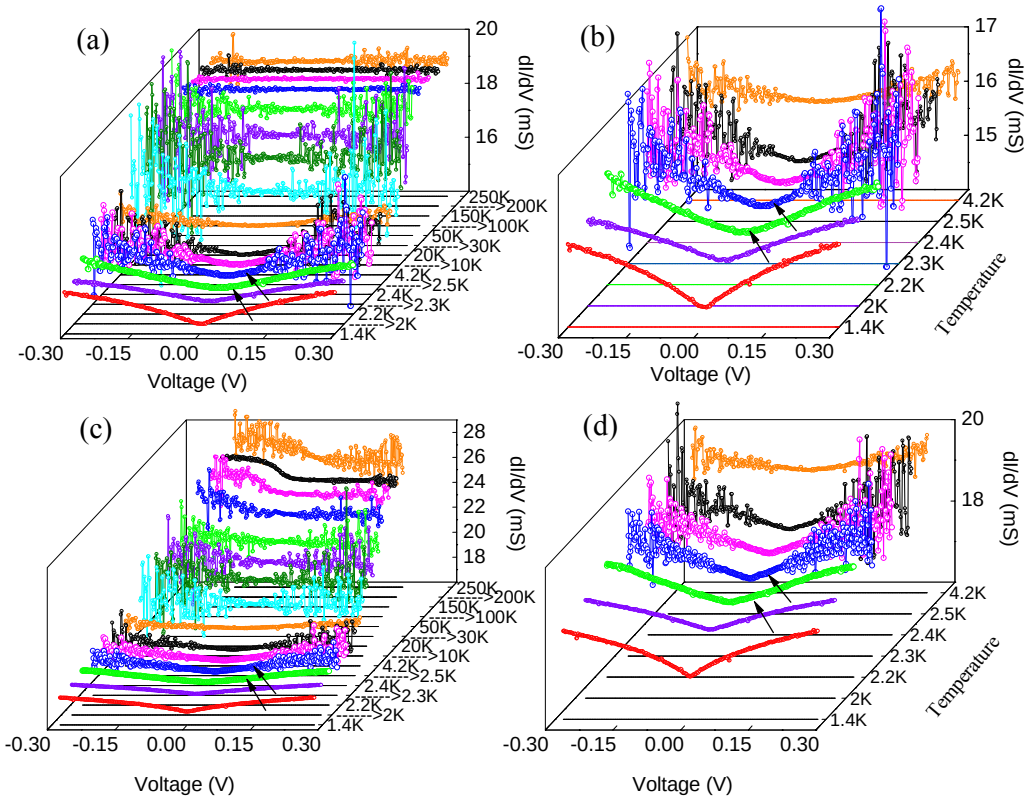

FIG. 4.4 The differential conductance of (a)-(b) 300 nm sample; (c)-(d) 450 nm sample, plotted as a function of applied voltage at different temperature.

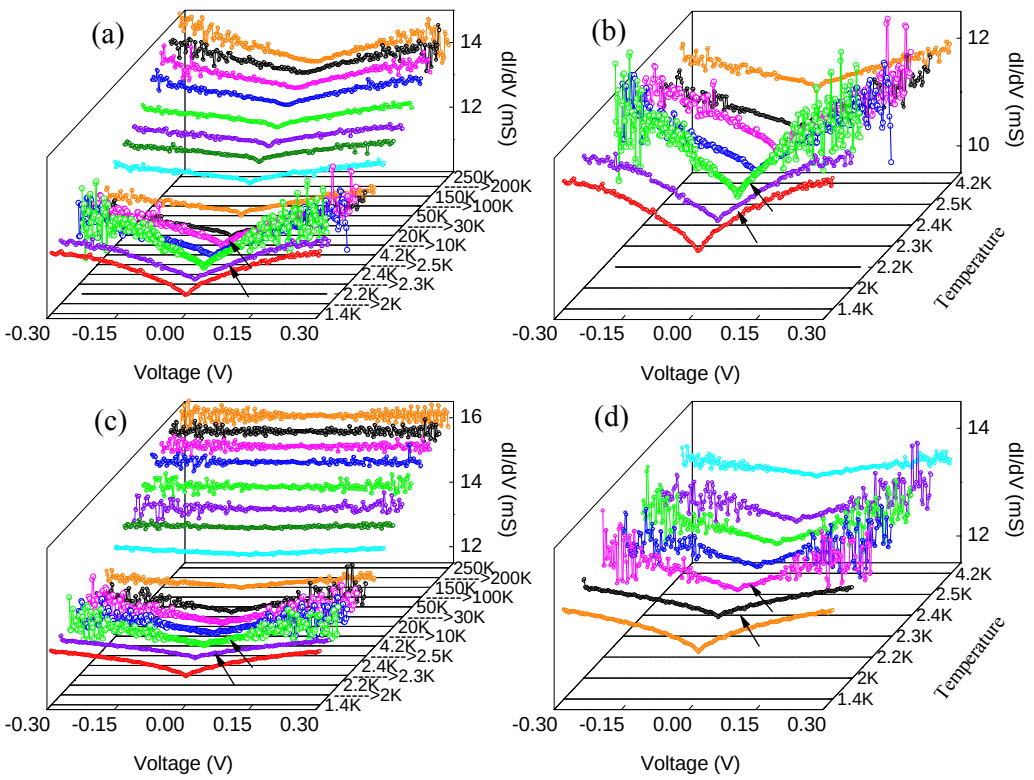

FIG. 4.5 The differential conductance of (a)-(b) 800 nm sample and (c)-(d) 1 μm sample, plotted as a function of applied voltage V for different temperature range.

Differential conductance data were collected for all the four samples at different temperatures ranging from 1.4 to 250 K. The temperature dependence of dI/dV of the four samples displays similar characteristics (Figure 4.4 and Figure. 4.5). Some of the common features that have been observed include (i) the dI/dV is almost independent of the bias voltage above 250 K, and it evolves gradually into a V-shape when the temperature decreases to below 10 K, (ii) the conductance fluctuation is small at both high and very low temperature, but increases significantly in the temperature range between 2.2 K and 4.2 K, depending on the electrode spacing, (iii) the conductance fluctuation decreases significantly for the samples with electrode spacing of 800 nm and 1 μm, while the conductance fluctuation rises again at 20 to 70 K in samples with 300 and 500 nm electrode spacing, and (iv) the conductance

fluctuation increases with the bias. As can be seen from Figure 4.4 and Figure 4.5, the conductance fluctuations are sensitive to both the bias voltage and temperature. To characterize the temperature-dependence of conductance fluctuation quantitatively, we calculate the root mean square of the magnitude of dI/dV fluctuation $rms[\delta G]$ in the current range from – 5 mA to 5 mA at each temperature point as follows:

$$rms[\delta G](T) = \sqrt{\frac{1}{N}\sum_{i=1}^{N}(G_i(T,V_i) - \overline{G}(T,V_i))^2} \tag{4-4}$$

where $G_i(T,V_i)$ and $\overline{G}(T,V_i)$ are experimental and smoothened values of the differential conductance at temperature T and bias voltage V_i . The smoothened curve is approximated by a six-order polynomial trend line. The $rms[\delta G]$ versus temperature graph is plotted and shown in Figure 4.6(a). The close-up of the low temperature region is shown in Figure 4.6(b). The $rms[\delta G]$ shows a sharp peak at approximately 2.3 K for the 800 nm sample, 2.1 K for the 1 μm sample and at 2.2 K for the other two samples. When the temperature increases further, the $rms[\delta G]$ first decreases, reaches a minimum at about 4.2 K and then increases again for the samples with an electrode gap of both 300 and 450 nm. The second peak rises quickly at 9-10 K with a broad high temperature tail, centering at about 20 and 50 K for samples with an electrode spacing of 300 and 500 nm, respectively. A further increase of temperature results in a sharp decrease of the conductance fluctuation at 50 and 70 K, respectively, for the 300 and 450 nm samples. The former decreases to almost minimum at 100 K, while the latter decreases to the minimum at about 200 K. On the other hand, the $rms[\delta G]$ for the 800 nm and 1μm samples are small and almost constant above 4.2 K.

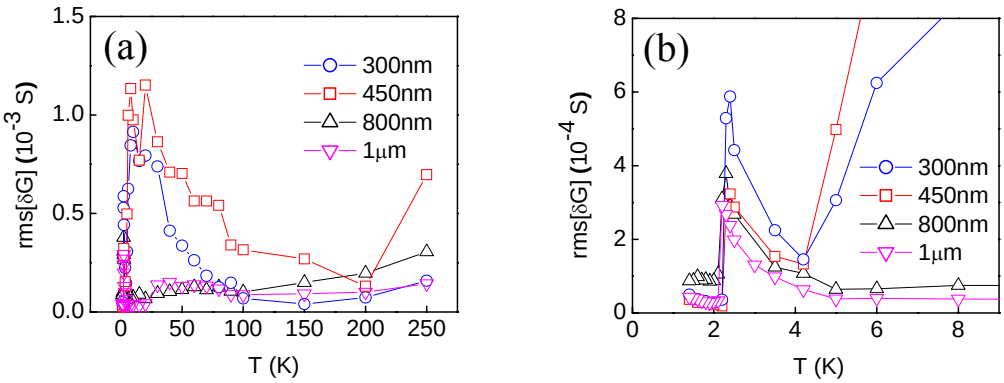

FIG. 4.6 A plot of rms[δG] vs. T for the four Ti/Carbon nanowalls/Ti samples. Insert: temperature dependence of rms[δG] for the four samples at low temperature.

The appearance of conductance fluctuations and their unique temperature dependence can be understood by looking at the energy and length scales of electrons in this system, as discussed in the introduction. The conductance fluctuation becomes prominent in the conductance measurement when the electrode spacing becomes comparable to the phase coherence length or thermal length, whichever is smaller. By using the typical momentum relaxation time, $\tau = 1\times10^{-13} s$, and phase relaxation time, $\tau_\phi = 6.5\times10^{-12} s$,[27] for graphite sheets at 4.2 K and $v_F = 1\times10^6 m/s$, one has $D = v_F^2 \cdot \tau/2 = 0.5 m^2 s^{-1}$, $L_\phi = (D\tau_\phi)^{\frac{1}{2}} = 567\ nm$, $L_T = 300\ nm$, $E_\phi = 1.025\ meV$ and $E_B = 2.2 - 6.6\ meV$ (at $L = 300 - 100\ nm$). This may explain why the magnitude of conductance fluctuations is large in the two samples with an electrode spacing of 300 and 450 nm, whereas it is small in the other two samples with a larger electrode gap above 4.2 K. We now look at the temperature-dependence of $rms[\delta G]$. The magnitude of UCF at zero temperature is of order of e^2/h, regardless of the sample size and degree of disorder. However, when temperature increases, the coherence length will decrease accordingly. If the coherence length is of the same order of sample size at zero temperature, the magnitude of UCF is expected to decrease monotonically with

temperature in normal metals. The conductance fluctuation due to quantum interference of electron waves scattered from the electrodes is also expected to increase with decreasing the temperature, though the magnitude of fluctuation shall depend on the sample size and structure. However, the temperature-dependence of conductance fluctuations shown in Figure 4.6(a) is far from this kind of "normal" behavior. Instead of monotonic decrease with temperature, the conductance fluctuations for samples with an electrode spacing of 300 and 450 nm exhibits two peaks, one at about 2.2 K for both samples and the other broad peak centering at ~ 20 K for the 300 nm sample and at ~ 50 K for the 450 nm sample. The latter agrees well with the bandgap of 1.62±0.09 meV and 3.72±0.43 meV for the samples with an electrode gap of 300 and 450 nm, respectively. This implies that thermal excitation of electrons from the valence band to the conduction band dominates the mesoscopic transport in CNWs above 4.2 K. In addition to global heating, the much enhanced fluctuations at high bias may also be due to current-induced local heating effect. It should be noted that the amplitude of conductance fluctuation in the peak temperature region is about one order larger than the UCF, in particular, at high bias. This again manifests the effect of thermal excitation across the small bandgap.

The minimum of conductance fluctuation appears around 4 K with amplitude on the order of e^2/h. This means that thermal-induced excitation is suppressed at low temperature. However, what is puzzling is the sharp upturn of conductance fluctuations below 4 K and an abrupt decrease again of conductance fluctuations below 2.1 - 2.2 K. A systematic study by using other different types of electrodes revealed that this trend is independent of the electrodes and samples and is observed in all measurements. As the onset temperature of conductance fluctuation reduction is near the "lambda point" of helium 4 (He 4), we believe that the conductance fluctuation suppression below 2.1

K is caused by the formation of a layer of superfluid He 4 on the nanowalls. The large thermal conductivity of superfluid He 4 greatly improves the temperature homogeneity of the nanowalls between the two electrodes, leading to the suppression of conductance fluctuation even at a high DC bias. By same reasoning, the upturn between 2.1-4 K can be easily understood as being caused by the thermal fluctuation due to the formation of piece-wise discontinuous regions of superfluid He 4.

4.6 Giant Gap-like Behavior of Differential Conductance

Beside the conductance fluctuation, we also found a gap-like behavior of dI/dV in some samples with large electrode spacing. Here we just give the sample with 1 μm electrode spacing as an example. We measured dI/dV curves by varying the temperature from 1.4 to 2.5 K. The differential conductance was measured during cooling samples and the results were shown in Figure 4.7(a). After repeating dI/dV measurement several times, the differential conductance at 1.4 K exhibits a high peak near 180 mV bias and increases faster beyond the peak bias. The peak of differential conductance is more sensitive with temperature than with magnetic field. And it could be eliminated by high temperature but it could survive sometimes under magnetic field as high as 6 Tesla. Once the soft gap was eliminated, it is difficult to be restored. The peaks of differential conductance shift toward zero bias by increasing temperature or magnetic field. Subsequently, the differential conductance as a function of applied voltage is measured when warming up in absence of magnetic field and the results are plotted in Figure 4.7(b). It is found that the differential conductance peak disappear at 1.9 K. The temperature dependence of zero bias resistance (ZBR) of both processes is plotted in Figure 4.8. It is found that the RT curve measured when cooling overlaps with that measured when warming up. We observe these similar phenomena in five

different samples with different configurations. It is very interesting that the peaks disappear near 2K in all the samples. The temperature just is the point where conductance of fluctuation disappears in CNWs.

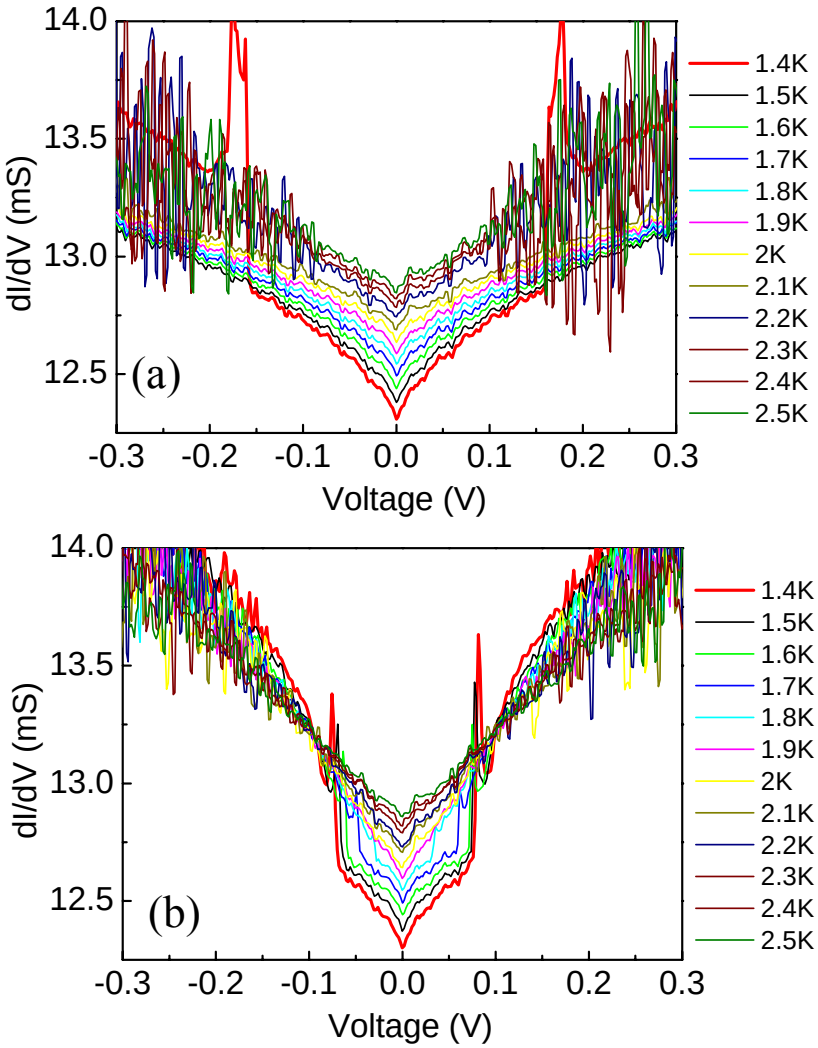

FIG. 4.7 Differential conductance curves at temperatures (a) decreasing and (b) increasing from 1.4 K to 2.5 K plotted as a function of applied bias voltage V for the sample with an electrode spacing of 1μm.

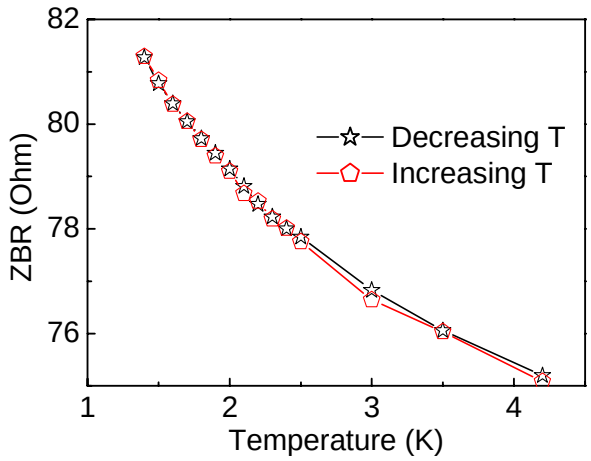

FIG. 4.8 Plot of zero bias resistance versus temperature in Figure 4.7.

To summarize, there are three features in dI/dV curves. One is the sudden appearance of huge conductance fluctuation above 2 - 2.2 K. These results were discussed in previous part. The second is the existence of the soft gap like behavior below 2 K. Both the first two phenomena begin to happen at the temperature very near lambda point of liquid helium (2.17 K). It is believed that both phenomena are related to superfluidity of liquid helium 4 although the mechanism behind is not clear so far. The third one is the soft energy gap width looks universal. The width of the soft gap is around 100-200 mV in all the samples and has no obvious relationship with the electrodes spacing and device configuration. Although more measurements are needed for a full understanding of the behavior, we argue that the edge state instability was observed in CNWs below 2 K. The edge state instability indicates the existence of Josephson-coupled superconducting grains in CNWs. The intrinsic superconductivity could not survive above 2K.

In fact, CNWs have a mutually supported network structure and the width of each piece of nanowall is about 0.5-1 μm. It is possible to form junctions between nanowall sheet and nanowall sheet or nanowall sheet and electrodes. We also observed

the soft gap like behavior on CNWs samples with real four probe configuration, by excluding the contact resistance. Although several CNWs sheets between the electrodes are involved, the experiment results exhibit the sum of the dI/dV due to the parallel configuration. Because we only observed the phenomenon in most of those devices with electrode spacing more than 450 nm, we believe the dI/dV gap feature comes from the junctions.

In order to understand the dI/dV gap like feature, some previous studies of related system should be introduced. In 1992, similar gap signature in dI/dV versus voltage was observed in density of state (DOS) measurements on the surface of pure HOPG by Agrait et al. [28] The gap has the order of 100 meV. Interestingly, this kind of curves is not only reproducible but occurs only in disordered surface regions. Agrait et al. suggested that the gap originates from single electron charging effect. The gap like behaviors between HOPG nanocontacts were also explained as electronic charging effect [29]. The gap-like features were also observed in very recent STS experiment of graphene/SiC [30, 31]. Recent angle resolved photoemission spectroscopy (ARPES) on graphite surface and graphene on SiC have been investigated. The weak additional intensity [32] near 100 meV from the Dirac point in graphite and a kink at 200 meV below Fermi level [33] on graphene/SiC were observed, they probably indicate the great influence of the edge, curvature, defect or disorder on graphite. Also, a semiconducting gap can be opened by doping and applying electrical field. A 100 meV gap at the neutral point for bilayer graphene/SiC opens after doping[34]. The energy gap in bilayer graphene on SiO_2 can be tuned to as high as 0.3 eV by using biased field.[35, 36] The energy feature below 200 meV in inelastic electron tunneling spectrum of graphite is believed to due to phonons [37, 38]. Considering the insulating phenomena in graphite in the introduction part, we conclude that the unique gap-like

features in graphite are not accidental. The possible explanations are summarized here: 1) electronic states in the 2D carbon, 2) electronic charging effect, 3) weak coupling between the graphene layers in graphene, 4) band bending effect by local intense electric fields, 5) inelastic coupling to surface excitations.[39] 6) phonon mediated tunneling[40] or some other phonon electron coupling[41].

Recently, Y. Kopelevich et al.[42] give other two causes to the gap like fearture. I) The gap may be also related to the Kondo effect observed in carbon nanotubes [43]. II) Either contamination produces an artifact or the structure of disordered graphite has local properties similar to superconductors and/or strongly correlated systems. The superconducting transition temperature can be deduced from the Bardeen-Cooper-Schriefer (BCS) equation. It would indicate a critical temperature as high as 400K. Y. Kopelevich et al. have also pointed out that the superconductivity is metastable in many carbon based systems. Carbon nanotubes were observed to exhibit intrinsic superconductivity [44, 45] and many graphite composites exhibit local superconductivity.[46] Most observations suggest that either adsorbed foreign atoms on graphite surface trigger superconductivity or the superconductivity occurs in small graphite fractions.

We believe that local densities of states at edges of CNWs contribute to bias induced enhancement of conductance. There are three reasons: i) edge states are strongly localized states with a finite width and have high density; ii) the edge states may act an important role on transport properties when graphite sheets are reduced to nanometer range, mentioned earlier; iii) CNWs form contacts with electrodes directly at and only at their edges. All of these made it possible to observe the transport properties at the edge states in CNWs. The energy dispersion of edge states have been observed by STM/STS [47,48] and ARPES [49] in graphite. The localized edge states

may become one of the main causes of charge density wave (CDW) [50], spin density wave (SPW) [51], superconductivity[52, 53] or ferromagnetism[54,55] in CNWs. However, the stabilization of edge states is not high in CNWs because the edges are difficult to control in CNWs. As we discussed, CNWs the edge state may dominate the transport in CNWs at low temperature. The edges of CNWs not only provide high density of states, but also exhibit strong electron phonon interaction. We are interested in why we could not find the superconductivity directly in Ti/CNWs/Ti junctions with smaller spacing. This phenomenon is due to the fact that the superconductivity is destroyed by the normal contacts when the coherence length of the Cooper pairs is larger than the junction spacing. Although it is possible for the edge states to exhibit CDW or 1D like characteristic such as Kondo effect, all explanations are possible according to the existing experiments.

However, why are the fluctuation positions in either highly disordered graphite sheet or HOPG almost near several hundred meV? Whether is the value universal? What is the real origin of the phenomenon? Those problems are still unclear and need further investigation. Regardless of its origin, the existence of the gap like behavior looks more obvious in disordered graphite and indicates the future potential applications.

4.7 Magnetic Field Dependence of Electronic Transport Properties

In normal conductor, there are many possible origins of magneto resistance such as elastic scattering, inelastic scattering, spin orbit coupling, magnetic impurity scattering, intrinsic ferromagnetism or hopping and tunneling between domains in which the electrons are delocalized.

In two dimensional carbon, to measure magnetoresistance (MR) can be used to study the localization effect. The weak localization corrections to the conductivity of graphene can either be positive or negative depending on the relative magnitude of the intervalley scattering time or the phase coherence time[56]. This weak anti-localization (WAL) effect is a signature of the isospin. It stands in contrast to the usual weak localization (WL) effect, characterized by a negative magnetoresistance. Negative magnetoresistance occurs in these materials at point defects that locally break the sublattice degeneracy, thereby causing intervalley scattering (from one Dirac cone to the other).

The special transport properties have their origin in the chiral nature of the charge carriers, causing reduced backscattering. A magnetic field suppresses the constructive quantum interference at point defects that locally break the sublattice degeneracy, thereby causing intervalley scattering (from one Dirac cone to the other). And the the suppression of the scattering will result in a negative magnetoresistance. Such phenomenon is known as weak localization. In some cases, especially graphene, interference can be destructive and the chances of backscattering are diminished. A magnetic field is applied to suppress the effect and a positive magnetoresistance is obtained. Weak antilocalization behaviour has been thus observed experimentally by Wu et al. on epitaxial graphene. [57]

The magnetotransport in CNWs were investigated by applying a magnetic field perpendicular to the substrates at two different temperatures (1.4 K and 2.5 K). The MR curves of the three carbon nanowalls samples are plotted in Figure 4.9. Figure 4.9 (a) (c) and (e) illustrates the MR effect over a magnetic field range of 1 Tesla whereas Figure 4.9(b), (d) and (f) shows the MR behavior over a magnetic field range of 6 Tesla.

From the magnetoresistance data in Figure 4.9 (a), (c) and (e), there are no signs of clear negative or positive MR response for all the samples except for the samples with electrode gaps of 300 nm sample at 1.4 K. These two samples present a negative magnetoresistance which indicates the presence of weak localization. As such, it is proposed that the magnetic field range is too small to detect weak localization behavior. From Figure 4.9, it was found that in general, the magnetoresistance curves presented an overall negative magnetoresistance response when a maximum field of 6 Tesla was applied to the samples. The magnetoresistance is found to decrease by 2.65 % for the 300 nm sample and 2.28 % for the other two samples at 1.4 K. At 2.5 K, the decrease was 1.38 %, 1.28 % and 1.09 % for the 300 nm, 450 nm and 800 nm samples, respectively. This is a clear indication of the presence of weak localization behavior in our carbon nanowalls. The observation of negative magentoresistance under high magnetic field may be explained by the fact that direction of magnetic field is parallel to the surface of carbon nanowalls sheet. Note that the investigation of the sample with 1μm spacing focus on the gap like feature, magnetotransport was not carried out.

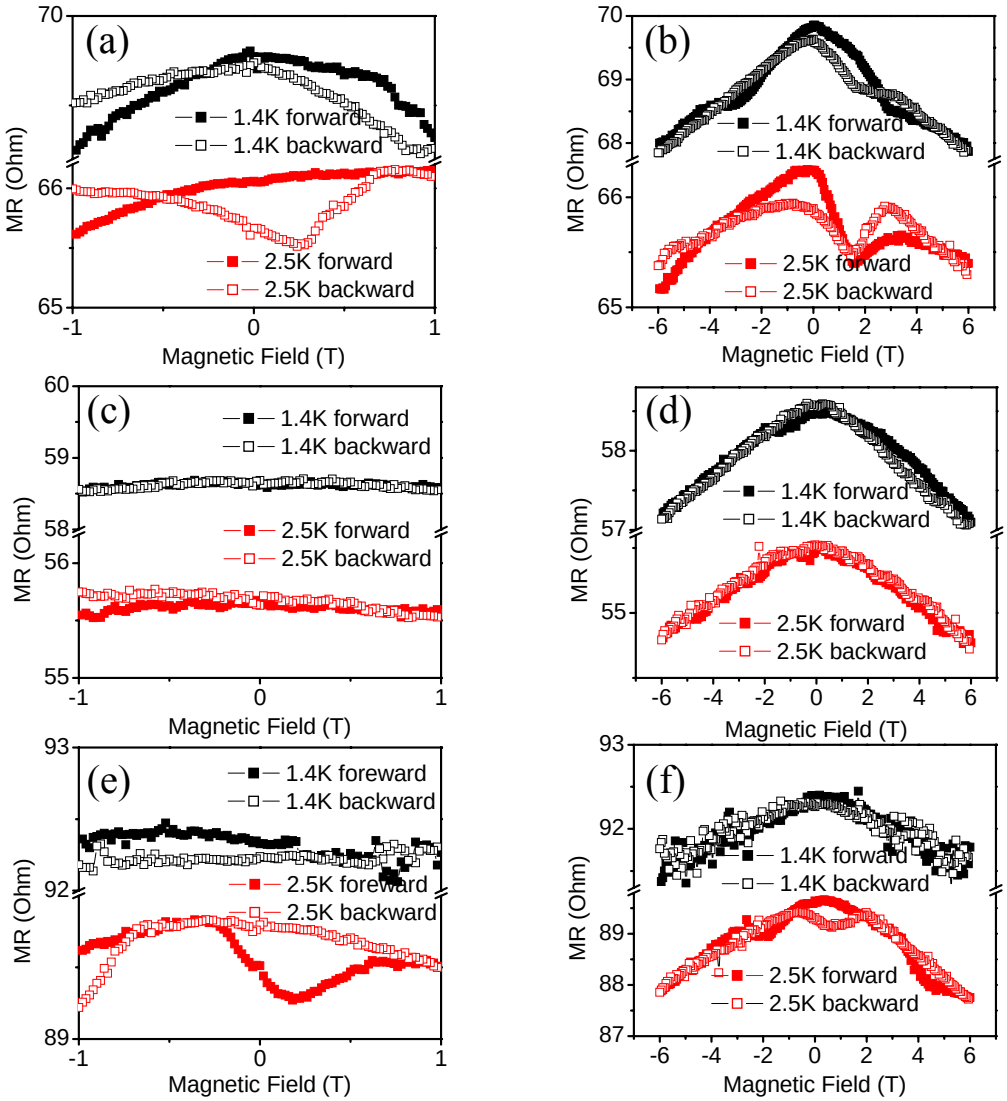

FIG. 4.9 Magnetoresistance behaviour of (a-b) 300 nm, (c-d) 450 nm and (e-f) 800 nm samples at 1.4 K and 2.5 K respectively.

The magneto resistance is negative for all the samples measurement in the view of large range of magnetic field. The negative magneto-resistance is characteristic to systems with coexist hole and electron carriers [58]. Weak localization is believed to attribute to the negative magneto-resistance. The weak localization in carbon nanowalls, in which a backscattering electron wave interferes constructively with time reversed wave, enhances the backscattering probability and zero bias resistance. In

some samples, the magneto resistance is asymmetric with respect to B = 0 as shown in Figure 4.9. The exact origin of this asymmetry is not clear at the moment. The available data suggest that lattice disorder and the characteristics of the single homogeneous grains or patches and their interfaces may play an important role in the observed asymmetry. The asymmetry is a strong fingerprint of disorder ferromagnetism, ferroelectricity, or granular superconductivity.

In order to understand the conductance fluctuation in CNWs, dI/dV curves are measured under different magnetic field at 1.4 and 2.5 K. We achieve the conductance fluctuation by using the same method adopted in section 3.5. The magnetic field dependence of conductance fluctuation is plotted in Figure 4.10. It is interesting to note that the amplitudes of the fluctuations for all the three samples dip when the samples were cooled down to 1.4 K. The amplitude of the fluctuations at 2.5 K increases to ten times than that at 1.4 K. In all samples, the fluctuations are reproducible and essentially independent of magnetic field. These phenomena are consistent with formation of uniform helium 4 superfluity, which we discussed previously.

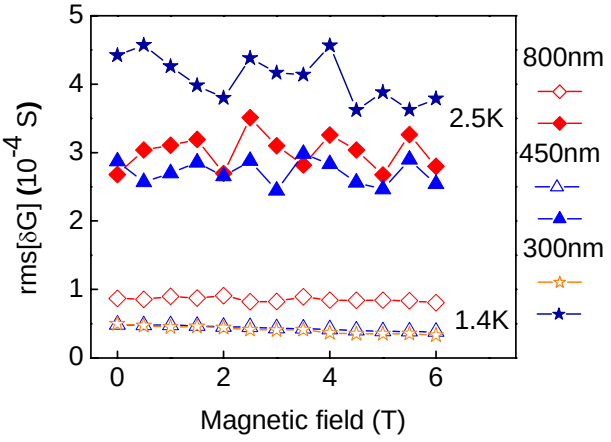

FIG. 4.10 A plot of root mean square of differential conductance fluctuation vs Magnetic field for the three Ti/Carbon nanowalls/Ti samples from 0T to 6T with a sweep of 0.5T per step at 1.4K and 1.5K respectively. The magnetic field was applied perpendicular to the substrate surface.

4.8 Conclusion

In summary, we presented an electrical transport study of CNWs with Ti electrodes. Excess conductance fluctuations are observed in the temperature range between 4 and 200 K, which are attributed to the quantum interference effect under the influence of thermally induced carrier excitation across a narrow bandgap. On the other hand, the sharp decrease of conductance fluctuation below 2.1 K is accounted for by the formation of a layer of He 4 superfluid on the nanowalls. The results obtained here have important implications for potential application of FLGs in electronics devices. We note that, very recently, conductance fluctuations have also been observed in nano-ribbon based field effect transistors [25, 59] and graphene [60] at low temperature. The conductance fluctuations found in graphene [61] is attributed to phase coherence multiple reflection of carriers between electrodes. Following that, the giant gap like behavior of dI/dV is discussed. We believe that local densities of states at edges of CNWs contribute to gap like behavior of dI/dV. Angle resolved photoemission spectroscopy (ARPES) and scanning tunneling spectroscopy (STS) measurement can study the electronic structure of CNWs and may help us to understand the origin. Finally, weak localization is evident only when a strong magnetic field range is applied. The magnetic field suppresses the resistance giving rise to a negative magnetoresistance.

References:

[1] S. Wu, L. Jing, Q. Li, Q. W. Shi, J. Chen, H. Su, X. Wang, and J. Yang, "Average density of states in disordered graphene systems", *Phys. Rev. B*, vol.77, pp.195411, 2008.

[2] C. W. J. Beenakker and H. van Houten, "Quantum Transport in Semiconductor Nanostructures", *Solid State Physics,* vol.44, pp.1-111, 1991. S. Washburn, and R.A. Webb, "Quantum transport in small disordered samples from the diffusive to the ballistic regime", *Rep. Prog. Phys*., vol.55, pp.1311, 1992. S. Datta, Electronic Transport in Mesoscopic Systems, Cambridge, England, 1995. B.L. Altshuler, P.A. Lee, R.A. Webb, Mesoscopic Phenomena in Solids, North Holland, Amsterdam, 1991.

[3] E. Abrahams, et al., "Scaling Theory of Localization: Absence of Quantum Diffusion in Two Dimensions", *Phys. Rev. Lett.,* vol.42, pp.673, 1979. P.W. Anderson, et al., "Possible Explanation of Nonlinear Conductivity in Thin-Film Metal Wires", *Phys. Rev. Lett*., vol.43, pp.718, 1979.

[4] P.A. Lee, A.D. Stone, "Universal Conductance Fluctuations in Metals", *Phys. Rev. Lett.*, vol.55, pp.1622, 1985. P.A. Lee, "Universal Conductance Fluctuations in Disordered Metals", *Physica A*, vol.140, pp.169, 1986.

[5] N.M.R. Peres, A.H. Castro Neto, and F. Guinea, "Conductance quantization in mesoscopic graphene", *Phys. Rev. B,* vol.73, pp.125411, 2006. J. Nilsson, A. H. Castro Neto, F. Guinea, and N. M. R. Peres "Electronic Properties of Graphene Multilayers", *Phys. Rev. Lett*., vol.97, pp.266801, 2006.

[6] K. Ziegler, "Robust Transport Properties in Graphene", *Phys. Rev. Lett*., vol.97, pp.266802 (2006). A. Altland, "Low-Energy Theory of Disordered Graphene", *Phys. Rev. Lett.,* vol.97, pp.236802, 2006.

[7] P.R. Wallace, "The Band Theory of Graphite", *Phys. Rev.,* vol.71, pp.622-634, 1947.

[8] K. Nakada, M. Fujita, G. Dresselhaus and M. S. Dresselhaus, "Edge state in graphene ribbons: Nanometer size effect and edge shape dependence", *Phys. Rev. B,* vol.54, pp.17954, 1996. Y.-W. Son, M. L. Cohen, and S. G. Louie, "Energy Gaps in Graphene Nanoribbons", *Phys. Rev. Lett*., vol.97, pp.216803, 2006.

[9] K. Wakabayashi, M. Fujita, H. Ajiki, M. Sigrist, "Electronic and magnetic properties of nanographite ribbons", *Phys. Rev. B,* vol.59, pp.8271, 1999. A.H. Castro

Neto, et al., "Edge and surface states in the quantum Hall effect in graphene", *Phys. Rev. B,* vol.73, pp.205408, 2006. V.M. Pereira, et al., "Disorder Induced Localized States in Graphene" *Phys. Rev. Lett*., vol.96, pp.036801, 2006. J. Nilsson and A. H. Castro Neto, "Impurities in a Biased Graphene Bilayer", *Phys. Rev. Lett*., vol.98, pp.126801, 2007.

[10] E. McCann, "Asymmetry gap in the electronic band structure of bilayer graphene", *Phys. Rev. B,* vol.74, pp.161403(R), 2006. S. Latil and . Henrard, "Charge Carriers in Few-Layer Graphene Films", *Phys. Rev. Lett.,* vol.97, pp.036803, 2006. M. Aoki and H. Amawashi, "Dependence of band structures on stacking and field in layered graphene", *Solid State Commun.,* vol.142, pp.123-127, 2007.

[11] Y. Zhang, T. Ichihashi, E. Landree, F. Nihey, and S. Iijima, "Heterostructures of Single-Walled Carbon Nanotubes and Carbide Nanorods", *Science,* vol.285, pp.1719-1722, 1999.

[12] J.-O. Lee, C. Park, J.-J. Kim, J. Kim, J. W. Park, and K.-H. Yoo, "Formation of low-resistance ohmic contacts between carbon nanotube and metal electrodes by a rapid thermal annealing method", *J. Phys. D,* vol.33, pp.1953- 1956, 2000.

[13] B. Huard, N. Stander, J.A. Sulpizio, and D. Goldhaber-Gordon, "Evidence of the role of contacts on the observed electron-hole asymmetry in graphene", *Phy. Rev. B,* vol.78, pp.121402(R), 2008.

[14] G. Giovannetti, P.A. Khomyakov, G. Brocks, V.M. Karpan, J. van den Brink and P.J. Kelly, "Doping graphene with metal contacts", *Phys. Rev. Lett.,* vol.101, pp.026803, 2008.

[15] N. F. Mott, "Conduction in non-crystalline materials. III. Localized states in a pseudogap and near extremities of conduction and valence bands", *Phil. Mag.,* vol.19, pp.835, 1969.

[16] J. E. Fischer, H. Dai, A. Thess, R. Lee, N. M. Hanjani, D. L. Dehaas, and R. E. Smalley, "Metallic resistivity in crystalline ropes of single-wall carbon nanotubes", *Phys. Rev. B,* vol.55, pp.R4921, 1997.

[17] H. Zhu, G.L. Zhao, C. Masarapu, D.P. Young, B. Wei, "Super-small energy gaps of single-walled carbon nanotube strands", *Appl. Phys. Lett.,* vol.86, pp.203107, 2005.

[18] B. T. Kelly, Physics of graphite, *Applied Science*, Englewood, NJ, pp.285, 1981.

[19] K. Nakada, M. Fujita, G. Dresselhaus, M. S. Dresselhaus, "Edge state in graphene ribbons: Nanometer size effect and edge shape dependence", *Phys. Rev. B,* vol.54, pp.17954, 1996.

[20] K. Wakabayashi, "Electronic transport properties of nanographite ribbon junctions", *Phys. Rev. B,* vol.64, pp.125428, 2001.

[21] B. Obradovic,; R. Kotlyar, F. Heinz,; P. Matagne, T. Rakshit, M.D. Giles, M.A. Stettler, D.E. Nikonov, "Analysis of graphene nanoribbons as a channel material for field-effect transistors", *Appl. Phys. Lett.,* vol.88, pp.142102, 2006.

[22] L. Brey, H. A. Fertig, "Electronic states of graphene nanoribbons studied with the Dirac equation", *Phys. Rev. B,* vol.73, pp.235411, 2006.

[23] Y.W. Son, M.L. Cohen, S. G.Louie, "Energy Gaps in Graphene Nanoribbons", *Phys. Rev. Lett.,* vol.97, pp.216803, 2006.

[24] M. Ezawa, "Peculiar width dependence of the electronic properties of carbon nanoribbons", *Phys. Rev. B,* vol.73, pp.045432, 2006.

[25] C. Berger, Z. M. Song, X. B. Li, X. S. Wu, N. Brown, C. Naud, D. Mayou, T. B. Li, J. Hass, A. N. Marchenkov, E. H. Conrad, P. N. First and W. A. de Heer, "Electronic confinement and coherence in patterned epitaxial graphene", *Science,* vol.312, pp.1191-1194, 2006.

[26] M. S. Gupta, "Conductance Fluctuations in Mesoscopic Conductors at Low Temperatures", *IEEE Trans. Electron Devices,* vol.41, pp.2093-2106, 1994.

[27] R. T. F. van Schaijk, A. de Visser, S. G. Ionov, V. A. Kulbachinskii, and V. G. Kytin "Magnetotransport in carbon foils fabricated from exfoliated graphite", *Phys. Rev. B*, vol.57, pp.8900, 1998. G. Moos, C. Gahl, R. Fasel, M. Wolf, and T. Hertel, "Anisotropy of Quasiparticle Lifetimes and the Role of Disorder in Graphite from Ultrafast Time-Resolved Photoemission Spectroscopy", *Phys. Rev. Lett.,* vol.87, pp.267402, 2001. T. Kampfrath, L. Perfetti, F. Schapper, C. Frischkorn, and M. Wolf, "Strongly Coupled Optical Phonons in the Ultrafast Dynamics of the Electronic Energy and Current Relaxation in Graphite", *Phys. Rev. Lett.,* vol.95, pp.187403, 2005.

[28] N. Agrait, J. G. Rodrigo, and S. Vieira, "On the transition from tunneling regime to point-contact : graphite", *Ultramicroscopy,* vol.42, pp.177-183, 1992.

[29] O. I. Shklyarevskii, S. Speller, and H. Van Kempen, "Conductance of highly oriented pyrolytic graphite nanocontacts", *Appl. Phys. A,* vol.81, pp.1533-1538, 2005.

[30] C. Berger, et al., "Ultrathin epitaxial graphite: 2D electron gas properties and a route toward graphene-based nanoelectronics", *J. Phys. Chem. B,* vol.108, pp.19912-19916 , 2004.

[31] Victor W. Brar, et al., "Scanning tunneling spectroscopy of inhomogeneous electronic structure in monolayer and bilayer graphene on SiC", *Appl. Phys. Lett.,* vol.91, pp.122102, 2007.

[32] S. Y. Zhou, et al., "First direct observation of Dirac fermions in graphite", *Nature Phys.*, vol.2, pp.595-598, 2006.

[33] A. Bostwick, T. Ohta, T. Seyller, K. Horn, and E. Rotenberg, "Quasiparticle dynamics in graphene", *Nature Phys*., vol.3, pp.36, 2007.

[34] T. Ohta, A. Bostwick, T. Seyller, K. Horn, and E. Rotenberg, "Controlling the Electronic Structure of Bilayer Graphene", *Science,* vol.313, pp.951-954, 2006.

[35] E. V. Castro, K. S. Novoselov, S. V. Morozov, N. M. R. Peres, J.M.B. Lopes dos Santos, J. Nilsson, F. Guinea, A. K. Geim, and A. H. Castro Neto, "Biased bilayer graphene: semiconductor with a gap tunable by electric field effect", *Phys. Rev. Lett*., vol.99, pp.216802, 2007.

[36] J. B. Oostinga, H. B. Heersche, X. Liu, A. F. Morpurgo and L. M. K. Vandersypen, "Gate-induced insulating state in bilayer graphene devices", *Nat. Mater*., vol.7, pp.151-154, 2007.

[37] D. P. E. Smith, G. Binnig, and C. F. Quate, "Detection of phonons with a scanning tunneling microscope", *Appl. Phys. Lett*., vol.49, pp.1641, 1986.

[38] L. Vitali, M. A. Schneider, K. Kern, L. Wirtz, and A. Rubio, "Phonon and plasmon excitation in inelastic electron tunneling spectroscopy of graphite", *Phys. Rev. B,* vol.69, pp.121414, 2004.

[39] B. C. Stipe, M. A. Rezaei, and W. Ho, "Single-Molecule Vibrational Spectroscopy and Microscopy", *Science,* vol.280, pp.1732-1735, 1998.

[40] Y. Zhang, V. W. Brar, F. Wang, C. Girit, Y. Yayon, M. Panlasigui, A. Zettl, and M. F. Crommie, "Giant phonon-induced conductance in scanning tunneling spectroscopy of gate-tunable graphene", *Nature Physics,* vol.4, pp.627-630, 2008.

[41] G. Li, A. Luican and E. Y. Andrei, "Scanning Tunneling Spectroscopy of Graphene" arXiv:0803.4016, 2008.

[42] Y. Kopelevich, and P. Esquinazi, "Ferromagnetism and Superconductivity in Carbon-based Systems", *J. Low Temp. Phys*., vol.146, pp.629-639, 2007.

[43] J. Nygård, D. H. Cobden, and P. E. Lindelof, "Kondo physics in carbon nanotubes" *Nature,* vol. 408, 342 (2000); B. Babić, T. Kontos, and C. Schönenberger, "Kondo effect in carbon nanotubes at half filling", *Phys. Rev. B,* vol.70, pp.235419, 2004.

[44] Z. K. Tang *et al.*, "Superconductivity in 4 Angstrom Single-Walled Carbon Nanotubes", *Science,* vol.292, pp.2462-2465, 2001; I. Takesue, et al., "Superconductivity in Entirely End-Bonded Multiwalled Carbon Nanotubes", *Phys. Rev. Lett*., vol.96, pp.57001, 2006.

[45] M. Kociak, A.Yu. Kasumov, S. Guéron, B. Reulet, I. I. Khodos, Yu. B. Gorbatov, V. T. Volkov, L. Vaccarini, and H. Bouchiat, "Superconductivity in Ropes of Single-Walled Carbon Nanotubes" *Phys. Rev. Lett*., vol.86, pp.2416, 2001.

[46] R. R. da Silva, H. Torres, and Y. Kopelevich, "Indication of Superconductivity at 35 K in Graphite-Sulfur Composites", *Phys. Rev. Lett.,* vol.87, pp.147001, 2001; S. Moehlecke, Y. Kopelevich, and M. B. Maple, "Interaction between superconducting and ferromagnetic order parameters in graphite-sulfur composites", *Phys. Rev. B,* vol.69, pp.134519, 2004; T. E. Weller, M. Ellerby, S. S. Saxena, R. P. Smith, N. T. Skipper, "Superconductivity in the intercalated graphite compounds C6Yb and C6Ca", *Nat. Phys.,* vol.1, pp.39-41, 2005; N. Emery, C. Herold, M. d'Astuto, V. Garcia, C. Bellin, J. F. Mareche, P. Lagrange, and G. Loupias, "Superconductivity of Bulk CaC6 ", *Phys. Rev. Lett.,* vol.95, pp.087003, 2005.

[47] Y. Niimi, et al., "Scanning tunneling microscopy and spectroscopy of the electronic local density of states of graphite surfaces near monoatomic step edges", *Phys. Rev. B,* vol.73, pp.85421, 2006.

[48] Y. Kobayashi, K. Fukui, T. Enoki, and K. Kusakabe, "Edge state on hydrogen-terminated graphite edges investigated by scanning tunneling microscopy", *Phys. Rev. B,* vol.73, pp.125415, 2006.

[49] K. Sugawara, T. Sato, S. Souma, T. Takahashi, and H. Suematsu, " Fermi surface and edge-localized states in graphite studied by high-resolution angle-resolved photoemission spectroscopy", *Phys. Rev. B,* vol.73, pp.45124, 2006.

[50] R. Egger and A. O. Gogolin, "Effective Low-Energy Theory for Correlated Carbon Nanotubes", *Phys. Rev. Lett.,* vol.79, pp.5082, 1997.

[51] A. Yamashiro, Y. Shimoi, K. Harigaya, and K. Wakabayashi, "Spin- and charge-polarized states in nanographene ribbons with zigzag edges", *Phys. Rev. B,* vol.68, pp.193410, 2003.

[52] J. González, F. Guinea, and M. A. H. Vozmediano, "Electron-electron interactions in graphene sheets", *Phys. Rev. B,* vol.63, pp.134421, 2001.

[53] K. Sasaki, J. Jiang, R. Saito, S. Onari, and Y. Tanaka, "Theory of Superconductivity of Carbon Nanotubes and Graphene", *J. Phys. Soc. Jpn.,* vol.76, pp.033702, 2007.

[54] Y-W Son, M. L. Cohen, and S. G. Louie, "Energy Gaps in Graphene Nanoribbons", *Phys. Rev. Lett.,* vol.97, pp.216803, 2006.

[55] P. Esquinazi, et al., "Ferromagnetism in oriented graphite samples", *Phys. Rev. B,* vol.66, pp.024429, 2002.

[56] H. Suzuura, T. Ando, "Crossover from Symplectic to Orthogonal Class in a Two-Dimensional Honeycomb Lattice", *Phys. Rev. Lett.,* vol. 89, pp.266603, 2002.

[57] X. Wu, X. Li, Z. Song, C. Berger, and W.A. de Heer, "Weak anti-localization in epitaxial graphene: Evidence for Chiral Electrons", *Phys. Rev. Lett*. vol.98, pp.136801, 2007.

[58] J. M. Ziman, Principles of the Theory of Solids, 2nd ed. Cambridge University Press, Cambridge, 1972. (Chapter 7)

[59] Z. Chen, Y.-M. Lin, M. J. Rooks and Ph. Avouris, "Graphene Nanoribbon Electronics", *Physica E,* vol.40, pp.228-232, 2007. M.Y. Han, M. Y. Han, B. Özyilmaz, Y. Zhang and P. Kim, "Energy Band-Gap Engineering of Graphene Nanoribbons", *Phys. Rev. Lett.,* vol.98, pp.206805, 2007.

[60] S. V. Morozov, K. S. Novoselov, M. I. Katsnelson, F. Schedin, L. A. Ponomarenko, D. Jiang, and A. K. Geim, "Strong Suppression of Weak Localization in Graphene", *Phys. Rev. Lett.,* vol.97, pp.016801, 2006. R. V. Gorbachev, F. V. Tikhonenko, A. S. Mayorov, D. W. Horsell, and A. K. Savchenko, "Weak Localization in Bilayer Graphene", *Phys. Rev. Lett.*, vol.98, pp.176805, 2007.

[61] F. Miao, S. Wijeratne, Y. Zhang, U.C. Coskun, W. Bao, C.N. Lau, "Phase-Coherent Transport in Graphene Quantum Billiards", *Science,* vol.317, pp.1530-1533, 2007.

CHAPTER 5

ELECTRICONIC TRANSPORT PROPERTIES OF CARBON NANOWALLS USING SUPERCONDUCTING ELECTRODES

5.1 Introduction

In Chapter 4, we have discussed the electrical transport properties of CNWs measured using two normal metal electrodes. CNWs, which are regarded as 2D graphite sheet with small size, show the presence of a narrow band gap. It is well known that materials contacted with superconducting electrodes also offer interesting transport phenomena. At a superconductor-normal metal interface, normal metal is found to possess superconductivity properties as a result of proximity effect. The proximity effect arises due to the injection of the Cooper pairs from the superconductor into the normal metal. Therefore, it is also interesting to study the transport properties of CNWs between superconducting electrodes.

In this chapter, we first give a brief introduction to superconductivity related phenomena. The phenomena are related to the experimental work in superconductor/CNWs/superconductor (S/CNWs/S) junctions. Following that, we will discuss the experimental results and evaluate the transport properties of Niobium (Nb)/carbon nanowalls/Nb junctions under different temperature and magnetic field.

5.2 Superconductivity

In this section, we give a brief introduction to superconductivity related phenomena that are related to the transport measurement in this chapter. As we will

see, CNWs give a new twist to the well known processes like, for example, Proximity effect, Josephson junction, weak link and Andreev reflection. In the following discussion, we consider CNWs as a normal metal. When a normal metal is brought to contact with superconductor, the normal metal is found to possess superconductivity properties at superconductor-normal metal interface as a result of proximity effect. The proximity effect arises due to the injection of the Cooper pairs from the superconductor to normal metal. The superconducting correlation is determined by the properties of the normal metal. To enter the normal metal, there is a characteristic length L_N which is given by either the phase coherence length, L_φ of the normal metal or the thermal length, L_T, whichever is smaller. When the length of normal metal is shorter than L_N, the normal metal can acquire the properties similar to those of the superconductor such as the critical temperature, the critical current, and demonstrate Josephson effect.

In some cases, supercurrent disappears when Cooper pairs in normal metal are destroyed due to some scattering mechanism; However, Andreev reflection may be present. A quasi-electron from the normal metal, having energy of E which is smaller than superconducting energy gap Δ, can enter the superconductor as a Cooper pair. The injection of quasiparticles is often termed as Andreev reflection. In the mean time, an equivalent quasi-hole is reflected back into the normal metal. In a Superconductor/Normal metal/Superconductor (SNS) junction, multiple Andreev reflections [1,2] (MARs) may occur when the normal metal's length is greatly shorter than L_N. Successive Andreev reflections of the quasiparticles increase their energy. When the energy exceeds the superconducting gap energy, the process ceases. The details of the phenomena (such as Josephson Effect, Andreev reflection, Multiple Andreev reflection) will be introduced below.

5.2.1 Josephson Effect

This phenomenon of superconductivity can be traced back to a hundred years ago. As early as 1911, mercury was found to conduct electrical current without any resistance when cooled down to sufficiently low temperatures [3]. In 1956, the phenomenon was explained by Bardeen, Cooper, and Schrieffer (BCS) in terms of the condensation of electrons into Cooper-pairs that are described by the same quantum state.[4] This quantum state has the condensate wave function:

$$\Psi = |\Psi| e^{i\phi_s} \tag{5.1}$$

where ϕ_s is the macroscopic quantum phase and $|\Psi|$ is Cooper pair density. Six years later, Josephson predicted that the supercurrent can even flow across a thin insulating layer between two superconductors [5]. The magnitude of the Josephson supercurrent I_{sc} depends on the phase difference ϕ in the two superconductors,

$$I_{sc} = I_c \sin(\phi) \tag{5.2}$$

with I_c denoting the critical supercurrent. Similarly, the relation between the voltage V across the junction and the phase difference is given by

$$\frac{d\phi}{dt} = \frac{2e}{\hbar} V \tag{5.3}$$

This relation indicates oscillating characteristics of supercurrent at a frequency, which is determined by the bias voltage. Not only were the predictions by Josephson experimentally confirmed, [6] but also more general 'weak links' between superconductors were turned out. A weak link can be formed by either constriction or a non-superconducting material. Proximity induced supercurrents in non-superconducting materials have been observed experimentally in many systems, like metals, semiconducting nanowires [7], carbon nanotubes[8], 2DEGs and graphene [9,10].

5.2.2 Andreev Reflection

In previous paragraphs, we described supercurrent through SNS junctions. Now we consider the micro-mechanism behind Cooper pair transport into the N region: Andreev reflection. The process of Andreev reflection is schematically shown in Figure 5.1. Due to the presence of a gap in the excitation spectrum of superconductor, no electron state is available at energies $E < \Delta$ (where Δ is superconducting gap). An electron with wavevector k_e, and energy $E < \Delta$ arrives at SN interface. The wavefunction of the electron is exponentially damped on a length scale $L_{T\_clean} = \frac{\hbar v_F}{\pi \Delta}$ in superconductor. [11] Charge transport across a clean SN interface occurs by pairing of the incoming electron with another electron with opposite spin and wavenumber to form a Cooper pair. Equivalently, one can say that the electron is Andreev reflected into a hole with equal wavenumber. Similarly, the opposite Andreev reflection process also can occur: a hole impinging on the N/S boundary will be reflected as an electron.

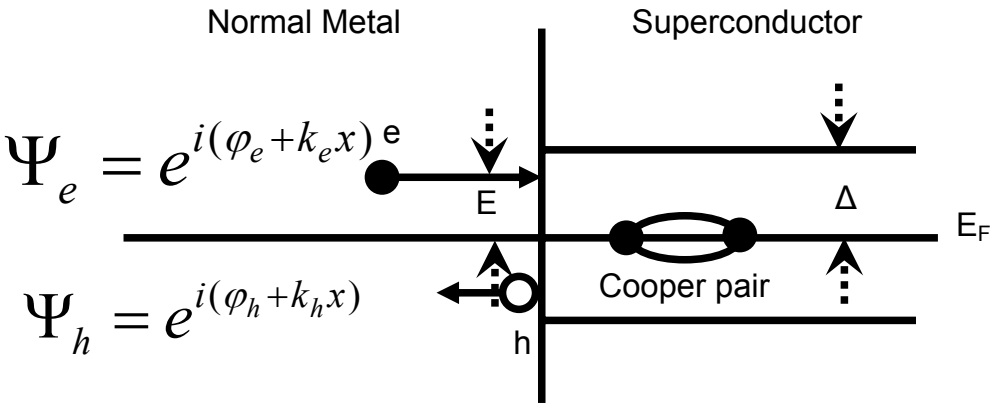

FIG. 5.1 Schematic illustration of Andreev reflection at N/S interface. An electron in the normal electrode with energy (E<Δ) pairs with another electron with opposite energy and wave vector to form a Cooper pair in the superconductor. The result is a hole (open circle) in N with opposite energy and equal wave vector reflected away from the interface. Adapted from Ref. [12].

5.2.3 Multiple Andreev Reflections

In an SNS junction, Andreev reflections leave a signature in the dissipative branch of the current-voltage characteristics. Multiple Andreev reflection (MAR) was first proposed as an explanation for subgap structures.[13] MAR between two NS interfaces could result in a subgap structure for bias voltages smaller than $2\Delta/e$. Figure 5.2 exhibits the qualitative image. When $eV > 2\Delta$ as in Figure 5.2(a), an electron (quasi-particle) moves directly from an occupied state below the gap in the left lead to an unoccupied state above the gap in the right one. At $\Delta < eV < 2\Delta$, the electron has to be retro-reflected at least once, as shown in Figure 5.2(b) and (c). In this process, an electron coming from the left lead is converted into a Cooper pair at the right NS interface. The retro-reflected hole is absorbed by hole states below the gap. At even lower bias, only higher order Andreev processes can give a contribution. In general, the contribution of n order Andreev reflection process results in an increase of the current at bias voltages exceeding $2\Delta/n$. The contribution of the process to the current is schematically indicated in Figure 5.2 (d).

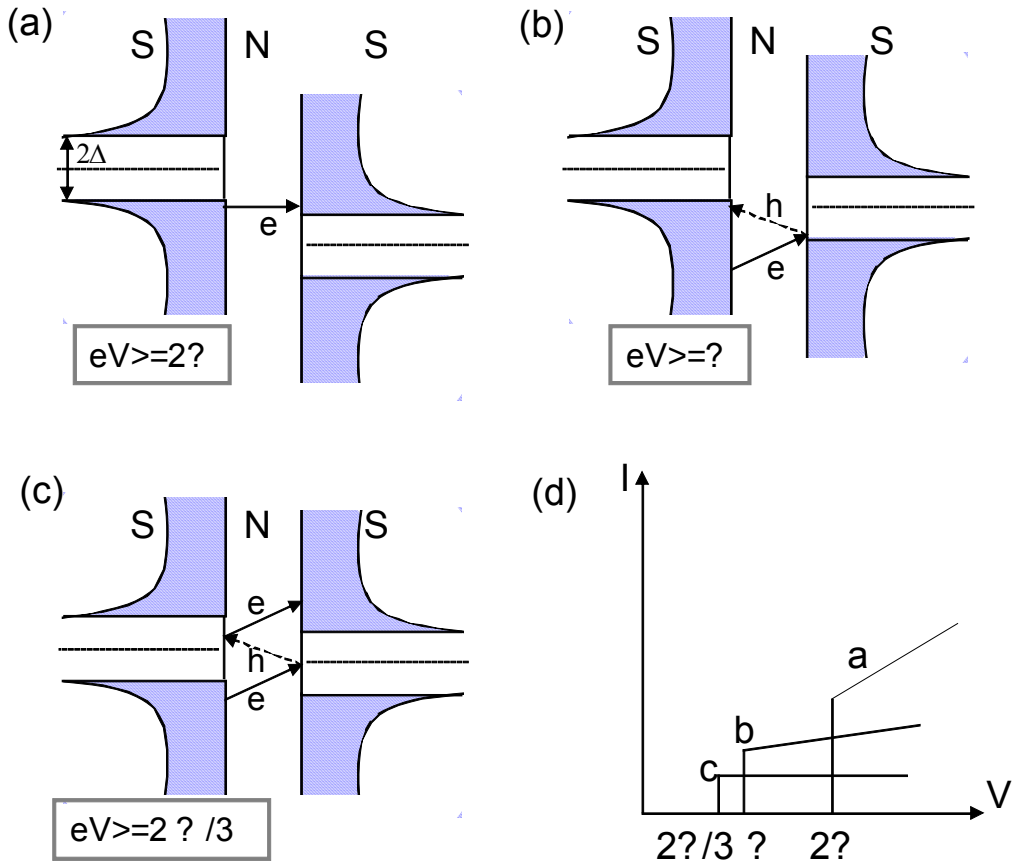

FIG. 5.2 a)-c) Schematic illustration of multiple Andreev reflection processes at different bias voltages. In d), the contribution to the current of the processes in (a-c) is indicated.

5.2.4 Possible Superconductivity in Graphitic Materials

Beside the proximity superconductivity, recent theoretical study suggested possibility of high Tc superconductivity in graphitic system, arising from electron correlation effects. [14-16] Experiment [17] also suggests that the structural disorder and the presence of light elements like hydrogen, oxygen and sulfur may trigger superconductivity in graphite. In addition, owing to the special characteristics of edge states, graphitic carbon can be modified into superconductor. [18] Recently, the

superconductivity found in carbon nanotubes [19] is believed to originate from edge states which are specific to graphene [20]. Edge states are π electron states which are localized near the edge. Edge states may alter local electronic properties and influence transport properties of graphitic materials [21]. The edge states may also drive finite 2D carbon to exhibit unique electronic properties. It is found that a peak is present for edge states which have flat energy dispersion band. The energy dispersion of edge states have been observed by STM/STS [22] and ARPES[23] near Fermi level in graphite.

CNWs are fabricated by MPECVD. As such, these nanographite sheets with a lot of disorder exhibit strong electron phonon interaction, especially at edges [24]. These features make CNWs a good platform to explore the transport properties in nanographite sheets, such as, superconductivity and other exotic ground state. Recent experiments exhibited that local electrical conductance decays quickly on graphene plane from the edges [25]. For these reasons, in our experiments, the electrodes are fabricated to contact directly with edges of nanographite sheets to probe the transport properties.

5.3 Sample Fabrication and Experimental Details

In this chapter, we discuss experiments on proximity effect on Nb/CNWs/Nb junctions. The configuration of the samples is quite similar to that of normal electrode samples described in Chapter 3. The electrode patterns were prepared on cleaned SiO_2 substrates by using standard electron beam lithography. The spacing between the electrodes varies from 200 nm to 1 μm, while the width of the contact is fixed at 1 μm. Niobium with a 100 nm thickness was deposited via sputtering and subsequently a thin

layer of titanium (3 nm) was deposited onto Nb film. After lifting off the resist, bilayer Nb/Ti electrodes were obtained. Subsequently, CNWs were deposited onto the substrates with the patterned electrodes. The details of the MPECVD conditions are described in Chapter 3 (Section 3.1.3 and 3.3.1).

The transport measurements were conducted in our liquid helium cryostat. The temperature was varied between 1.4 and 250 K by controlling the liquid helium flow. A magnetic field of up to 6 Tesla can be applied to the samples. Differential conductance measurements were conducted using the combination of Keithley 6220 current source and 2182A nanovoltmeter. All the measurements were carried out after the temperature was stabilized at each setting point. In the following sections, the experimental results will be discussed.

5.4 Temperature Dependence of Resistance in Nb/CNWs/Nb

The temperature dependence of zero bias resistance (ZBR) measured in total six samples with varying electrode spacing (187, 243, 239, 387, 429 and 702 nm) is shown in Figure 5.3. Only three of them (243, 239 and 429 nm) exhibit the superconducting proximity effect. The resistance exhibits a transition at 8 K for the 239 nm sample and at 9 K for 429 and 387 nm sample. Unlike ideal cases where the transition to the superconducting state is extremely sharp. In addition, these transition temperatures of the samples are a little lower than the critical transition temperature of bulk Nb which has a typical value of 9.3 K. Below the critical temperature, the resistance dips and eventually has a residual resistance of 0.25, 9.89 and 0.28 Ω at 1.4 K for 239, 387 and 429 nm samples, respectively. Although the presence of the

residual resistance indicates the absence of supercurrent, proximity effect is still pronounced from the decrease in resistance. It is believed that the Cooper pairs are injected from the superconducting electrodes into carbon nanowalls or electron-hole pairs are created and destroyed at the interface of Nb/CNWs. As such, the nanowalls exhibit behavior similar to that of the superconducting electrodes. The absence of supercurrent could be due to the insufficient refrigeration of temperature since proximity effect becomes the strongest at 1.4 K in our case. Shailos et al. also reported in the absence of supercurrent in their few-layer graphene sample with tungsten electrodes [26]. They suggested one possibility that Cooper pairs with finite transverse momentum will suffer dephasing due to specular reflections when they propagate through graphene.

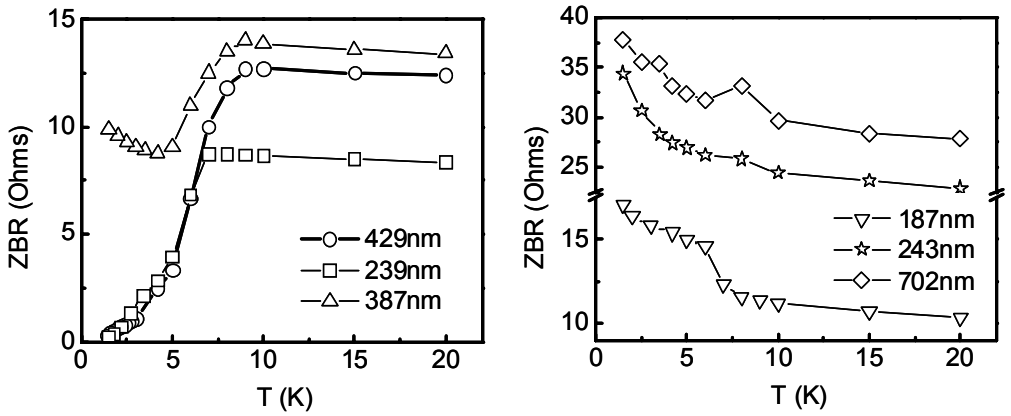

FIG. 5.3 Temperature dependence of zero bias resistance (ZBR) for samples of various electrode gaps.

While the resistances of 239 and 429 nm sample demonstrate a continuous downward trend below their critical temperatures, the resistance of the 387 nm sample turns to increase at 4.2 K. Such a trend is similar to that of a reentrance effect which involves nonequilibrium effects between the quasiparticles injected by the N reservoir

and electron pairs leaking from superconductor [27]. For other samples with electrode spacing of 187, 243 and 702nm, their resistances increase with the decrease of temperature.

5.5 Electrode Spacing Effect

According to the analysis above, the samples can be classified into 3 categories. Sample 239 and Sample 429 nm demonstrate an obvious proximity behavior below the critical temperature of electrodes, while the 387 nm sample shows a reentrance effect below 4.2 K. For samples with electrode spacing of 187, 243 and 702 nm, their resistance increases with the decrease of temperature. From the view of theoretical work, superconducting proximity effect could be observed in Josephson junctions where superconducting coherence lengths are comparable with the distance between the superconducting leads. In other words, it is more possible to observe the proximity effect in short junction samples. Based on our data, RT curves did not show very clear relationship with the electrodes spacing. The discrepancies in the R-T behavior for various junction widths indicate the complexity of the S/CNWs/S system. A possible explanation is related to the strength of finite scattering barrier at the interface between Nb and CNWs. Beside the junction spacing of devices, the transparency of Nb/CNWs interface is critical to the presence of Andreev reflection and superconducting proximity effect. The absence of proximity effect in samples (187, 243, 387 and 702nm) may be caused by the low transparency at Nb/CNWs interface.

The measurement of differential conductance/resistance is a very efficient route to investigate the transparency at Nb/CNWs interface. Hence, differential conductance/resistance data were obtained for all the samples. In the coming sections, it will be shown that two different shapes of the differential conductance versus

voltage graphs were observed at 1.4 K. In the samples (187, 243, 387 and 702nm), the differential conductance dips to a minimum at zero bias. BTK model was adopted to analyze the experimental data and to estimate the transparency of those Nb/CNWs interfaces in Section 5.6. For samples having electrode gap of 239 and 429 nm, the differential resistance was found to attain a minimum at zero bias. This is a mark of proximity induced superconductivity effect. We will discuss those two samples in Section 5.7 and onward.

5.6 Transparency at Nb/CNWs Interface

First of all, it is important to understand the physics governing the charge transfer processes at a NS interface. From these first considerations, it becomes clear that transport at an N-S boundary strongly depends on whether the applied bias voltage across the junction is smaller or bigger the superconducting gap. When the bias voltage is larger than the superconducting gap, quasiparticle transport is possible; when the bias voltage is smaller than the gap, two electrons from the normal metal have to form a Cooper pair in order to enable transport. The underlying processes are so called Andreev Reflections, where, a hole has to be reflected into normal metal in order to conserve spin and charge. The transmission probability of a single electron through the N-S interface is described as $t = \frac{1}{1+Z^2}$, where Z represents the barrier strength. In addition to the original electron, a second electron enters the superconductor and a hole is reflected back into normal region. Electrical transport through an N-S interface characterized by a certain transmission has been described quantitively by BTK theory [28]. Figure 5.4 shows the normalized differential conductance (dI/dV) for various values of Z in SNS junction. Z represents the strength of interfacial scattering, as

mentioned above. Here, we estimate the BCS superconducting gap $\Delta = 1.76 k_B T_c = 1.36\ meV$, where k_B is Boltzmann constant, critical temperature $T_c = 9\ K$. In the case of tunnel barriers (the value of Z is very high), the differential conductance directly reflects the BCS quasiparticle density of states since Andreev processes are strongly suppressed. For an increasingly transparent junction, the probability of Andreev processes increases enabling transport within the superconducting gap. In the extreme case of Z = 0, the differential conductance inside the superconducting gap is twice as big as that in normal state due to the back-reflected hole originating from Andreev process. However, in this picture of a normal superconductor junction, we have neglected any energy dependence of the barrier transmission. In mesoscopic systems, however, the wave nature of charge carriers and charging effects often lead to resonant transport, i.e., strongly energy dependent transmissions.

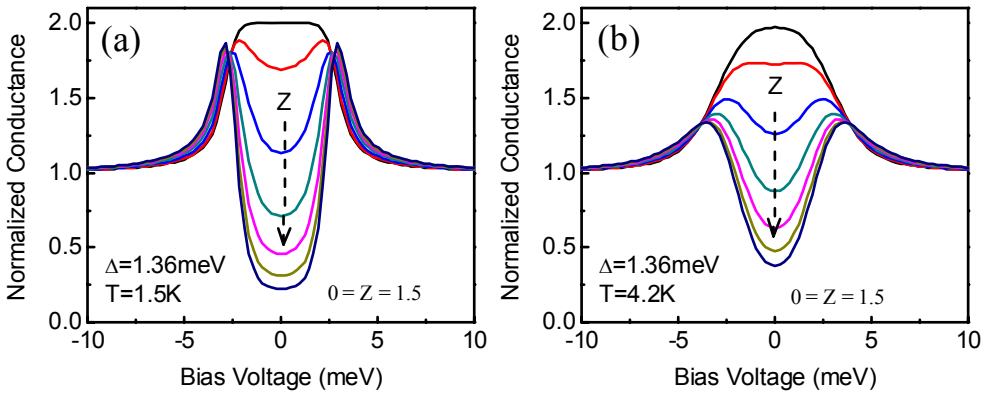

FIG. 5.4 The normalized conductance of an SNS calculated with BTK theory with various values of Z at 1.5 K (a) and at 4.2 K (b). The arrows indicated the trend with increasing Z from 0 to 1.5 with an interval of 0.25.

Our experimental dI/dV data for the four samples are plotted in Figure 5.5. It is found that dI/dV curves exhibit a platform (in sample 187 nm), a peak (in sample 387 nm within a small range of temperature) or a dip (in sample 243, 387 and 702 nm) at

the vicinity of zero bias. They follow a typical BTK behavior for finite scattering barrier at the interface despite the fact that the shapes of dI/dV curves are different for each sample with different electrode spacing. A possible reason for the difference is that CNWs are inhomogeneous in nature. As such, we attempt to compare our data with the results from BTK model, plotted in Figure 5.4. Z values can be estimated by comparing the normalized dI/dV data with BTK model at zero and high bias regime. The Z values in the four samples fall in the range from 0.55 to 0.65. The results mean that strong interfacial scattering exist at the Nb/CNWs interface and suppress the proximity induced superconductivity in these samples.

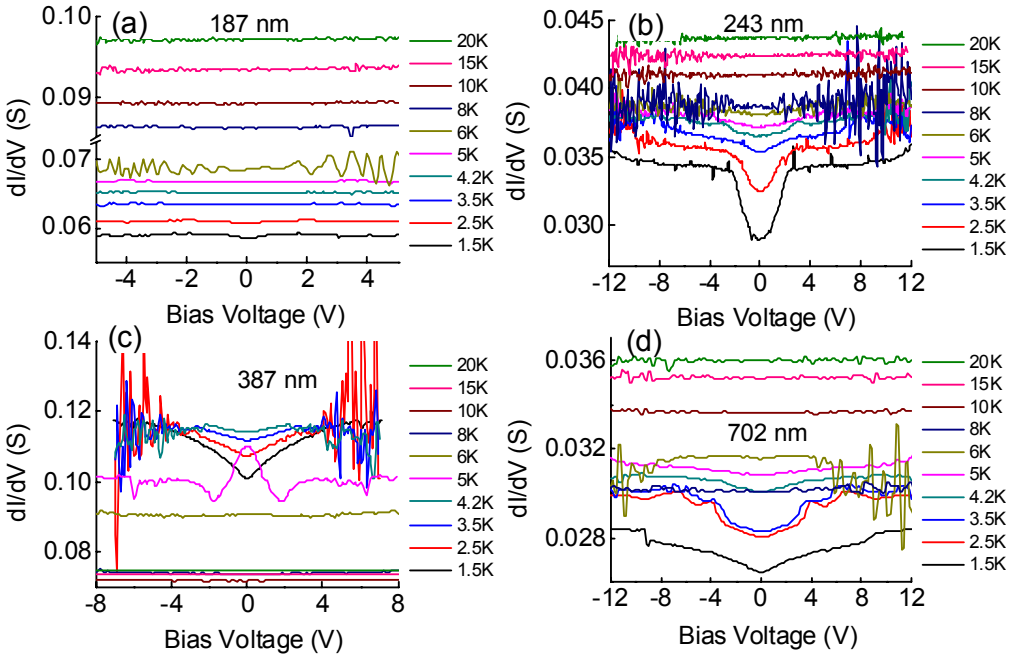

FIG. 5.5 The temperature dependence of differential conductance of (a)187 nm, (b) 243 nm, (c) 387 nm and (d) 702 nm.

5.7 Temperature-dependence of Differential Resistance/Conductance

As discussed in Section 5.4, the temperature dependence of resistance demonstrates a continuous downwards trend in the samples with electrode spacing of 239 and 429 nm when cooling down the samples. The phenomena mean that the transparency of CNWs/Nb interface is comparatively high and superconducting carriers penetrate into CNWs. The experimental results of the temperature dependence of dV/dI versus current are plotted in Figure 5.6. For both of the samples, dV/dI is found to attain a minimum at zero bias. This is another signature of proximity induced superconductivity effect.

In Figure 5.6, a few characteristic features catch our attention. 1) differential resistance indicated by a pronounced minimum at zero bias; 2) the presence of critical current marked by two high peaks, one on each side of the bias scale and 3) the presence of local maxim in differential resistance near superconducting gap region. In following parts, we will attempt to analyze all features to the best of our understanding.

5.7.1 Zero Bias Resistance (ZBR)

In our Nb/CNWs/Nb hybrid junction, it is likely that a scattering barrier exists in system due to the presence of defects and disorders. To understand the transport mechanism in our samples, it is therefore important to analyze the results from the differential resistance data. In this study, the differential resistance (dV/dI) data were obtained for temperatures ranging from 1.4 to 20 K. The graph of low temperature dV/dI versus current is presented in Figure 5.6. It is observed that a single zero-bias resistance dip evolved when cooling down. Such a phenomenon is different from the

typical BTK behavior for a normal metal-superconductor junction in ballistic transport regime. For such systems, even when Z = 0, zero-bias conductance is enhanced twice by Andreev reflection. Normally, the zero-bias conductance is reduced in the presence of infinite barrier strength. In our case, conductance in the two samples is enhanced at least 20 times than normal state. It is likely that the superconducting properties deviate from the BTK prediction.

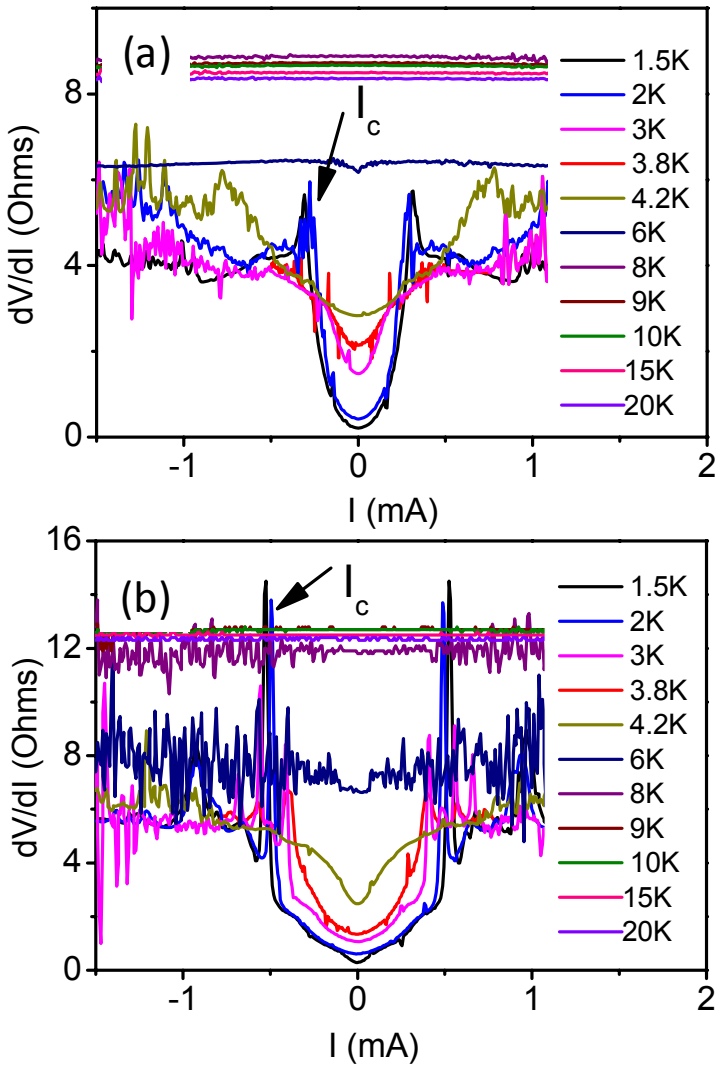

FIG. 5.6 The differential resistance vs current of the Nb/CNWs/Nb junction with a gap width of (a) 239 nm and (b) 429 nm under different temperature.

The large resistance drop of graphene in a SNS junction was observed by other groups [9,10,29,30] Such observations in our samples only persist up to the transition temperature and thus it is likely to be caused by proximity effect from superconducting electrodes. A possible explanation for the occurrence of the feature in our system is due to the presence of localized band introduced by edges and defects. The disorders will enhance density of states and result in reduction of resistance.

5.7.2 Critical Current

The existence of the critical current I_c through a SNS junction is the most striking signature of induced superconductivity. It indicates the transition between the superconducting state and the dissipative state. For 239 and 429 nm samples at 1.4 K, there are two obvious peaks, one of each side of the scale in Figure 5.6. Two obvious peaks seem to correspond to the critical current. Critical current have the value of 0.308 and 0.523 mA in the 239 and 429 nm sample respectively. All the peaks are shifted to lower current with increasing temperature and become unobservable above 3.8 K, as shown in Figure 5.6. The temperature dependence of the critical current extracted from raw data is plotted in Figure 5.7(a). The relationship seems following the behavior expected for SNS junctions in the limit of long junctions where an exponential decay of the critical current is expected.

In Figure 5.7 (a), the solid symbols illustrate a linear decrease in the critical current as the temperature is raised. As the temperature rises above 4.2 K, the critical current peaks are not observable. In order to understand the transport properties of our devices, the measured critical current is fitted with both the Josephson coupling energy in the long junction's model and the Ginzburg-Landau relationship.

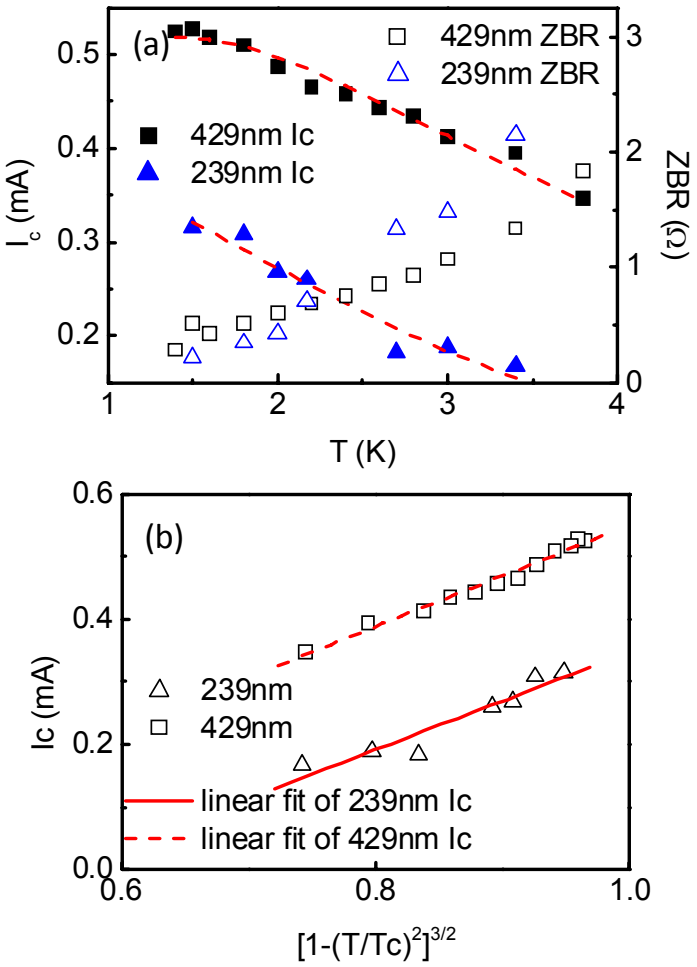

FIG. 5.7 (a) Temperature dependence of critical current, I_c, and zero bias resistance (ZBR) of the 239 and 429 nm samples. The dotted lines represent the theoretical fit from Josephson coupling energy model. (b) Temperature dependence of I_c fitted with Ginzburg Landau relationship.

To be considered as a mesoscopic diffusive SNS junction, the sample length should be much larger than the superconducting coherent length ($\xi << L$). By using the parameters from the literature [31-33], the typical momentum relaxation time, τ, equals to $1\text{x}10^{-13}$ s and the phase relaxation time, τ_φ has a value of $6.5\text{x}10^{-12}$ s for graphite sheets, the electron diffusion coefficient, D, thermal length, L_T, superconducting coherence length, ξ and mean free path, L_{mfp} can be obtained. These values are calculated based on hypothetical graphite sheets which are sandwiched

between two Nb electrodes separated by a gap of 300 nm at 1.4 K. The electronic parameters are tabulated in Table 5.1.

Table 5.1 Electronic parameters of carbon nanowalls sandwiched between Nb electrodes with an electrode gap of 300 nm at 1.4 K. Values are derived from the parameters given by van Schaijk et al.[31]. Fermi velocity, v_F, is taken to be 1x10^{6}m/s, $\hbar$ and k_B refers to the Plank constant and Boltzmann constant respectively.

Electron diffusion coefficient, D	$D = \frac{v_F^2 \tau}{2}$	0.5 m^2s^{-1}
Phase coherence length, L_φ	$L_\varphi = (D\tau_\varphi)^{\frac{1}{2}}$	567 nm
Thermal length, L_T	$L_T = (\frac{\hbar D}{2\pi k_B T})^{\frac{1}{2}}$	480 nm
Mean free path, L_{mfp}	$L_{mfp} = v_F \tau$	100nm
Superconducting coherence length, ξ	$\xi = \sqrt{\hbar D / \Delta}$	154 nm
Thouless energy, E_c	$E_C = \frac{\hbar D}{L^2}$	3.66 meV

As we know, the maximum low temperature value of the critical current in SNS junctions of normal state resistance I_c is $\pi\Delta / eR_N$ in the short junction limit ($L << \xi$ or $\Delta << E_c$) [34] and $\alpha E_c / eR_N$ in the limit of long junctions $\xi << L$ or $E_c << \Delta$ [35], here α is a numerical factor of the order of 10 and E_c is the Thouless energy $E_c = \hbar D / L^2$. It is noteworthy that Thouless energy E_c in some samples is so high that the proximity effect superconductivity would be suppressed. From the tabulated results, it is noted that the calculated superconducting coherence length (154 nm) in the sample with 300 nm junction is much smaller than our sample length of 239 and 429 nm. Therefore, both 239 and 429 nm samples belong to long Josephson

junction. The Josephson energy for a long diffusive junction, without interaction effects, can be calculated from the equation: [35, 36]

$$I_c = \frac{32}{3+2\sqrt{2}} \frac{E_c}{eR_N} \left[\frac{L}{L_T} \right]^3 \exp(-\frac{L}{L_T}) \propto T^{\frac{3}{2}} \exp(-\sqrt{\frac{T}{T_o}}) \tag{5.4}$$

where $L_T = \sqrt{\hbar D / 2\pi k_B T}$ [37] and R_N is the normal state resistance of the junction. Combining the above equations will yield an analytical formula for I_c where D is the only fitting parameter. In the limit of $\frac{\Delta}{E_c} \to \infty$ when $T \cong \frac{3E_c}{k_B}$. The above equation is simplified as follows:

$$I_c = a_1 T^{\frac{3}{2}} \exp(a_2 \sqrt{T}) \tag{5.5}$$

where a_1 and a_2 are independent parameters. Applying this equation to our experimental data, an excellent fit is obtained using Origin Software (Figure 5.7(a)). The values of a_1 and a_2 are calculated to be 8.34 ± 1.46 and -3.16 ± 0.12 respectively for the 239 nm sample while the sample of with an electrode gap of 429 nm has a a_1 value of 5.96 ± 0.25 and a_2 value of -2.49 ± 0.028. Using these values, diffusion coefficient, D and normal resistance, R_N can be determined from the following relationships with a_1 and a_2:

$$D = \left(\frac{L}{a_2} \right)^2 \frac{2\pi k_B}{\hbar} \approx \frac{L_{mfp} v_F}{2} \tag{5.6}$$

and

$$R_N = \frac{32L}{(3+2\sqrt{2})ea_1} \frac{(2\pi k_B)^{\frac{3}{2}}}{(\hbar D)^{\frac{1}{2}}} \tag{5.7}$$

The electronic parameters obtained are shown in Table 5.2.

Table 5.2 Principle characteristics of the superconducting junctions obtain with CNWs. a_1 and a_2 are the fitting parameters in SNS junction agreement with the long junction limit. D is the diffusive coefficient deduced from (5.6) and L_{mfp} is the mean free path deduced from (5.6). Fitting R_N is is the normal state resistance deduced from formula (5.7). E_c is the Thouless energy deduced from $E_c = \hbar D / L^2$.

Sample	D (m^2/s)	L_{mfp} (nm)	R_N	E_c (meV)
239 nm	0.00472	9.44	0.001126	0.0545
429 nm	0.02440	48.8	0.001240	0.0873

The mean free paths of the two samples are found to be relatively small after tabulation. This could be due to the frequent electron phonon interactions which are likely to be caused by the disorders and defects present in the carbon nanowalls. From the fitting, the normal state resistance, R_N is found to be much smaller than those obtained from the experimental data. The experimental R_N value is taken at the point just before the carbon nanowalls acquire superconductivity properties and thus resulting in the R_N to be approximately 4.05 and 5.60 Ω for the 239 and 429 nm sample respectively. The reason behind the huge discrepancies between the two values indicates that the proximity effect may not be the only reason for superconductivity. Intrinsic superconductivity may exist in CNWs. The small value of L_{mfp} is also understandable. Small value of L_{mfp} means frequent electron scattering because of the defects and disorder in CNWs.

The behavior of the critical current (I_c) as a function of the normalized temperature is also in excellent qualitative agreement with the Ginzburg-Landau critical current behavior for a homogeneous order parameter, $I_c \propto [1-(T/T_c)^2]^{3/2}$,[38] (see Figure 5.7(b)). The relationship was also observed in both samples with 239 and 429 nm spacing. This indicates that proximity effect can be associated with BCS type

related superconductivity. In fact, the phenomena such as weak Andreev reflection and Ginzburg-Landau behavior, distinguish the superconductivity of CNWs from normal superconductivity or PE superconductivity. The superconductivity in CNWs probably originates from a combination of intrinsic superconductivity and PE superconductivity. In this case, the observation of Josephson current is sensitive to the length of CNWs and the position of the Fermi energy. These may explain the low reproducibility of the results presented above in nanographite sheets based SNS structures.

Now, it is meaningful to compare the values of E_J, eV and k_BT. We find some interesting contradictions in our results. 1) If we adapt experimental R_N, the $E_J = \frac{\hbar I_c}{2e}$ value from fitting results is thousands of times than k_BT. 2) If we estimate I_c by using the experimental value of I_c (shown in Table 5.3), it is also found that the value of E_J from the fitting results is more than one thousand times larger than that of the bias eV and k_BT. Actually, superconductivity in the junction has been destroyed by the voltage bias in the experimental results. 3) The product R_NI_C at 1.4 K varies between 1.24 mV and 2.91 mV. If we deduce $\alpha E_c / e$ (0.545 meV for sample 239 nm and 0.873 meV for sample 429 nm) from the fitting result of parameter D, it is found that R_NI_C is 2 or 4 times larger than the maximum expected values $\alpha E_c / e$ for long junction limit to which all samples correspond. The interesting contradictions are difficult to be explained in the frame work of conventional proximity induced superconductivity. In particular, we have already mentioned that IV curve exhibit nonlinearities, and signs of superconductivity at a very large bias, i.e. much larger than $\alpha E_c / e$. Such nonlinearities recall characteristics observed in carbon nanotubes [39, 40]. They have not ever been observed before in SNS junctions. The unexpectedly high measured values of the critical current in CNW sheets, along with nonlinearities in the I-V

characteristics at voltages much higher than the superconducting gap of the contacts raise the question of possible intrinsic superconductivity. Similar high critical current have been observed in usual superconducting granular materials, due to the breakdown of the weak superconducting links.[41] Certainly, further experimental evidence for or against the possible superconductivity state in CNWs is necessary in the future.

Table 5.3 Principal features of the superconducting junctions obtains with CNWs. T_c is the transition temperature of the Nb/CNWs/Nb junction., I_c is the critical current of the junction and R_N is the normal state resistance. E_J is the Josephson coupling energy estimated from I_c. eV is charging energy at I_c. k_BT is the thermal energy under 1.4K.

Sample	T_c (K)	I_c (mA)	R_N (Ohm)	E_J (meV)	eV (meV)	k_BT (meV)
239 nm	8	0.308	4.05	635.48	0.465	0.13
429 nm	9	0.523	5.57	1077.26	0.985	0.13

5.7.3 Multiple Andreev Reflection

Apart from the peaks which correspond to the critical current, several small peaks are observed at higher bias in the differential resistance vs voltage graph for the two samples at 1.4 K. As shown in Figure 5.8, in the sample with 239 nm gap, differential resistance at 1.4 K exhibits small peaks at ± 2.89 mV and ± 1.53 mV in a symmetrical way. Similar peaks appear at ± 3.34 mV and ± 1.85 mV in the sample with 429 nm spacing. Peaks locations are indicated by marks P2 and P1 respectively in Figure 5.8. Symbols "+" and "-" indicate the sign of the peaks with respect to the origin. These phenomena are believed as a result of multiple Andreev reflection (MAR). This is because when the electron transport between two identical superconductors is mediated by MAR, a series of differential resistance maxima is likely to be observed within the subgap region at bias voltages $V = 2\Delta/ne$ where n = 1,2,3… The MAR peaks are less prominent than what we would expect for a long

diffusive contact on the basis of a recent numerical analysis by Cuevas et al.[42]. From the bias of MAR peaks, the superconducting gaps could be estimated. From Figure 5.8, the superconducting gap Δ is about 1.45 meV for 239 nm sample and 1.67 meV for 429 nm sample at T = 1.4 K. However, these results are higher than superconducting gap (1.23 meV for 239 nm sample (Tc = 8 K), 1.38 meV for 429 nm sample (Tc = 9 K)) by BCS theory, where $\Delta = 1.76 k_B T_c$. The experimental gap features could be attributed to the presence of a superconductor with wider superconducting energy gap, such as NbC. [43]. NbC is formed during the fabrication of device at the interface between CNWs and Nb. The process of PECVD helps to form NbC on Nb electrode during the deposition of CNWs [44] In addition, noise-like differential resistance fluctuation was observed in Figure 5.8 when the bias becomes higher than P2 in both the samples. It is then also interesting to note that the normal state resistance is not recovered above the critical current, and differential resistance shows the Andreev reflection like behavior.

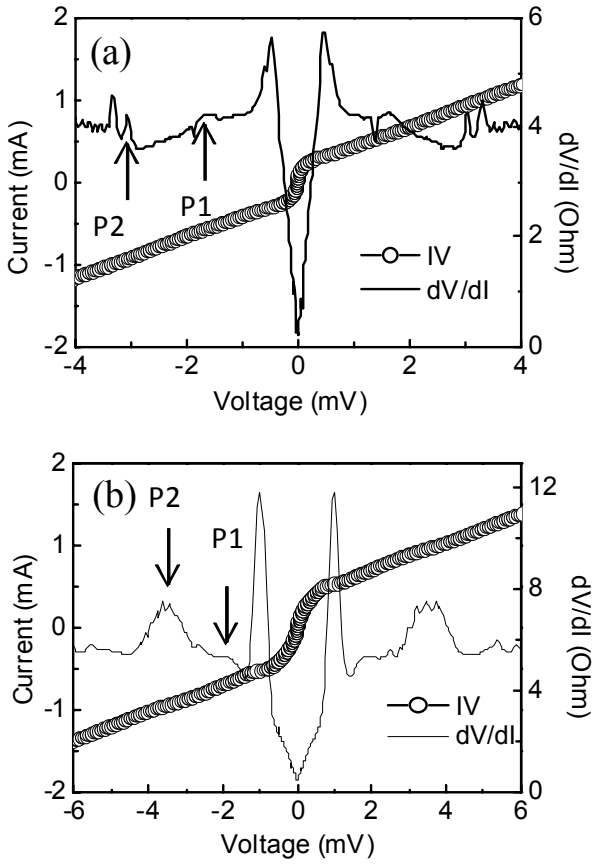

FIG. 5.8 dI/dV and IV curve as a function of bias Voltage at 1.4 K of (a) 239 nm sample and (b) 429 nm sample.

The temperature dependence of the differential resistance-voltage graphs for sample 239 nm and sample 429 nm are shown in Figure 5.9. The peaks shift to lower bias as the temperature is increased and are suppressed at 3 K and 3.8 K respectively. The temperature dependence of P2 and two times P1 in both samples and the temperature dependence of superconducting gap Δ(T) is shown in Figure 5.10. With increasing temperature, the gap decreases and finally vanished at critical temperature T_c. In the BCS theory [45], Δ(T) follows: $2\Delta(T) = 3.52 k_B T_c \sqrt{1 - T/T_c}$. Here, critical temperatures equals to 9.1 K for Nb or 12.3 K for NbC. However, it is found that the

P2 does not follow the simple BCS theory in both samples. These observations also strongly suggest the possibility of intrinsic superconducting transitions in CNWs.

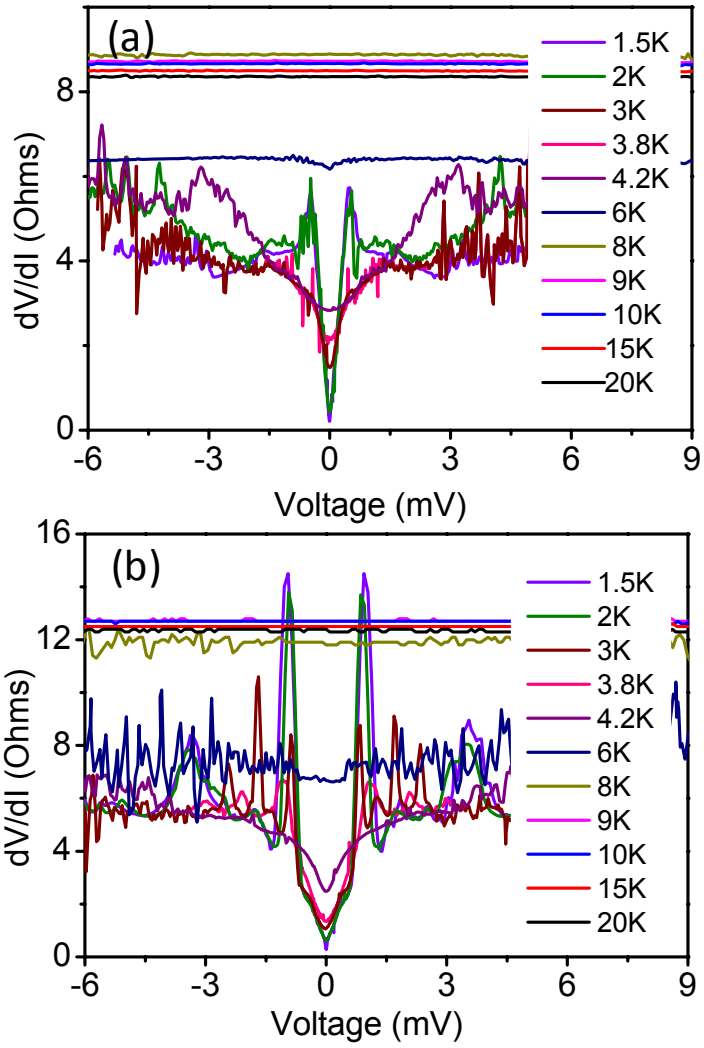

FIG. 5.9 Differential resistance versus voltage of (a) 239 nm and (b) 429 nm sample under different temperature.

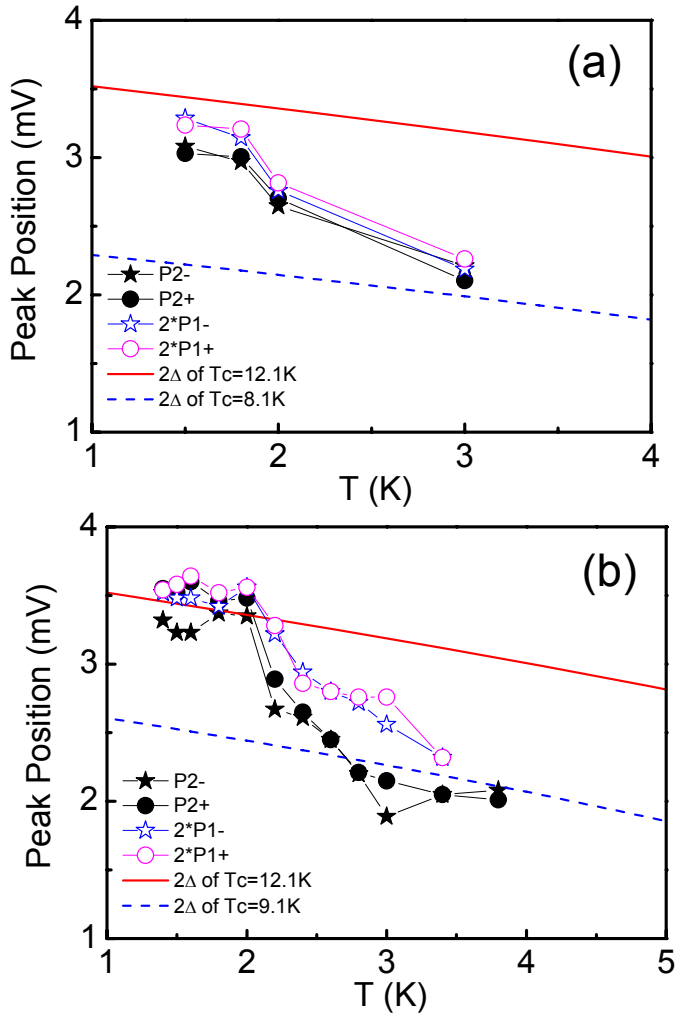

FIG. 5.10 Temperature dependence of the peaks indicated in Figure 5.8. (a) Sample 239 nm, (b) 429 nm. The solid and dashed lines display the temperature dependence of $\Delta(T)$ which corresponding to different critical temperature T_c based on the BCS theory.

In the section, the temperature dependence of the differential resistance for 239 and 429 nm samples is discussed. The magnetic field also influences the differential resistance greatly; in the coming section we are going to discuss the magnetoelectrical transport in the 239 and 429nm samples.

5.8 Magnetoelectrical Transport Properties

5.8.1 Zero Bias Resistance

The magnetic influence on zero bias resistance (ZBR) is shown in Figure 5.11. In the presence of a magnetic field which is applied in the plane of the contacts, the resistance increases with magnetic field. Considering the 239 nm sample, at lower field, ZBR is less sensitive to magnetic field, comparing to that at higher field. The critical field is taken at the point of inflection of the magnetoresistance graph and is found to be approximately 3.5 T. For the 429 nm sample, an abrupt change in zero bias resistance is observed when the magnetic field is increased to 3 T. The results indicate that the superconducting state in both of the samples can not survive in the presence of a magnetic field greater than a critical value. Above the value, magnetic fields can penetrate the samples by destroying zero electric resistivity paths. The process leads to the increase of resistance in both of the samples.

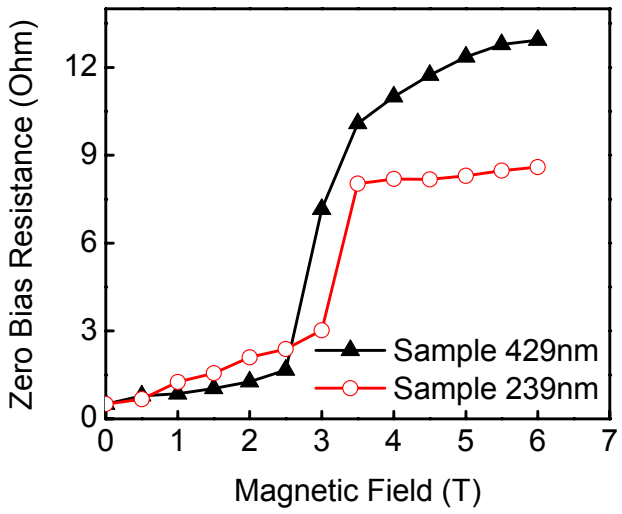

FIG. 5.11 Zero bias resistance as a function of magnetic field at 1.4 K.

5.8.2 Critical current

The magnetic influence on the differential resistance at 1.4 K is illustrated in the color plot in Figure 5.12. As shown in Figure 5.12, all dV/dI peaks shift to lower current with increasing magnetic field. In order to investigate further the superconducting properties of our devices, we plotted the dependence of I_c on magnetic field in Figure 5.13. The two relationship exhibits interesting phenomena. Similarly "+" and "-" sign the bias of the current. Firstly, the critical current exhibits an oscillatory and asymmetric pattern. Differential resistance usually displays a sharp peak at critical currents. The peak corresponds to a hysteretic feature in the dc V-I curve. The peaks are shifted to lower current when increasing magnetic field and all disappear above 2.8 T. Secondly, the magnetic field dependence is not monotonous. The critical current under the positive bias first increases up to 0.2 T where it goes through a maximum and decreases at higher field up to 2 T, and so do that under the negative bias. Such nonmonotonous behavior has been predicted in a number of models describing nonhomogenous superconductors [46, 47] and could be related to interference between different electronic trajectories along the various routes and the existence of negative Josephson coupling in CNWs.

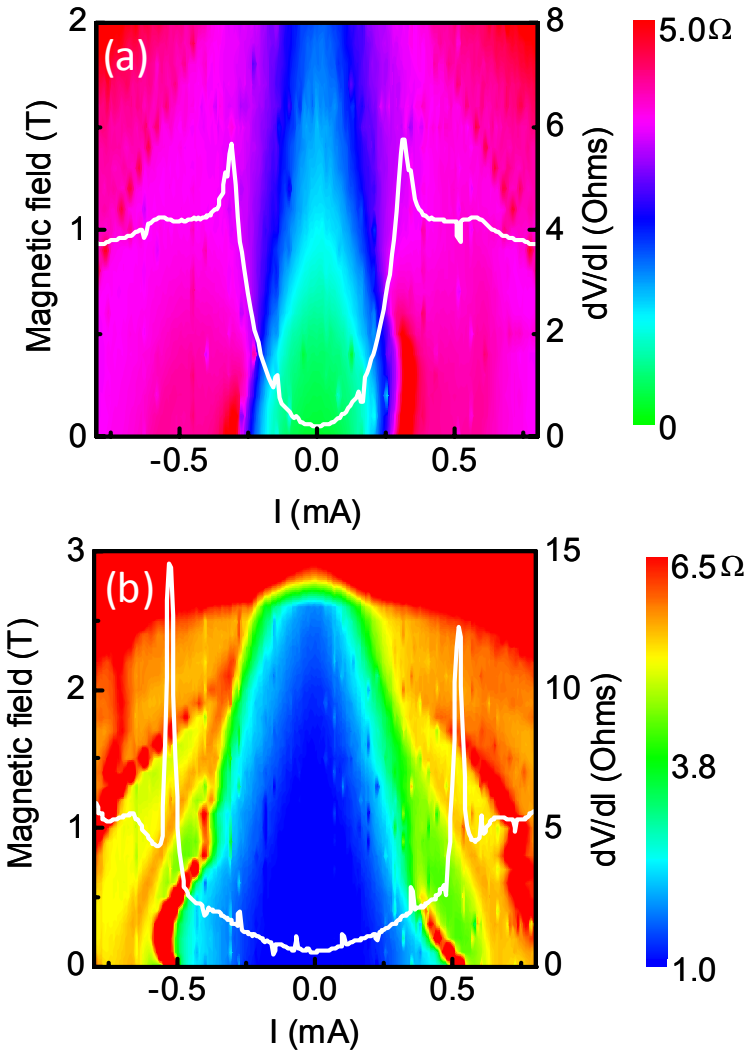

FIG. 5.12 Differential resistance as a function of current and magnetic field up to a maximum field of (a) 2 T in the sample 239 nm and (b) 3 T in the 429 nm sample.

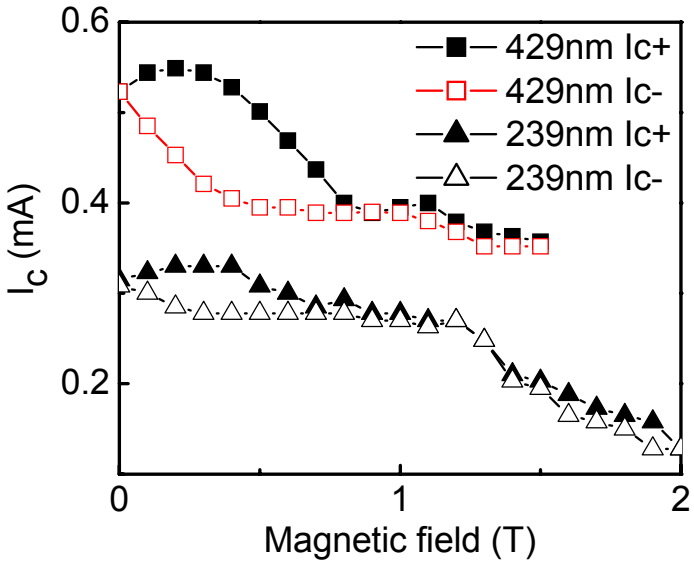

FIG. 5.13 Critical currents Ic as a function of the magnetic field under 1.4 K in sample 239nm and sample 429nm.

5.8.3 Multiple Andreev Reflection

The magnetic field dependence of dV/dI at 1.4 K is presented in Figure 5.14. In the presence of a magnetic field which is applied in the plane of the contacts, the resistance increases with increasing magnetic field. For the 239 nm sample, an abrupt change is zero bias resistance is observed when the magnetic field increased to 3.5 T. Considering the 429 nm sample, at lower field, ZBR is less sensitive to magnetic field as compared to that at higher field. The critical field is taken at the point of inflection of the magnetoresistance graph and is found to be approximately 3 T.

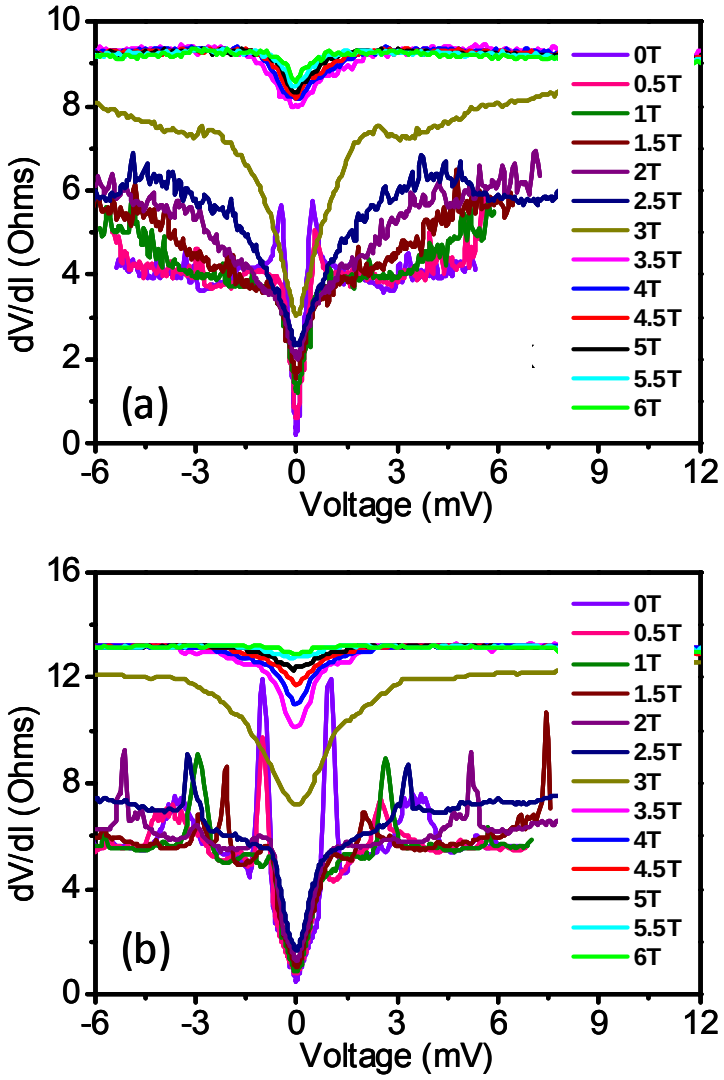

FIG. 5.14 Magnetic field dependence of differential resistance vs bias voltage of (a) 239nm and (b) 429nm samples.

Magnetic field dependence of peaks position: P1+, P1-, P1+ and P1- are shown in Figure 5.15 (a) and (b) for 239 nm and 429 nm samples, respectively. The meaning of P1 and P2 has been discussed in Figure 5.8. Similarly "+" and "-" sign the bias of the peaks. These different resistance peaks persist up to 2.5 T, while following the BCS dependence for classical superconductors. As mentioned previously, P1 position suggests the presence of a superconductor with Tc higher than Nb. That means there

are two superconducting gap existing at the interface. For quantitative comparison, we fit the two energy gaps of a superconductor as a function of magnetic field, using classical Bardeen-Cooper-Schrieffer functional: [48]

$$\Delta(H) = \Delta(0)\sqrt{1-\left(\frac{H}{H_c}\right)^2} \tag{5.8}$$

Taking $b_1 = \Delta(0)$ and $b_2 = H_c(0)$ directly from the data, the resulting curve is superimposed on the Figure 5.15 (c) and (d), in excellent agreement with data. Thus, the magnetic field dependence of these conductance dips is consistent with that of a superconductor with a relatively large energy gap.

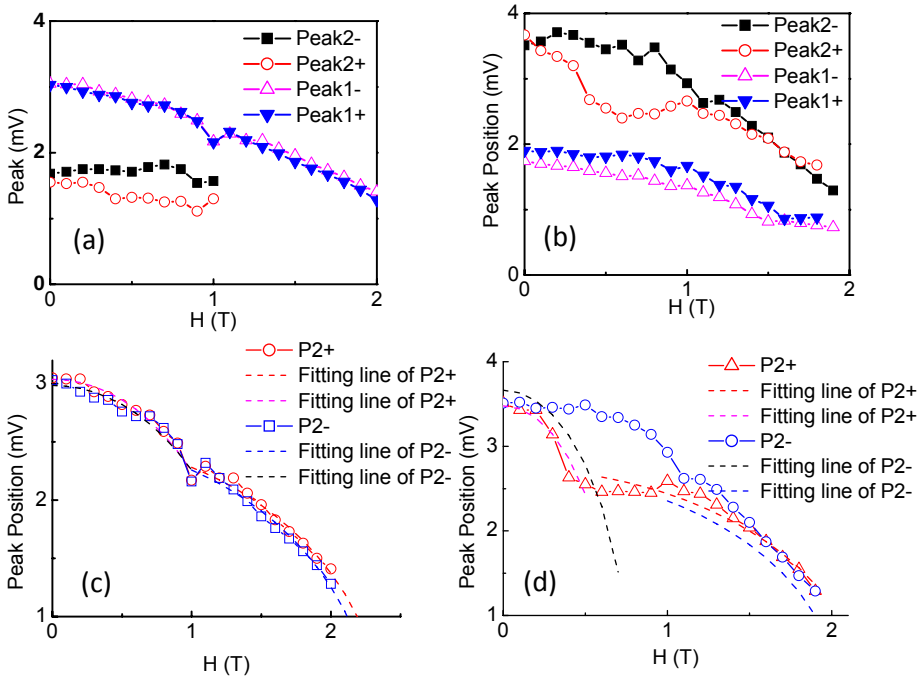

FIG. 5.15 (a) and (b) magnetic field dependence of the peaks indicated in Figure 5.14; respectively; (d) and (c) Peak positions (symbols) are fitted as a function of magnetic field, theoretical fitting curve is derived from Eqs. (5.8) with different superconducting gap in sample 239 nm and sample 429 nm.

The fitting results are tabulated in Table 5.4. From Table 5.4, it is found that there are two superconducting gaps in 239 nm sample. The width of the energy gaps

are about 3.5 meV and 2.7 meV respectively. The critical fields corresponding to the energy gaps are about 0.7 T and 2.1 T. It is also found that there are two superconducting gaps in 429 nm sample. The width of the energy gaps are about 3.01 and 2.5 meV respectively. The critical fields corresponding to the energy gaps are about 0.5 T and 2.1 T. All results are very near to the superconducting gap and critical magnetic field of NbC and Nb. It convinces us that there is NbC formation at the interface of CNWs/Nb .

Table 5.4. Principle fitting features of the superconducting junctions of CNWs. "low" and "high" means the low magnetic field and high magnetic field region.

Sample	Peak2	b_1(low)	b_1(high)	b_2 (low)	b_2 (high)
239 nm	Peak2+	3.48±0.077	2.77±0.053	0.70±0.0404	2.19±0.045
	Peak2-	3.67±0.34	2.70±0.24	0.77±0.094	2.05±0.11
429 nm	Peak2+	3.04±0.02	2.51±0.036	1.49±0.034	2.39±0.039
	Peak2-	2.98±0.026	2.50±0.37	1.53±0.049	2.31±0.034

5.9 Conclusion

In summary, we presented an electrical transport study of Nb/CNWs/Nb. Several samples with electrode gap distance that varies between 200 to 750 nm were prepared. Proximity effect was only observed for samples with electrode spacing of 239 and 429 nm. Their temperature dependence of critical current has good agree with both Josephson coupling energy of long diffusive model and Ginzburg-Landau relationship. The unexpectedly high measured values of the critical current in the two Nb/CNWs/Nb, indicates possible intrinsic superconductivity. The above gap feature and Andreev reflection were observed in the two samples. The magnetic field dependence of dV/dI was also discussed.

Unfortunately, consistent results of proximity effect in Nb/CNWs/Nb junction with respect to the electrode spacing could not be obtained. This may be due to many reasons, such as the orientation of CNWs, quality of CNW sheet, the transparency of

Nb/CNWs interface. As it is very difficult to control the growth of CNWs laterally on substrate surface, CNW sheets could not be well aligned across the gap of Nb electrodes during the PECVD process. In addition, the process nature of PECVD limits the precise control on the quality of CNW sheet and the transparency of CNWs/Nb interface. However, we attempt to analyze each feature of the results measured in all the Nb/CNWs/Nb devices to the best of our understanding. The experiments should have been more meaningful if more reliable devices could be constructed by making better defined 2D carbon. This would allow systematic study and understanding of proximity effect in 2D carbon.

Although the 2D carbons with edges and disorders have rich interesting properties, it is challenging to control the edges and defects experimentally by current technologies. From the next chapter, we start to discuss the transport properties in a well defined crystalline 2D carbon: graphene flakes made from bulk graphite.

References:

[1] A. F. Andreev, Sov. *Phys. JETP*, vol.19, pp.1228, 1964.

[2] M. Pctavio, M. Tinkham, G.E. Blonder, and T.M. Klapwijk, "Subharmonic energy-gap structure in superconducting constrictions", *Phys. Rev. B,* vol.27, pp.6739, 1983.

[3] Kamerlingh Onnes, H., Akad. van Wetenschappen (Amsterdam) vol.14, pp.818, 1911.

[4] J. Bardeen, L. N. Cooper, and J. R. Schrieffer, "Microscopic Theory of Superconductivity", *Phys. Rev.,* vol.106, pp.162-164, 1957.

[5] B. D. Josephson, *Phys. Lett.*, vol.1, pp.251, 1962.

[6] P. W. Anderson and J. M. Rowell, "Probable Observation of the Josephson Superconducting Tunneling Effect", *Phys. Rev. Lett.,* vol.10, pp.230, 1963.

[7] J. Doh, J.A.van Dam, A.L.Roest, E.P.A.M.Bakkers, L. P. Kouwenhoven, and S. De Franceschi, "Tunable Supercurrent Through Semiconductor Nanowires", *Science*, vol.309, pp.272-275, 2005.

[8] P. Jarillo-Herrero, J. A. van Dam, and L. P. Kouwenhoven, "Quantum supercurrent transistors in carbon nanotubes", *Nature*, vol. 439, pp.953-956, 2006.

[9] H. B. Heersche, P. Jarillo-Herrero, J. B. Oostinga, L. M. K. Vandersypen, and A. F. Morpurgo, "Bipolar supercurrent in graphene", *Nature*, vol.446, pp.56-59, 2007.

[10] X. Du, I. Skachko and E.Y. Andrei, "Josephson Current and Multiple Andreev Reflections in Graphene SNS Junctions", *Phys. Rev. B,* vol.77, pp.184507, 2008.

[11] M. Tinkham, Introduction to Superconductivity, McGraw-Hill, Singapore, 1996.

[12] Jochem Baselmans, Controllable Josephson Junctions, Ph.D thesis, 2002.

[13] T.M. Klapwijk, G.E. Blonder, and M. Tinkham, M., "Explanation of subharmonic energy gap structure in superconducting contacts", *Physica B,* vol.109, pp.1657, 1982.

[14] G. Baskaran, "Resonating-valence-bond contribution to superconductivity in MgB2", *Phys. Rev. B,* vol.65, pp.212505, 2002.

[15] H. Terrones, M. Terrones, E. Hernández, N. Grobert, J-C. Charlier, and P. M. Ajayan, "New Metallic Allotropes of Planar and Tubular Carbon", *Phys. Rev. Lett.*, vol.84, pp.1716, 2000.

[16]A. M. Black-Schaffer and S. Doniach, "Resonating valence bonds and mean-field d-wave superconductivity in graphite", *Phys. Rev. B,* vol.75, pp.134512, 2007.

[17] Y. Kopelevich and P. Esquinazi, "Ferromagnetism and Superconductivity in Carbon-based Systems", *J. Low Temp. Phys.*, vol.146, pp.629-639, 2007.

[18] B. Uchoa and A. H. Castro Neto, " Superconducting States of Pure and Doped Graphene", *Phys. Rev. Lett.,* vol.98, pp.146801, 2007. T. E. Weller, et al, *Nature Physics,* vol. 1 pp.39-42, 2005. A. Bostwick, et al., *Nature Phys.,* vol.3, pp.36-39, 2007.

[19] Z. K. Tang, et al., "Superconductivity in 4 Angstrom Single-Walled Carbon Nanotubes", *Science,* vol.292, pp.2462-2465, 2001 ; I. Takesue, J. Haruyama, N. Kobayashi, S. Chiashi, S. Maruyama, T. Sugai, and H. Shinohara, "Superconductivity in Entirely End-Bonded Multiwalled Carbon Nanotubes", *Phys. Rev. Lett.,* vol.96, pp.57001, 2006.

[20] K. Sasaki, J. Jiang, R. Saito, S. Onari, and Y. Tanaka, "Theory of Superconductivity of Carbon Nanotubes and Graphene", *J. Phys. Soc. Jpn.,* vol.76, pp.033702, 2007.

[21] M. Fujita, K. Wakabayashi, K. Nakada, and K. Kusakabe, "Peculiar Localized State at Zigzag Graphite Edge", *J. Phys. Soc. Jpn.,* vol.65, pp.1920, 1996. K. Nakada, M. Fujita, G. Dresselhaus and M. S. Dresselhaus "Edge state in graphene ribbons: Nanometer size effect and edge shape dependence ", *Phys. Rev. B,* vol.54, pp.17954, 1996.

[22] Y. Niimi, T. Matsui, H. Kambara, K. Tagami, M. Tsukada, and H. Fukuyama, "Scanning tunneling microscopy and spectroscopy of the electronic local density of states of graphite surfaces near monoatomic step edges", *Phys. Rev. B,* vol.73, pp.85421, 2006. Y. Kobayashi, K. Fukui, and T. Enoki, K. Kusakabe, "Edge state on hydrogen-terminated graphite edges investigated by scanning tunneling microscopy", *Phys. Rev. B,* vol.73, pp.125415, 2006.

[23] K. Sugawara, T. Sato, S. Souma, T. Takahashi, and H. Suematsu, "Fermi surface and edge-localized states in graphite studied by high-resolution angle-resolved photoemission spectroscopy", *Phys. Rev. B,* vol.73, pp.45124, 2006.

[24] Z. H. Ni, Fan H. M., Feng Y. P., Shen Z. X. Shen, Yang B. J. and Wu Y. H., "Raman spectroscopic investigation of carbon nanowalls" *J. Chem. Phys.,* vol.124, pp.204703, 2006. S. Kurita, A. Yoshimura, H. Kawamoto, T. Uchida, K. Kojima, M. Tachibana, P. Molina-Morales and H. Nakai, "Raman spectra of carbon nanowalls grown by plasma-enhanced chemical vapor deposition", *J. Appl. Phys.,* vol.97, pp.104320, 2005.

[25] S. Banerjee, M. Sardar, N. Gayathri, A. K. Tyagi, and B. Raj, "Enhanced conductivity in graphene layers and at their edges", *Appl. Phys. Lett.,* vol.88, pp.062111, 2006.

[26] A. Shailos, W. Nativel, A. Kasumov, C. Collet, M. Ferrier, S. Gueron, R. Deblock, H.Bouchiat, "Proximity effect and multiple Andreev reflections in few-layer graphene", *Europhys. Lett.,* vol.79, pp.57008, 2007.

[27] P. Charlat, H.Courtois, Ph. Gandit, D.Mailly, A.F.Volkov, and B.Pannetier, "Reentrance of the Metallic Conductance in a Mesoscopic Proximity Superconductor", *Phys. Rev. Lett.,* vol.77, pp.4950, 1996.

[28] G. E. Blonder, M. Tinkham and T.M. Klapwijk , "Transition from metallic to tunneling regimes in superconducting microconstrictions: Excess current, charge imbalance, and supercurrent conversion", *Phys. Rev. B,* vol. 25, pp.4515, 1996.

[29] A.Shailos, W. Nativel, A. Kasumov, C.Collet, M.Ferrier, S.Gueron, R.Deblock, H.Bouchiat, *Europhys. Lett.,* vol. 79, pp.57008, 2007.

[30] T. Sato, et al., "Gate-controlled superconducting proximity effect in ultrathin graphite films", *Physica E: Low-dimensional Systems and Nanostructures*, vol.40, pp.1495-1497, 2008.

[31] R. T. F. van Schaijk, A. de Visser, S. G. Ionov, V. A. Kulbachinskii, V. G. Kytin, "Magnetotransport in carbon foils fabricated from exfoliated graphite", *Phys. Rev. B,* vol.57, pp.8900, 1998.

[32] G. Moos, C. Gahl, R. Fasel, M. Wolf, T. Hertel, "Anisotropy of Quasiparticle Lifetimes and the Role of Disorder in Graphite from Ultrafast Time-Resolved Photoemission Spectroscopy", *Phys. Rev. Lett.,* vol.87, pp.267402, 2001.

[33] T. Kampfrath, L. Perfetti, F. Schapper, C. Frischkorn, M. Wolf, " Strongly Coupled Optical Phonons in the Ultrafast Dynamics of the Electronic Energy and Current Relaxation in Graphite", *Phys. Rev. Lett.,* vol.95, pp.187403, 2005.

[34] K. Likharev, "Superconducting weak links", *Rev. Mod. Phys.,* vol.51, pp.101, 1979.

[35] P. Dubos, et al., "Josephson critical current in a long mesoscopic S-N-S junction", *Phys. Rev. B,* vol.63, pp.064502, 2001.

[36] A. D. Zaikin and G. F. Zharkov, *Sov. J. Low Temp. Phys.,* vol.7, pp.184, 1981. F.K. Wilhelm, A.D.Zaikin and G. Schön, *J. Low Temp. Phys.,* vol.106, pp.305, 1996.

T. Tsuneta, L. Lechner, and P.J. Hakonen, "Gate-Controlled Superconductivity in a Diffusive Multiwalled Carbon Nanotube", *Phys. Rev. Lett.,* vol.98, pp.087002, 2007.

[37] H. Grabert, G.L. Ingold, B. Paul, *Europhys. Lett.,* vol.44, pp.360, 1998.

[38] M. Tinkam, Introduction to Superconductivity, McGraw-Hill, New York, 1996.

[39] A. Yu. Kasumov, R. Deblock, M. Kociak, B. Reulet, H. Bouchiat, I. I. Khodos, Yu. B. Gorbatov, V. T. Volkov, C. Journet, and M. Burghard, "Supercurrents Through Single-Walled Carbon Nanotubes", *Science,* vol.284, pp.1508-1511, 1999.

[40] A. Kasumov, M. Kociak, M. Ferrier, R. Deblock, S. Guéron, B. Reulet, I. Khodos, O. Stéphan, and H. Bouchiat, "Quantum transport through carbon nanotubes: Proximity-induced and intrinsic superconductivity", *Phys. Rev. B,* vol.68, pp.214521, 2003.

[41] L. Ji, M. S. Rzchowski, N. Anand, and M. Tinkham, "Magnetic-field-dependent surface resistance and two-level critical-state model for granular superconductors", *Phys. Rev. B,* vol.47, pp.470, 1993.

[42] J. C. Cuevas, J. Hammer, J. Kopu, J. K. Viljas, and M. Eschrig, "Proximity effect and multiple Andreev reflections in diffusive superconductor–normal-metal–superconductor junctions", *Phys. Rev. B,* vol. 73, pp.184505, 2006.

[43] A. L. Giorgi, E. G. Szklarz, E. K. Storms, Allen L. Bowman, and B. T. Matthias, "Effect of Composition on the Superconducting Transition Temperature of Tantalum Carbide and Niobium Carbide", *Phys. Rev*., vol.125, pp.837-838, 1962.

[44] D. Li, W. F. Li, S. Ma, and Z. D. Zhang, "Electronic transport properties of NbC(C)-C nanocomposites", *Phys. Rev. B,* vol.73, pp.193402, 2006.

[45] J. Bardeen, L. N. Cooper, and J. R. Schrieffer, "Theory of Superconductivity", *Phys. Rev.,* vol. 108, pp.1175 – 1204, 1957.

[46] F. Sharifi, A.V. Herzog, R.C. Dynes, "Crossover from two to one dimension in in situ grown wires of Pb", *Phys. Rev. Lett.,* vol. 71, pp.428, 1993.

[47] P. Xiong, A.V. Herzog, and R.C. Dynes, "Negative Magnetoresistance in Homogeneous Amorphous Superconducting Pb Wires", *Phys. Rev. Lett.,* vol.78, pp.927, 1997.

[48] D.H. Douglass, "Magnetic Field Dependence of the Superconducting Energy Gap", *Phys. Rev. Lett.,* vol.6, pp.346, 1961.

CHAPTER 6

ELECTRONIC TRANSPORT IN GRAPHENE AND ITS FEW LAYERS ON SILICON DIOXIDE SUBSTRATES

6.1 Introduction

In Chapter 4 and 5, electrical properties are characterized in CNWs. The uncertainty of structure in CNWs makes it difficult to clarify the exact causes of the corresponding properties. According to current deposition technologies, it is difficult for us to precisely control the disorder and edges in CNWs. As such, the research through top-down approach can be more substantive in graphene. Further investigation in graphene may be meaningful. The basic strategy is to isolate the influence of each factor by deliberately magnifying the corresponding factor to dominate all others. Compare to vertically aligned CNWs, graphene sheets are laid on SiO_2 substrate. The interaction between graphene and substrate may influence the electric properties of graphene.

In this chapter, we first discuss the electric characterization of graphene device on SiO_2 substrate with different number of layer under ambient condition. By examining carrier mobility, minimal conductivity and conductance hysteresis in graphene devices, it is found that substrate interface and the surface impurity may greatly affect the transport properties of graphene on SiO_2 substrate. Following that, transport properties of those devices at low temperature will be discussed. Our experimental results indicate that magneto transport and conductance fluctuation in graphene devices are greatly affected by the charged impurities existing at the substrate/graphene surface.

6.2 Electrical Field Effect in Graphene and its Multilayers

6.2.1 Electrical Field Effect

In this section, the electrical field effect in graphene devices is studied. The fabrication of our graphene FETs began with mechanically exfoliated graphene from the same parental graphite crystal (ZYA HOPG from SPI). The micro-fabrication and measurement procedures are detailed in Chapter 2 (Section 2.6, 2.9). The electrical transport properties of the devices were measured by using a HP 4156A semiconductor parameter analyzer under ambient condition. Note that all the samples examined in Section 6.2 were fabricated and measured together.

Figure 6.1 shows an example of our typical graphene devices. This is a trilayer graphene sample (s1p4) with several current and voltage probes. The width of the all graphene regions in Figure 6.1(a) is about 5 μm. The standard four probe measurements involve driving current I_{14} through contact 1-4 and measuring the induced voltage drop V_{36} between contact 3 and 6. Graphene's conductivity is then given by four probe conductance $G_{I14V36}= I_{14}/ V_{36}$ multiplied by the device's aspect ratio of squares between the voltage probes. The black curve in Figure 6.1(a) plots the experimentally measured four probe conductance as a function of applied gate voltage. The conductance exhibits the behavior typical for graphene with the minimum indicating charge neutrality point (NP) at -19 V. The minimum conductivity is $1.87\frac{4e^2}{h}$. Two probe characterizations were performed by measuring the potential drop V_{36} between two invasive contacts 3 and 6 by driving current I_{36} through contact 3-6, and hence contact effects are not excluded from the device resistance. The two-probe conductance as a function of applied voltage is plotted as the black curve in Figure 6.1(a). Similarly, two and four probe sheet resistances of the graphene are

plotted in Figure 6.1(b). Nevertheless, by comparing the two and four probe resistances, it is observed that the contact resistance exhibits a weak dependence on gate bias voltage. The contact varies from about 260 Ω near the NP to about 310 Ω near $V_g = 40\,V$. The contacts impart about 15% contribution to the two probe resistance of the device.

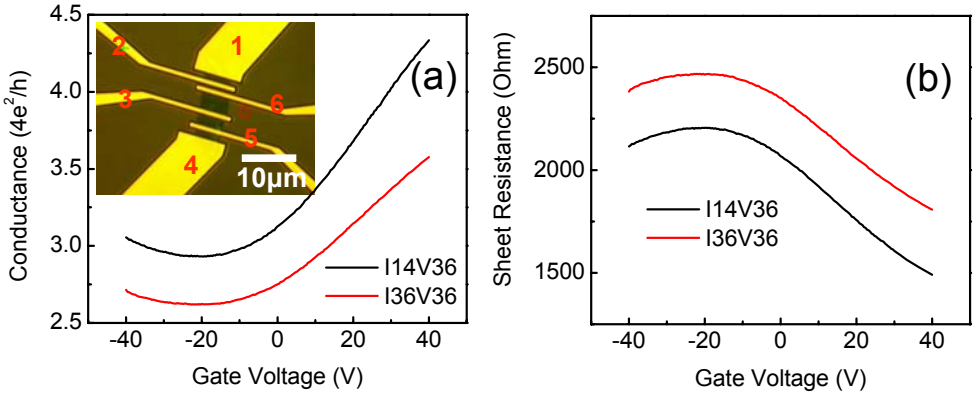

FIG. 6.1 Electrical characterization of a trilayer graphene device. (a) Conductance as a function of backgate voltage; Two- (red line) and four probe (black line) conductance at room temperature. The inset is optical images of the corresponding devices. Contact numbers are used in the main text to explain different geometries; (b) resistance versus gate voltage.

As most of our devices are not measured in a standard Hall bar configuration, we are unable to measure directly the mobility μ; however, we may estimate the field effect mobility (μ_{FE}) of the devices from the induced charge via the back gate. Starting from the definition of $\sigma_{2D} = e\mu_{FE} n_{2D}$, where e is the electronic charge, σ_{2D} is a 2D conductivity and n_{2D} is the 2D carrier density. The conductivity (σ_{2D}) and the conductance (G) of the device are related by $\sigma_{2D} = G\frac{L}{W}$, where L and W are the length and the width of the device, respectively. As σ_{2D} exhibit a nonlinear relationship with n_{2D}, we define the field effect mobility as $\mu_{FE} = \frac{1}{e}\frac{d(\sigma_{2D})}{d(n_{2D})}$, where

$d(\sigma_{2D})$ and $d(n_{2D})$ denote the change in σ_{2D} and n_{2D} due to ramping of the back gate voltage V_g, respectively. Note that $n_{2D} = \frac{C_g|V_g - V_{np}|}{e}$, where V_{np} is the NP of graphene, V_g is the gate voltage, C_g is capacitance per unit area for the capacitor formed by the 300 nm SiO_2 layer, between graphene and the back gate (degenerated Si), and it is given by $C_g = \frac{\varepsilon\varepsilon_0}{t_{ox}} = \frac{8.85\times10^{-14}\times3.9}{3\times10^{-7}} = 1.14\times10^{4}(F/m^2)$, where ε is the dielectric constant of SiO_2 (3.9) and ε_0 is the permittivity of free space. Finally, we have $\mu_{FE} = \frac{1}{C_g}\left|\frac{d(\sigma_{2D})}{d(V_g)}\right|$. Away from NP where the value of μ_{FE} becomes constant, the field effect mobility μ_{FE} should be close to the mobility μ.

Because of the limitation of dimension of some graphene flakes, only two electrodes could be applied onto the samples. We had to carry out the two probe measurement on these samples. The experimentally measured conductance (G') consists of two parts, one is the actual conductance of the graphene device (G) while the other contribution by the contact resistance (R_c). Therefore, we have $G' = \left(\frac{1}{G} + R_c\right)^{-1} = \left(\frac{L/W}{C_g|V_g - V_{np}|\mu_{FE}} + R_c\right)^{-1}$. By adopting the simple model, we are able to estimate the device mobility μ_{FE}, and contact resistance R_c. V_{np} is equivalent to the value of the gate voltage where minimum conductivity of the graphene lies. The gate voltage V_g, which is manually controlled in the experiment, is the independent variable while the conductance G', which can be experimentally measured, is the dependent variable. By fitting the data in the region away from the NP

with the help of Origin software, we can obtain the contact resistance, mobility and conductivity of graphene device.

To verify the validity of the model introduced above, the device shown in Figure 6.1 is used as an example. From Figure 6.1(a), we deduce $\mu_{FE}= 480\, cm^2/V\cdot s$ from the four probe conductance (I14V36). The contact varies from about 260 Ω near the NP to about 310 Ω near $V_g = 40\, V$. By using the model introduced above to fit the two probe conductance data (I36V36) away from NP, we can deduce $\mu_{FE}= 461\, cm^2/V\cdot s$ and $R_c = 331\,\Omega$. The mobility μ_{FE} and the contact resistance R_c deduced from the two probe conductance give a good agreement with the direct results of four probe measurement. Therefore, the simple model is valid for the approximate calculation of the essential parameters, such as mobility, conductivity and minimum conductivity, in graphene devices using the two probe configuration.

6.2.2 Carrier Mobility

We performed a statistical analysis over all the samples measured in order to examine carrier mobility. 57 samples in total are examined, where the quantities of monolayer to 6-layer graphene are 13, 10, 11, 8, 7 and 8, respectively. The relationship between mobility and the number of layer of graphene flakes was summarized in Figure 6.2. In this figure, three characteristic features draw our attention: 1) The mean value of mobility for graphene increases from 1000 $cm^2\cdot V^{-1}s^{-1}$ for bilayer graphene to about 3200 $cm^2\cdot V^{-1}s^{-1}$ for six layer graphene; 2) when the number of layer is decreased from bilayer graphene (BLG) to single layer graphene (SLG), the mobility increases drastically from 1000 $cm^2\cdot V^{-1}s^{-1}$ for BLG about 1800 $cm^2\cdot V^{-1}s^{-1}$ for SLG; and 3) the variation of mobility in SLG is much larger than few layer graphene (FLG).

In following sections, we will attempt to analyze all features to the best of our understanding.

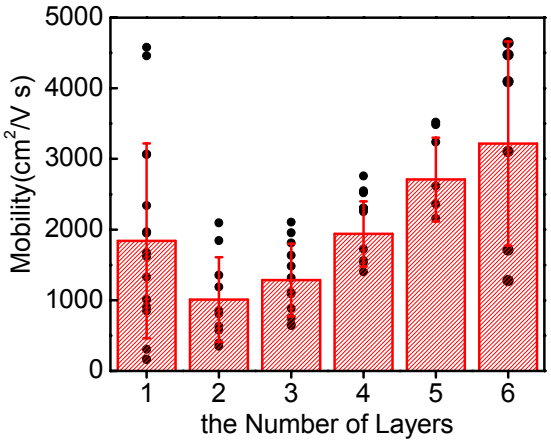

FIG. 6.2 Mean mobility as a function of the number of layers before deposition of SiO_2. The column represents the mean value of the mobility of graphene sample. The error bar represents the standard deviation of all the raw data. Solid circles represent the raw data of mobility.

It has been reported that the conductivity of graphene is limited by charged impurity scattering under graphene. [1] The screening length in multilayer graphene films is reported, theoretically, to be 0.5 nm [2] and 0.7 nm [3], and experimentally to be 1.2 nm [4]. Therefore, inner-layers receive less influence from the charged impurity or other extrinsic scattering center than the surface layer. Hence, when the layer number increases from the bi- to six layer graphene, the mobility is less suppressed in thicker graphene.

When the number of layers decreases from the BLG to SLG, energy dispersion changes from a quadric relationship in BLG to a linear relationship in SLG. In addition, the current modulation may be enhanced due to the reduction of the interlayer scattering. Therefore, the mobility in SLG increases drastically. On the other hand, because of the screening effect, the charges induced by the gate voltage are mainly

located within two or three layers considering the intergraphene layer distance of 0.335 nm. Due to the screening effect reduction, electric transport of SLG should be most sensitive to scattering centers such as charged impurities. It is concluded that the large mobility variation for SLG is caused by variations in charged impurities density.

6.2.3 Minimal Conductivity

Beside the carrier mobility, the minimal conductivity of all samples near NP also attracted our interest. The relationship between the minimum conductivity per layer and flake thickness is shown in Figure 6.3(a). The dotted lines serve as a guide for the eyes. Although the conductivity fluctuates in a large range, it is interesting to note that the average conductivity for SLG approaches $\frac{4e^2}{\pi h}$, which is close to that of SLG at low temperature.[1, 5] However, the average conductivity of BLG and FLG per layer starts to deviate from this value; it is about $0.6\times\frac{4e^2}{h}$ for BLG, $0.8\times\frac{4e^2}{h}$ for three layer stack and saturates at $\frac{4e^2}{h}$ for thicker layers. The above results suggest that the electrical conduction of thinner graphene sheets is limited by the substrate. This can be better understood from the results shown in Figure 6.3 (b) for samples covered by SiO_2 capping layers, which were deposited by electronic beam evaporation.

To examine the variation of the minimum conductivity with the number of layer more easily, we compare the two sets of data before and after deposition of SiO_2 capping layer side by side, in Figure 6.3 (c). It is noticed that the starting point of saturation in conductivity shifts from n = 3 to 4, where n is the number of layers. The phenomenon indicates that the interface between graphene and SiO_2 capping layer causes carrier scattering in graphene. It is also observed that the decrease in

conductivity for 5 layer graphene is quite large. The exact reason is not clear so far. One possible explanation is that the SiO_2 capping layer not only causes the carrier scattering, but also alternates the electronic structure in 5 layer graphene. Moreover, it is found that the in-plane conductivity per layer in BLG is reduced to $0.33\times\frac{4e^2}{h}$ after deposition of SiO_2 capping layer, while that of monolayer decreases slightly to $0.27\times\frac{4e^2}{h}$. The large decrease of conductivity for BLG can also be accounted for the carrier scattering by the influences from SiO_2 capping layer. Although our experiments were performed at room temperature, it is still meaningful to compare the minimum conductivity values obtained in this work with those predicted by theory because the minimum conductivity of bilayer graphene exhibits a weak temperature-dependence from 4 to 300 K. [6]

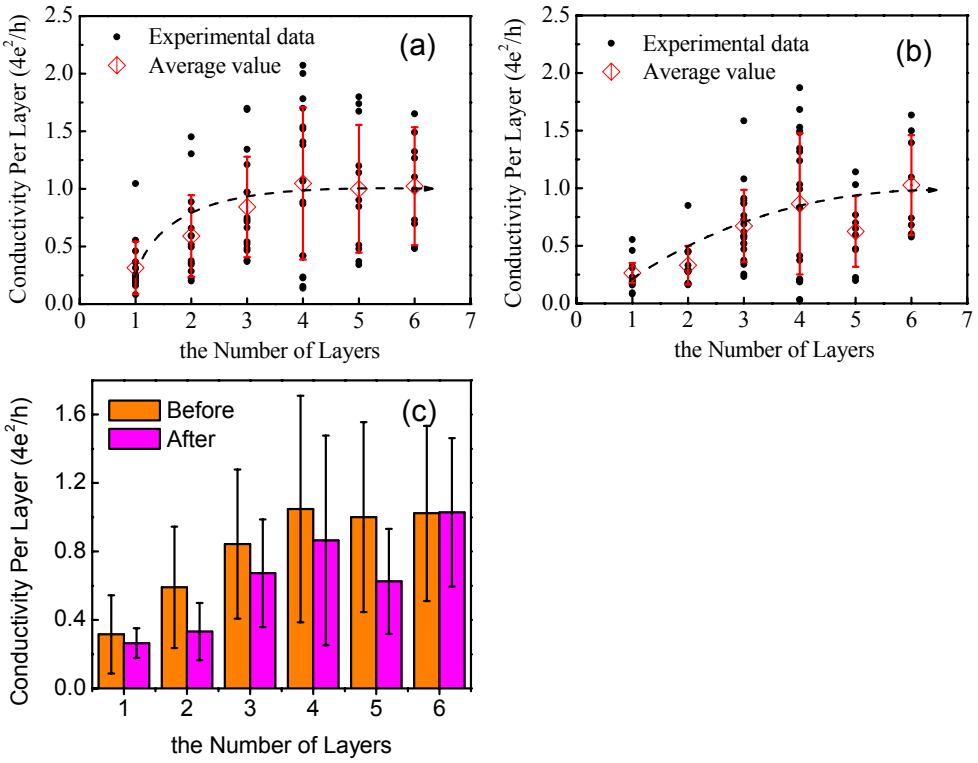

FIG. 6.3 Mean minimum conductivity per layer as a function of the number of layers before a) and after b) deposition of SiO_2. The error bar represents the standard

deviation of all the raw data. The dashed lines are guide for eyes; c) column diagram for comparison of data before and after the deposition of SiO_2.

So far, several different values have been predicted theoretically for the minimum conductivity per layer for BLG. Using self-consistent Born approximation, Koshino and Ando[7] found a minimum conductivity of $4e^2/\pi h$ and $12e^2/\pi h$ in the strong and weak-disorder regimes, respectively. Katsnelson [8] obtained a different value $2e^2/h$ using the Landauer approach. Cserti *et al.* [9] found that trigonal warping plays an important role in determining the minimum conductivity: they obtained a value of $4e^2/\pi h$ without taking into account the trigonal warping and a much larger value $12e^2/\pi h$ when it is included. In the case of FLG, Nakamura and Hirasawa [10] shows that average minimum conductivity per layer is $4e^2/\pi h$. The large scatter of theoretical values shows that the issue of minimum conductivity for BLG and FLG still remains open. However, our experimental data illustrate clearly that the influence from the substrate should be more prominent in thinner graphene than in thicker one.

In summary, we have investigated the mobility, the minimal conductivity of SLG, BLG and FLGs. The experimental data obtained indicate clearly that the transport properties in graphene are greatly affected by the interface of graphene/subtrates (such as phonon in SiO_2 or charged impurities trapped in SiO_2). The influence is greater in thin flakes than thicker ones. In the coming section, we are going to examine the charge density trapped in SiO_2 by sweeping gate bias.

6.3 Hysteresis in Graphene Devices

Graphene devices exhibit ambipolar behavior, in spite of an unexpectedly high conductivity minimum.[11] This observation was recently explained by the formation of electron hole puddles at the Dirac point. [12] The puddles are believed to arise from

charged impurity centers [1,13,14] or graphene ripples [15]. In addition to the low density of states, the large surface-to-volume ratio in graphene makes it very easy to adsorb a lot of adsorbates. Recent TEM experiment exhibits clearly that many molecules, atoms, or other adsorbates land on the surface on graphene. [16, 17] In these ways, the environment has a direct impact on the physical properties of graphene. Sticking and bonding of atoms and molecules may change by orders of magnitude as well as the transport properties across and parallel to the interface. Although the influence from the surroundings has been taken into account in different ways in the literature [18, 19], the hysteresis of the transport properties in graphene has yet to be explored. Therefore, it is worth understanding the origins of hysteresis.

Here, we present the first investigation of the conductance via sweeping gate bias by forward and backward scans in graphene. Hysteresis of conductance was observed. The action of hysteresis is attributed to charge trapping from/to graphene or capacitive gating effect. All graphene sheets were produced from the same parent natural graphite. The electrical transport properties of the devices are measured at a low driving current (100 nA) by using low-frequency lock-in technique. The details of the fabrication and measurement were introduced in Chapter 2.

6.3.1 Charge Transfer Hysteresis

All of the investigated graphene devices revealed reproducible hysteresis in conductance versus gate potential (V_{gate}) characteristics in ambient environment. A representative example with Hall bar geometry is displayed in Figure 6.4. When the gate voltage was swept continuously from -80 to 0 V, then to +80 V and back to -80 V. conductance hysteresis is observed. The gate scans lead to the positive shift of NP in graphene. In other words, the system corrects for the applied gate voltage over some

time scale. We could determine the direction of the hysteresis by comparing the location and sign of trapped charges to the avalanching field. When the bias of back gate starts from negative value, holes in graphene are slowly trapped into the trapping centers, so that after some time the graphene sees a more positive potential than that simply due to the gate voltage (and vice versa for the opposite sweep direction). These trapped charges under graphene dope the graphene into opposite polarity, whose static condition could be observed in scanning single electron transistor [12].

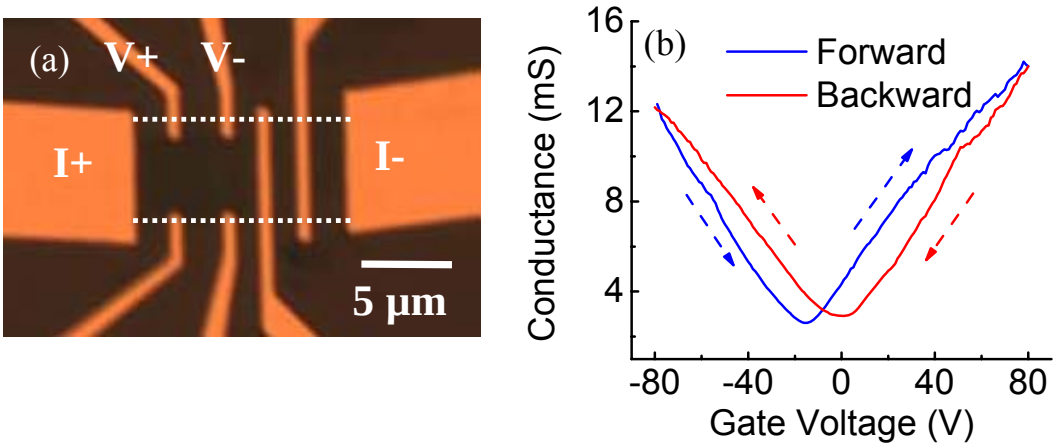

FIG. 6.4 a) Optical image of a BLG device (bs4q3p7) lying on SiO_2; b) Conductance versus gate voltage curves recorded under a sweep rate of 1.25 V/s in ambient condition. As the gate voltage is swept from negative to positive and back, a hysteresis is observed, as indicated by the arrows denoting the sweeping direction.

As shown in Figure 6.5(a), the magnitude of the hysteresis in V_{gate} exhibited a significant dependence on sweeping rate of the gate voltage (dV_{gate}/dt). The voltage different of NP caused by hysteresis increases from 8V (dV_{gate}/dt = 5 V/s), 14.5V (dV_{gate}/dt = 1.25 V/s) to 15 V dV_{gate}/dt = 0.313 V/s). Device hysteresis increases steadily with reducing the sweeping rate due to slow charge traps that discharge on a

time scale longer than few seconds. It almost saturates when the sweeping rate is lower than 1.25 V/s, and the sweeping rates are adapted in the next experiments.

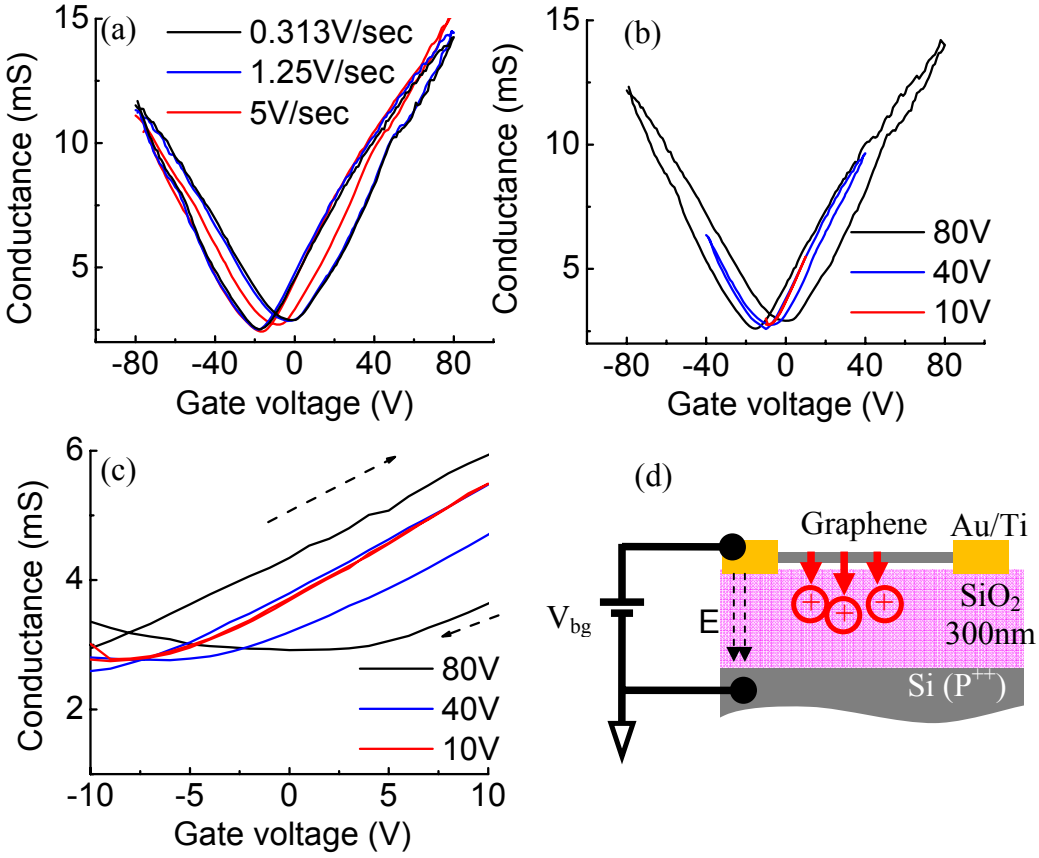

FIG. 6.5 a) Conductance hysteresis recorded under three different V_{gate} sweep rates in ambient condition; b) Conductance versus gate voltage curves recorded for the same device as in Figure 6.4 under three different gate voltage range in ambient condition; Device hysteresis increases steadily with increasing voltage range due to avalanche charge injection into charge traps; c) Close up of (b) within the low voltage region; d) Diagram of avalanche injection of holes into interface or bulk oxide traps from the graphene FET channel.

Figure 6.5(b), (c) compares conductance ~ V_{gate} curves of the graphene FET for different voltage ranges at room temperature. The hysteresis becomes larger as the range of V_{gate} increases. It indicates that hysteresis originates from avalanche charge injection into interface or bulk oxide traps at higher gate bias. When the voltage is in a

range of 10 V, the NP shift is only about 1 V. When the range of V_{gate} increases beyond 10 V, the hysteresis becomes more pronounced. The NP shift goes up to about 4.3 V (in the range of 40 V) and 15 V (in the range of 80 V). The enhanced hysteresis can be quantitatively explained here. Silicon dioxide has interface and bulk (dangling bond) traps whose charge state changes with gate voltage. Thermally grown silicon oxide have effective trap densities $N_{it} \sim 5\times10^{10}\ cm^{-2}$ and $N_{ot} \sim 5\times10^{11}\ cm^{-2}$ for interface traps and oxide traps, respectively.[20, 21] Interface traps are populated continuously as the gate voltage is tuned, usually oxide traps are charged only with injection at gate fields above $3\times10^{-2}\ V\cdot nm^{-1}$ before SiO_2 breaks down at about $0.27\ V\cdot nm^{-1}$.[20] The graphene FET capacitance per unit area is derived from simple capacitor model $C_g = 115\ aF/(\mu m)^2 = 712\ e\cdot(\mu m)^{-2}\cdot V^{-1}$. The number of charges trapped per unit area $Q = C_g\cdot\Delta V_{np}$ is estimated from the NP shift ΔV_{np} and an effective capacitance C_g. Therefore, NP shift in a range of 9V should be $\Delta V_{np} = 2\dfrac{eN_{it}}{C_g} \sim 1.4\ V$, the conductance shift in a range of 80 V should be $\Delta V_{np} = 2\dfrac{eN_{ot}}{C_g} \sim 14\ V$. The calculated values are near our measurement results. Therefore, the movement of NP can be explained by the effective trapping charges density. Inversely, the effective trapping charges could also be estimated, they are around $5.76\times10^{10}\ cm^{-2}$ (0.8V in the range of 10 V) and $5.4\times10^{11}\ cm^{-2}$ (15 V in the range of 80 V). It is noted that the ratio between the charge density and the back gate bias yields a value of $7.2\times10^{10}\ cm^{-2}V^{-1}$. Note that the results agree well with the value of charge nonuniformity ($\delta n = 2\sim15\times10^{11} cm^{-2}$ in SLG and BLG) obtained from other experimental methods [12, 13, 22, 23]. The hysteresis clearly demonstrates dynamic process how the charges

inject into traps centers. Figure 6.5(d) illustrates the diagram of avalanche injection of holes into interface or bulk oxide traps from the graphene FET channel.

We performed a statistical analysis over all the samples measured in order to examine the hysteresis strength of all the graphene flakes ranging from 1 to 10 layers. The relationship is shown in Figure 6.6 (a). The dotted lines serve as guide for eyes. Although the NP shift fluctuates in a large range, it is noticed that the average conductivity for SLG approaches 12.6 V. However, the NP shift in BLG and FLG starts to deviate from this value; it is about 9.3 V for BLG, 6 V for three layer stack and saturates at about 5 V for thicker layers. The phenomena are due to the charge distribution, which is brought about by the interplay between interlayer hopping and interlayer screening in multilayer graphene. Degree of charge trapping under certain gate sweeping rate usually is proportional to carriers' density in the first graphene layer near SiO_2 surface. The saturation of NP shift starting from 4-layer graphene indicates that the electrical field induced carriers are mainly located within three near-surface layers. Other planes are almost not affected by backgating. As a consequence, gating induced carriers in thick graphene flakes spatially distributes in the 2-3 planes most near the SiO_2 surface. The distribution exists in both the A-B (Bernal) stacking case [24] and the case of rotationally stacking [25]. We notice that the shift of NP in SLG and BLG fluctuates in a large range. A possible cause could be lateral inhomogeneity, i.e., fluctuations in the carriers' concentration, within the thin graphene plane.[12]

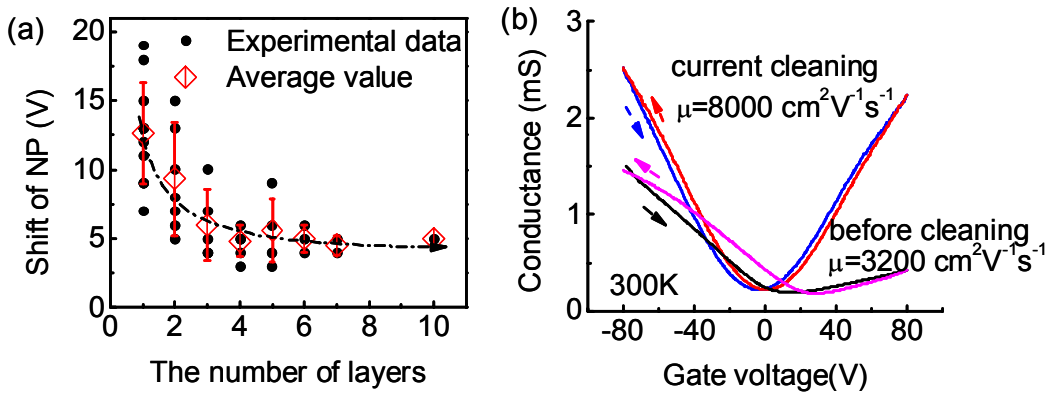

FIG. 6.6 (a) Shift of the neutrality point as a function of the number of layers. The error bar represents the standard deviation of all the raw data. The dashed line is guide for eyes; (b) Two-point conductance as a function of gate voltage in a bilayer sample LF5 before and after the application of a large current in helium gas atmosphere and at T=300 K.

Graphene always is found to be p-type due to unintentional doping of adsorbates (e.g., water, oxygen, tape residue) after exposure to air. The doping states are quite stable even in vacuum. Current annealing can remove the foreign impurities on the graphene surface, and then improve the quality of graphene. [26] Figure 6.6 (b) shows the conductance G as a function of V_{gate} for a bilayer graphene sample (LF5) before and after current annealing under helium atmosphere at room temperature. The graphene device exhibits p-type characteristic before annealing. DC current is gradually ramped across the device up to 5 mA (accordingly about 0.5 mA/μm per layer) and kept for about 10 minutes, and then gradually reduced to zero. After that, the electrical transport properties of the graphene device are recorded again. The procedure is repeated until NP shifts back to zero voltage. The phenomenon indicates that many of the residues acting as dopants are removed upon current annealing. As shown in Figure 6.6(b), current annealing has been shown to significantly reduce hysteresis. The difference in the NP voltage value due to hysteresis decreases from 13.6 V (dV_{gate}/dt = 1.25 V/s) to 4.3 V (dV_{gate}/dt = 1.25 V/s). These results suggest that

residues may help charge trapping. However, the current annealing treatment could not reduce the hysteresis further. Most likely, impurities permanently trapped in "dead layer" [11] and the SiO_2 substrate may be responsible for this lack of further improvement. We also notice that current annealing improve carriers mobility from $3200\ cm^2V^{-1}s^{-1}$ (for holes) and $1400\ cm^2V^{-1}s^{-1}$ (for electrons) to $8000\ cm^2V^{-1}s^{-1}$ (for both carriers). It is interesting that current heating improves mobility even for samples in contact with substrates. Normally, adsorbates lead to doping, while not causing significant change in carriers mobility. [19] The most likely reason is that the rippled graphene become partly suspended after annealing. Some parts of graphene sheet were lifted up and no longer contact the underlying substrate. The partly free standing configuration exhibits the intrinsic rippling of graphene [27], which has a lower amplitude than the surface of substrate. In addition, the increase of spacing between graphene and substrate may reduce the possibility of charge trapping and create less hysteresis. It is necessary to mention that hysteresis becomes less than 1 V at 4.2 K in helium gas, even without current annealing. It means the action of trapping is very sensitive to temperature. And it is suppressed at low temperature.

6.3.2 Capacitive Gating Hysteresis

In Figure 6.7(a), charge transfer from/to graphene led to the positive shift of conductance. However, sometimes hysteresis of conductance may go opposite to the direction of the previous results due to carrier density enhancement in graphene (Figure 6.7(b)). Figure 6.7(c) illustrates this kind of hysteresis in graphene devices. This hysteresis could be observed in electrolyte-gated graphene device.[28] For an electrolyte-gated device, the electrode will create a electric field and attract oppositely charged ions from the solution, forming what is know as electrical double layer, the two layers of the charge (surface charge and the layer of counterions) can be

approximated very well as a parallel plate capacitors.[29] And the capacitance rises exponentially with the potentials applied onto the electrodes. [30] Similarly, for an electrolyte-gated graphene, when positive voltage is applied to gate, free cations tend to accumulate near the negative electrode (graphene), creating a positive charge layer near graphene. The accumulation is limited by the concentration gradient, which opposes the Coulombic force of the electrical field. The charge layer with inversed charges (called Debye layer) accumulate near the electrolyte and provides a much higher gate capacitance than the commonly used SiO_2 back gate, the high capacitance origins from the small distance between Debye layer and electrode (graphene). Therefore, when the gate voltage sweeps, the graphene "remembers" the conductance at the last gate voltage it saw. The hysteresis of conductance shifts left with respect to gate bias, this is because it takes some time for the potential to be distributed in solution. The hysteresis could be reduced by decreasing the gate sweeping rate or by increasing the concentration of ions in the solution. We believe that the hysteresis observed in literature [28] should be the case shown in Figure 6.7(c) although the authors did not give the details about the hysteresis.

Although the NP positively shifts during forward and backward gate voltage scans under ambient condition, it shifts toward more negative voltage after the samples was mounted on cryostat in flowing cold helium gas. The results are reproducible at 1.4, 4.2, 50 and 200 K. The two representative devices and experiments results at 4.2 K are shown in Figure 6.7(d), 6.7(e). The phenomena may be caused by the surface dipole moment near graphene such as tape residue [31], water, [18, 31] or e-beam resist. The carrier density in graphene near dipoles could be increased by capacitive gating from dipoles. The dipoles usually sit on graphene with some orientation, and flap randomly due to the thermal fluctuation. After applying external electrical field,

the dipoles will be oriented along the electrical field direction, which causes the enhancement of local electrical field near dipoles. The carrier density in graphene near dipoles could be increased due to capacitive gating from oriented dipoles. In addition, it takes some time for the dipoles to be aligned and settle down under electrical field. Therefore, the hysteresis of conductance shifts left with respect to gate bias. In most cases, the phenomena are difficult to be observed in graphene lying on SiO_2 because the charge transfer may dominate the hysteresis by shifting in opposite direction. The negative hysteresis could be observed when the charge transfer could be suppressed at low temperature.

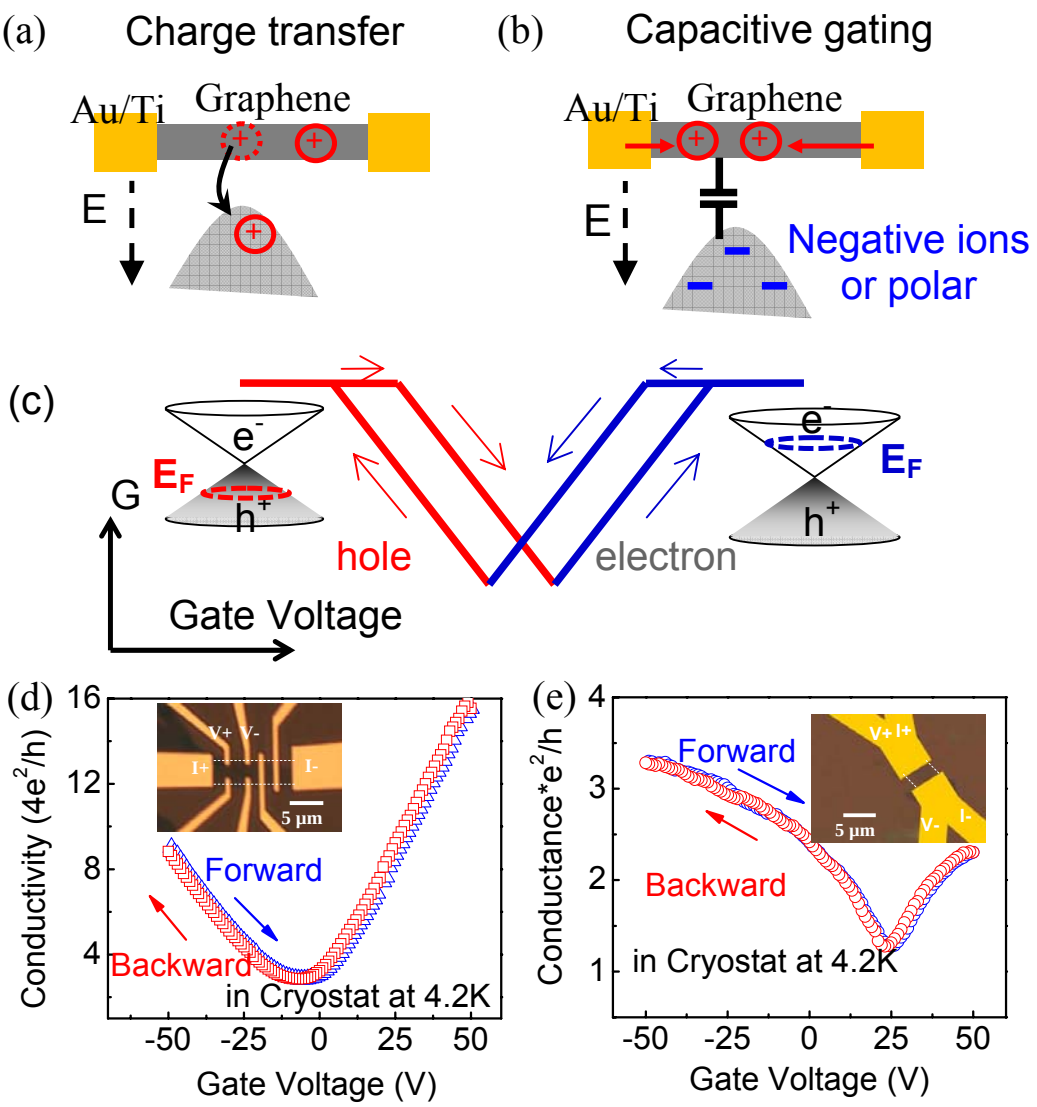

FIG. 6.7 The carrier density in graphene is affected by two mechanisms. a) Transferring charge carriers (hole) from graphene to charge traps causes the right shift of conductance, and vise versa; b) Capacitive gating occurs when the charged ion or polar alters the local electrostatic potential around the graphene, which pulls more opposite charges onto graphene from the contacts. c) Schematics of hysteresis caused by the capacitive gating, where the arrows denoting the sweeping direction; this kind of hysteresis observed in some of our samples in helium vapor at 4.2 K. (d) 4-layer graphene device (Bs4q3p8) and (e) monolayer graphene device (Bs5q1p14) are representatives. (The arrows denote the sweeping direction. the insets are optical images of the corresponding devices, and graphene was profiled between dashed lines).

In summary, charge transfer and capacitive gating cause different hysteresis in graphene when sweeping the gate voltage. In both cases, variation of the carrier

density in graphene causes the shift in the conduction with respect to gate voltage on the time scale. In the first case, when a total charge Δq is transfer from\to the graphene, it will cause the positive shift of conductance ΔV given by $\Delta q = C\Delta V$ where C is the dielectric capacitance. In the second case, capacitive gating increases the carrier density in graphene, and more charges are pulled onto graphene from the contacts. The effect changes the graphene conductance as with back-gating. The two mechanisms will shift the conductance with respect to gate voltage in opposite direction. Our experimental results indicate the influence from environment. In the next section, we are going to discuss their influence on the magneto-transport properties of the graphene devices.

6.4 Magneto Transport Study at Low Temperature

6.4.1 Four-layer Graphene Device

As shown in previous section, the transport in graphene flakes should be different from clean graphene devices in presence of charged impurities and surface absorbates. We studied the magnetoresistance of our devices at liquid helium temperature. A large perpendicular magnetic field (B) was applied to sample surface. Figure 6.8 shows longitudinal resistance $R_{xx}(B)$ observed in a four layer graphene device (bs4q3p8). There is a strong increase in $R_{xx}(B)$ with magnetic field. Shubnikov-de Haas (SdH) oscillations are clearly seen on top of the $R_{xx}(B)$ curve. Increasing of magetoresistance may be due to the so called parallel conductance effect, where the electric current redistributes and is attracted to regions with lower mobility with increasing B. Under high perpendicular magnetic field, the constant two dimension density of states becomes a series of sharp peaks centered at Landau levels. The SdH oscillations occur

as each successive Landau level is emptied by increasing the magnetic field. There is a dip in the longitudinal resistance when the Fermi energy equals the energy of the Landau level giving oscillations that are periodic in the inverse magnetic field. Figure 6.9 plots the measured change in longitudinal resistance (ΔR_{xx}) as a function of inverse magnetic field (B) after the background subtraction of data in Figure 6.8.

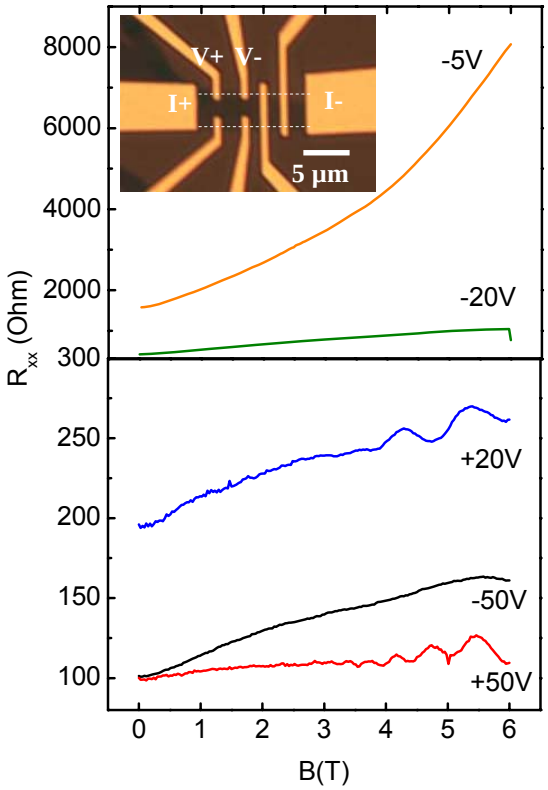

FIG. 6.8 Gate electric field modulation of the magneto-resistance as a function of magnetic field measured at T = 4.2 K for a 4 layer graphene (bs4q3p8). Numbers near each curve indicate the applied gate voltage. The inset shows an optical image of the sample with measurement geometry.

This measurement was repeated for several V_g , which tunes the carrier density. The SdH oscillations are observed to be periodic in inverse magnetic field. Their period gives the carrier density using the formula $n_s = 4e/(h\Delta(1/B))$ where e is the electron charge, h is Planck's constant and $\Delta(1/B)$ is the period ($1/B_F$) of the

oscillations. It is also found that minima in $R_{xx}(B)$ under high B occur at integer N times of the periods. (Figures 6.9 (a), (b), (c) and (d)). The integers are known as the Landau index. The landau index of each oscillation is plotted against its location in terms of 1/B in Figure 6.9(f). It is found that the slope of a linear fit to data give the intercept at the origin. The observed minima can be separated into different sets of the SdH frequencies, indicating different carriers characterized by different B_F. Note that B_F is the field corresponding to a filling factor N=1. In the inset of Figure 6.9 (f), B_F as a function of V_g observed in the 4 layer graphene is shown. The important feature we found is the fact that B_F depends almost linearly on V_g. The V_g varies as $\propto n$. It is different from $B_F \propto n^{\frac{2}{3}}$ expected for 3D carriers in bulk graphite [32]. This proves the 2D nature [21,33] of the field induced carriers in the 4 layer graphene.

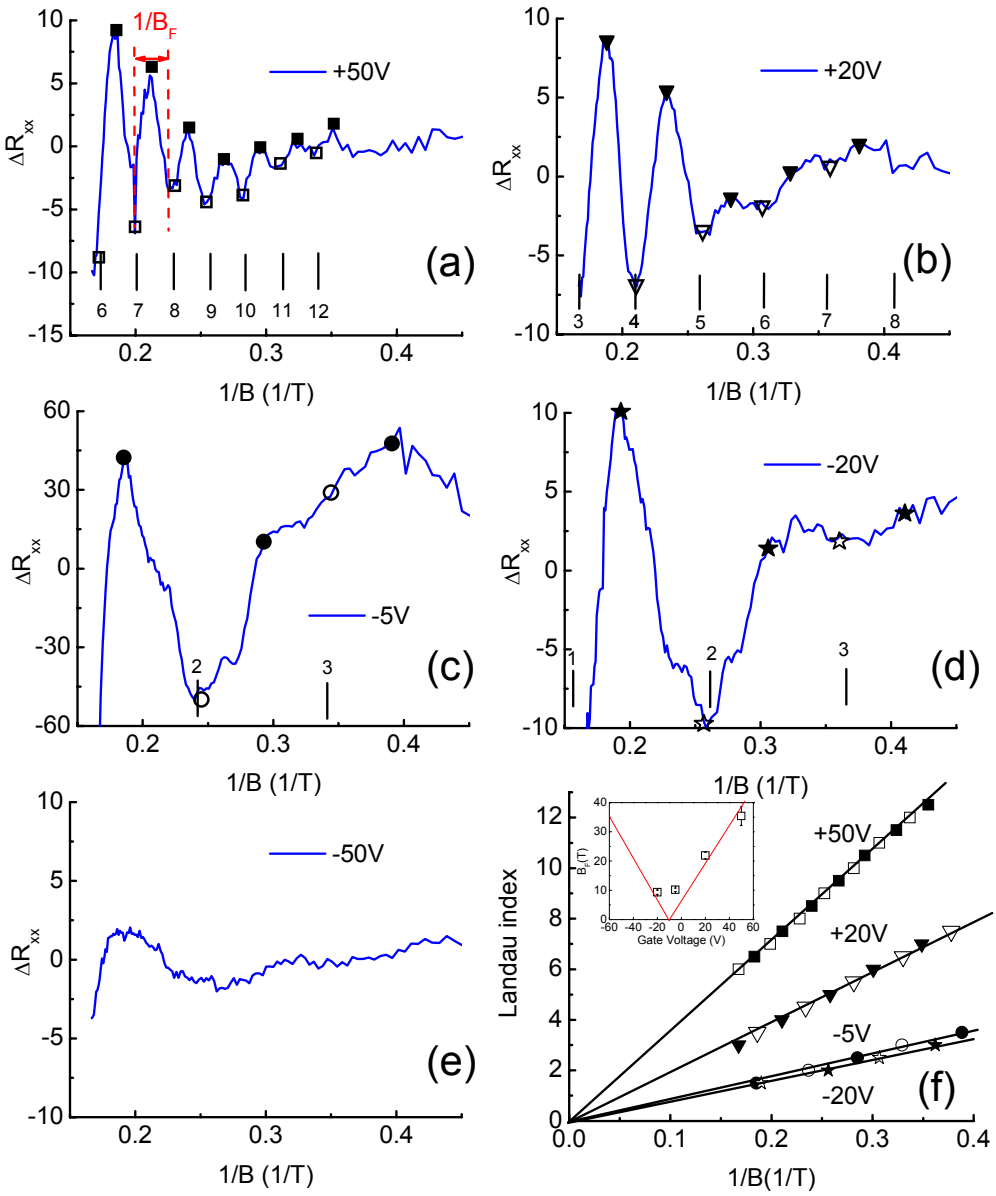

FIG. 6.9 ΔR_{xx} as a function of inverse magnetic field at (a) +50 V, (b)+25 V, (c)-5 V, (d)-25 V and (e)-50 V. ΔR_{xx} obtained from the measured R_{xx} by subtracting a smooth background. Solid (open) symbols correspond to peak (valley) of the oscillations. (f) Landau plots (see text) obtained from (a)-(d). Lines are linear fits to each set of points at different V_g. Inset: the frequency of the SdH oscillations obtained from the slopes of the line fits in (f) as a function of gate voltage.

Following the longitudinal magneto-resistance, the conductance as the function of gate voltage is investigated under high magnetic field. Results are shown in Figure 6.10. For comparison, the zero magnetic field results are also shown. It is found that

the magnetic field suppressed the sample conductance in the full range of gate voltage. In Figure 6.10(b), we observed some weak peaks, which may correspond to Landau levels under high magnetic field. [34, 35]

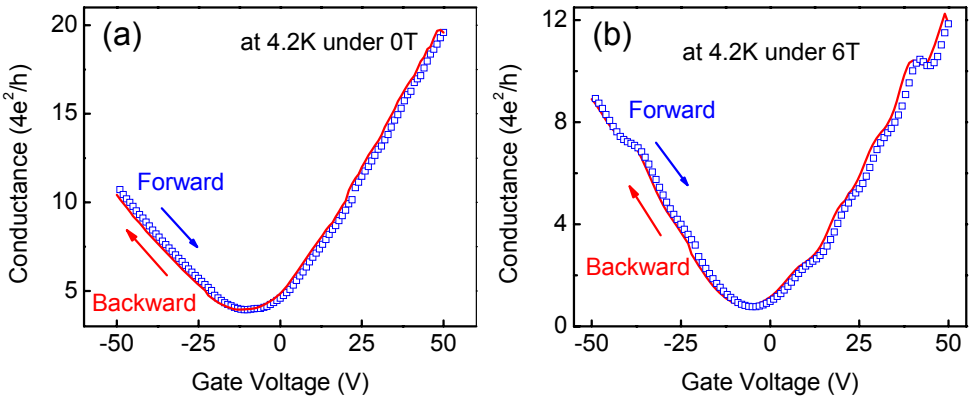

FIG. 6.10 Conductance as a function of gate voltage at T=4.2K (a) B=0T, (b) B=6T for the four layer graphene sample (bs4q3p8).

6.4.2 Monolayer Graphene Device

Similarly, a monolayer graphene was characterized by analyzing the SdH oscillations in the flake resistance R(B) studied as a function of a magnetic field B applied perpendicular to the sample surface. The $R_{xx}(B)$ observed in the monolayer graphene device is shown in Figure 6.11. The measurement geometry is shown in the inset. A strong increase in $R_{xx}(B)$ with magnetic field is observed in the monolayer sample.

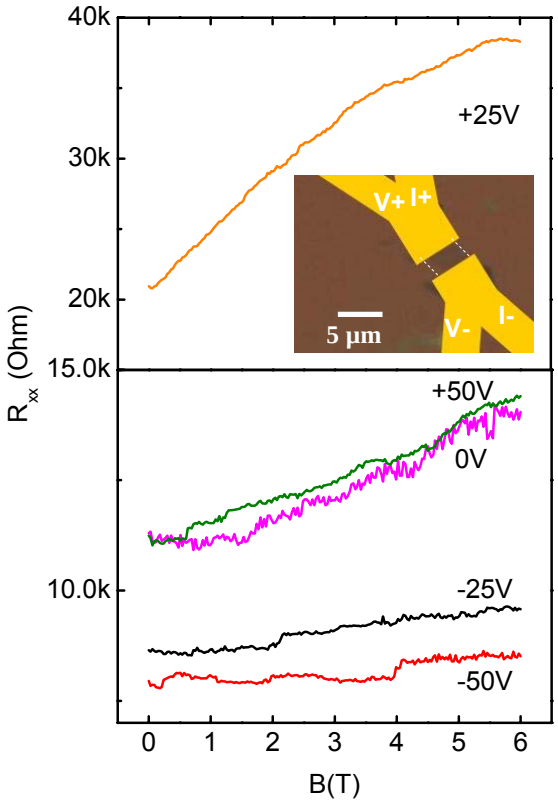

FIG. 6.11. Gate electric field modulation of the magneto-resistance as a function of magnetic field measured at T = 1.4 K in a monolayer graphene (bs5q1p14). Numbers near each curve indicate the applied gate voltages. The inset shows an optical image of the sample with measurement geometry.

Figure 6.12 plots the measured change in longitudinal resistance (ΔR_{xx}) as function of inverse magnetic field after the background subtraction from data in Figure 6.11. At all fixed back gate voltages, the magnetoresistance plotted versus 1/B does not display very regular oscillations. It may be due to the large inhomogeneity of charged impurity distribution at the substrate/graphene interface. Although we could not observe SdH oscillations in the monolayer graphene, it is necessary to mention that SdH oscillation in monolayer is different from few layer graphene. The Berry's phase π characteristic of electrons in monolayer graphene is directly related to the appearance of SdH oscillations minima at filling factors $\nu_{\min} = 4(i + 1/2)$, in contrast to bilayer or few-

layer graphene $\nu_{\min} = 4i$ where the electron's Berry's phase is 2π and the SdH oscillations minima appear at filling factors $\nu_{\min} = 4i$ with $\nu = \frac{nh}{eB}$ being filling factors, n the carrier concentration and i an integer. For comparison, ideal SdH oscillations of both monolayer and few-layer graphene are plotted in Figure 6.12(f). After locating the peaks and valleys of the SdH oscillations in terms of 1/B, a phase shift of π can be found between the SdH oscillation of monolayer graphene (solid curve in Figure 6.12(f)) and that of few layer graphene (dashed line in Figure 6.12(f)). It is a consequence of the combination of time reversal symmetry with the Dirac band structure near Fermi level in monolayer graphene. [36, 37]

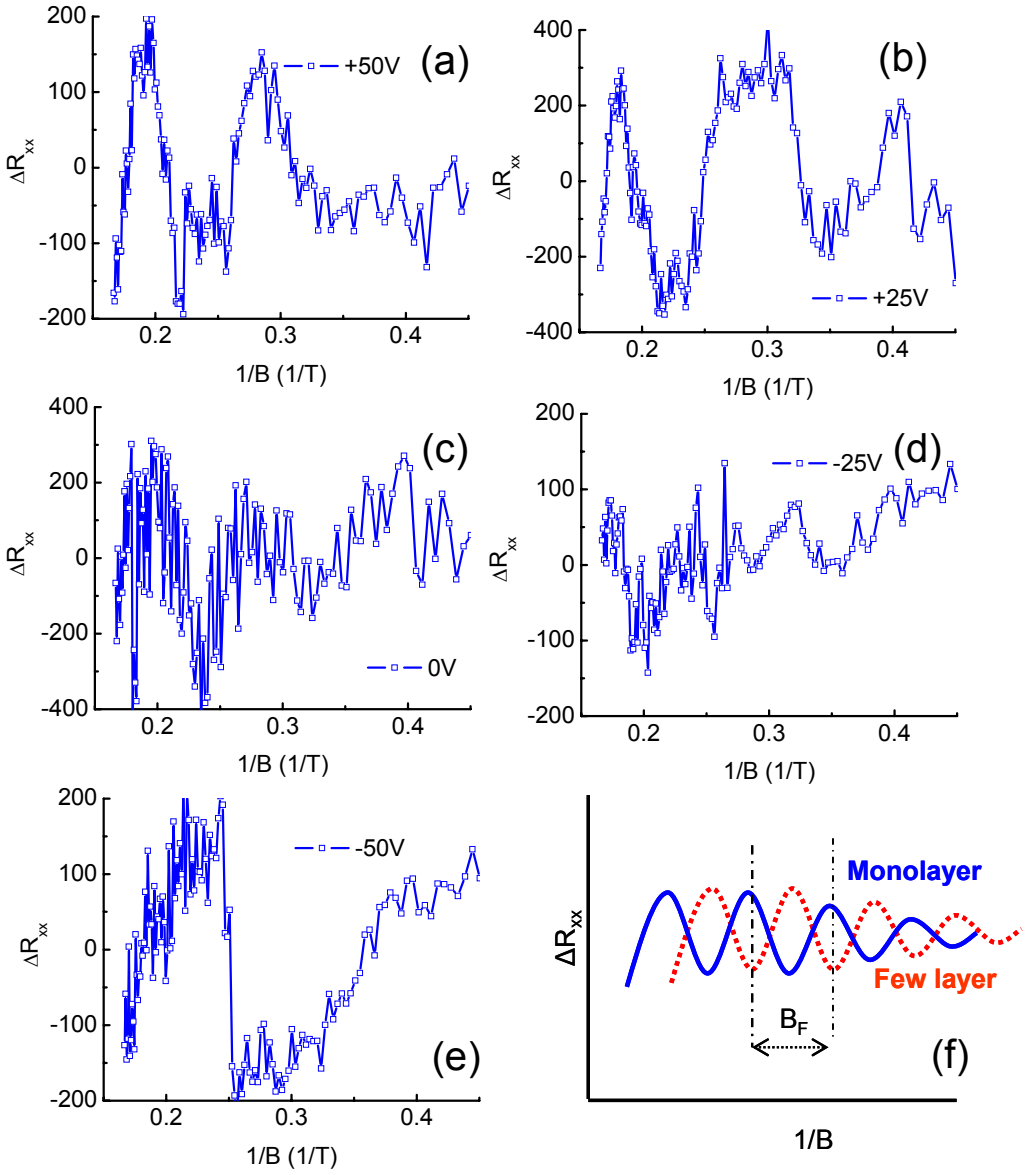

FIG. 6.12 ΔR_{xx} as a function of inverse magnetic field at (a) +50 V, (b) +25 V, (c) 0 V, (d) -25 V and (e) -50 V. ΔR_{xx} obtained from the measured ΔR_{xx} in Figure 6.11 by subtracting a smooth background. (f) Illustration of ideal cases for ΔR_{xx} as a function of inverse magnetic field in monolayer graphene and its few-layer.

The conductance as the function of gate voltage is also investigated under high magnetic field in the monolayer graphene. Results are shown in Figure 6.13. For comparison, the zero magnetic field results are shown together. It is found that the magnetic field of 6 T suppressed the sample conductance in the full range of gate

voltage in Figure 6.13(b). Indeed, the measurement of conductance versus V_g at B = 6 T shows clearly identifiable Hall plateaus at $\frac{e^2}{h}$. In single layer graphene, Hall plateaus of the QHE should appear half-integer multiples of $\frac{4e^2}{h}$. The conductance (G) measured in 2 probe configuration is a mixture of longitudinal and Hall signals. Under very high magnetic field, $G = G_{Hall}$ (this approximation is exact at the Hall plateaus) [38]. Clear Hall plateaus at $\frac{e^2}{h}$ indicates that longitudinal signals are not suppressed and the contact resistance could not be neglected.

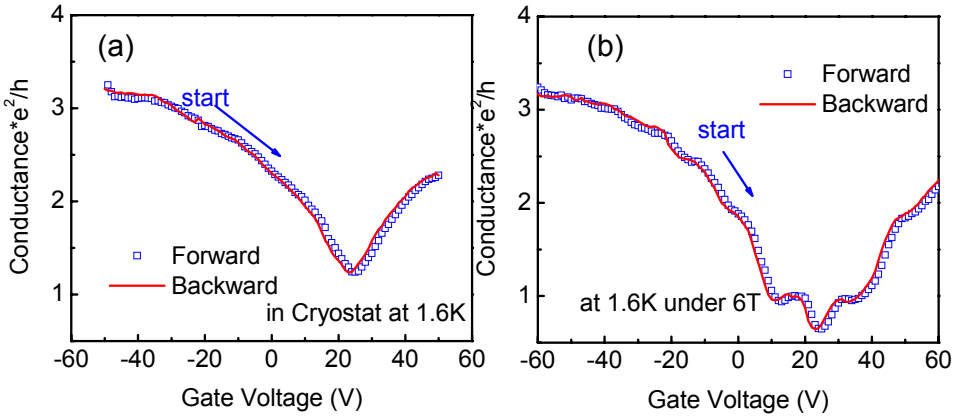

FIG. 6.13 Conductance as a function of gate voltage at T = 4.2 K (a) B = 0 T, (b) B = 6 T for monolayer graphene sample.

Note that we measured a bilayer graphene (Sample LF5), but observed neither clear SdH oscillation nor Hall plateaus.

In this section, we examined the magneto-transport of graphene devices without special treatment (such as annealing). The SdH oscillations were observed in thicker graphene devices while absent in thinner samples. The scattering factors (such as phonon in SiO_2, charges trapped in SiO_2, inhomogeneity of charged impurities) suppressed the SdH oscillation in thinner graphene flakes. These results are consistent

with those of previous investigations. As scattering centers play critically important roles for the quantum inference in conductor, it must be interesting to study quantum interference in these samples.

6.5 Conductance Fluctuation at Low Temperature

Since the successful isolation of graphene, many remarkable phenomena have been predicted and observed in both SLG and BLG. One of the important questions that has risen is the interplay between disorder and quantum interference.[39,40] Universal Conductance Fluctuation (UCF) in graphene is not affected by the inter- and intra-valley scattering, but influenced by inelastic scattering. Weak localization (WL) could be present only when the chiral symmetry of graphene was broken.[41] When the phase coherence length of carriers decreases below the same order of sample scale for some reason, the measured magnitude of UCF and WL is suppressed. Both WL and UCF were found decay near the charge neutral point in graphene. [41, 42] The most possible reason should be that the disorders enhance the inelastic scattering near the Dirac point, where the density of state vanishes in graphene.

The disorder not only acts as a source of scattering, but also changes the local charge density in samples. As a kind of important disorder, doping impurities could effectively shift the local Fermi level away from the average value and then tune the charge density. In response to the random spatial distribution of impurities, the charge density becomes very inhomogeneous. In this way, the charge inhomogeneity occurs in graphene and generates a very visible impact on the electronic transport. However, most of the previous research focused on the properties of well defined graphene layers. Their NP is achieved near zero gate bias.[12,14] These weak charge puddles could be effectively screened by the smooth electrostatic potentials from a small gate

voltage. Little effort was put on an investigation of graphene without special treatment. Recent optical mapping experiments [43, 44, 45] indicates the presence of strongly inhomogeneous charge distribution in single-layer graphene flake without any treatment. The charge inhomogeneity is similar to the situation of electron-hole puddle [12] near Dirac point in "clean" graphene, but the former could have an offset and stronger fluctuation. Normally the charged domain has a submicron size in graphene. The fluctuation of charge density could be up to $10^{13}\ cm^{-2}$ in a monolayer graphene. Hence, the influence of the charge inhomogeneity is of fundamental interest. A deeper physical understanding of the inhomogeneity is important for clarifying the true nature of disorder in graphene. So far, little investigation of strong random spatial potential effect on the transport has been reported in graphene flakes. Next, studies will focus on the conductance fluctuation in monolayer and bilayer graphene with strong charge inhomogeneity.

We fabricated graphene devices with micrometer size to include enough doping charged domains to examine the influence of charge inhomogeneity on conductance fluctuation. The graphene flakes used in this study were fabricated by mechanical exfoliation from bulk natural graphite. The charge inhomogeneity automatically forms in all freshly prepared graphene devices without any special treatment under ambient condition. Because of the presence of surface impurities on the graphene sheet, most of devices are generally strongly hole-doped with NP situated at a positive back-gate voltage. Water and oxygen are believed to be among the dominant doping species. The quality and charge inhomogeneity of graphene were identified by Raman spectra. [46] The fluctuation of unintentional doping is up to a few$10^{12}\ cm^{-2}$ in the same graphene flake. The samples are measured in a cryostat with the base temperature as low as 1.4

K. Standard lock-in technique with 100 nA AC current is used to investigate the transport properties of the devices.

6.5.1 Four-layer Graphene

Figure 6.14 (a) shows the conductivity versus V_{gate} on a 4 layer graphene at 4.2 K and 60 K. The geometry and measurement configuration of the device are inserted. The dimension of the 4 layer graphene is $L \times W = 3\ \mu m \times 3.2\ \mu m$. The field-effect mobility μ is about 4000 cm^2/Vs away from NP. NP is seen at $V_{gate} = -12\,V$ with a conductivity of about $14.9\frac{e^2}{h}$ at 4.2 K and $17.1\frac{e^2}{h}$ at 60 K. It is also found that the conductance of graphene exhibits very weak temperature dependence, especially far from NP. In order to quantify the conductance fluctuation, the conductance back ground was subtracted. The background was achieved by fitting the curves with six order polynomials. After the background subtraction, a clear conductance fluctuation was clearly plotted in Figure 6.14(c). It is found that the amplitude of conductance fluctuation decreases from $0.4\frac{e^2}{h}$ near +50 V to about $0.02\frac{e^2}{h}$ near NP at 4.2 K. Similarly, the amplitude of conductance fluctuation is roughly $0.15\frac{e^2}{h}$ near +50 V and decreases to $0.02\frac{e^2}{h}$ near NP at 60 K. The fluctuation amplitudes decrease with increasing temperature especially in the regime away from NP. The conductance fluctuations are suppressed near NP. The results are very similar with previous studies by other groups. [42, 47, 48] The results indicate that an important component of the conductance fluctuation on the 4LG sample is UCF. Normally, amplitude of UCF is proportional to the phase coherence length and phase coherence lengths are inversely

proportional to temperature. Actually, carrier phase coherence could be destroyed by the disorder in mesoscopic system. The situation leads to the shortening of phase coherence length and suppression of UCF. In fact, the value of $k_F l = \frac{\sigma h}{e^2}$ is used to estimate the homogeneity of 2D system and disorder level. [41,42] k_F is Fermi wave vector, l is mean free path and σ is measured conductivity of 2D system. The value of $k_F l$ is proportional to the conductivity of 2D system. At 4.2 K, the conductance starts fluctuating from +20 V where the conductivity is about $38\frac{e^2}{h}$. The value of $k_F l$ at 20 V in this 4LG is about 38. We may adopt the value of $k_F l$ as "critical" value. If $k_F l$ is below 38, the UCF could be suppressed. The value is much higher than the strongly disordered limit of $k_F l = 1$. The results indicate high charge homogeneity above 20V in the 4LG. The charge inhomogeneity is effectively screened by the gating potential above 20 V. That may explain the presence of the universal conductance fluctuation and its dependence of temperature and gate bias.

Figure 6.14(b) illustrates the resistance versus V_{gate} on a 4 layer graphene at 4.2 K and 60 K. It is found that the resistance decreases by 250 Ω near NP after heating up, while the values of resistance almost remain the same far away from NP. This is due to the metallic properties of 4LG even near NP. The resistance fluctuation is plotted in Figure 6.14(d) after the background subtraction. The resistance fluctuation does not show obvious temperature dependence. And the amplitude of resistance fluctuation near NP is about twice of that away from the NP. The value of $k_F l$ is 15.2 near NP where the conductivity is about $3.78\frac{e^2}{h}$. The reasons for the sudden variation of ΔR at -20 V and 20 V are not clear.

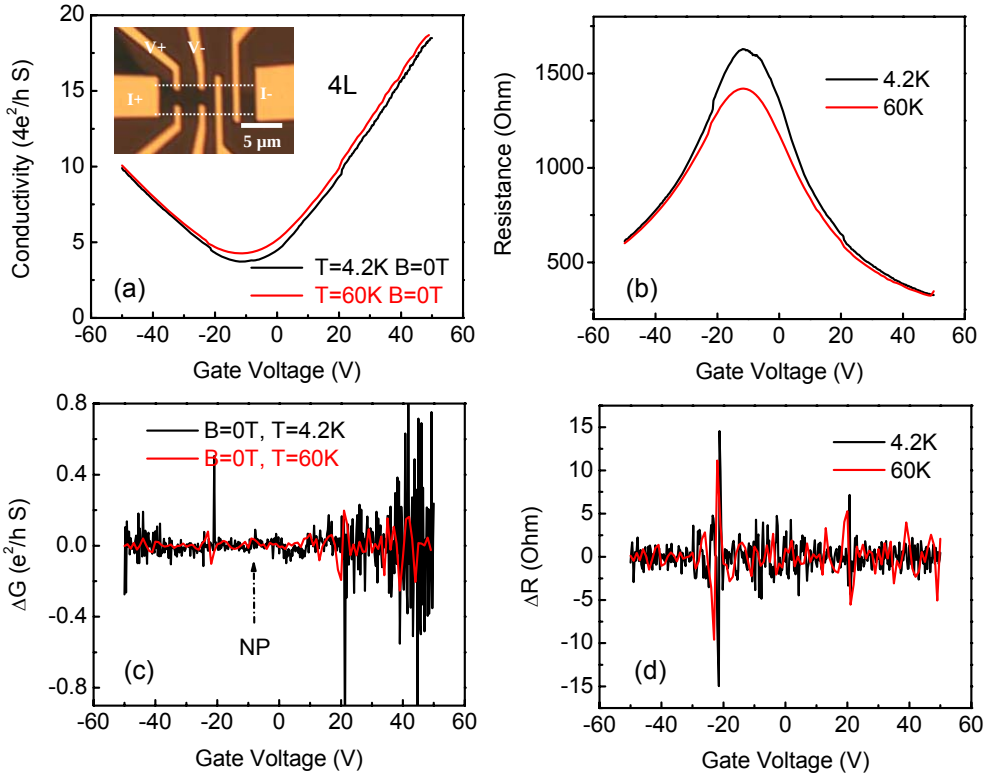

FIG. 6.14. (a) The back gate voltage dependence of conductivity for a 4 layer graphene device (inset: the sample geometry and measurement configuration. The boundary of graphene is denoted by a dashed line.); (b) The gate voltage dependence of resistance for the same sample; (c) the ΔG vs gate voltage at 1.4 K and 60 K;(d) the ΔR vs gate voltage at 1.4 K and 60 K.

The presence of UCF and the high mobility in the 4 layer graphene shows that the properties of the 4LG are not affected greatly by charged impurities on the surface of graphene. The possible reason is that the inner planes of multilayer graphene are less affected by the impurities than the surface plane. [49] Further investigation on monolayer or bilayer graphene should be more meaningful.

6.5.2 Monolayer Graphene Device

Figure 6.15 (a) shows conductance vs gate voltage for SLG device at different temperature. The dimension of the SLG is $L \times W = 2.1\ \mu m \times 4.2\ \mu m$. The conductance

minimum that corresponds to zero doping is found to be at about +22 V instead of 0 V at most temperatures and at +26 V at 300 K. The phenomenon attributed to an average charging effect by contaminant molecules. The mobility of this sample is about 120 cm^2/Vs away from neutrality point at all temperatures. The mobility is at least one order smaller than that of samples treated by annealing. The minimal conductivity of the sample gradually increases from about $0.62\frac{e^2}{h}$ at 1.4 K to $0.84\frac{e^2}{h}$ at 300 K. The contact resistance is ignored. The conductance of graphene exhibits weak temperature dependence. After the background subtraction, ΔG versus gate voltage from 1.4 K to 300 K was plotted in Figure 6.15(c). The traces at different temperature were successively added with $0.04\frac{e^2}{h}$ except 1.47 K for clarity. To our surprise, unlike the 4LG sample, the conductance fluctuations of the monolayer graphene remained suppressed at $0.02\frac{e^2}{h} \sim 0.03\frac{e^2}{h}$ over the full range of gate voltage. In the monolayer sample, the maximal value of $k_F l$ (about 2.1) is achieved under the gate bias -50 V at 300 K. The value is greatly smaller than previous "critical" value (38) and quite near to the strongly disordered limit of $k_F l = 1$. The monolayer sample is a disordered system. In monolayer, phase coherence lengths are suppressed and much smaller than the sample size. The charge inhomogeneity is too strong to be effectively screened even under -50 V gate bias. The carriers in the SLG could not maintain their phase coherence across the potential barriers. That explains the absence of the universal conductance fluctuation even at 1.4 K.

Figure 6.15(b) shows the resistance versus V_{gate} on the SLG at different temperature. It is found that the resistance decreases in the full range of gate voltage

after heating up. The resistance fluctuation ΔR versus gate voltage at different temperature was plotted in Figure 6.16(d) after the background subtraction. It is found that the resistance fluctuation is pronounced near NP and exhibit very week temperature dependence. And the amplitude of resistance fluctuation near NP is about 100 times larger than that away from the NP. The strong resistance fluctuation may rise from the strong charge inhomogeneity near NP in the SLG. Thermal energy 26 meV at 300 K could not screen the charge inhomogeneity. The presence of resistance fluctuation may appear when the carriers travel across the boundary between the adjacent puddles. It could be used to indentify a strongly disordered system.

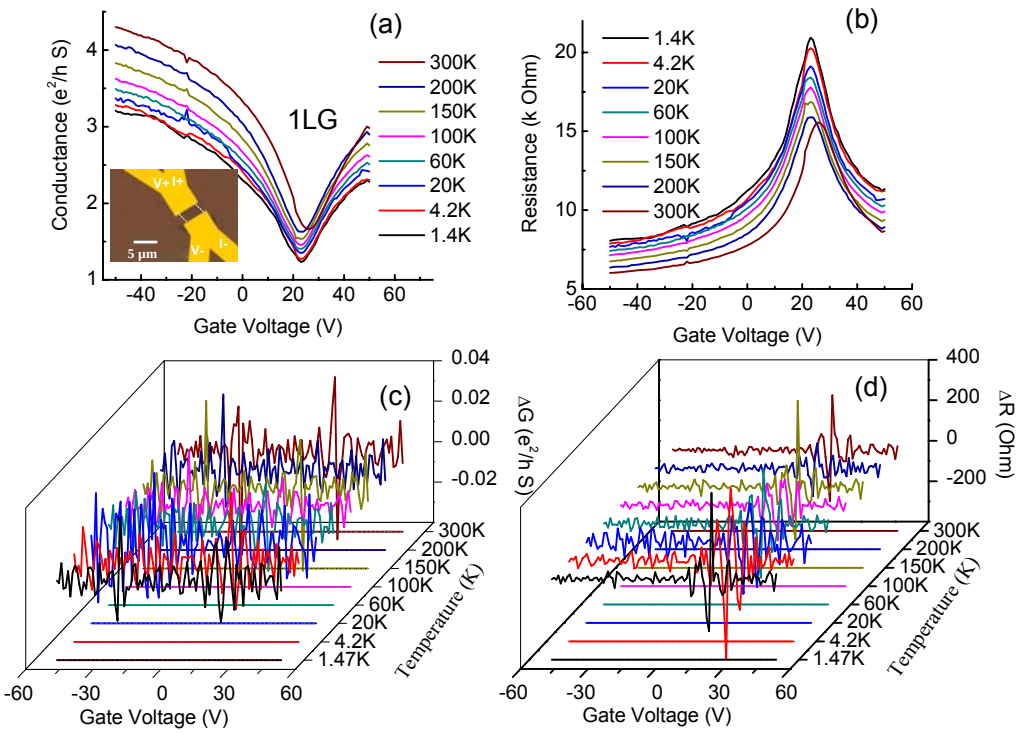

FIG. 6.15 (a) Conductance vs gate voltage for a monolayer graphene device (inset: the sample geometry and measurement configuration. The boundary of graphene is denoted by a dashed line.); (b) The gate voltage dependence of resistance for the same sample; (c) the ΔG vs gate voltage at different temperatures from 1.4 K to 300 K. (d) the ΔR vs gate voltage at different temperature.

6.5.3 Bilayer Graphene Device

Figure 6.16(a) shows conductance versus gate voltage for a BLG device at different temperatures. The inset is the sample geometry and measurement configuration. The dimension of the BLG is $L \times W = 10\ \mu m \times 4\ \mu m$. The mobility of this sample also remains about 2300 cm^2/Vs away from NP at all temperatures. NP locates near +52 V at most temperatures and near +60 V at 300 K. The small shift of NP is reasonable because of the average effect of inhomogeneous doping. The minimal conductivity of the sample gradually increases from about $6.25\frac{e^2}{h}$ at 1.4 K to $9.5\frac{e^2}{h}$ at 300 K. The maximal conductivity of $91.1\frac{e^2}{h}$ is achieved under the gate bias of -80 V at 1.4 K. The conductance of graphene exhibits very weak temperature dependence below 54.45 K. After the background subtraction, ΔG versus gate voltage at different temperatures from 1.4 K to 300 K was plotted in Figure 6.16(c). To our surprise, the conductance fluctuations behave strikingly different in the monolayer graphene. The conductance fluctuations in the BLG are obviously away from NP and suppressed near NP at all the temperatures. The further away from NP, the stronger is their amplitude. The amplitude of the conductance fluctuation decreases a little from 1.4 K to 4.2 K and then slowly increases again. The weak temperature dependence indicates the conductance fluctuation may not arise from UCF. A further discussion about the origin of the conductance fluctuation is discussed later. The value of $k_F l$ near minimal conductance in the bilayer device is about 6.25 at 1.4 K, which was achieved at the gate bias of 50 V. Sitting between the critical value 38 and disorder limit, the value of $k_F l$ indicates the bilayer system is weakly disordered. That may explain the absence of the conductance fluctuation near NP. The maximal value of $k_F l$ in the bilayer

device is about 91.1 at 1.4 K, which was achieved at the gate bias of -80 V. The value of $k_F l$ is obviously larger than "critical" point value 38. Normally, UCF could be observed near -80 V. The results are consistent with the weak decrease of conductance fluctuation from 1.4 to 4.2 K. UCF contributes a little to the observed conductance fluctuation, but we believe that the dominating mechanism of the conductance fluctuation is not UCF.

Figure 6.16 (b) shows the resistance versus back gate voltage on the BLG at different temperature. It is found that the resistance exhibits a decreasing trend near NP after heating up in spite of small variation. The resistance fluctuation ΔR versus gate voltage at different temperature was plotted in Figure 6.16(d) after the background subtraction. And the amplitude of resistance fluctuation near NP is at least 10 times larger than that away from the NP at different low temperatures. ΔR near NP decreases first from 1.4 K to 4.2 K and then increase again at 54.45 K. Finally, the resistance fluctuation ΔR is found to be suppressed at 300 K in the full range of sweeping gate voltage. The strong resistance fluctuation at low temperature indicates that the BLG is strongly disordered, due to the strong charge inhomogeneity near NP in the BLG. The charge inhomogeneity in the sample looks partially screened by the thermal energy 26 meV at 300 K. The partial screening may happen away from NP due to gate electrostatic effect.

Pronounced conductance fluctuations were observed in the BLG away from NP. They were suppressed near NP. Normally, UCF exhibits similar behavior at very low temperature and decays with the increase of temperature. However, the weak temperature dependence of conductance fluctuations in the bilayer graphene sample suggests that the dominant mechanism of ΔG is not UCF. UCF could not survive at 300K.

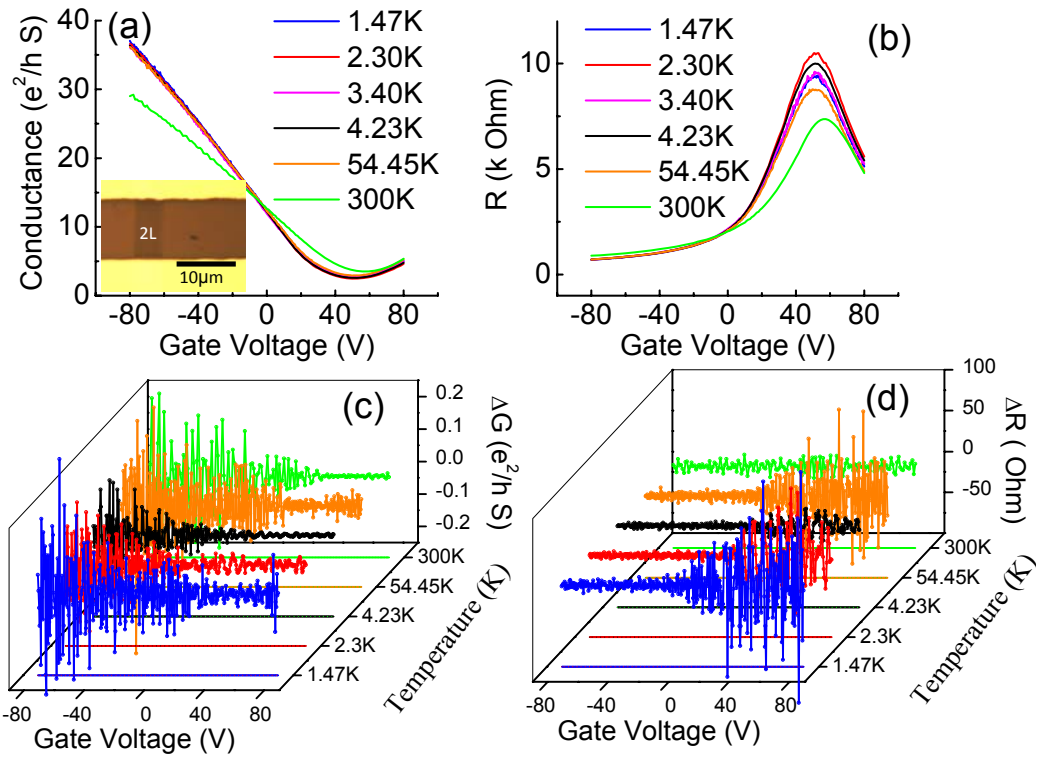

FIG. 6.16 (a) Conductance vs gate voltage for bilayer graphene device (inset: the sample geometry. The boundary of graphene is denoted by a dashed line.); (b) The gate voltage dependence of resistance for the same sample; (c) the ΔG vs gate voltage at different temperatures from 1.4K to 300K;(d) the ΔR vs gate voltage at different temperature.

In order to gain more insight into the conductance fluctuation, we have performed time duration measurement at different temperature. The differential conductance was recorded once every 3 seconds at a setting point of the applied gate voltage V_g. During a time interval of 300 seconds, the differential conductance under one gate bias was acquired. An average procedure was applied to the extracted data trace to achieve the conductance fluctuation data. After the background subtraction, the conductance fluctuation data at 1.4 K were plotted in Figure 6.17 (a). The root mean square of the conductance fluctuation (Rms(ΔG)) was plotted with respect to gate voltage at 1.4, 4.23, and 54.45K in Figure 6.17 (b). The conductance fluctuations are

suppressed near NP at all temperatures examined. And the fluctuation away from NP looks robust. The further away form NP, the stronger its amplitude. The amplitude of the conductance fluctuation decreases a little from 1.4 to 4.2 K and then slowly increases again. The results of Rms(ΔG) are in a good agreement with the results shown in Figure 6.16.(c), even the amplitude of conductance fluctuation. In fact, only a small part of the conductance fluctuations arises from UCF at low temperature. UCF are suppressed in almost full range of gate voltage. We attribute the suppression of UCF to the presence of the charge domains in the doped bilayer graphene.

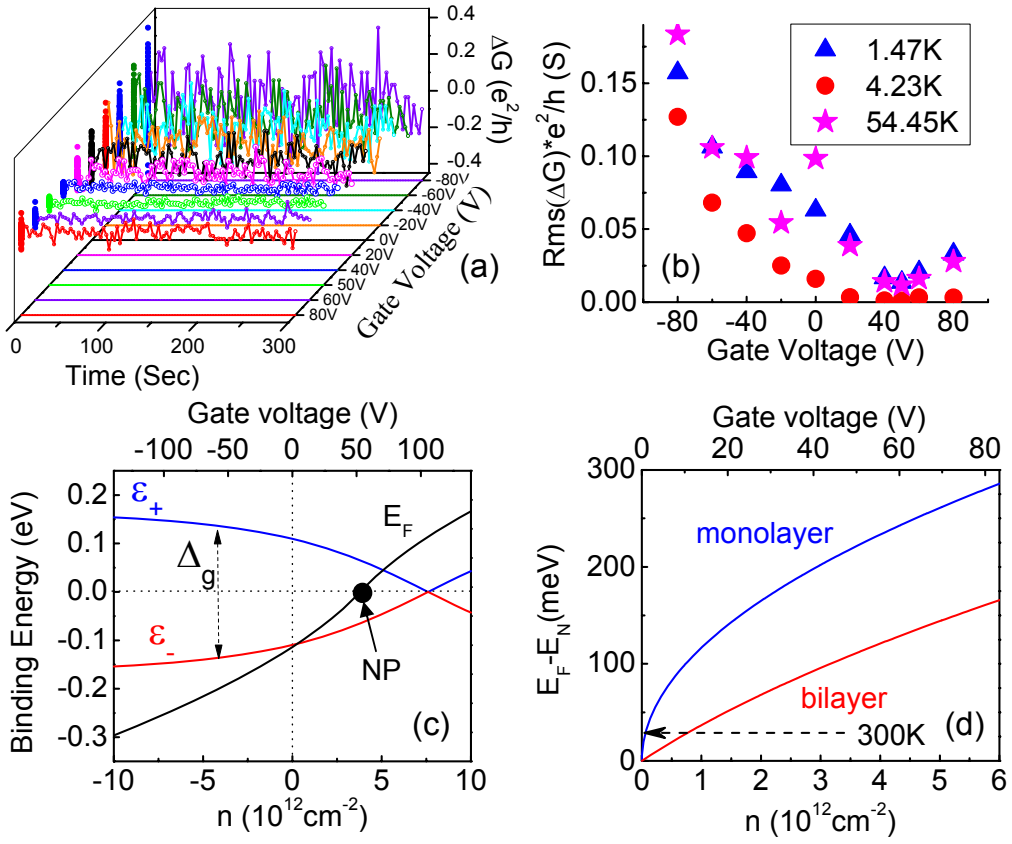

FIG. 6.17 a) Differential conductance fluctuation at gate bias from -80 to 80 V plotted as a function of duration time for the bilayer graphene at 1.4 K; b) Rms[ΔG] versus gate voltage at 1.4 K, 4.23 K, 54.45 K for the bilayer graphene; c) Bottom of conduction band ε+ , top of valance band ε- and Fermi level E_F as the function of carrier density n (bottom axis) and V_g (top) in a biased bilayer graphene with top p type doping (3.81×10^{12} cm^{-2}), d) the relationship of $E_F - E_D$ vs n and gate voltege in bilayer and monolayer graphene. The Fermi energy goes up much faster with charge density in the monolayer.

Recently, gap opening in a doped bilayer graphene was observed.[50-53] When bilayer graphene is placed in a suitably configured field effect device, the carrier concentration can be made different in each layer and an asymmetry gap can be generated. This provides a tunable semiconducting gap, and the valence and conductance bands no longer meet at the two Dirac points of the graphene Brillouin zone. We calculate the gap of such a semiconductor with particular emphasis on the charge redistribution brought about by changes in gap and chemical potential due to charging. This method was developed by E. V. Castro et al.[53] For the experiments described in the present work, we use $\gamma_1 = 0.35eV$, $v_F = 8.0\times10^5\ m/s$ and $\varepsilon_0 = 8.8542\times10^{-12}\ F/m$. The chemical doping was set to $n_0 = 3.81\times10^{12}\ cm^{-2}$ (equivalent of $V_D = 53\,V$). The evolution of Fermi level (E_F), bottom of conduction band (ε_+) and top of valence band (ε_-) with respect to carriers density n (bottom) and gate voltage (top) are plotted in Figure 6.17(c). It is found that the Fermi energy is placed in the band gap when gate voltage varies from 10 to 60 V or equivalent n varies from $7.2\times10^{11}\ cm^{-2}$ to $5\times10^{12}\ cm^{-2}$. Although the fluctuation of doping could have the order of a few $10^{12}\ cm^{-2}$ in the same graphene flake, the gap should open more or less everywhere. The charge inhomogeneity induced by unintentional doping can create inhomogeneous gap opening near NP in bilayer graphene. However, we only observe a weak insulating transition from our temperature dependence of resistance in Figure 6.16(b). The weak transition suggests the small gap opening. One of the possible explanations is that the unintentional doping partially comes from the interface of graphene and substrate instead of from the top of graphene. Another possible reason is the low accuracy of the model we used. Recent experiments illustrate that obvious temperature dependence of resistance was only observed under one electrical polarity

below 1.2 K. [52] The insulating transition in our samples may be observed under further refrigeration. Most recently, theoretical work illustrates that the weak disorder could smear the Mexican hat structure and strong disorder will induce the tail states in biased bilayer graphene. [54, 55] The additional tail state could narrow down the band gap in bilayer graphene. Different from the suppression mechanism in the monolayer, inhomogeneous gap opening in bilayer near NP suppressed conductance fluctuation. And potential fluctuation at high gate bias could suppress UCF in the bilayer graphene in principle. That may explain why we only observed some UCF residue at very high gate bias. Now let us turn to the origin of the conductance fluctuation we observed in the bilayer graphene. Beside UCF, many other mechanisms could cause conductance fluctuation in mesoscopic graphene, such as Fabry-Perot interference, inter-band tunneling and thermal excitation, especially confined nanostructure.[56, 57] Here our result is not any one of the cases. We purpose three possible situations which may cause the conductance fluctuation. Firstly, the fluctuation could be due to the presence of new density states caused by the impurities, [58] such as, H_2O and O_2. The H_2O and O_2 are very reactive chemicals, and therefore the impurities may modify density of states in bilayer graphene, especially at edges. Because of the parallel configuration, the conductance measured just is the sum of conductance of edges and the bulk body in bilayer graphene. Alternatively, the conductance fluctuation could be caused by the opening of the band gap. Note that the true value of the gap between the conduction and valence band does not occur at the K point because of the "Mexican hat" like energy dispersion at low energies.[53] Transport may be different when Fermi level locates across "Mexican" hat region. The third, metal induced doping underneath the contact and the adjacent region could contribute to the conductance fluctuation. The

different band structure in bilayer graphene may lead to much more complicated metal contact interface than that in monolayer. [59,45]

Finally, we turn to resistance fluctuation in the 4 layer, monolayer and bilayer graphene. All of samples exhibit pronounced resistance fluctuation near NP at most of temperatures examined. The phenomena indicate the strong disorder near NP, which is caused by the inhomogeneous charge distribution. The bilayer at 300 K is the exception. In bilayer graphene, the resistance fluctuation near NP is suppressed at 300 K. However, it is present in monolayer graphene. To explain the observed phenomenon, Fermi level E_F of graphene and its bilayer with respect to the carrier density n is depicted in Figure 6.17(d). In monolayer graphene, $E_F = \hbar v_F k = \hbar v_F \sqrt{n\pi}$ and the Fermi velocity $v_F == 10^6\ m/s$ is independent of n so that the interaction depends on the carrier density n only. In bilayer, the Fermi energy E_F is related to the electron (or hole) density by $E_F = \frac{1}{2}(-\gamma_1 + \sqrt{3n\pi a^2\gamma_0^2 + \gamma_1^2})$ in the regime $|E_F| < \gamma_1$, [60] where $a = 2.42\ \dot{A}$ is the lattice constant, $\gamma_0 \approx 3.15\ eV$ is the in-plane nearest neighbor tight-binding parameter and $\gamma_1 \approx 0.35\ eV$. From the Figure 6.17(d), it is clearly shown that the Fermi level E_F in bilayer changes much faster with n than the monolayer in the low carrier density regime. The thermal energy at 300 K leads to the mesoscopic Fermi energy broadening. The variation of charge carriers corresponding to E_F broadening near NP has the value of $7\times10^{11}\ cm^{-2}$ in bilayer, which is more than ten times then the value of $5\times10^{10}\ cm^{-2}$ in monolayer. The variation of charge carriers caused by thermal energy in bilayer graphene is efficient to smooth the charge inhomogeneity ($\sim 10^{12}\ cm^{-2}$) caused by unintentional doping. The charge domain or e-h puddles could be screened by the thermal energy. And therefore resistance fluctuation could be effectively suppressed in bilayer graphene at 300 K. in

addition, the electronic structure of four-layer graphene is strongly depending on its stacking order.[61] Currently, there is no efficient method to determine the stacking order of multilayer graphene. The weak temperature dependence of resistance fluctuation in our 4-layer sample discussed in Section 6.5.1 needs further investigation in the future.

6.5.4 Summary

We have shown that the unusual gating and temperature dependencies of the conductance and resistance fluctuation in graphene flakes with strong charge inhomogeneity (up to a few10^{12} cm^{-2}). UCF was observed in the 4 layer graphene. It means that the transport properties of thicker graphene were less affected by the surface impurities. The universal conductance fluctuations are absent in our SLG at both low and high gate bias regime. It is explained in terms of charge inhomogeneities, which are expected to cause carrier inelastic scattering either near or far away from the NP. Moreover, the conductance fluctuations in the bilayer graphene are pronounced away from NP and suppressed near NP. The features are robust in a wide range of temperatures investigated. The dominating mechanism behind should not be UCF. Several possible origins of the fluctuation are proposed. We also examined the resistance fluctuation in graphene flakes. The presence of resistance fluctuation may be caused when the carriers travel across the boundary between the adjacent charges domains. It could be used to indentify the disorder strength. Further studies are necessary before the conductance fluctuations in the bilayer graphene with strong charge inhomogeneities are fully understood.

6.6 Conclusion

In this chapter, we first discussed the electric characterization of graphene device on SiO_2 substrate without any special treatment. By examining carrier mobility and minimal conductivity, it is found that substrate interface and the charged impurities may greatly affect electrical transport of graphene. Thicker graphene devices receive less influence than the thinner because of the screening effect. Detailed investigation indicates that the charges induced by external electrostatics are mainly located within two or three layers near substrate surface.

Following that, we quantitatively investigated the density of charge impurities by studying conductance hysteresis in graphene devices. According to study on hysteresis magnitude, the trapped charges have the value of $\sim 5\times10^{11} cm^{-2}$, which are determined by the nature of thermally grown silicon oxide,. Note that the results agree well with the value of charge impurities ($\delta n = 2 \sim 15\times10^{11} cm^{-2}$ in "clean" SLG and BLG) obtained from other experimental method. The large spatial inhomogeneities of charged impurities (as high as $\sim 10^{13} cm^{-2}$) are most probably caused by the adsorbates on top of or under graphene flakes.

After that, magneto-transport properties at low temperature were discussed in those samples with large spatial inhomogeneities of charged impurities. Our experimental results indicate that SdH oscillations were suppressed in SLG and BLG while they survive in thicker graphene. In addition, UCFs were only found in four layer graphene, and suppressed in SLG and BLG. In addition, robust conduction fluctuations were found in the BLG in a wide range of temperatures. The possible mechanisms were discussed.

The performance of graphene became very sensitive to scattering origins (such as, charged impurities, surface phonon of substrate). The practical implication of our

experiments is that improvement in the oxide quality, surface passivation and surface cleaning of graphene will be crucial for performance improvement in graphene devices. Note that the mobility for graphene samples from HOPG ZYA is lower than that of the natural graphite. The fact indicates the high quality of graphene made from natural graphite in atomic level.

Finally, the work described here indicates necessary conditions that are needed to achieve high quality graphene devices. 1) High quality graphite should be used for exfoliation of graphene layer; 2) Trapped charges in the gate dielectric have to be eliminated. 3) Trapped impurities at the graphene surface, such water and organic residue, should be avoided by carrying out the deposition in a controlled and cleaned environment. We expect that graphene devices fabricated under these guidelines will be helpful in further investigation in chemical functionalization of graphene. Many novel physical properties that are expected to emerge when the disorder and edges could be precisely and separately controlled. Future work should clarify the exact causes for the interesting phenomena observed in our CNW samples.

References:

[1] S. Adam, E. H. Hwang, V. M. Galitski, and S. Das Sarma, "A self-consistent theory for graphene transport", *Proc. Natl. Acad. Sci. USA,* vol.104, pp.18392, 2007.

[2] P. B. Visscher, and L. M. Falicov, "Dielectric Screening in a Layered Electron Gas", *Phys. Rev. B,* vol.3, pp.2541, 1971.

[3] F. Guiena, "Charge distribution and screening in layered graphene systems", *Phys. Rev. B*, vol.75, pp.235433, 2007.

[4] H. Miyazaki, S. Odaka, T. Sato, S. Tanaka, H. Goto, A.Kanda, K. Tsukagoshi, Y. Ootuka, and Y. Aoyagi, "Inter-Layer Screening Length to Electric Field in Thin Graphite Film", *Appl. Phys. Express,* vol.1, pp.034007, 2008.

[5] K. S. Novoselov, A. K. Geim, S. V. Morozov, D. Jiang, M. I. Katsnelson, I. V. Grigorieva, S. V. Dubonos, and A. A. Firsov, "Two-Dimensional Gas of Massless Dirac Fermions in Graphene", *Nature*, vol.438, pp.197-200, 2005.

[6] K. S. Novoselov, E. McCann, S. V. Morozov, V. I. Fal'ko, M. I. Katsnelson, U. Zeitler, D. Jiang, F. Schedin, and A. K. Geim, "Unconventional quantum Hall effect and Berry's phase of 2π in bilayer graphene", *Nat. Phys.,* vol. 2, pp.177-180, 2006.

[7] M. Koshino and T. Ando, "Transport in bilayer graphene: Calculations within a self-consistent Born approximation", *Phys. Rev. B,* vol. 73, pp.245403, 2006.

[8] M. I. Katsnelson, "Minimal conductivity in bilayer graphene", *Eur. Phys. J. B,* vol.52, pp.151-153, 2006.

[9] J. Cserti, A. Csordás, and G. Dávid, "Role of the Trigonal Warping on the Minimal Conductivity of Bilayer Graphene", *Phys. Rev. Lett.,* vol.99, pp.066802, 2007.

[10] M. Nakamura and L. Hirasawa, "Electric transport and magnetic properties in multilayer graphene", *Phys. Rev. B*, vol.77, pp.045429, 2008.

[11] K. S. Novoselov, A.K. Geim, S.V. Morozov, D. Jiang, Y. Zhang, S.V. Dubonos, I.V. Grigorieva, and A.A. Firsov, "Electric Field Effect in Atomically Thin Carbon Films", *Science,* vol.306, pp.666-669, 2004.

[12] J. Martin, N. Akerman, G. Ulbricht, T. Lohmann, J. H. Smet, K. von Klitzing and A. Yacoby, "Observation of electron–hole puddles in graphene using a scanning single-electron transistor", *Nature Phys*., vol.4, pp.144-147, 2008.

[13] Y. W. Tan, et al. "Measurement of Scattering Rate and Minimum Conductivity in Graphene", *Phys. Rev. Lett*., vol.99, pp.246803, 2007.

[14] S. Cho and M. S. Fuhrer, "Charge transport and inhomogeneity near the minimum conductivity point in graphene", *Phys. Rev. B.*, vol.77, pp.081402, 2008.

[15] M. I. Katsnelson, A. K. Geim, "Electron scattering on microscopic corrugations in graphene", *Phil. Trans. R. Soc. A,* vol.366, pp.195-204, 2008.

[16] J. C. Meyer, C. O. Girit, M. F. Crommie, and A. Zettl, "Imaging and dynamics of light atoms and molecules on graphene", *Nature,* vol.454, pp.319-322, 2008.

[17] T. J. Booth, P. Blake, R. R. Nair, D. Jiang, E. W. Hill, U. Bangert, A. Bleloch, M. Gass, K. S. Novoselov, M. I. Katsnelson, and A. K. Geim, "Macroscopic Graphene Membranes and Their Extraordinary Stiffness", *Nano Lett*., vol.8, pp.2442-2446, 2008.

[18] J. Sabio et al., "Electrostatic interactions between graphene layers and their environment", *Phys. Rev. B*, vol.77, pp.195409, 2008.

[19] F. Schedin, A.K. Geim, S. V. Morozov, E. W. Hill, P. Blake, M. I. Katsnelson and K.S. Novoselov, "Detection of individual gas molecules adsorbed on graphene", *Nature Materials,* vol.6, pp.652-655, 2007.

[20] Wolf, S.; Tauber, R. N. Silicon Processing for the VLSI Era; Lattice Press: Sunset Beach, CA, 1986.

[21] T. Ando, A. B. Fowler and F. Stern, "Electronic properties of two-dimensional systems", *Rev. Mod. Phys.,* vol.54, pp. 437-672, 1982.

[22] J. Yan, Y. Zhang, P. Kim, and A. Pinczuk, "Electric Field Effect Tuning of Electron-Phonon Coupling in Graphene", *Phys. Rev. Lett.*, vol.98, pp.166802, 2007.

[23] J. Yan, E. A. Henriksen, P. Kim, and A. Pinczuk, "Observation of Anomalous Phonon Softening in Bilayer Graphene", *Phys. Rev. Lett*, vol.101, pp.136804, 2008.

[24] F. Guinea, "Charge distribution and screening in layered graphene systems", *Phys. Rev. B,* vol.75, pp.235433, 2007.

[25] M. L. Sadowski et al., "Landau Level Spectroscopy of Ultrathin Graphite Layers", *Phys. Rev. Lett.,* vol.97, pp.266405, 2006.

[26] J. Moser, A. Barreiro, and A. Bachtold, "Current-induced cleaning of graphene", *Appl. Phys. Lett*., vol.91, pp.163513, 2007.

[27] J. C. Meyer, A. K. Geim, M. I. Katsnelson, K. S. Novoselov, T. J. Booth, and S. Roth, "The structure of suspended grapheme membrane", *Nature,* vol.446, pp.60-63, 2007.

[28] A. Das et al., "Monitoring dopants by Raman scattering in an electrochemically top-gated graphene transistor", *Nature Nanotech.,* vol.3, pp.210-215, 2008.

[29] A. J. Bard and L. R. Faulkner, Electrochemical Methods, Fundamentals and Applications, John Wiley&Sons, New York, NY, 2nd edition, 2001.

[30] A. Kitahara and A. Watanabe. Electrical Phenomena at interfaces, Marcel Dekker, Inc., New York, 1984.

[31] J. Moser, et al., "The environment of graphene probed by electrostatic force microscopy", *App. Phys. Letts.,* vol.92, pp.123507, 2008.

[32] M. S. Dresselhaus and G. Dresselhaus, "Intercalation compounds of graphite", *Adv. Phys*., vol.51, pp.1-186, 2002.

[33] V.P. Gusynin and S. G. Sharapov, "Magnetic oscillations in planar systems with the Dirac-like spectrum of quasiparticle excitations. II. Transport properties", *Phys. Rev. B,* vol.71, pp.125124, 2005.

[34] D. A. Abanin and L. S. Levitov, "Conformal invariance and shape-dependent conductance of graphene samples", *Phys. Rev. B,* vol.78, pp.035416, 2008.

[35] J. R. Williams, D. A. Abanin, L. DiCarlo, L. S. Levitov, and C. M. Marcus, "Quantum Hall conductance of two-terminal graphene devices", *Phys. Rev. B,* vol.80, pp.045408, 2009.

[36] K.S. Novoselov, A.K.Geim, S.V.Morozov, D.Jiang, M.I.Katsnelson, I.V.Grigorieva, S.V.Dubonos and A.A.Firsov, "Two-Dimensional Gas of Massless Dirac Fermions in Graphene", *Nature,* vol.438, pp.197-200, 2005.

[37] Y. Zhang, Y.-W. Tan, H. L. Stormer and P. Kim, "Experimental observation of the quantum Hall effect and Berry's phase in graphene", *Nature,* vol.438, pp.201-204, 2005.

[38] Datta, S. Electronic Transport in Mesoscopic Systems, Cambridge Univ. Press, Cambridge, UK, 1995.

[39] C. W. J. Beenakker and H. van Houten, "Quantum Transport in Semiconductor Nanostructures", *Solid State Physics,* vol. 44, pp.1-111, 1991.

[40] M. S. Gupta, "Conductance Fluctuations in Mesoscopic Conductors at Low Temperatures", *IEEE Trans. Electron Devices,* vol. 41, pp.2093-2106, 1994.

[41] S. V. Morozov, K. S. Novoselov, M. I. Katsnelson, F. Schedin, L. A. Ponomarenko, D. Jiang, and A. K. Geim, "Strong Suppression of Weak Localization in Graphene", *Phys. Rev. Lett*., vol.97, pp.016801, 2006.

[42] N. E. Staley, C. P. Puls, and Y. Liu, "Suppression of conductance fluctuation in weakly disordered mesoscopic graphene samples near the charge neutral point", *Phys. Rev. B,* vol.77, pp.155429, 2008.

[43] C. Casiraghi, S. Pisana, K. S. Novoselov, A. K. Geim, and A. C. Ferrari, "Raman fingerprint of charged impurities in graphene", *Appl. Phys. Lett.*, vol.91, pp.233108, 2007.

[44] C. Stampfer, F. Molitor, D. Graf, K. Ensslin, A. Jungen, C. Hierold and L. Wirtz, "Raman imaging of doping domains in graphene on SiO_2", *Appl. Phys. Lett.*, vol.91, pp.241907, 2007.

[45] E. J. H. Lee, K. Balasubramanian, R. T. Weitz, M. Burghard, K. Kern, "Contact and edge effects in graphene devices", *Nature Nano*., vol.3, pp.486-490, 2008.

[46] Z. H. Ni, H. M. Wang, J. Kasim, H. M. Fan, T. Yu, Y. H. Wu, Y. P. Feng, Z. X. Shen, "Graphene Thickness Determination Using Reflection and Contrast Spectroscopy", *Nano Lett*., vol.7, pp.2758-2763, 2007.

[47] F. V. Tikhonenko, D. W. Horsell, R. V. Gorbachev, and A. K.Savchenko, "Weak Localization in Graphene Flakes", *Phys. Rev. Lett*., vol.100, pp.056802, 2008.

[48] D.-K. Ki, D. Jeong, J.-H. Choi, and H.-J. Lee, "Inelastic scattering in a monolayer graphene sheet: a weak-localization study", *Phys. Rev. B,* vol.78, pp.125409, 2008.

[49] H. M. Wang, Y. H. Wu, Z. H. Ni, and Z. X. Shen, "Electronic transport and layer engineering in multilayer graphene structures", *Appl. Phys. Lett*., vol.92, pp.053504, 2008.

[50] T. Ohta, A. Bostwick, T. Seyller. K. Horn, E. Rotenberg, "Controlling the Electronic Structure of Bilayer Graphene", *Science,* vol.313, pp.951-954, 2006.

[51] E. McCann, "Asymmetry gap in the electronic band structure of bilayer graphene", Phys. Rev. B, vol.74, pp.161403(R), 2006.

[52] J. B. Oostinga, H. B. Heersche, X. Liu, A. F. Morpurgo and L. M. K. Vandersypen, "Gate-induced insulating state in bilayer graphene devices", *Nat. Mater.,* vol.7, pp.151-157, 2007.

[53] E. V. Castro et al., "Biased Bilayer Graphene: Semiconductor with a Gap Tunable by the Electric Field Effect", *Phys. Rev. Lett*., vol.99, pp.216802, 2007.

[54] J. Nilsson and A. H. Castro Neto, "Impurities in a Biased Graphene Bilayer", *Phys. Rev. Lett.,* vol.98, pp.126801, 2007.

[55] V. V. Mkhitaryan and M. E. Raikh, "Disorder-induced tail states in gapped bilayer graphene", *Phys. Rev. B,* vol.78, pp.195409, 2008.

[56] M. Y. Han, B. Özyilmaz, Y. Zhang, and P. Kim, "Energy band-gap engineering of graphene nanoribbons", *Phys. Rev. Lett*. vol. 98, pp.206805, 2007.

[57] H. Wang, C. Choong, J. Zhang, K. L. Teo and Y. Wu, "Differential conductance fluctuation of curved nanographite sheets in the mesoscopic regime", *Solid State Commun.*, vol. 145, pp.341-345, 2008.

[58] Johan Nilsson, A. H. Castro Neto, F. Guinea, N. M. R. Peres, "Electronic properties of bilayer and multilayer graphene", *Phys. Rev. B,* vol. 78, pp.045405, 2008.

[59] G. Giovannetti, P. A. Khomyakov, G. Brocks, V. M. Karpan, J. van den Brink, and P. J. Kelly, "Doping Graphene with Metal Contacts", *Phys. Rev. Lett.*, vol.101, pp.026803, 2008.

[60] T. Ando, "Anomaly of Optical Phonons in Bilayer Graphene", *J. Phys. Soc. Jpn.,* vol.76, pp.104711, 2007.

[61] S. Latil and L. Henrard, "Charge Carriers in Few-Layer Graphene Films", *Phys. Rev. Lett.,* vol.97, pp.036803, 2006.

CHAPTER 7

CONCLUSIONS AND RECOMMENDATIONS ON FUTURE WORK

7.1 Conclusions

This thesis explored the electrical transport properties of new two dimensional materials: CNWs and graphene flakes. CNWs between normal electrodes (Ti) and superconducting electrodes (Nb) were investigated. Very interesting phenomena were observed from these nanodevices. The uncertainty of structure in CNWs does not allow us to clarify the exact causes of some of those interesting phenomena. Following that, transport results were studied in graphene, which is a well defined crystalline material. Some scattering origins were clarified in graphene flakes devices on SiO_2. The results are crucial for performance improvement in graphene devices for our further research objectives. Here, we briefly summarize the results obtained from this study.

Chapter 1 included an overview of the basic concepts relevant to the experimental results in Chapters 3-6. Chapter 1 began by discussing classification of carbon dimensionality, fabrication methods of two dimensional carbon and the electrical properties of mesoscopic system. Chapter 2 gives an overview of the work done so far on graphene modified. Chapter 3 presented the fabrication and measurement techniques used for CNWs and graphene samples. We first discussed the deposition and characterization of carbon nanowalls. And then, fabrication of CNWs devices was introduced. Following that, we discussed the fabrication of graphene, and the thickness determination using Raman and optical contrast spectroscopy. Following

that, we summarized the e-beam lithography fabrication method for graphene based devices. In addition, we introduced a model to study the visibility of graphene on different substrates, and we also presented some ideas how to produce a free standing graphene device with the help of the model. Finally, measurement setup and techniques that have been used to characterize transport properties of samples in this study were also discussed.

In Chapter 4, electrical transport property of carbon nanowalls using Ti electrodes was evaluated. The systematic study of the transport properties revealed that a narrow energy band gap that varies between 1.6-3.7 meV existed in the carbon nanowalls. In addition, excess conductance fluctuations were observed in the temperature range between 4 and 200 K, which are attributed to the quantum interference effect under the influence of thermally induced carrier excitation across a narrow bandgap. On the other hand, the sharp decrease of conductance fluctuation below 2.1 K is accounted for by the formation of a layer of He 4 superfluid on the nanowalls. Following that, the giant gap like behavior of dI/dV was discussed at liquid helium temperature. Its origin is not clear at the moment. Finally, weak localization is evident only when a strong magnetic field range was applied. The magnetic field suppresses the resistance giving rise to a negative magnetoresistance.

In Chapter 5, detailed studies were conducted on Nb/CNWs/Nb samples with different electrode gaps. It was found that proximity effect with the absence of supercurrent was observed from the samples with electrode gap of 239 and 429 nm. The resistance-temperature graph demonstrated a decrease in the resistance as the temperature was lowered below the transition temperature of niobium. The current corresponding to the differential resistance peaks was termed the critical current and it shows temperature dependence which can be fitted with both Josephson coupling

energy in the long, diffusive model and the Ginzburg-Landau relationship. From the differential resistance measurements, multiple Andreev reflection was observed. BTK model was applied to the samples with electrode gap of 185, 243, 387 and 702 nm. The experimental data did not agree well to BTK theory. These samples demonstrate different characteristics which could be an indication towards complicated systems. The explanation to our experimental results might not be conclusive but nevertheless they can serve as a platform and a guide for future experimental work.

In Chapter 6, we first discussed the electric characterization of graphene devices on SiO_2 substrate without any special treatment. By examining carrier mobility, minimal conductivity, it is found that substrate interface (e.g. phonon, charged impurities) greatly affect mobility and minimal conductivity of graphene on SiO_2 substrate. The thicker graphene devices received less influence than the thinner ones because of the screening effect, which is known as the fact that the charges induced by external electrostatics are mainly located within two or three layers near interface considering the intergraphene layer distance of 0.335 nm. Large mobility variations in monolayer graphene could be explained by a decrease in the screening effect. We quantitatively investigated the density of trapped charges by studying conductance hysteresis in graphene devices. According to study on the separation between NPs of the trace and retrace, the trapped charge impurities are determined by the nature of thermally grown silicon oxide, and they have the value of $\sim 5\times10^{11} cm^{-2}$. Note that the results agrees well with the value of charge density ($\delta n = 2 \sim 15\times10^{11} cm^{-2}$ in "clean" SLG and BLG) obtained from other experimental method. The large spatial inhomogeneities of charged impurities (as high as $\sim 10^{13} cm^{-2}$) are probably caused by the adsorbates on top of or under graphene flakes.

Magneto-transport properties at low temperature were discussed in those samples with large spatial inhomogeneities of charged impurities. Our experimental results indicate that SdH oscillations were suppressed in SLG and BLG while they survived in four layer graphene. In addition, UCFs were only found in four layer graphene, and suppressed in SLG and BLG. In addition, robust conduction fluctuations were found in the bilayer graphene in a wide range of temperatures. The possible mechanisms were discussed.

The performance of graphene became very sensitive to scattering origins (such as, trapped charges, surface phonon of substrate, and charged impurities). The practical implication of our experiments is that improvement in the oxide quality, surface passivation and surface cleaning of graphene will be crucial for performance improvement in graphene devices. Note that the mobility for graphene samples from HOPG ZYA is lower than that of the natural graphite. The fact indicates the high quality of graphene made from natural graphite in atomic level.

7.2 Recommendation for Future Work

Although in my work the experiments have been designed carefully and the study was carried out as systematically as possible, there are still many problems which remain unsolved. The problems include both the technical and scientific issues. Here, several key aspects are recommended for future research. The recommendations are divided into two parts.

For CNWs samples:

1. To fabricate CNWs devices sandwiched between ferromagnetic electrodes. Systematic transport studies can be conducted on these samples and a

comparison can be made between different electrode materials, such as NiFe, Fe, and Co.

2. It is very necessary to apply leads to only one carbon nanowall sheet. The attempt is particularly helpful in understanding the edge states in CNWs, which may result in possible intrinsic superconductivity or ferromagnetism.
3. Disorders and defects from carbon nanowalls are thought to influence the properties of carbon nanowalls. It is necessary to carry out systematic transport studies on samples which have been annealed in different gaseous environments (such as, vacuum, H_2, O_2, et al.). This study will be able to allow better understanding on the origin of those properties of the CNWs system.

For graphene samples

1. Based on our experimental results, surface adsorbates introduce charged impurities. Obtaining a clean graphene surface in the preparation is a crucial step for graphene devices with high preference. Because of the lack of heater in sample chamber of our cryostat, current induced cleaning of graphene is recommended before the transport measurement. An ultrahigh current density is able to remove contaminations adsorbed on the surface due to the local heating of the graphene. Note that the probability of damaging the device could be high by sending high currents.
2. In order to minimize the effect from substrates, suspended graphene based devices are recommended to be primary focuses for future work. Free standing graphene help to study their intrinsic transport properties and clarify influence of different external impurities.

3. To identify all possible factors which could tune the electronic properties of CNWs different from graphene flakes. And then study the impact of various factors on the transport properties of graphene flakes. The basic strategy was to isolate the influence of each factor by deliberately magnifying the corresponding factor to dominate all others. This method can be used to study material defects (such as, hydrogen terminated edges, hydrogenation on surface, etc), the presence of graphitic domains, the presence of amorphous hydrocarbon, invasiveness of metallic contacts, substrate.
4. It must be interesting to fabricate graphene samples with superconducting/ferromagnetic electrodes and study their transport properties, over various parameters such as electrode spacing, the number of graphene layers, graphene channel width and the carrier type/density.

LIST OF PUBLICATIONS

Journal papers with main contribution

[1] **Haomin Wang**, Catherine Choong, Jun Zhang, Kie Leong Teo and Yihong Wu, "Differential conductance fluctuation of curved nanographite sheets in the mesoscopic regime", *Solid State Commun.*, vol. 145, pp.341-345, 2008.

[2] **H. M. Wang**, Y. H. Wu, Z. H. Ni, and Z. X. Shen " Electronic transport and layer engineering in multilayer graphene structures", *Appl. Phys. Lett.*, vol. 92, pp.053504, 2008.

[3] **H. M. Wang**, Z. Zheng, Y.Y. Wang, J.J. Qiu, Z.B. Guo, Z. X. Shen, T. Yu, "Fabrication of graphene nanogap with crystallographically matching edges and its electron emission properties", *Appl. Phys. Lett.*, vol. 96, pp. 023106, 2010. (Note: the samples have been fabricated at NUS when the first author was a student at NUS.)

[4] Z. H. Ni, **H. M. Wang**, J. Kasim, H. M. Fan, T. Yu, Y. H. Wu, Y. P. Feng and Z. X. Shen, "Graphene Thickness Determination Using Reflection and Contrast Spectroscopy", *Nano Lett.*, vol. 7 (9), pp.2758 -2763, 2007.

Conference papers with main contribution

[5] **Wang Haomin**, Wu Yihong, Choong Kaishin Catherine, Zhang Jun, Teo Kie Leong, Ni Zhenhua and Shen Zexiang "Disorder Induced Bands in First Order Raman Spectra of Carbon Nanowalls" (P64), 2nd MRS-S Conference on Advanced Materials

(incorporating the Symposium on Physics and Mechanics of Advanced materials), Singapore, Jan. 18 th –Jan. 20 th, 2006.

[6] **Haomin Wang**, Yihong Wu, Kaishin Catherine Choong, Jun Zhang, Kie Leong Teo, Zhenhua Ni and Zexiang Shen "Disorder Induced Bands in First Order Raman Spectra of Carbon Nanowalls" The 6th IEEE International Conference proceedings on Nanotechnology, Cincinnati-Ohio, USA, July. 16 th -20 th , 2006.

[7] Yihong Wu, **Haomin Wang** and Catherine Choong, Two-dimensional carbon nanostructures and their electrical transport properties, 26th International Congress on Applications of Lasers & Elctro-Optics (ICALEO) Conference Date: 29 October - 01 November 2007.

[8] **Haomin Wang**, Yihong Wu, Zhenhua Ni, and Zexiang Shen " Electronic transport and layer engineering in multilayer graphene structures" P7.19 MRS Spring Meeting, San Francisco, CA, USA, April.24th-28th, 2008.

[9] Y. Wu, **H. Wang**, S.S. Kushvaha, S.Y.H. Lua, Electrical Transport Properties of Two-Dimensional Carbon Nanostructures, AVS 55th International Symposium and Exhibition October 19th-24th, 2008.

[10] **Haomin Wang**, Catherine Choong, Yihong Wu, Electrical Transport Properties of Carbon Nanowalls with Normal and Superconducting Electrodes, The 2008 Asia Conference on Nanoscience and Nanotechnology, 3rd-6th November 2008.

Other journal papers

[11] Guoquan Teo, **Haomin Wang**, Yihong Wu, Zaibing Guo, Jun Zhang, Zhenhua Ni and Zexiang Shen "Visibility study of graphene multilayer structures", *J. Appl. Phys*. vol.103, pp.124302, 2008.

[12] Z. H. Ni, **H. M. Wang**, Y. Ma, J. Kasim, Y. H. Wu, Z. X. Shen, "Tunable stress and controlled thickness modification in graphene by annealing", *ACS Nano.*, vol.2, pp.1033, 2008.

[13] Y.Y. Wang, Z. H. Ni, and Z. X. Shen, **H. M. Wang**, and Y. H. Wu "interference enhancement of Raman signal of graphene" *Appl. Phys. Lett.*, vol. 92, pp.043121, 2008.

[14] Y.Y. Wang, Z. H. Ni, T. Yu, Z. X. Shen, **H. M. Wang**, Y. H. Wu, W. Chen, A. T. S. Wee, "Raman studies of monolayer graphene: the substrate effect", J*ournal of Physical Chemistry C*, vol. 112, pp.10637, 2008.

[15] Z. H. Ni, H. M. Fan, X. F. Fan, **H. M. Wang**, Z. Zheng, Y. P. Feng, Y. H. Wu, Z. X. Shen "High temperature Raman spectroscopy studies of carbon nanowalls", *J. Raman Spectrosc.*, vol. 38 (11), pp.1449–1453, 2007.

Other conference papers

[16] Zhenhua Ni, Haiming Fan, Yuanping Feng, Zexiang Shen, **Haomin Wang** and Yihong Wu, "Raman Spectroscopy Investigation of Carbon Nanowalls". Z3.25, 2006 MRS Spring Meeting, San Francisco, CA, USA, April.17th-21th, 2006.